Corrosion and Environmentally-Assisted Cracking of Rapidly Solidified Neodymium-Iron-Boron Permanent Magnets

by

Steven A. Attanasio

B.S. Metallurgical Engineering
Lafayette College (1989)

Submitted to the
Department of Materials Science and Engineering
in partial fulfillment of the requirements for the degree of

Doctor of Philosophy

in

Materials Science and Engineering

at the

Massachusetts Institute of Technology

February 1996

© Massachusetts Institute of Technology, 1996. All rights reserved.

The author hereby grants to MIT permission to reproduce and
to distribute copies of this thesis document in whole or in part.

Signature of Author____
Department of Materials Science and Engineering, January 12, 1996

Certified by____
Ronald M. Latanision
Professor of Materials Science and Engineering
Thesis Supervisor

Accepted by____
Professor Michael F. Rubner
TDK Professor of Materials Science and Engineering
Chair, Departmental Committee on Graduate Students

MASSACHUSETTS INSTITUTE
OF TECHNOLOGY

MAR 26 1996

LIBRARIES

Corrosion and Environmentally-Assisted Cracking of Rapidly Solidified Neodymium-Iron-Boron Permanent Magnets

by

Steven A. Attanasio

Submitted to the Department of Materials Science and Engineering
in partial fulfillment of the requirements for the Degree of
Doctor of Philosophy in Metallurgy on January 12, 1996

Abstract

Neodymium-iron-boron (Nd-Fe-B) was discovered in 1983 and is currently the most powerful permanent magnet known to man. Nd-Fe-B is lighter and less expensive to produce than comparable permanent magnets, and the alloy is therefore capable of providing significantly more magnetic flux per unit weight or volume than any other permanent magnet available. Such advantages have provided a strong incentive for manufacturers to replace existing permanent magnet materials with Nd-Fe-B. Despite the potential benefits of employing the Nd-Fe-B magnet, however, its known susceptibility to corrosion has been cited as a problem with its use in many applications. Magnetic flux is dependent upon the volume of magnetic material present, and corrosive metal loss therefore directly decreases the power of a permanent magnet. If a substantial portion of a permanent magnet is lost due to corrosive dissolution, the magnet can eventually become incapable of performing its intended function. Many parts of industrial machines are exposed to potentially corrosive environments, and the technological impact of this new alloy may thus be limited unless its corrosion problems can be reduced.

The current research project was initiated in an attempt to address this possible obstacle to the viability of the Nd-Fe-B magnet. The project was divided into two related tasks: studying the corrosion behavior of the alloy in an attempt to learn about the types of corrosion which control its behavior, and devising a practical, cost-effective corrosion control method which is capable of protecting the alloy from degradation in service. Both electrochemical and microscopic investigation methods were utilized in the present study. Electrochemical techniques were employed in an effort to determine corrosion rates and mechanisms; the specific methods utilized include potentiodynamic polarization, electrochemical impedance spectroscopy (EIS), galvanic corrosion testing, and hydrogen permeation testing. Microscopy was used in order to evaluate the dissolution morphology of the alloy. Corroded surfaces were analyzed using a scanning electron microscope, a confocal laser microscope, and an electron probe microanalyzer. Since the alloy is expected to be exposed to in-service environments containing chloride ions as well as sulfate ions, testing was performed in aerated, non-agitated NaCl and Na_2SO_4 solutions at 23°C, and to a lesser extent in both NaCl and Na_2SO_4 at 80°C.

Pitting attack was found to be the primary form of corrosion in rapidly solidified Nd-Fe-B alloys in NaCl and Na_2SO_4 solutions at both 23°C and 80°C. It is believed that this form of corrosion has not been previously reported for RSP Nd-Fe-B. Pits were found to initiate within 15 minutes of immersion, and propagated to a depth of more than 200 μm within three months in NaCl at 23°C. Intergranular corrosion was not found to be a significant attack mode in rapidly solidified Nd-Fe-B. It had been previously believed by many researchers that intergranular corrosion was the primary mode of attack for this material.

Pitting is considered to be a less severe form of attack than intergranular corrosion in terms of the magnetic flux loss expected to result from corrosive attack during service. Flux loss is directly related to the volume of metal dissolved, rather than to the rate of metal penetration. Since pitting results in a high metal penetration rate but only a moderate loss in metal volume, the corrosion problems of the alloy are not as serious as they would be if intergranular attack were occurring. Corrosive metal loss is still expected to be a problem for this material in many environments, however. Permanent magnets are typically thin by design, and even the moderate metal loss associated with pitting can cause such a magnet to lose a significant percentage of its flux over time. The actual amount of pitting which can be tolerated will depend upon the geometry and the design requirements of the magnet considered.

Pits were found to initiate preferentially but not exclusively at the boundaries between adjacent rapidly solidified ribbons in the material. Enrichment of both neodymium and oxygen was detected at the ribbon boundaries, as a result of oxidation of the free ribbon surfaces prior to hot pressing. Pores were also found to be located preferentially at the ribbon boundaries, as a result of incomplete metallurgical bonding of the adjacent ribbons during pressing. It is believed that pit initiation may be related to the pre-existing porosity within the material; pit initiation at pore sites is thought to occur by a microcrevice type of mechanism.

Environmentally-assisted cracking (EAC) of Nd-Fe-B was found to occur under free corrosion conditions in NaCl, and to a lesser extent in Na_2SO_4. Hydrogen permeation tests indicate that the fracture is related to an *anodic* cracking mechanism rather than to hydrogen embrittlement. It is believed that the observed EAC may be specifically related to the presence of pitting attack. The combination of localized anodic dissolution and stress concentration within a pit can conceivably lead to crack initiation and ultimately to fracture. Insoluble corrosion products formed as a result of metal dissolution within pits can also contribute to fracture by exerting a wedging action which creates tensile stresses at the base of cavities in the material.

Two modes of corrosive degradation can therefore be identified for RSP Nd-Fe-B alloys: metal loss and anodic cracking. Both degradation modes can lead to a loss of magnetic flux, and eventually to magnet failure if corrosion is not controlled. In particular, the elimination of pitting attack should be targeted in order to increase the resistance of Nd-Fe-B to both magnetic flux loss and anodic cracking.

It has been conclusively demonstrated that zinc coatings are capable of providing complete protection to Nd-Fe-B at breaks in the coating. A zinc coating-organic coating protection scheme thus appears to be a cost-effective corrosion control method which is able to provide both barrier and sacrificial protection to Nd-Fe-B. It may additionally be possible to produce a magnet with increased resistance to pitting attack by modifying the ribbon boundaries, perhaps via improved processing techniques which result in full densification of the metal. Elimination of pre-existing porosity may remove the sites of pit initiation. It is believed that several levels of corrosion protection can be conferred to Nd-Fe-B through the use of both ribbon boundary modifications and a zinc coating-organic coating protection scheme. The zinc and organic coatings will initially act as barrier layers which shield the Nd-Fe-B base metal from the corrosive electrolyte. If the coating is penetrated due to cracking or prolonged corrosion of the zinc, the sacrificial coating will protect the exposed Nd-Fe-B. When the protection is finally exhausted due to zinc consumption, the Nd-Fe-B will have improved pitting resistance due to the ribbon boundary modifications.

Thesis Supervisor: Ronald M. Latanision, Professor of Materials Science and Engineering

Table of Contents

Page

Abstract 2

Table of Contents 4

List of Figures 6

List of Tables 11

Acknowledgements 12

Dedication 15

1. Introduction 16

2. Literature Review 17

2.1 Permanent Magnets 17

2.2 Characteristics of Nd-Fe-B 25

2.3 Corrosion of Nd-Fe-B 39

3. Research Objectives 49

4. Experimental Work 50

4.1 Materials 50

4.2 Electrolytes 50

4.3 Electrochemical Testing 51

4.4 Microscopy 68

5. Corrosion Behavior of the Alloy 72

5.1 Polarization Behavior of h.p. and d.u. Alloys . . 73

5.2 Corrosion Behavior of Nd-Fe-B at Short Times (≤ 1 hour) . 88

5.3 Corrosion Behavior at Longer Immersion Times . . 112

5.4 Sites of Pit Initiation 162

6. Environmentally-Assisted Cracking 207

6.1 Observation of Environmentally-Assisted Cracking . . 208

- 6.2 Mode of Environmentally-Assisted Cracking . . . 211
- 6.3 Additional Topics Related to EAC 227

7. Corrosion Control Methods 244
   - 7.1 Corrosion Control via Sacrificial Zinc Coatings . . 245
   - 7.2 Corrosion Control by Ribbon Boundary Modification . 279
8. Conclusions 285
9. Future Work 287
10. Appendices 289
    - 10.1 Fundamentals of Electrochemical Methods . . . 290
    - 10.2 Equivalent Circuit Modeling of EIS Data . . . 321
    - 10.3 Kramers-Kronig Transformations 360
    - 10.4 Source Code for KK Transformation Program . . 370
    - 10.5 Evaluation of Cracking Mechanism 2 via LEFM . . 375
11. Bibliography 383
12. Biographical Note 389

List of Figures

Page

Figure 2.1 Automotive applications involving permanent magnets . 18
Figure 2.2 Hysteresis loop for a typical permanent magnet . . 20
Figure 2.3 Typical demagnetization curves for Nd-Fe-B and $SmCo_5$. 22
Figure 2.4 Schematic representation of the process used to fabricate die upset magnets 25
Figure 2.5 Magnetic flux lines emerging from a die upset alloy which has been magnetized along its c-axis . . . 26
Figure 2.6 Micrograph showing porosity typical of hot pressed Nd-Fe-B 27
Figure 2.7 Microstructure of h.p. Nd-Fe-B alloys . . . 31
Figure 2.8 Microstructure of d.u. Nd-Fe-B alloys . . . 31
Figure 2.9 Ribbon structure for h.p. and d.u. alloys . . . 33
Figure 2.10 Anodic polarization of sintered Nd-Fe-B in 0.5M H_2SO_4 . 41
Figure 2.11 Polarization curves for sintered magnets in 0.5M Na_2SO_4 . 41
Figure 2.12 Anodic polarization of sintered Nd-Fe-B in various solutions 42
Figure 2.13 Cyclic voltammograms for Nd-Fe-B in NaH_2PO_4 . . 43
Figure 2.14 Proposed corrosion mechanism of sintered Nd-Fe-B in Co-free alloys 45
Figure 4.1 Construction of a typical electrode for electrochemical testing 53
Figure 4.2 Schematic representation of the cell setups used in polarization tests and EIS tests 55
Figure 4.3 Cartesian and polar representations of impedance . . 60
Figure 4.4 Discrete steps involved in the hydrogen permeation technique 64
Figure 4.5 Schematic representation of the permeation cell and the sample mounting assembly 66
Figure 4.6 Schematic representation of the hydrogen permeation sample arrangement 67
Figure 5.1 Anodic polarization of h.p. and d.u. alloys at 30°C . . 74
Figure 5.2 Anodic and cathodic polarization of h.p. Nd-Fe-B at 30°C . 75
Figure 5.3 Cathodic polarization of h.p. and d.u. alloys at 30°C . . 76
Figure 5.4 Anodic polarization of h.p. and d.u. alloys at 80°C . . 78
Figure 5.5 Anodic and cathodic polarization of h.p. Nd-Fe-B at 80°C . 79
Figure 5.6 Cathodic polarization of h.p. and d.u. alloys at 80°C . . 80
Figure 5.7 EIS data after 1 hour in NaCl 89
Figure 5.8 EIS data taken from the work of Dawson and Ferreira . 91

Figure 5.9 Cyclic anodic polarization in NaCl at 30°C . . . 92
Figure 5.10 Potentiostatic anodic polarization in NaCl at 30°C . . 93
Figure 5.11 Low magnification SEM image of a Nd-Fe-B surface after 15 minutes of immersion (NaCl, 23°C) . . . 95
Figure 5.12 SEM image of a pit present on Nd-Fe-B after 1 hour of immersion 95
Figure 5.13 Confocal images of pits profiled after 15 minutes and 1 hour of immersion in NaCl at 23°C 99
Figure 5.14 Representative pit depth distribution after 15 minutes and 1 hour 101
Figure 5.15 EIS data after 1 hour at open-circuit in Na_2SO_4 . . 102
Figure 5.16 Forward and reverse anodic polarization in Na_2SO_4 . . 104
Figure 5.17 Potentiostatic anodic polarization in Na_2SO_4 . . . 104
Figure 5.18 Confocal image of a pit profiled after 15 minutes in Na_2SO_4 . 105
Figure 5.19 Confocal images of pits profiled after 1 hour of immersion in NaCl at 80°C 109
Figure 5.20 Cyclic anodic polarization in NaCl as a function of time . 113
Figure 5.21 EIS data after 1, 24, and 72 hours of immersion . . 114
Figure 5.22 Nyquist representation of EIS data after 1, 24, and 72 hours 115
Figure 5.23 Cathodic polarization of Nd-Fe-B after 1, 24, and 72 hours . 117
Figure 5.24 SEM image of a representative pit after 12 hours of immersion 121
Figure 5.25 Confocal microscope image and profile of a 12 hour pit . 121
Figure 5.26 Representative pit depth distributions over a 72 hour period . 123
Figure 5.27 Confocal microscope image and profile of a pit after 24 hours 125
Figure 5.28 Confocal microscope image and profile of a pit after 72 hours 125
Figure 5.29 Confocal microscope images and profiles of pits after 1 month 129
Figure 5.30 SEM images of a pit after 3 months 131
Figure 5.31 Representative pit depth distribution during 3 months . 133
Figure 5.32 Dissolution of the surface between the pits, as observed on a 12 hour sample 135
Figure 5.33 Dissolution of the metal surface as shown at low magnification 135
Figure 5.34 Surface dissolution as illustrated in the confocal microscope . 137
Figure 5.35 Schematic diagrams illustrating general and intergranular attack 142
Figure 5.36 Calculated and measured penetration rates in Nd-Fe-B . 145
Figure 5.37 A high resolution SEM image of the Nd-Fe-B surface . 149
Figure 5.38 SEM image illustrating the insoluble corrosion products surrounding a pit 153
Figure 5.39 A high resolution SEM image showing the morphology of corrosion products 153
Figure 5.40 SEM images illustrating the absence of substantial

inter-ribbon attack 155
Figure 5.41 Confocal laser microscope image of Nd-Fe-B after 1 hour of immersion in NaCl showing pits and ribbon boundaries 165
Figure 5.42 SEM image of Nd-Fe-B after 24 hours of immersion showing pit/ribbon boundary intersection 167
Figure 5.43 SEM image illustrating preferential location of pits on boundaries 167
Figure 5.44 Confocal image showing pits and ribbon boundaries 171
Figure 5.45 Two images of the same pit formed on Nd-Fe-B illustrating corrosion product blockage of the ribbon boundary 173
Figure 5.46 SEM photos showing corrosion product around a pit 177
Figure 5.47 EPMA quantitative line scan across a ribbon boundary 181
Figure 5.48 SEM image of an as-polished surface showing pre-existing porosity, predominately at the ribbon boundaries 187
Figure 5.49 A magnified view of a portion of Figure 5.48 187
Figure 5.50 SEM image of an as-polished sample 189
Figure 5.51 SEM image of an as-polished sample 189
Figure 5.52 Secondary electron image of an as-polished sample 199
Figure 5.53 Backscattered electron image of an as-polished surface 199
Figure 5.54 Schematic representation of a pore whose tip has been removed by machining 202
Figure 5.55 Vertical representation of the schematic in Figure 5.54 202
Figure 6.1 Rate of EAC of Nd-Fe-B under two conditions: open-circuit and coupled to zinc 208
Figure 6.2 Extent of cracking exhibited by uncoupled and coupled samples 209
Figure 6.3 Cathodic polarization of Nd-Fe-B in NaCl at 23°C 212
Figure 6.4 Flux of hydrogen through 310 stainless steel as a function of applied current in 8% HCl 214
Figure 6.5 Hydrogen permeability through an aluminum alloy in 3% NaCl as a function of applied potential 215
Figure 6.6 Effect of pitting on hydrogen generation at anodic potentials 216
Figure 6.7 Effect of anodic and cathodic polarization on the rates of environmentally-assisted cracking 217
Figure 6.8 Effect of electrode potential on the rate of EAC 218
Figure 6.9 Effect of electrode potential on EAC with axes inverted 218
Figure 6.10 Absorption and permeation of hydrogen through a 12% Cr martensitic stainless steel in 3% NaCl at 25°C 221
Figure 6.11 Permeation transients for three different input conditions (E_{corr}, E_{couple}, -1250 mV) 223
Figure 6.12 Cumulative hydrogen throughput for the three input conditions 225
Figure 6.13 Effect of hydrogen on the EAC of Nd-Fe-B 225

Figure 6.14 Effect of electrolyte anion on the rate of EAC . . 228
Figure 6.15 Residual stresses measured in a hardened steel which had been subjected to three different types of machining treatments 230
Figure 6.16 Effect of machining upon the cracking rate of Nd-Fe-B . 232
Figure 6.17 Schematic illustration of two mechanisms which could possibly lead to the anodic cracking of Nd-Fe-B . . 238
Figure 7.1 Anodic and cathodic polarization of Nd-Fe-B and zinc at 30°C 249
Figure 7.2 Anodic and cathodic polarization of Nd-Fe-B and zinc at 80°C 250
Figure 7.3 Galvanic corrosion data for a Zn : Nd-Fe-B couple at 30°C . 252
Figure 7.4 Galvanic corrosion data for a Zn : Nd-Fe-B couple at 80°C . 253
Figure 7.5 Extrapolation of the Tafel region of the Nd-Fe-B anodic polarization curve to E_{couple} 257
Figure 7.6 Nd-Fe-B samples which were at open-circuit and coupled to Zn 263
Figure 7.7 Pourbaix diagrams for Fe, Nd, and B at 25°C . . 265
Figure 7.8 Rate of EAC of Nd-Fe-B at open-circuit and when coupled to Zn 270
Figure 7.9 Extent of cracking exhibited by uncoupled and coupled samples 271
Figure 7.10 Galvanic current values measured during long-term coupled test 276
Figure 10.1 Schematic illustration of a potentiostat . . . 291
Figure 10.2 Schematic anodic polarization curves indicating spontanteous passivation, active-passive behavior, and active behavior . 292
Figure 10.3 Typical cathodic polarization curves in near-neutral solutions 293
Figure 10.4 Use of the Tafel extrapolation technique to estimate i_{corr} . 294
Figure 10.5 Cyclic anodic polarization scans with and without hysteresis 295
Figure 10.6 Potentiostatic anodic polarization tests where the material exhibits charge-transfer dissolution, passivation, and local attack 297
Figure 10.7 Schematic representations of interfacial double layers . 300
Figure 10.8 Typical Randles circuit for a simple electrochemical system . 302
Figure 10.9 EIS data from a test RC circuit 303
Figure 10.10 Series processes for electrochemical reactions . . 307
Figure 10.11 General equivalent circuit model for a corroding metal . 308
Figure 10.12 Metallic coatings which act as an effective barrier layer and permit base metal exposure due to coating penetration . 313
Figure 10.13 Principle of cathodic protection for a metal which does not exhibit an active-passive transition 315
Figure 10.14 Analysis of a coating metal - base metal system using the mixed potential theory 317
Figure 10.15 Initial equivalent circuit model 324
Figure 10.16 Intermediate equivalent circuit model, which has been reduced using information from polarization curves . . . 328

Figure 10.17 Current paths through the surface and through the pit . 329
Figure 10.18 Intermediate equivalent circuit model which has been reduced using standard parallel resistor and capacitor relationships . 330
Figure 10.19 Final equivalent circuit model for Nd-Fe-B after 1 hour . 333
Figure 10.20 EIS data after 1 hour of immersion in NaCl . . . 334
Figure 10.21 Simulated data for a sinusoidal cycle with negative resistance 335
Figure 10.22 Kramers-Kronig transformations of the real component and the imaginary component of EIS data in NaCl . . 338
Figure 10.23 Kramers-Kronig transformations after removal of non-conforming EIS data 339
Figure 10.24 EIS data for 1 hour, NaCl with non-conforming points removed 342
Figure 10.25 EIS data with superimposed CNLS fit . . . 344
Figure 10.26 Kramers-Kronig transformations of 24 hour data . . 351
Figure 10.27 Equivalent circuit used to model the data exhibiting a pseudoinductive loop at low frequencies . . . 352
Figure 10.28 EIS data from 24 hour tests with CNLS fit . . . 353
Figure 10.29 $R_{t,pit}/F$ at immersion times from 1 to 72 hours . . 354
Figure 10.30 Changes in the charge-transfer resistance associated with pits before and after the data were corrected for area increases . 357
Figure 10.31 Flow chart of overall sequence of the imaginary-to-real Kramers-Kronig transformation 362
Figure 10.32 Overview of the generation of the extended data set . . 364
Figure 10.33 Division of the impedance data into segments to facilitate polynomial fitting 365
Figure 10.34 Polynomial fitting to one segment of the acquired data . 366
Figure 10.35 Extended data set which was generated at closely spaced angular frequencies by interpolation of the measured data . 367
Figure 10.36 Estimate of the thickness at the tip of a growing pit in the cylindrical samples used for the EAC investigation . . 382
Figure 10.37 Determination of the thickness after 9 days of immersion, using geometric considerations 382

List of Tables

Page

Table 2.1 Applications of permanent magnets 18

Table 2.2 Approximate cost of Sm-Co and Nd-Fe-B magnets . . 21

Table 2.3 Room termperature magnetic properties of Sm-Co and Nd-Fe-B 22

Table 2.4 Cost of $SmCo_5$ and Nd-Fe-B on a per energy product basis . 23

Table 2.5 Temperature limitations for Sm-Co and Nd-Fe-B alloys . 24

Table 2.6 Typical magnetic properties of h.p. and d.u. alloys . . 27

Table 4.1 Standards used in the calibration of the EPMA . . 71

Table 5.1 Average electrochemical data from polarization of Nd-Fe-B . 77

Table 5.2 A comparison of the representative pit depth distributions at 23°C and 80°C 107

Table 5.3 Representative pit depth distributions after 1 and 12 hours . 119

Table 5.4 Depths, widths, and depth-to-radius ratios for pits at 1, 24, and 72 hours of immersion 127

Table 5.5 Representative pit depth distributions for 3 months of immersion 133

Table 5.6 Calculated penetration rates for general and intergranular attack 146

Table 5.7 Estimated percent flux loss resulting from pitting attack . 160

Table 5.8 Likelihood of the occurrence of pitting and crevice corrosion under certain conditions 194

Table 6.1 Estimated hydrogen reduction current densities at various values of electrode potential 212

Table 7.1 Average data from galvanic corrosion testing of Zn/Nd-Fe-B 254

Table 7.2 Cathodic polarization experienced by Nd-Fe-B on coupling to Zn 255

Table 7.3 Predicted values from the mixed potential theory analysis . 257

Table 7.4 Predicted penetration rates for coupled Nd-Fe-B . . 259

Table 7.5 Deviations between measured data from galvanic corrosion tests and predicted data from the mixed potential theory . 260

Table 7.6 ICP-AES solution analysis for long-term immersion tests . 268

Table 10.1 Abbreviations used in equivalent circuit modeling . . 325

Table 10.2 Average error for the full and modified EIS data sets . . 340

Table 10.3 Parameters obtained from the CNLS fit to the EIS data . 345

Table 10.4 Capacitance values for ferrous metals in various test solutions after short immersion times (< 5 hours) . . . 346

Table 10.5 Parameters obtained from CNLS fit to 24 hour data . . 354

Table 10.6 Plane-strain fracture toughness values for three metals . 379

Acknowledgements

I am greatly indebted to Professor Ron Latanision for giving me the opportunity to plan and execute my own research program under his able guidance. His unfailing focus on the practical impact of my results prevented me from falling into the common research pitfall of becoming fixated on the scientific aspects of my work. On a personal level, I am extremely grateful for the respect and kindness which Professor Latanision has shown me during my stay in the H.H. Uhlig Corrosion Laboratory. His patience during my struggles and his sincere happiness in my times of success will not be forgotten.

I would also like to thank Professors John Vandersande and Linn Hobbs for agreeing to serve on my thesis committee, and for providing me with constructive criticism which has added substantially to the quality of the final thesis. The outstanding teaching ability of Professor Donald Sadoway is also acknowledged; the current work was greatly influenced by several of Professor Sadoway's beliefs and research philosophies.

Dr. Bryce Mitton of the H.H. Uhlig Corrosion Laboratory has been a research collaborator and a great friend to me during my stay at MIT. He is the one person whom I really cannot thank enough for his time and effort on my behalf. Bryce's insight in terms of how a particular experiment can best be performed has been invaluable to me during this work; his willingness to critically review my work and offer useful suggestions was also important.

The hydrogen permeation experiments described in Chapter 6 could not have been completed without the able assistance of Dr. En-Hou Han and Mr. Charles Clay. Dr. Han was instrumental in solving some of the difficult sample preparation problems which impeded the progress of the permeation experiments. Charles was a very talented and dedicated undergraduate assistant who took on a task that I myself had failed at, that of successfully cutting thin Nd-Fe-B wafers for the permeation tests.

There are also a great number of people whom I would like to thank for their able technical assistance in specific areas. Thanks to Len Sudenfield for his expertise in scanning electron microscopy, to Neel Chaterjee for his help with electron probe microanalysis, to Gina Middaugh for assistance with confocal microscopy, to Rich Pirelli for his work in palladium deposition, and to Cathy Jordan for her help in microscopy. Special thanks go to Jim Kerner of Lehigh University for expertise in high resolution SEM work. Assistance was also received from several people in various fields of electrochemistry. Thanks to Dr. Omar Abdul-Hamid (hydrogen permeation), Dr. Krassimir Nenov (electrochemical impedance spectroscopy), Dr. Marius Kloppers (polarization testing and computer-assisted data acquisition), and Dr. En-Hou Han (environmentally-assisted cracking).

All test samples utilized in the present study were kindly furnished by the Magnequench® division of the General Motors Corporation. I would like to acknowledge the assistance of the following people at Magnequench®: Tim Trueblood, John Shain, and Ed Welker; special thanks go to Roberta Mason for her tireless efforts in answering my many questions about the Nd-Fe-B magnets. Thanks also to Dr. Carl Fuerst of the G.M. Research Laboratory for providing $Nd_2Fe_{14}B$ samples.

I would also like to acknowledge several additional scientists and engineers who have served as mentors to me over the past decade. My professors from Lafayette College (Chester Van Tyne, Mehmet Uz, Fred Sauerwine, and C.B. Gill) are responsible for imparting a great deal of metallurgy knowledge to me, along with a desire to continue my studies. A summer internship under Dr. John Murray of the Naval Surface Warfare Center in Annapolis was also very important to my professional development. I'd also like to thank Dr. Ron Outlaw of NASA Langley for his interest in me during his stay at MIT.

I would also like to express my gratitude to the teachers of the Westwood (N.J.) Regional School System, whose hard work helped to prepare me for college and beyond. On a personal level, I must thank all of the present and past members of the H.H. Uhlig Corrosion Laboratory for their friendship during the years of my stay at MIT. Thanks also to all of my friends (especially Mr. Chris Saunders) who have helped me to forget my research anxiety during our too-infrequent social gatherings over the past few years.

There were a few people in my life who were even more critical to the success of this project than any of the individuals mentioned above: my fianceé, Miss Cathy Jordan, and my parents, Madeline and Arthur Attanasio.

It is likely that Cathy is the only person who truly knows how difficult this project was for me. She was there to hear all of the complaints, the frustration, and especially the desperation during times when I honestly didn't think I was going to make it. Her ability to understand and empathize with my struggles has been a great benefit to me along the way, as have all of the wonderful times we have spent together during the past years. As for my parents and family, I can only say that their unconditional support has been essential to the completion of my education. It is to my parents that I owe my self-esteem, my work ethic, and my belief that just being a good person is more important than anything else in life. Their emotional support has kept me from despairing even when the research work got very difficult, and their financial support enabled me to have some of the good things in life even when I wasn't earning enough money to afford them myself.

My sincere thanks go out to each and every one of the contributors mentioned above.

This thesis is dedicated to Madeline and Arthur Attanasio

for their lifelong love and devotion

1. Introduction

Neodymium-iron-boron (Nd-Fe-B) was discovered in 1983 and is currently the most powerful permanent magnet known to man. Nd-Fe-B is also lighter and less expensive to produce than comparable permanent magnets, and the alloy is therefore capable of providing significantly more magnetic flux per unit weight or volume than any other permanent magnet available. Such advantages have provided a strong incentive for manufacturers to replace existing permanent magnet materials with Nd-Fe-B.

Despite the potential benefits of employing the Nd-Fe-B magnet, however, its known susceptibility to corrosion has been cited as a problem with its use in many applications. Magnetic flux is dependent upon the volume of magnetic material present, and corrosive metal loss therefore directly decreases the power of a permanent magnet. If a substantial portion of a permanent magnet is lost due to corrosive dissolution, the magnet can eventually become incapable of performing its intended function. Many parts of industrial machines are exposed to potentially corrosive environments, and the technological impact of this new alloy may thus be limited unless its corrosion problems can be reduced.

The current research project was initiated in an attempt to address this possible obstacle to the viability of the Nd-Fe-B magnet. The project was divided into two related tasks: studying the corrosion behavior of the alloy in an attempt to learn about the types of corrosion which control its behavior, and also to devise a practical, cost-effective corrosion control method which is capable of protecting the alloy from degradation in service.

2. Literature Review

2.1 Permanent Magnets

Permanent magnets are typically used to supply magnetic energy in motors and other engineering devices. Magnetic flux is present at the surface of a permanent magnet. This flux can be employed to perform useful work if a small opening (known as an air gap) is designed into the magnetic circuit, thus creating a usable magnetic field in the gap [1].

Applications of permanent magnets are numerous. Permanent magnets are used in brushless d.c. motors, voice coil actuators, accelerator systems such as free electron lasers and synchrotron light sources [2], stepper motors, synchronous motors, limited motion actuators [3], industrial machine tool drives, computer disk drives, aerospace flight control surface acuators, and aerospace generators [4]. A more extensive list of permanent magnet applications is shown in Table 2.1. A graphical example of the pervasive nature of these magnets is shown in Figure 2.1, which illustrates automotive applications that involve permanent magnets.

In addition to the traditional permanent magnet applications outlined above, new markets are also emerging which involve devices that are intended to replace components based on electromagnets [5,6,7]. Electromagnets produce a magnetic field by passing an electrical current through a wound coil. Replacement of electromagnets with permanent magnets allows the heating losses associated with the wound field to be eliminated, thus improving motor efficiency. Permanent magnet devices are smaller and lighter than those employing a wound coil, and have a lower overall cost since no power supply is needed to maintain the field excitation [6]. Development of improved, lower cost permanent magnets is expected to lead to an expansion of the permanent magnet market [4].

Table 2.1 Applications of Permanent Magnets [8].

General property of magnets used	More specific method of application	Particular devices
Mechanical forces exerted by or on magnets	Torque on magnet in magnetic field	Compass, magnetometer
	Attraction between magnet and iron or other magnets	Notice boards, games, door catches, magnetic filtration, retrieval devices, drives and couplings, switches, thermostats.
	Attraction induced between other iron parts	Reed switches, railway warning systems, magnetic clutches
	Repulsion: magnet and magnet	Bearings, levitated transport, toys
	Electromagnet and magnet	Brake for coil winder
Electromagnetic forces	Moving coil devices	Loudspeakers and telephone receivers, instruments, d.c. motors
	Moving magnet devices	Synchronous and brushless motors, clocks, hysteresis motors
	Moving iron devices	Some telephone receivers, polarized relays
Electromagnetic induction	Relative motion of coil and magnet	Flux measurement, generators, sensing devices, microphones
	Eddy currents	Damping devices, brakes, speedometers
Forces on moving electrons and ions	Focusing	Electron microscope, klystron, traveling wave tube
	Crossed field action	Magnetron, mass spectrometer, ion pump, blow-out on switches
Magnetic resonance	NMR	Chemical analysis, magnetocrystalline anisotropy
Action of magnetic fields on solid and liquid media	Magnets in magnetic circuits	Saturistors, magnetizers and magnetic heat treatment
	Electronic and semiconductor	Wave guides, circulators, Hall and magnetoresistance devices

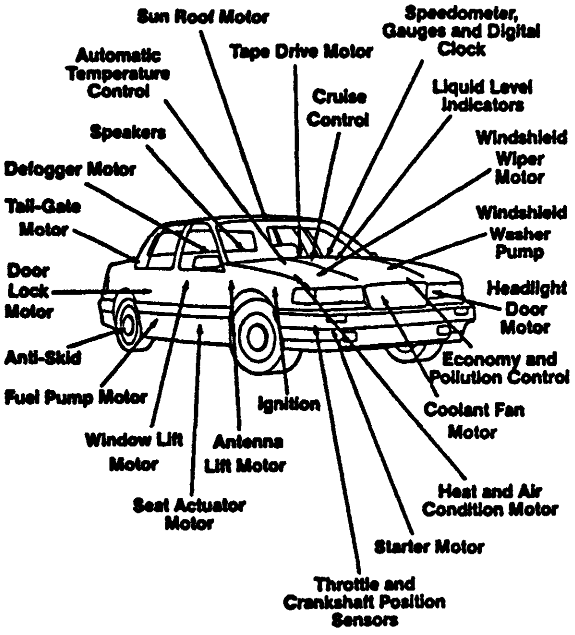
Sun Roof Motor
Speedometer, Gauges and Digital Clock
Automatic Temperature Control
Tape Drive Motor
Cruise Control
Liquid Level Indicators
Speakers
Windshield Wiper Motor
Defogger Motor
Tail-Gate Motor
Windshield Washer Pump
Door Lock Motor
Headlight Door Motor
Anti-Skid
Economy and Pollution Control
Fuel Pump Motor
Ignition
Coolant Fan Motor
Window Lift Motor
Antenna Lift Motor
Seat Actuator Motor
Heat and Air Condition Motor
Starter Motor
Throttle and Crankshaft Position Sensors

Figure 2.1 Automotive applications involving permanent magnets [9].

2.1.1 Magnetic Properties

Permanent magnets derive their useful properties from the presence of strong atomic moment spin alignment in ferromagnetic materials. Small areas of the material which have a constant magnetic moment orientation are known as domains [10]. When an external magnetic field is applied, a driving force exists for all atomic moments in the material to align with the external field. This process can occur by three possible paths: favorably oriented domains can grow in size (propagation), new domains can form whose magnetic moment is parallel to the applied field (nucleation), or domain rotation can occur.

An external magnetic field (designated H) can be applied incrementally to the material, and the resulting field induced within the material (known as induction, B) can be measured. A plot of B vs. H is called a hysteresis loop, as shown in Figure 2.2. Starting from the origin of the plot, an incremental application of an external field ($H > 0$) will eventually result in complete alignment of all domains in the direction of the applied field. At this point, the induced field in the material is known as the saturation induction (B_s). Most of the domains will remain aligned upon removal of the external magnetic field ($H \rightarrow 0$) [1]. The remanent induction, or remanence (designated B_r), indicates the amount of magnetism that will be left in the material after it is removed from the magnetization coils and placed into service. B_r is an important property for a permanent magnet. A reverse field ($H < 0$) must be applied to demagnetize the material. At a value H_c, known as the coercive force (or coercivity) of the magnet, the domain orientation is totally random and the induction in the material is equal to zero. H_c is a relevant permanent magnet property, since the coercivity of a magnet indicates how well it can resist stray demagnetizing fields in practice.

The power of a permanent magnet is most readily indicated [11] by a property known as its maximum energy product, $(BH)_{max}$, which is shown as the shaded region in Figure 2.2.

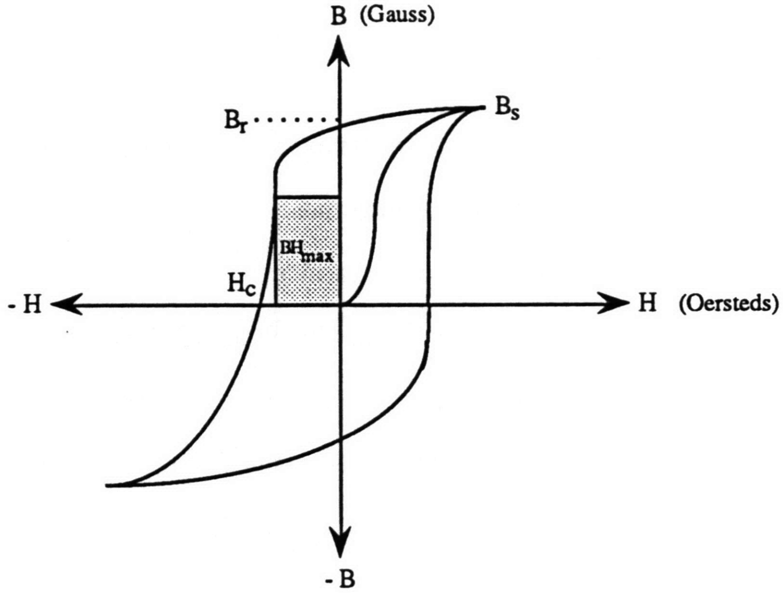

Figure 2.2 Hysteresis loop for a typical permanent magnet [12]. The shaded region indicates the maximum energy product, $(BH)_{max}$. The unit of $(BH)_{max}$ is the Gauss-Oersted.

$(BH)_{max}$ is obtained by determining the maximum rectangular area in the second quadrant of the hysteresis loop, and is *not* simply the product of B_r and H_c. The maximum energy product is the most frequently cited figure of merit for a permanent magnet.

Another relevant magnetic property is the Curie Temperature (T_c) of a permanent magnet. Thermal energy tends to randomize the alignment of the domains, and all magnets will thus become thermally demagnetized at some elevated temperature. The upper limit of service temperature (usually $< T_c$) is an important quantity for a permanent magnet.

Microstructure is known to have a significant effect on permanent magnet properties [8]. Precipitates or other second phase particles, for example, can pin domain walls and force domain reorientation to occur by nucleation rather than by simple domain propagation. The same second-phase particles can also promote demagnetization, however, by serving as domain nucleation sites. Material inhomogeneities can thus significantly affect coercivity.

2.1.2 Comparison of Existing Permanent Magnets

Nd-Fe-B was discovered in 1983 by the General Motors Corporation (USA) and by the Sumitomo Special Metals Company of Japan. The premier high performance permanent magnet prior to this discovery was Samarium-Cobalt (Sm-Co), which is typically produced in two different forms: $SmCo_5$ and Sm_2Co_{17}. The magnetic properties of Sm-Co alloys are excellent in many respects, but these magnets have at least one rather serious drawback. Material costs are relatively high for all Sm-Co alloys, owing to the scarcity of samarium and to the relatively high market price of cobalt [13]. In fact, the search for substitute elements which would allow a high performance permanent magnet to be produced at a lower cost was actually the driving force behind the discovery of Nd-Fe-B.

Replacement of Sm and Co with Nd and Fe, respectively, leads to a substantial reduction in the cost of raw materials. These savings are reflected in the relative price per pound for the permanent magnets, as shown in Table 2.2. The density of Nd-Fe-B (0.27 lb/in^3) is slightly less than that of Sm-Co (0.3 lb/in^3) [6], resulting in a lower cost per unit volume as well (Table 2.2).

In addition to the cost savings conferred by Nd-Fe-B, the alloy additionally possesses

Table 2.2 Approximate cost of Sm-Co and Nd-Fe-B on the basis of weight and volume [14].

Magnet	Cost/lb.	Cost/in^3
$SmCo_5$	$125	$38
Nd-Fe-B	$80	$22

magnetic properties which are superior in many respects to those of Sm-Co alloys. Nd-Fe-B offers significantly higher remanence, coercivity, and maximum energy product than Sm-Co. Table 2.3 contains a comparison of typical magnetic properties for the alloys, and Figure 2.3 is a demagnetization curve (second quadrant of hysteresis loop) for both alloys.

Table 2.3 A comparison of room temperature magnetic properties of Sm-Co and Nd-Fe-B [15].

Magnet Type	Remanence (kilogauss)	Coercivity (kilooersteds)	Energy Product (MGOe)
$SmCo_5$	8.8	8.8	19
Sm_2Co_{17}	10	7.5	23
Nd-Fe-B	11.8	10.3	33

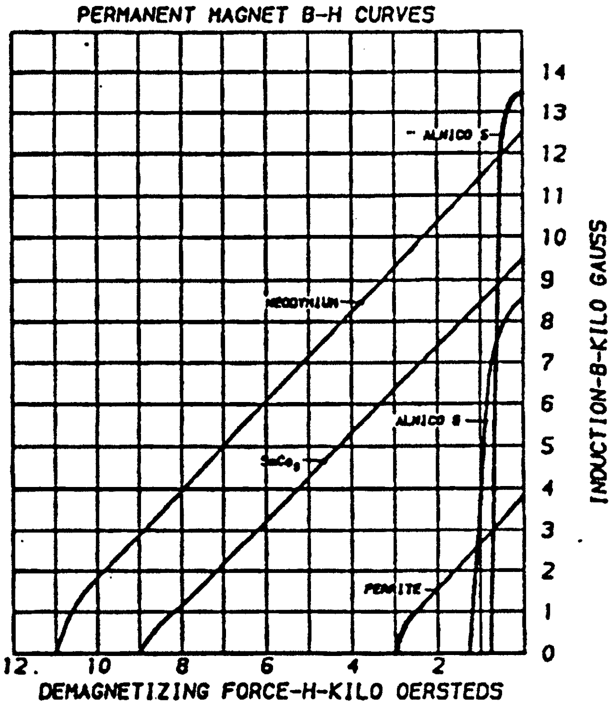

Figure 2.3 Typical demagnetization curves for Nd-Fe-B and $SmCo_5$ [6].

The ability of Nd-Fe-B to provide significantly more magnetic flux than Sm-Co (owing to its higher $(BH)_{max}$) suggests that the cost benefits of Nd-Fe-B may be even more pronounced than indicated by Table 2.2. Users of permanent magnets are primarily concerned with cost per unit of magnetic energy rather than cost per unit weight, and it is therefore relevant to recompare the two materials on this basis. As shown in Table 2.4, Nd-Fe-B is markedly less expensive than $SmCo_5$ on an energy product basis.

Table 2.4 Cost of $SmCo_5$ and Nd-Fe-B on a per energy product basis [14].

Magnet	Cost/MGOe
$SmCo_5$	$6.25
Nd-Fe-B	$2.50

It is apparent that the Nd-Fe-B alloy is capable of providing significantly more magnetic flux per unit weight or volume than Sm-Co permanent magnets, at a substantially reduced cost. These advantages have provided a strong incentive for manufacturers to replace Sm-Co permanent magnets with Nd-Fe-B.

Despite the superior room temperature magnetic properties of Nd-Fe-B, however, its temperature limitations are more stringent than those of Sm-Co alloys. As shown in Table 2.5, the Curie temperature and the maximum service temperature of Nd-Fe-B are both lower than for the Sm-Co materials. Since Nd-Fe-B is not effective above ~150°C, Sm-Co is still the premier high performance permanent magnet available at elevated temperatures.

Table 2.5 Temperature limitations for Sm-Co and Nd-Fe-B alloys [14,15].

Magnet Type	Curie Temperature (°C)	Maximum Service Temperature (°C)
$SmCo_5$	690	250
Sm_2Co_{17}	910	400
Nd-Fe-B	310	150

It is important to realize that if the maximum useful service temperature is exceeded, even on a transient basis, the alloy will be demagnetized and will no longer perform its intended function. The degradation of magnetic properties with temperature is therefore a significant limitation on the use of Nd-Fe-B. In practice, temperature constraints provide an even more severe limitation on the use of Nd-Fe-B than its susceptibility to corrosion.

Numerous permanent magnet applications still exist below 150°C, however. In this temperature range, Nd-Fe-B is the preeminent permanent magnet from a performance standpoint. The main problem with the use of this alloy in applications below 150°C is its inherent susceptibility to corrosion. Many analysts have cited the importance of addressing the corrosion problems of this alloy, and it is believed that the continued market penetration of Nd-Fe-B will depend in great part on its ability to resist environmental degradation [16]. The corrosion behavior of Nd-Fe-B will be discussed in detail in Section 2.3.

2.2 Characteristics of Nd-Fe-B

2.2.1 Processing of Rapidly Solidified Nd-Fe-B Alloys

Rapidly solidified Nd-Fe-B alloys are typically prepared using a technique developed by the General Motors Corporation. The first step in the rapid solidification process (RSP) consists of directing a fine stream of molten Nd-Fe-B onto the surface of a cold rotating substrate in order to form a brittle ribbon. A large number of these ribbons are then crushed and compacted together in a die at approximately 700°C and 100 MPa to form a fully dense product known as a hot pressed (h.p.) magnet [7]. The energy-product of the Nd-Fe-B alloy is less than optimal in the hot pressed form, due to the isotropic nature of the h.p. magnet. The energy-product of a permanent magnet can be increased by crystallographically aligning its axis of easy magnetization in a common direction. The direction of easy magnetization for the Nd-Fe-B alloy is the c-axis of its ferromagnetic phase, $Nd_2Fe_{14}B$. In order to produce a high energy-product anisotropic magnet, the h.p. alloy is subjected to a thermomechanical treatment known as die upsetting, which consists of anisotropic pressing at approximately 700°C and 70 MPa [17], as shown in Figure 2.4. This procedure results in a crystallographically textured product known as a die upset (d.u.) magnet, in which the c-axis of the $Nd_2Fe_{14}B$ grains are aligned.

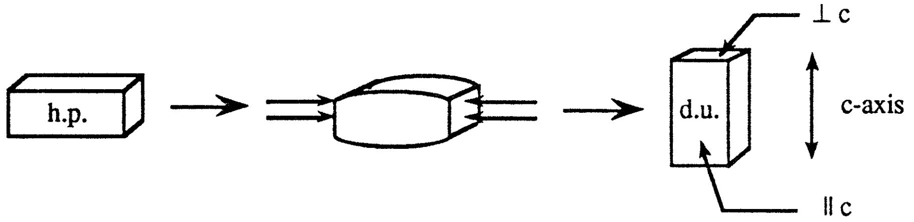

Figure 2.4 Schematic representation of the process used to fabricate die upset magnets.

Although both the h.p. and d.u. alloys emerge from their final processing dies in a non-magnetized state, these alloys can subsequently be magnetized by placing them in an external magnetic field. Optimal magnetic properties are obtained for the die upset material if it is magnetized along the axis of easy magnetization (c-axis), as shown in Figure 2.5.

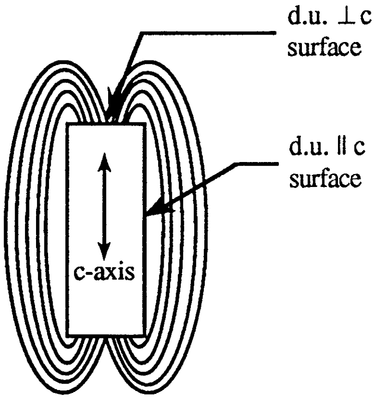

Figure 2.5. Magnetic flux lines emerging from a d.u. alloy which has been magnetized along its c-axis. Surfaces which lie perpendicular and parallel to the c-axis (d.u. ⊥ c, d.u. ǁ c) are indicated on the diagram.

2.2.2 Commercial RSP Products

Magnetic properties for magnetized h.p. and d.u. alloys are shown in Table 2.6 (note that intrinsic coercive force is used as a measure of coercivity). Due to their crystallographic anisotropy, d.u. magnets have a considerably higher energy product than h.p. magnets. Die upset alloys are therefore utilized when magnetic flux output is of primary importance.

The resistance of the h.p. magnets to thermal demagnetization is superior to that of the d.u. magnets. The h.p. magnet is thus used extensively in applications where the maximum service temperature is expected to approach the useful limit of the alloy (150°C), or if resistance to demagnetization is needed at slightly elevated temperatures [7].

Table 2.6 Typical magnetic properties of h.p. and d.u. alloys at room temperature [18].

Magnet Type	Remanence (kilogauss)	Intrinsic Coercive Force (kilo-oersteds)	Energy Product (MGOe)
h.p.	8	16	14
d.u.	12	13	37

The Nd-Fe-B alloy is sold commercially in both the h.p. and the d.u. forms. Either product may be used directly in its fully dense form, or may be pulverized and mixed with resin to form a product known as a bonded magnet. The fully dense h.p. and d.u. alloys are fabricated to near-net shape and then subsequently machined to net shape [19].

The term fully dense (as used above) refers to the fact that an intact metal part is produced with no accompanying polymer matrix. The use of this term does *not* imply the absence of internal pores. In fact, the h.p. and d.u. alloys are found to contain significant amounts of pre-existing porosity, which is typical of most materials produced by hot pressing. Figure 2.6 shows a photographic representation of typical porosity observed in an h.p. alloy.

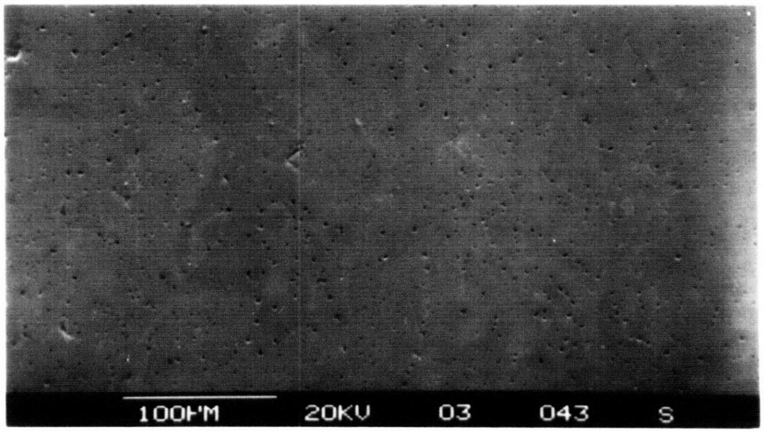

Figure 2.6 Pre-existing porosity in h.p. Nd-Fe-B (as-polished surface).

The current study is solely concerned with the fully dense products (h.p., d.u.), but the general principles of corrosion behavior observed should also be applicable to bonded magnets since the starting material is identical in both cases.

2.2.3 Microstructure of the Rapidly Solidified Alloys

2.2.3.1 Grain Structure

Transmission electron microscopy studies [20-22] indicate that the primary constituent of h.p. Nd-Fe-B is ferromagnetic $Nd_2Fe_{14}B$. This phase generally appears in the form of isotropic, polygonal grains which are 80-100 nm in diameter, as shown in Figure 2.7. Most of the $Nd_2Fe_{14}B$ grains are surrounded by a continuous 1-5 nm wide Nd-rich grain boundary phase [23-25]. The characteristics of the $Nd_2Fe_{14}B$ and Nd-rich phases are discussed in Section 2.2.5 and Section 2.2.6, respectively.

Die upsetting results in the formation of elongated $Nd_2Fe_{14}B$ grains which lie perpendicular to the press direction, as shown in Figure 2.8. The platelet-shaped grains in the d.u. magnet are approximately 300 nm in diameter and 60 nm thick, with most of the grains surrounded by the Nd-rich phase.

The magnetic anisotropy exhibited by the d.u. alloys is related to the crystallographic alignment of the c-axis of the $Nd_2Fe_{14}B$ grains. The die upsetting process creates a texture in which the axis of easy magnetization (c-axis) is preferentially aligned along the longitudinal axis of the grains; the long axes of adjacent grains are nearly parallel, which results in large-scale alignment of the c-axis. As a result of this crystallographic alignment, greater magnetic flux can be developed along the axis of a d.u. magnet than along the axis of an h.p. magnet.

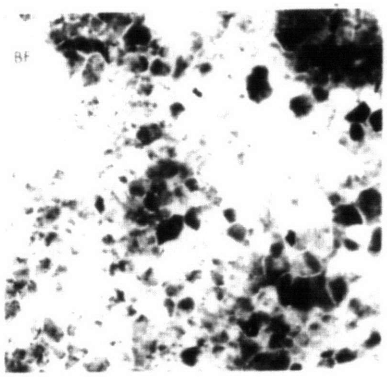

Figure 2.7 Microstructure of h.p. Nd-Fe-B alloys. Note that no scale was provided with the photograph; grains are approximately 80-100 nm in diameter [21,22]

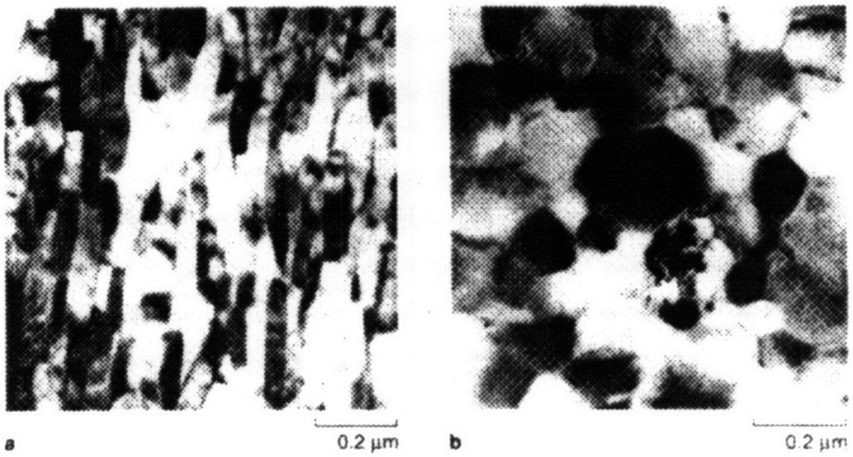

Figure 2.8 Microstructure of the d.u. magnets (a) parallel to the c-axis (|| c), and (b) perpendicular to the c-axis (⊥ c) [26].

2.2.3.2 Macrostructure

In addition to the grain structure discussed above, the RSP alloys have an additional level of structure which must be considered. During the hot pressing process, adjacent ribbon fragments in the die are metallurgically bonded to one another, thus forming the fully dense alloy part. The fusion between adjacent ribbons is incomplete, however, and the ribbon boundaries in the final material thus tends to contain a significant number of pores. The boundaries are visible in the as-polished state, and can be revealed even more clearly by etching in nital, as shown in Figure 2.9 (a). Ribbon boundaries are also present in the d.u. alloy, though they tend to be elongated as a result of anisotropic pressing (Figure 2.9 (b)).

It is emphasized that *each* individual ribbon contains thousands of grains. Two levels of structure therefore exist in the RSP alloys: ribbons with approximate dimensions 40 μm x 500 μm x 500 μm [27], and grains with much finer diameters (80-100 nm).

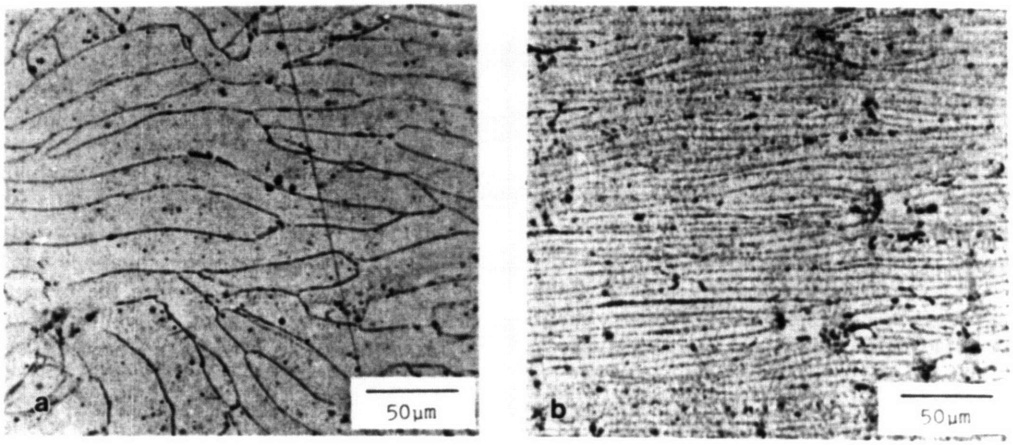

Figure 2.9 Ribbon Structure for (a) h.p. and (b) d.u. alloys [28].

2.2.4 Production of Nd-Fe-B Alloys by Sintering

Although the alloys tested in this study were produced by rapid solidification methods, it is important to note that Nd-Fe-B can also be produced using a sintering technique initially developed by the Sumitomo Special Metals Company of Japan. The microstructure of alloys produced by sintering differs from the RSP alloy structure by the size of the $Nd_2Fe_{14}B$ grains formed, and also by the minor phases present in the magnets [29]. In sintered magnets, the $Nd_2Fe_{14}B$ grains (~ 5-15 μm in diameter) are approximately 2 orders of magnitude *coarser* than those in the RSP magnets [30]. Magnets produced by sintering also contain a third phase, a non-continuous boron-rich compound ($Nd_{1.1}Fe_4B_4$), which is located at the grain boundaries. The Nd-rich phase in the sintered magnets (~ 20 nm wide) tends to surround both the $Nd_2Fe_{14}B$ phase and the $Nd_{1.1}Fe_4B_4$ phase [31]. Sintered magnets do not contain the ribbon structure described in Section 2.2.3.2.

2.2.5 The $Nd_2Fe_{14}B$ Phase

The $Nd_2Fe_{14}B$ phase comprises 85-95 vol.% of the h.p. and d.u. alloys. This phase has a tetragonal structure and is ferromagnetic with all of its moments parallel to the c-axis of its unit cell [32]. The inherent magnetic moment of this phase is responsible for the outstanding remanent magnetization exhibited by Nd-Fe-B. The fact that the magnetic moment of $Nd_2Fe_{14}B$ is far stronger along its c-axis than in any other direction (known as magnetocrystalline anisotropy) contributes to the high coercivity of the Nd-Fe-B alloy.

2.2.6 The Nd-rich Phase

The Nd-rich phase comprises about 5-15 vol. % of the Nd-Fe-B alloy, depending upon the composition used to produce the magnets. This phase resides at the grain boundaries in the

RSP (and sintered) alloys; its width has been reported as 1-5 nm in RSP materials [23-25].

According to Hütten and Haasen [23], the Nd-rich phase is present on all RSP $Nd_2Fe_{14}B$ grain boundaries. Li *et al* [24] also investigated RSP magnets and state that the Nd-rich phase is found on most but not all grain boundaries; the exact percentage of $Nd_2Fe_{14}B$ grains which are fully surrounded by the Nd-rich phase is thus not definitively known.

The Nd-rich phase is believed to be important in the deformation processes associated with die upsetting, owing to the lack of plastic deformation exhibited by the $Nd_2Fe_{14}B$ phase. Although the exact deformation mechanism is not known, it is believed that some type of grain boundary sliding occurs during the die upsetting process [33]. The Nd-rich phase also contributes to the high coercivity exhibited by the alloy, as discussed in Section 2.2.7.

Two main forms of the Nd-rich phase have been reported, depending on whether or not Nd-Fe-B has been alloyed with cobalt. The different formulations of the alloy are described below as Co-free and Co-containing.

Despite numerous TEM investigations and the establishment of the Nd-Fe-B phase diagram [34-37], the Nd-rich phase in Co-free magnets is not well-understood [39]. This phase has been reported to have a hexagonal close packed (hcp) structure [30,35,40,41] or a face centered cubic (fcc) structure [8,24,32,41,42,43], depending upon the amount of oxygen admitted to the system during processing. The approximate composition of this phase has been reported as 70-85 wt% Nd and 15-30 wt% Fe [21,23,45], with an undetermined amount of oxygen in the phase. It appears that the Nd-rich grain boundary phase in RSP (and sintered) magnets contains Nd, Fe, and O, with little or no B present. The presence of oxygen in RSP ribbons [25,45] as well as the final alloys indicates that this element enters the system with the starting materials or during the melt-spinning process (perhaps due to oxidation of the free ribbon surface). In both cases, the oxygen is likely assimilated into the bulk alloy during heat treatment at high temperature.

Co-containing Nd-Fe-B magnets were developed in an attempt to improve the magnetic properties of the alloy. Nd-Fe-B was initially formulated with only Nd, Fe, and B present in the alloy melt. Many subsequent studies were conducted in an attempt to increase the useful temperature range of the magnet by using various alloying additions. Much of this work was aimed at partially replacing Fe in the $Nd_2Fe_{14}B$ phase with Co in order to obtain $Nd_2Fe_{14-x}Co_xB$. One result of these studies is that additions of Co were found to reduce the susceptibility of *sintered* Nd-Fe-B alloys to intergranular corrosive attack, as shown by Ohashi et al [43]. Nd-Co intermetallic phases which form at the grain boundaries in Co-containing magnets are thought to be less electrochemically active than the Nd-rich phase in the Co-free alloys, thus reducing the driving force for galvanically-driven intergranular attack. Diffraction patterns obtained by Hirosawa *et al* [44] for the grain boundary phase in a Co-containing alloy indicate that this phase may correspond to Nd_3Co.

Studies have not been performed to investigate the effects of Co alloy additions on the corrosion behavior of rapidly solidified Nd-Fe-B. In fact, one of the goals of the present study is to determine whether or not Co-containing RSP alloys suffer from intergranular attack (note that RSP alloys containing 2.5 wt.% Cobalt will be utilized in this study).

2.2.7 Relationship between Coercivity and Microstructure

The high coercivity of Nd-Fe-B is partly derived from the magnetocrystalline anisotropy of the $Nd_2Fe_{14}B$ phase. The dual-phase structure of the alloy is also essential if high coercivity is to be attained, however, because sufficient coercivity cannot be acquired from a single crystal of $Nd_2Fe_{14}B$. The paramagnetic Nd-rich grain boundary phase acts to magnetically isolate each ferromagnetic grain, which precludes domains from propagating from one grain to another. The Nd-rich phase is thus considered to act as a pinning site for magnetic domain walls in RSP magnets. Each grain is forced to reverse its magnetization independently [8], which results in high coercivity. If the microstructure consisted of single-phase $Nd_2Fe_{14}B$, the barrier to magnetization reversal would be far less effective and coercivity would decrease dramatically as a result. Similarly, a grain boundary phase consisting of a ferromagnetic material such as α-Fe would not be effective at magnetically isolating the $Nd_2Fe_{14}B$ grains from one another.

2.2.8 Alloy Composition

According to the above discussion, the optimal Nd-Fe-B microstructure consists of $Nd_2Fe_{14}B$ grains surrounded by a paramagnetic grain boundary phase such as the Nd-rich or Nd_3Co phases typically found in industrially produced materials. The composition needed to produce this structure must be richer in Nd than the stoichiometric $Nd_2Fe_{14}B$ compound. The nominal composition used to prepare RSP magnets is Nd15 - Fe77 - B8 (at. %); preparation of the Nd-Fe-B alloy using lower Nd contents has been found to lead to reductions in coercivity [37].

$Nd_2Fe_{14}B$ forms peritectically from liquid and solid iron ($L + Fe (s) \rightarrow Nd_2Fe_{14}B$) [46]. If the starting alloy melt is rich in Nd relative to the stoichiometric $Nd_2Fe_{14}B$ composition, not all liquid will solidify to $Nd_2Fe_{14}B$ during the peritectic reaction. When the $Nd_2Fe_{14}B$ phase nucleates to form grains, the remaining Nd-rich liquid will reside in between these grains, eventually forming a grain boundary phase upon solidification. Since this liquid is rich in Nd (and Co in alloys containing this element), a Nd-rich phase (or a Nd_3Co phase) will be present at the grain boundaries.

2.3 Corrosion of Nd-Fe-B

It was demonstrated in Section 2.1 that in applications below 150°C, Nd-Fe-B possesses marked advantages relative to Sm-Co permanent magnets in terms of cost, weight, and magnetic performance. The poor corrosion resistance of Nd-Fe-B has been cited as a problem with its use in a large number of engineering applications [2,13-15], however, owing to the fact that many machines are exposed to potentially corrosive environments. The technological impact of this relatively new alloy may be limited unless its corrosion problems can be addressed. According to Hirosawa *et al* [44] of the Sumitomo Special Metals Company, improvements in corrosion resistance are crucial if the application area of Nd-Fe-B is to be expanded past its present level.

Corrosion resistance is an important property for Nd-Fe-B and other permanent magnets. Magnetic flux is directly dependent on the volume of magnetic material present, and metal loss due to corrosion therefore decreases the power of a permanent magnet. It was observed by Minowa *et al* [47], for example, that a 25% loss in magnetic flux resulted from a 72 hour exposure of sintered Nd-Fe-B to an autoclave environment (120°C, 2 atm.) [47].

An important problem relating to the corrosion of this alloy is that rare earth permanent magnets (such as Nd-Fe-B) are typically thin by design, which results in the utilization of magnets with a relatively high surface area to volume ratio [48]. Such geometry is necessary in order for the material to fulfill its primary function as a magnet, but is deleterious to the alloy in terms of corrosion resistance. Corrosive degradation is a function of exposed surface area, and a given amount of corrosion will lead to a greater percentage of magnetic flux loss if the magnet considered has a relatively low total volume. The amount of corrosive degradation experienced by a permanent magnet is clearly dependent on both corrosion resistance and magnet geometry.

The susceptibility of Nd-Fe-B to corrosive degradation is not unexpected in view of its composition. Fe-based alloys are known to be susceptible to corrosion in atmospheric and near-neutral aerated environments, and it is expected that the addition of reactive elements such as Nd and B might lead to increased corrosion susceptibility under such conditions. Weight loss and electrochemical tests have in fact conclusively demonstrated the fact that Nd-Fe-B generally exhibits poor resistance to corrosive attack [17,49,49a].

Although previous testing has been able to confirm the susceptibility of Nd-Fe-B to corrosion, the majority of these studies have been quite limited in nature. A detailed understanding of the corrosion behavior of Nd-Fe-B has generally not been obtained, especially in the case of magnets produced by rapid solidification techniques. A summary of the previous work performed on the corrosion of Nd-Fe-B alloys is provided in the remaining sections of the present chapter.

2.3.1 Electrochemical Testing

Anodic polarization diagrams were acquired by Bala *et al* [49] in deaerated 0.5M H_2SO_4 (25°C) for sintered Nd-Fe-B alloys with various starting compositions, as shown in Figure 2.10. Curve 3 corresponds to the typical alloy composition of Nd15 - Fe77 - B8. Active behavior is observed for all three materials in the vicinity of the corrosion potential, and the alloys also exhibit a various reduction in current density at oxidizing potentials. Bala *et al* [49a] also performed polarization tests on sintered magnets in deaerated Na_2SO_4 (25°C), as shown in Figure 2.11. The solid line represents Nd15 - Fe77 - B8, and the remaining curves represent alloys containing dysprosium (Dy) and other alloying elements. Again, the Nd-Fe-B alloys show a slight reduction in current density at oxidizing potentials, but no significant passivation was observed in this solution. The lack of passivation observed in these test solutions would likely result in a relatively high corrosion rate for Nd-Fe-B.

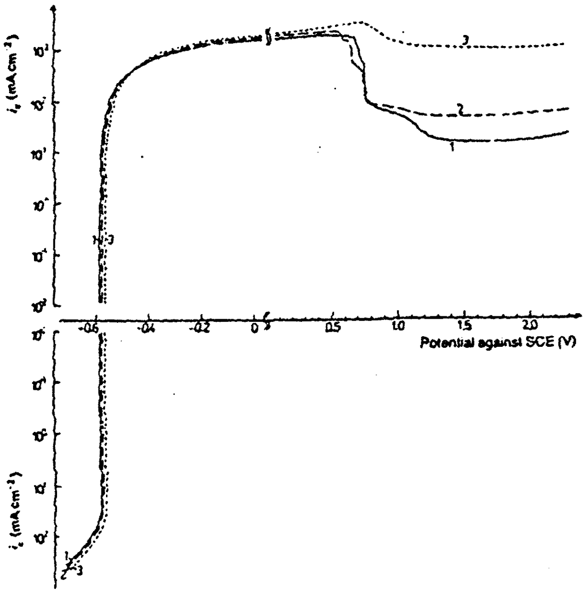

Figure 2.10 Anodic polarization of sintered Nd-Fe-B in deaerated 0.5 M H_2SO_4 at 25°C. Alloys with various compositions were tested; curve 3 corresponds to Nd15 - Fe77 - B8 [49].

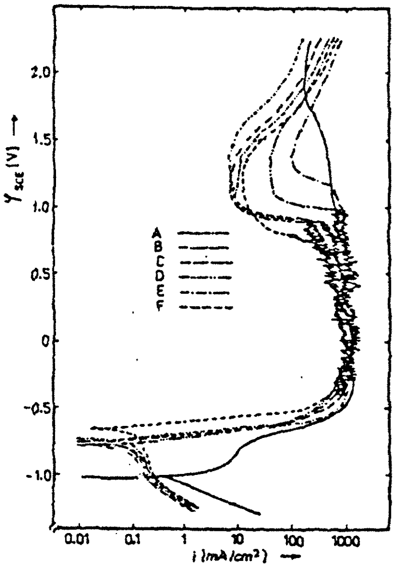

Figure 2.11 Polarization curves for sintered magnets in deaerated 0.5 M Na_2SO_4 at 25°C The solid line represents the Nd15 - Fe77 - B8 composition [49a]

Anodic polarization tests were conducted on sintered Nd-Fe-B by Chin *et al* [50] in deaerated test solutions, as shown in Figure 2.12. Active behavior was obtained in both 1 N H_2SO_4 and Ringers solution (9 g NaCl, 0.425 g KCl, 0.119 g $CaCl_2$, 0.1 g $NaHCO_3$ in 1 L H_2O). Limited passivation was observed in dilute (10 wt %) orthophosphoric acid.

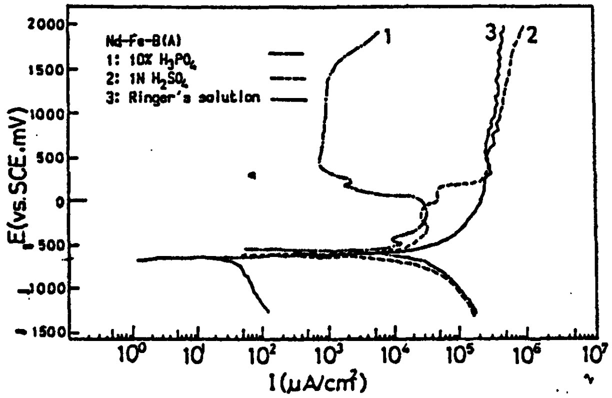

Figure 2.12 Anodic polarization behavior of sintered Nd-Fe-B in various deaerated solutions (30°C) [50].

The three studies cited above were each conducted using sintered Nd-Fe-B alloys. It was more difficult to locate electrochemical tests employing rapidly solidified Nd-Fe-B, but two studies utilizing RSP materials were found to be available, as described below.

Cyclic voltammetry experiments were performed by Warren *et al* [51] on several types of Nd-Fe-B alloys in deaerated 0.15 M NaH_2PO_4 (pH 4), as shown in Figure 2.13. The curve marked "GM" represents the results of the test performed on RSP magnets. Active-passive behavior is evident for the RSP material, with a relatively high passive current density of about 0.25 mA/cm^2 observed. It was reported that passivity could be completely eliminated by adding 1000 ppm or more of NaCl to the 0.15 M NaH_2PO_4 test solution.

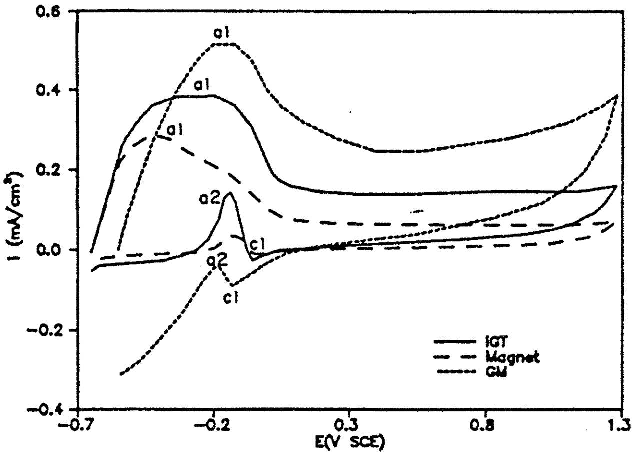

Figure 2.13 Cyclic voltammograms in deaerated NaH_2PO_4 (pH 4) at 5 mV/sec [51].

Anodic polarization tests were performed by Kang *et al* [52] on rapidly solidified Nd-Fe-B ribbons (the ribbons were fabricated in the author's laboratory) . The alloy was found to exhibit active behavior in NaCl test solutions. Limited passivation was observed in both H_3PO_4 and NaOH solutions.

According to the results of previous electrochemical tests, Nd-Fe-B appears to have poor resistance to solutions containing Cl^- and SO_4^{2-} ions, whether the alloys are prepared by RSP or by sintering [49,49a,50,51,52]. The corrosion behavior of the alloy in Cl^--containing solutions is relevant because of the presence of chloride ions in marine atmospheres, as well as in road de-icing salts and other potential service environments for the alloy. Tests performed in sulfate solutions are also relevant, since SO_4^{2-} ions are often present in the atmosphere, especially in industrial environments where SO_2 gases are released into the air and then converted to sulfuric acid by water.

Several of the previous electrochemical studies have been conducted in electrolytes such as H_3PO_4 [50], H_2SO_4 [49,50], NaH_2PO_4 [51], NaOH [52], and Ringer's solution [50], primarily under deaerated conditions. Since corrosion of Nd-Fe-B is a concern in industrial and marine environments, it is believed that tests performed in aerated, near-neutral electrolytes such as NaCl and Na_2SO_4 are likely to be more relevant to actual service conditions than tests performed in the various electrolytes mentioned above [53].

2.3.2 Dissolution Morphology

The microstructure which is so beneficial to the magnetic properties of the alloy may also be detrimental to its corrosion resistance, as materials with dual-phase microstructures are often susceptible to micro-galvanic corrosion. Nd is an electrochemically active element, and the preferential location of the Nd-rich phase at the grain boundaries of the RSP Nd-Fe-B alloy suggests that intergranular attack could occur.

No evidence is available regarding intergranular corrosion in rapidly solidified Nd-Fe-B, however. The extremely fine grains present in RSP alloys provide a significant barrier to such a study, and it is likely that the lack of available information is related to the relative difficulty of such an analysis.

Intergranular attack in sintered Nd-Fe-B is more readily investigated, however, and several studies have been performed to evaluate whether or not preferential grain boundary corrosion occurs in these materials. The answer to this question has been found to be highly dependent on the Co content of the alloy, as discussed below.

In Co-free Nd-Fe-B, the Nd-rich grain boundary phase is believed to be anodic to the $Nd_2Fe_{14}B$ phase, due to the electrochemical activity of elemental Nd. The presence of a thermodynamically active phase at the grain boundary has led Sugimoto *et al* [54] to propose a general corrosion mechanism for Co-free Nd-Fe-B, as shown in Figure 2.14.

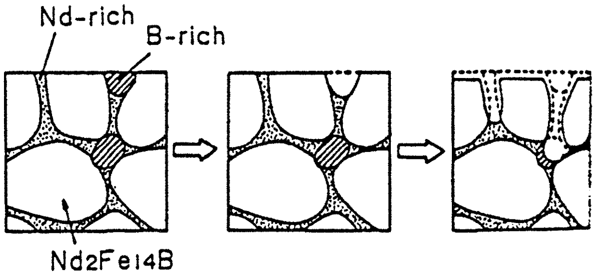

Figure 2.14 Proposed corrosion mechanism of the sintered Nd-Fe-B magnet in Co-free alloys [54].

Intergranular corrosion *has* been observed in sintered Nd-Fe-B by several authors [43,54] using conventional scanning electron microscopy analysis of corroded surfaces. Evidence of intergranular attack consisted of grains shown in relief, as well as preferential metal loss at the grain boundaries.

A related type of attack was observed in sintered Nd-Fe-B by Cygan and McNallan [55]. Co-free alloys were exposed to several autoclave tests and intergranular corrosion was observed, which is consistent with the results described above. The authors additionally reported that the intergranular attack sometimes tended to collect into shallow localized areas resembling pits; such morphology had not been reported in previous work.

The resistance of sintered Nd-Fe-B alloys to intergranular attack is substantially increased if Co is added to the material. Ohashi *et al* [43] have demonstrated the general absence of intergranular attack in corroded samples which contain 5% Co. The observed resistance of Co-containing alloys to intergranular corrosion has been attributed to the presence of Nd-Co intermetallic phases (e.g. Nd_3Co) at the grain boundaries. The Nd-Co intermetallic phase(s) are believed to be less electronegative than the Nd-rich phase which resides at the grain boundaries in the Co-free magnets.

2.3.3 Summary of the Corrosion Behavior of Nd-Fe-B

Some important advances have been made towards the understanding of corrosion phenomena in sintered Nd-Fe-B. A great deal of information remains to be obtained, however, and further study certainly appears to be warranted, given the importance of corrosive degradation to the engineering viability of Nd-Fe-B. These comments are even more appropriate in the discussion of corrosion studies in RSP materials. It is clear that the current understanding of corrosion in rapidly solidified Nd-Fe-B is very rudimentary. Since the viability of the Nd-Fe-B permanent magnet in many different applications is dependent upon its ability to withstand environmental degradation, a more thorough understanding of its corrosion behavior would appear to be important. Several authors have in fact called attention to the need for long-term study of this problem [10,13].

2.3.4 Environmentally-Assisted Cracking

In addition to the magnetic flux loss resulting from corrosive dissolution, another potential degradation mechanism for the Nd-Fe-B alloy is environmentally-assisted cracking (EAC). Cracking of Nd-Fe-B has been reported by three investigators under different conditions.

Bala and Szymura [49,49a] have observed cracking of sintered Nd-Fe-B, for example under extreme cathodic polarization ($i_c \sim 0.4 - 1.3$ A/cm^2 in H_2SO_4 of pH 0 to 1). The authors attributed the observed failures to hydrogen-assisted cracking, a logical conclusion based on the known susceptibility of Nd-Fe-B to hydrogen degradation [56]. Because of the very severe testing conditions employed, this finding is not expected to be relevant to the corrosion behavior of the material in its service environment. Hydrogen-assisted fracture such as that observed by Bala and Szymura is unlikely to occur in Nd-Fe-B in practice, since the material will not be subjected to extreme cathodic polarization. Cracking was also observed by Minowa *et al* [47] on sintered Nd-Fe-B, as test sample(s) were reported to have cracked after removal from an autoclave environment. The authors were not certain whether or not the observed cracking was directly related to corrosion, and it was considered possible that the sample(s) were thinned by corrosion and were broken during handling; further details were not available [57]. Cracking resulting from corrosive attack has been observed for rapidly solidified Nd-Fe-B by Magnequench®, a primary manufacturer of the RSP alloys. Cracking occurred in salt spray environments [58], which is significant because no external polarization is imparted to the magnets during such a test. Cracking observed in salt spray tests is believed to be much more relevant to in-service behavior than the cracking reported by Bala and Szymura, which took place under extreme cathodic polarization. In the study conducted by Magnequench®, cracking was found to occur *especially* in cases where the magnet parts had been machined prior to testing. It is likely (as discussed in Section 6.3) that the specific effect of the machining treatment is to either impart residual tensile stresses to the surface of the part, or to produce grinding cracks which can lead to fracture.

2.3.5 Corrosion Control Methods

Nd-Fe-B is currently protected using either epoxy coatings or metallic coatings such as nickel. Both types of coatings have been found to provide protection to the Nd-Fe-B alloy as long as the coating itself remains intact. Neither epoxy coatings nor nickel coatings, however, are capable of protecting Nd-Fe-B, however, in cases where the base metal is exposed due to coating degradation. In fact, nickel can even accelerate the corrosion of Nd-Fe-B galvanically by acting as a cathode. According to Kang *et al* [52], once a coating is broken (degraded), significant corrosion of Nd-Fe-B magnets often occurs at the portion of the coating which failed. The ability of barrier coatings such as epoxy and nickel to resist degradation is thus an important criterion to be used in evaluating their effectiveness.

Autoclave testing (160°C, 6 atm) of epoxy-coated sintered samples was conducted by Willman and Narasimhan [59]. The epoxy was considered to be effective for the first 100 hours of testing, after which corrosion eventually results as the coating becomes more permeable to atmospheric constituents. The epoxy-coated sintered samples of Minowa *et al* [60] were found to be markedly deteriorated after autoclave testing (120°C, 2 atm, saturated with water vapor). Minowa *et al* [60] also evaluated Al-ion and Ni coatings on sintered magnets, and found both to withstand a similar autoclave test. However, both metallic coatings showed evidence of pitting in 96 hour salt spray tests (35°C, 5 % NaCl). An unfavorable evaluation of metallic coatings was reported by Kim and Jacobson [61], who found that most metallic coatings, including Al, Cu, Cd, Ni, and TiN, exhibited depletion from the surface of the sintered magnet after being kept in air for a couple of years.

In summary, corrosion control methods which can provide reasonable short-term protection to Nd-Fe-B (e.g. epoxy or nickel coatings) have been devised. The primary limitations of these types of barrier coatings are their known propensity to degrade at some point during their service life, combined with their inability to protect the base metal once the coating itself has been compromised. The fact that coating degradation will lead to a loss of magnetic flux (and possibly also to cracking) of the substrate Nd-Fe-B indicates that improvements in corrosion control are needed. It is important to either develop coatings which can provide protection to Nd-Fe-B upon penetration of the coating, or to improve the resistance of the substrate Nd-Fe-B to corrosion so that the alloy will not degrade rapidly upon coating failure; the importance of the corrosion resistance of the coated Nd-Fe-B substrate has been emphasized by Kim *et al* [62]. Ideally, both of these goals should be accomplished in order obtain a material with acceptable long-term resistance to corrosive degradation. The first step in improving the corrosion susceptibility of the substrate Nd-Fe-B is to understand the types of corrosion which occur in the alloy system and their causes; such insight clearly facilitates the development of useful corrosion control methods.

3. Research Objectives

The current study was initiated with two primary goals in mind: to develop a detailed understanding of the corrosion behavior of the Nd-Fe-B alloy, and to devise a practical, cost-effective method to control its corrosion while in service. The objectives were later extended to include a study of the environmentally-assisted cracking behavior of the alloy.

The corrosion behavior of the alloy was studied in an attempt to learn about the types of corrosion which control its behavior. Greater understanding of these issues assists in accurately evaluating the severity of the corrosion problem, and also allows a focus on what the problems are in terms of using the material. It is also difficult to intelligently design a corrosion control method without knowledge of how the material actually corrodes. Electrochemical techniques and microscopic analysis were used to study the corrosion behavior of the alloy, as described in Chapter 5.

Corrosion control methods were studied in an attempt to improve the engineering viability of the material. In this phase of the work, emphasis was placed on developing a *practical* solution to the problem of Nd-Fe-B corrosion, one which could actually be utilized to protect the material in service. Corrosion control methods are discussed in Chapter 7.

Environmentally-assisted cracking was also studied in this work. Several test samples were observed to fracture during immersion in the test electrolytes, and it was judged that cracking might be a significant degradation method for this alloy under certain conditions. The environmentally-assisted cracking of the alloy is discussed in Chapter 6.

4. Experimental Work

4.1 Materials

All of the Nd-Fe-B alloys tested in this study (h.p. and d.u.) were produced via rapid solidification techniques by the Magnequench® Division of the General Motors Corporation. Industrially-produced alloys were utilized in order to ensure that the results of the study were as relevant to actual service application as possible. Although exact alloy specifications were not available due to the proprietary nature of the products, the metallurgical characteristics of the test samples were stated by Magnequench [19] to be very similar to those reported in the literature. Details pertaining to the metallurgical properties of both h.p. and d.u. Nd-Fe-B alloys are summarized in Section 2.2. The h.p. alloys were obtained in non-magnetized form and the d.u. alloys in magnetized form. All alloy samples were cylindrical in shape. Some of the samples were ground and polished directly from the as-received condition, and other samples were first subjected to a centerless grinding treatment in order to obtain test specimens with a constant diameter.

High purity zinc metal (> 99.9%) was obtained from Johnson-Matthey Chemicals Limited.

4.2 Electrolytes

Corrosion of Nd-Fe-B is a major concern in environments containing sulfate ions, such as industrial atmospheres. The presence of chloride ions is also a concern, since the alloy can be exposed to marine atmospheres as well as environments which may contain road de-icing salts. Although exposure to nitrate ions is also expected in service, experiments were not performed in nitrate-containing solutions since the oxidizing power of these ions would likely provide an overly aggressive testing environment.

The electrochemical techniques utilized in this study required the use of liquid electrolytes rather than salt spray or humidity test environments. Near-neutral environments are believed to be more relevant to actual service applications than acidic or alkaline environments [22], and 0.5M NaCl ($pH \cong 6$) and 0.5M Na_2SO_4 ($pH \cong 6$) were therefore chosen as test solutions. All test solutions were prepared using analytical grade reagents (Mallinckrodt AR®) along with high-purity deionized water ($18\ M\Omega \cdot cm$).

As most service applications are believed to involve exposure to air, all solutions were aerated prior to testing by purging with Airco® compressed air for at least 45 minutes before the start of each experiment. The purge gas was shut off prior to sample immersion in order to establish a reproducible degree of convection.

4.3 Electrochemical Testing

Electrochemical tests are commonly used in corrosion science in order to obtain quantitative and mechanistic information about the metal-electrolyte system of interest. The use of electrochemical tests is based upon Faraday's Law, which states that the weight lost by a corroding metal is directly proportional to the charge passed across the metal-electrolyte interface. The amount of charge passed per unit time is measured as electrical current. Since the *rate* of metal loss can be defined as the weight lost by a corroding metal in a unit time period, the cell current is actually a quantitative measure of the metal loss rate. This relationship between cell current and metal loss rate is a very powerful tool in the study of metallic corrosion. For example, a determination of the corrosion current density, i_{corr}, by electrochemical methods allows the rate of metal loss to be estimated using Faraday's Law. Five main types of electrochemical testing were performed in this study: potentiodynamic polarization, electrochemical impedance spectroscopy (EIS), galvanic corrosion, long-term immersion, and hydrogen permeation testing. The sample preparation and test cells used in the potentiodynamic polarization, EIS, and galvanic corrosion tests are rather similar, and are therefore collectively described below (Sections 4.3.1 - 4.3.3). The sample preparation procedure used in the long-term immersion tests and hydrogen permeation tests are discussed in Sections 4.3.7 and 4.3.8, respectively.

4.3.1 Test Samples

Electrochemical test samples were prepared using the following procedure. An electrical contact was affixed to the back of each cylindrical test specimen using conductive silver paint and a 24 gauge copper wire. The mechanical integrity of this joint was subsequently ensured by cementing the contact to the sample using 5-minute® epoxy. The electrical resistance of the joint was measured to ensure that it was smaller than 0.5 Ω in order to minimize IR voltage drop through the electrical contact apparatus during testing. The sample was then embedded in Epon® 828 epoxy resin in order to facilitate mechanical polishing. The copper wire was shielded from the test solution by encapsulating it within a Pyrex® tube which was affixed to the mounted sample via Epoxi-Patch® resin.

All test samples were wet polished to a 1200 grit finish using a series of Extec™ silicon carbide grinding papers. The polished specimens were then cleaned in a detergent solution consisting of Alconox® and water, degreased with acetone, and masked with a thin layer of room temperature vulcanization (RTV) silicone rubber adhesive (Shin-Etsu Chemical Co.) in order to expose a rectangular section of sample to the solution. Neutral-cure silicone rubber was used to ensure that acetic acid was not released upon curing. The masking agent was allowed to cure in a dessicator for at least 16 hours prior to testing. The area to be exposed to the test solution (normally ~ 0.1 cm^2) was measured using calipers prior to immersion. A typical electrochemical sample is shown schematically in Figure 4.1.

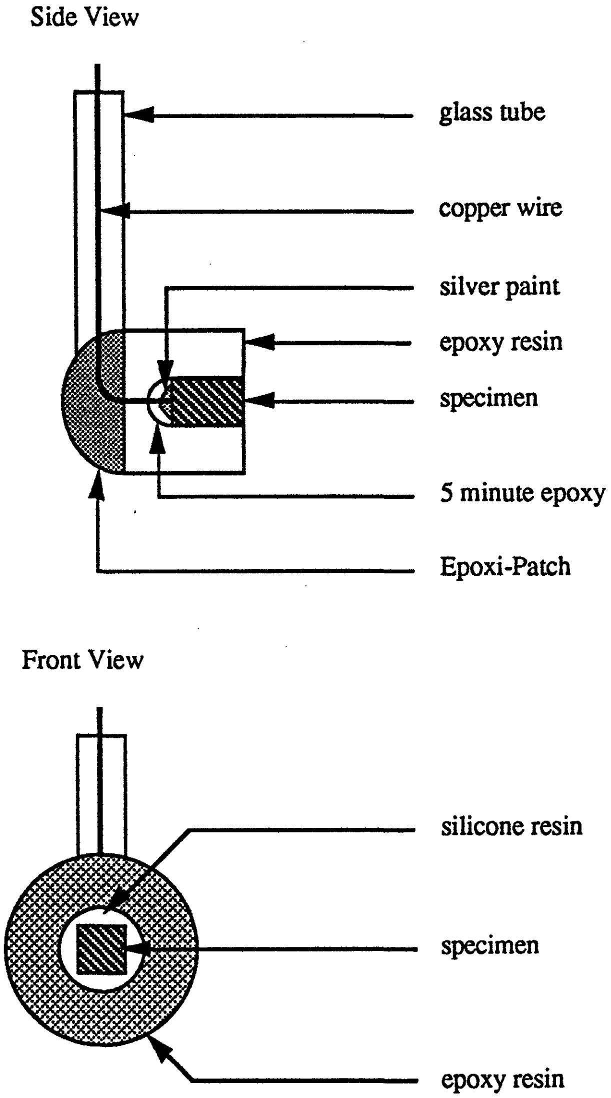
Side View
glass tube
copper wire
silver paint
epoxy resin
specimen
5 minute epoxy
Epoxi-Patch
Front View
silicone resin
specimen
epoxy resin

Figure 4.1 Construction of a typical electrode utilized for electrochemical testing.

4.3.2 Test Cell

The electrochemical cell was an airtight Pyrex® unit containing ports through which cell elements could be introduced. The counter electrode in all tests was platinum gauze with an area of approximately 12 cm^2. Two types of reference electrodes were normally employed:

a saturated calomel electrode (SCE) for tests performed at 30^{o}C or less, and a silver/silver chloride electrode (Ag/AgCl) for tests performed at temperatures higher than 30°C.

In the polarization and galvanic corrosion tests, the reference electrode was placed in an auxiliary cell adjacent to the main cell. Both cells were filled with the same test solution, and ionic continuity between the reference and working electrodes was established by placing a Luggin capillary filled with test solution into both cells (Figure 4.2 (a)).

Due to the finite resistivity of the test electrolytes, current flow between the working and counter electrodes leads to an IR or ohmic voltage drop in the solution between the two electrodes. The existence of IR voltage drop can prevent the potential of the working electrode from being accurately maintained unless steps are taken to minimize the extent of this error. In this work, the effects of IR drop were minimized by placing the tip of the Luggin capillary approximately 2 mm away from the working electrode surface .

Use of the Luggin capillary in the EIS tests led to an unacceptably high level of electrical noise, however, and the reference electrode therefore had to be placed directly into the test cell during EIS measurements (2-3 mm from sample), as shown in Figure 4.2 (b). Note that IR voltage drop through the electrolyte was not considered to be problematic in these particular tests due to the low value of the currents which flow during EIS experiments.

A more significant consequence of eliminating the Luggin capillary from the setup is the inevitable leakage of Cl^- ions from the SCE into the vicinity of the test electrode. In order to avoid the problem of Cl^- ion contamination in EIS tests performed in Na_2SO_4, a mercury/mercurous sulfate electrode (Hg/Hg_2SO_4) was used in place of the SCE. Since the leakage from the Hg/Hg_2SO_4 electrode will consist of SO_4^{2-} ions rather than Cl^- ions, utilization of the Hg/Hg_2SO_4 electrode allows the Cl^- contamination problem to be avoided.

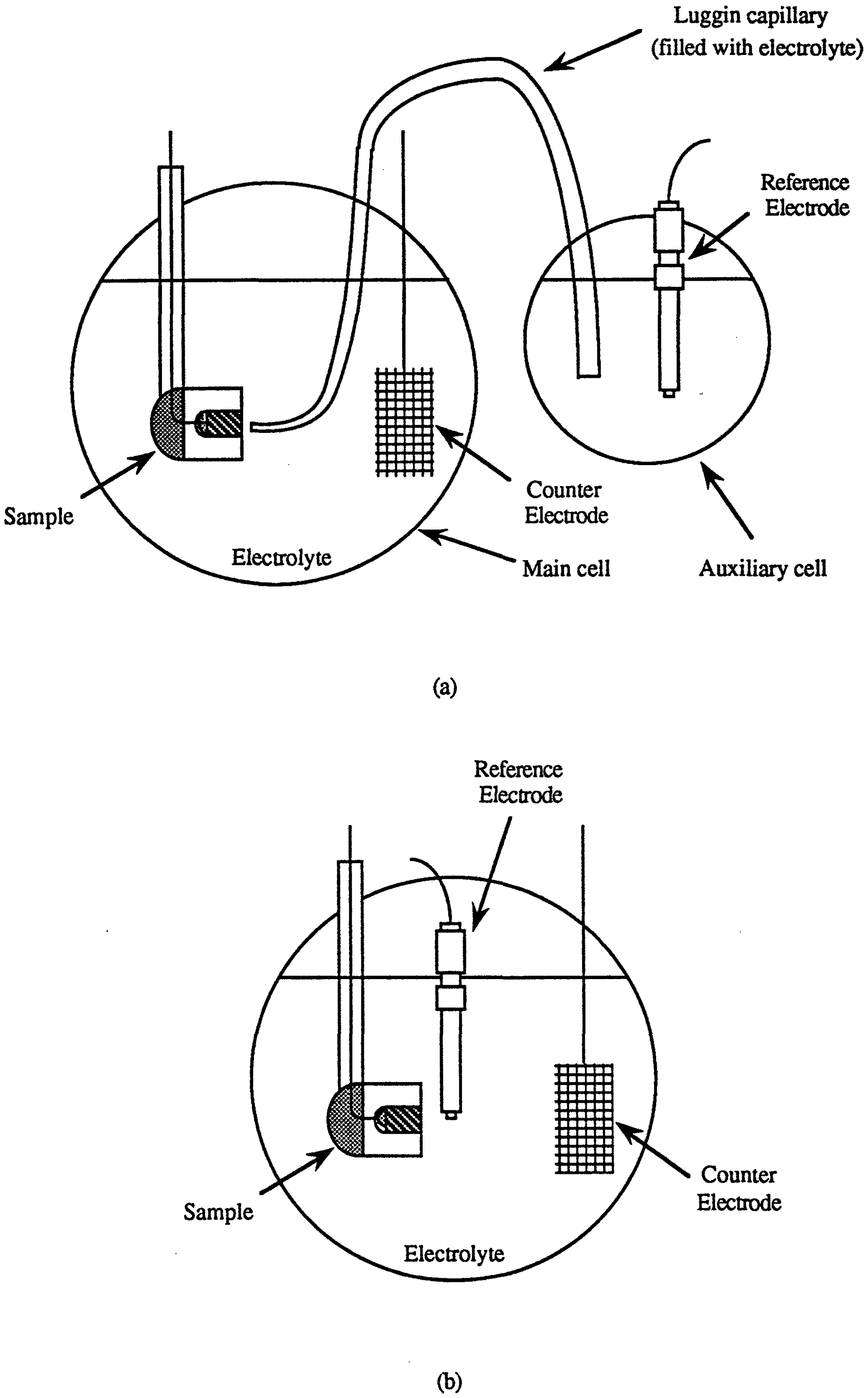
Luggin capillary
(filled with electrolyte)
Reference
Electrode
Sample
Counter
Electrode
Electrolyte
Main cell
Auxiliary cell
(a)
Reference
Electrode
Sample
Counter
Electrode
Electrolyte
(b)

Figure 4.2 Schematic representation of the cell setup used in (a) polarization tests and (b) EIS tests.

4.3.3 Electrolyte Temperature

It was found that reproducible, noise-free EIS data could not be obtained when the temperature of the test solution was controlled by a thermostatic device. All EIS experiments were therefore performed at ambient temperature. In order to facilitate a correlation to the EIS work, many of the other electrochemical tests in this study were also conducted at ambient temperature. The test solutions in these experiments had an average temperature of approximately 23°C. A number of polarization and galvanic corrosion tests were also performed at 30°C and 80°C. Temperatures were controlled at 30 ± 0.5°C using a Cole-Parmer Lab Monitor® III thermoregulator in conjunction with a nichrome resistance wire heating coil and a standard mercury thermometer. Temperatures were controlled at 80 ± 1°C using two Dyna-Sense® thermoregulators in conjunction with a thermal bath heated by a pair of 250 watt Vycor® heating elements. Changes in the concentration of the test solution due to evaporation were minimized by connecting the cell to a condenser tube chilled by flowing cold water. The temperature of the Ag/AgCl reference electrode was maintained at 80 ± 1°C by immersing the electrode in an auxiliary cell within the heated bath and connecting the main and auxiliary cells with a Luggin capillary.

Five main types of electrochemical tests were performed in this study: potentiodynamic polarization, electrochemical impedance spectroscopy (EIS), galvanic corrosion tests, long-term immersion tests and hydrogen permeation tests. A brief introduction to each of these techniques appears below, and Appendix 10.1 contains a comprehensive discussion of these electrochemical methods. In Appendix 10.1, emphasis was placed on the discussion of topics judged too lengthy to be included in the present section. Subjects discussed in the appendix include an in-depth description of the modeling process used to quantitatively analyze EIS data, and the detailed procedure used to evaluate galvanic corrosion systems.

4.3.4 Potentiodynamic Polarization Testing

Determination of the polarization curve (current-potential relationship) for the metal-electrolyte system under study is a very basic and important test method in corrosion science. A current-potential, or polarization curve is generated by scanning the electrode potential at a known rate and measuring the current as a function of potential. The electrode potential is known to have a substantial effect on the rate of electrochemical reactions. For example, polarization of the electrode to more electropositive (anodic) potentials generally increases the rate of oxidation reactions in the system while decreasing the rate of reduction reactions. These changes in rate are registered experimentally as changes in the cell current. The proportionality between reaction rate and current is derived from Faraday's Law, as described in Section 4.3. Both anodic and cathodic polarization diagrams are normally measured for each metal-electrolyte system of interest. Polarization diagrams can provide an investigator with much useful information; for example, the important electrochemical reactions in a system can often be inferred from polarization testing. The presence or absence of passivation in a given metal-electrolyte system can also be established using this method, and corrosion rates can additionally be estimated from the current-potential relation using the Tafel extrapolation technique.

Potentiodynamic anodic polarization tests can also be used to indicate the presence or absence of localized corrosion, if scan reversal (cyclic polarization) techniques are employed. The presence of higher current densities in the reverse scan is known as hysteresis, which normally indicates that the rate of anodic dissolution has increased as a direct result of the corrosion process which took place during the forward scan. The increase in current density is typically attributed to the compositional changes (such as acidification) which occur during corrosive attack in localized environments such as pits or crevices. As anodic dissolution proceeds within a local environment, the restricted mass-transfer out of the local area causes the concentration of metal cations to increase markedly within the localized or occluded region. The metal cations can then react with water to form both a metal hydroxide and hydrogen ions in a process known as hydrolysis. The production of H^+ ions will result in acidification of the local area, which normally leads to an increase in the rate of local corrosive attack; the increase in attack rate is observed experimentally by a rise in the measured dissolution current during the reverse scan. The presence of localized corrosion can also be diagnosed using the potentiostatic anodic polarization method in which the potential is held at a constant anodic value and the dissolution current is monitored as a function of time. An increase in current with time usually indicates that a local electrolyte is becoming more aggressive, leading to an increase in the rate of corrosive attack and to a corresponding rise in the dissolution current.

All polarization samples were allowed to stabilize at open-circuit for a predetermined length of time before testing was initiated; pre-polarization immersion times of 1, 24, and 72 hours were employed. At the end of the immersion period, the test sample was polarized at a rate of 0.167 mV/sec in either the anodic or the cathodic direction. Polarization of the test samples was generally conducted using a Model 173 EG&G Princeton Applied Research (PAR) potentiostat/galvanostat equipped with an Aardvark Model Scan-4 Scanning Unit.

4.3.5 Electrochemical Impedance Spectroscopy

Electrochemical Impedance Spectroscopy (EIS) is emerging as an extremely powerful tool in the analysis of corrosion and other electrochemical systems. When employed correctly, this technique can provide mechanistic information about the nature of the electrochemical reactions occurring at a metal-electrolyte interface, as well as instantaneous estimates of corrosion rates. Despite these advantages, data generated using the EIS technique are difficult to analyze and often require rigorous modeling in order to be interpreted correctly.

The EIS experiment is typically conducted by applying a small amplitude, fixed frequency sinusoidal voltage perturbation, $E(\omega)$, to the metal-electrolyte system. Measurement of the resulting current, $I(\omega)$, allows the cell impedance, $\vec{Z}(\omega)$, to be determined via:

$$\vec{Z}(\omega) = \frac{E(\omega)}{I(\omega)} \tag{4.1}$$

where $\omega = 2\pi f$ is the angular frequency of the perturbation signal.

The actual EIS measurement is performed using a potentiostat in conjunction with a frequency response analyzer (FRA). The FRA is used to generate the sinusoidal perturbation voltage, which is then attenuated by the potentiostat and applied to the electrochemical cell. The potentiostat measures the resulting current (which will also be sinusoidal in nature), and passes the current and voltage signals to the FRA. The analyzers of the FRA will use these signals to determine the phase change undergone by the current as well as the magnitude of the impedance. The magnitude of the impedance, $|\vec{Z}|$, is equal to the amplitude of the voltage signal divided by the amplitude of the current signal. The phase angle, ϕ, is equal to the amount by which the current signal either leads or lags the voltage signal in time. The phase angle is considered to be negative if the current leads the voltage, as in capacitive systems.

The impedance is a complex quantity since the measured current may be changed both in amplitude and in phase angle from the perturbation voltage. The measured impedance will therefore consist of two components, which can be reported alternatively in either polar form ($|\vec{Z}|,\phi$) or cartesian form ($Z',-Z''$), where Z' is the real or in-phase part of the impedance and $-Z''$ is the imaginary or quadrature part of the impedance. These alternative representations are not independent, and the impedance can be converted from one form to the other using standard polar/cartesian relationships. The impedance can be mathematically represented as:

$$[4.2] \qquad \vec{Z}(\omega) = |\vec{Z}|\exp(j\cdot\phi) = |\vec{Z}|[\cos(\phi) - j\cdot\sin(\phi)] = Z' - j\cdot Z''$$

A schematic description of the relevant impedance parameters is shown in Figure 4.3. Note that complex plane plots are usually constructed as Z' vs. -Z" in order that EIS data can be plotted in the first quadrant of the cartesian axis system. EIS data tend to have a negative imaginary component (as well as a negative phase angle), due to the fact that capacitive reactance is much more common in electrochemical systems than is inductive reactance.

EIS measurements are typically performed at a number of different frequencies over a wide bandwidth in order to generate an impedance spectrum, where one (Z', -Z") data pair is acquired for each individual frequency in the spectrum. A large number of frequencies are

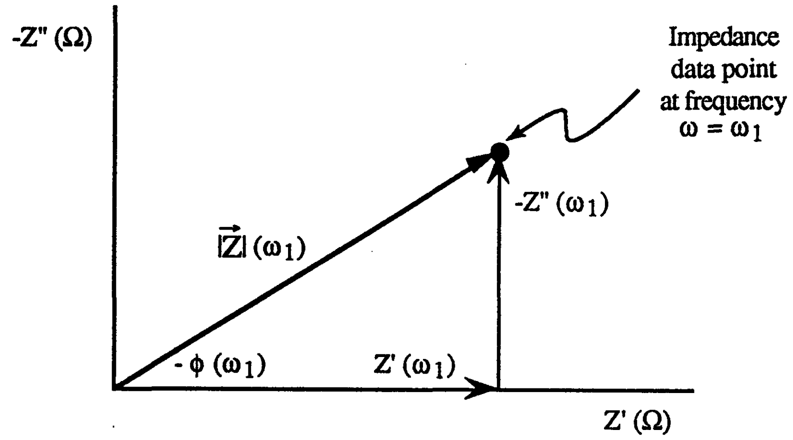

Figure 4.3 Schematic diagram showing how the impedance of a given data point can be alternatively represented in polar form or in cartesian form.

utilized as a result of the fact that the impedance associated with processes in an electrochemical cell are often frequency dependent. Measurement of impedance spectra over a wide frequency bandwidth can provide information about the types of processes present in the electrochemical system, and can also provide important data from which instantaneous corrosion rates can be derived. Impedance data are normally presented in three different graphical forms: a complex plane or Nyquist plot (-Z" vs. Z'), a Bode-magnitude plot (log $|\vec{Z}|$ vs. log f), and a Bode-angle plot ($-\phi$ vs. log f).

The preferred method of analyzing EIS data is to model the measured cell impedance using electrical analogs such as capacitors and resistors, where each electrical analog is chosen to represent a type of physical process believed to occur in the electrochemical system of interest. The detailed process used to analyze EIS data is referred to as equivalent circuit modeling; this process is described at length in Appendix 10.1.

All EIS samples were allowed to stabilize at the open-circuit potential for a predetermined length of time before the experiment was begun; pre-test immersion times of 1, 24, and 72 hours were used in order to provide a correlation to the results of the polarization tests and microscopic analysis. EIS measurements were conducted using a Model 273 PAR potentiostat interfaced with a Solartron® Model 1260 FRA. The perturbation voltage in all cases was 3 mV rms (4.24 mV amplitude). All samples were held at the open-circuit potential during the measurement using a d.c. bias voltage. Impedance spectra were acquired over a frequency range of 19 kHz to ~ 2 mHz.

4.3.6 Galvanic Corrosion Testing

Galvanic corrosion techniques are employed when it is relevant to study the electrochemical properties of metals which are placed in electrical and electrolytic (ionic) contact with one another. In this work, galvanic corrosion testing was utilized to evaluate the feasibility of employing sacrificial zinc coatings as a corrosion control method for Nd-Fe-B. Galvanic corrosion properties are of interest as they relate to the Zn/Nd-Fe-B galvanic couples which are likely to form during service at breaks in the zinc coating. An established technique for analyzing galvanic systems consists of utilizing the mixed potential theory, usually in combination with galvanic corrosion testing. The mixed potential theory is capable of predicting the rates of electrochemical reactions in a corroding system as a function of electrode potential. The approximate electrode potential attained by a Zn/Nd-Fe-B couple at a break in a zinc coating can be determined using galvanic corrosion tests, and the mixed potential theory can then be utilized to predict the rate of anodic dissolution on Nd-Fe-B at the couple potential; such an analysis is capable of predicting whether or not Zn can provide sacrificial protection to Nd-Fe-B at breaks in a zinc coating. The detailed procedure used to evaluate corrosion control via sacrificial metallic coatings is described in Appendix 10.1.

The galvanic corrosion experiments were performed by measuring the open-circuit potential (E_{corr}) of each specimen about 10 minutes after immersion in the test electrolyte; the two samples were then electrically shorted together through a zero resistance ammeter (ZRA). The galvanic current (I_g) and the couple potential (E_{couple}) were monitored for 20 hours.

4.3.7 Long-term Immersion Tests

Long-term immersion tests were conducted in order to measure either the amount of anodic dissolution or the cracking rate of Nd-Fe-B samples subjected to different polarization conditions. The long-term immersion samples were originally designed to maximize the accuracy of weight loss measurements. Sample weight loss was to be measured after removal from the test solution in order to evaluate the anodic dissolution rate at various electrode potentials. The sample design outlined earlier (Section 4.3.1) was not suitable for these purposes, because of the relatively small surface area exposed to the electrolyte (~ 0.1 cm^2). Samples with small exposed area will experience a relatively low weight loss, which can lead to erroneous results if weighing inaccuracies contribute significantly to the measured weight change. Another shortcoming of the previous electrode design is that solution uptake into the epoxy resin is liable to result in some degree of weight gain during immersion.

In order to circumvent these limitations, a different sample configuration was utilized, with the entire circumference and one face of each cylindrical sample polished to 1200 grit and exposed to the solution. This sample design allowed a significantly larger area (~ 2 cm^2) to be exposed to the electrolyte than in the previous electrode arrangement, and also avoided the use of epoxy resin. The electrical contact procedure described in Section 4.3.1 was used to affix a copper wire to the back of each sample, and the contact was then masked off from the test solution using two coats of Microstop® electroplating lacquer (Micro Products). A rubber stopper was used to attach the sample securely to a glass tube. A similar procedure was used to prepare cylindrical samples of high purity zinc metal for long-term galvanic couple tests.

4.3.8 Hydrogen Permeation

The hydrogen permeation technique is based on using electrochemical means to create a hydrogen concentration gradient across a metallic membrane [63]. The membrane effectively becomes a bi-electrode in two separate electrical circuits. Hydrogen atoms are generated on one side of the metallic membrane sample, either by deliberate electrochemical reduction or as a by-product of a corrosion reaction on the surface of the metal. The side of the membrane on which hydrogen production occurs is known as the input or charging side of the sample. The other side of the membrane is electrochemically polarized to a potential at which hydrogen atoms are thermodynamically unstable and will oxidize to form protons. This side of the membrane is referred to as the output or discharge side of the sample.

The hydrogen atoms generated on the input side of the membrane may either combine to form hydrogen molecules or become absorbed into the metal itself. Absorbed hydrogen atoms will diffuse through the sample, due to the concentration gradient created by the electrochemically maintained zero hydrogen concentration boundary condition on the output side of the membrane. The permeation process is illustrated schematically in Figure 4.4.

Hydrogen atoms which diffuse through the metal will be electrochemically oxidized at the discharge surface according to the reaction:

[4.22] $$H \rightarrow H^+ + e^-$$

The potentiostat will remove the electrons produced by [4.22], and the permeating hydrogen flux will therefore be registered as an electron current. The number of electrons

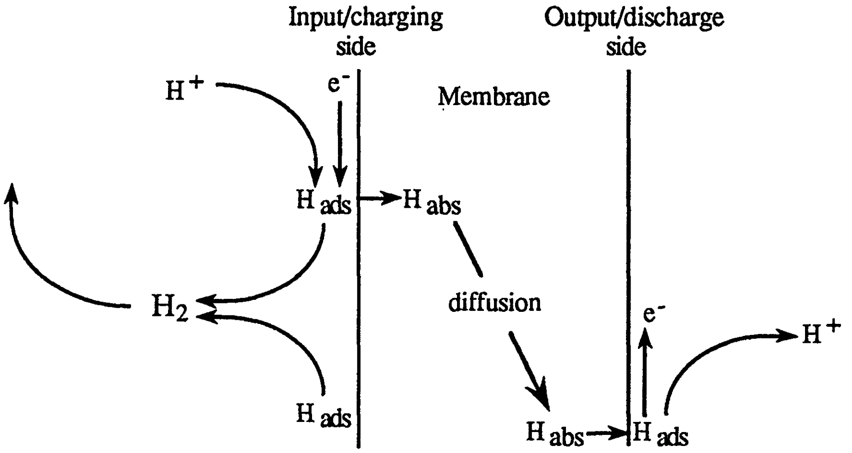

Figure 4.4 Discrete steps involved in the electrochemical permeation technique [63].

collected at the discharge side is a quantitative measure of the amount of hydrogen permeating through the sample. Data are generally reported as hydrogen flux versus time.

The hydrogen permeation technique requires the use of a relatively thin wafer or foil of the metal to be analyzed. Nd-Fe-B and other permanent magnets are generally not fabricated as foil or sheet specimens, and sections therefore needed to be cut from existing cylindrical samples. Even if fabricated thin sheets were available, it would be preferable to use wafers which had been sectioned from bulk samples. The ultimate objective of the permeation experiments is to compare the data to results obtained in the long-term immersion tests, and thin samples could have properties which are very different from those of the bulk material.

Nd-Fe-B wafers (approximately 3 mm thick) were cut from the cylindrical h.p. samples supplied by Magnequench®. Sectioning was performed using an Accutom-2® (Struers) cutting saw equipped with a diamond-impregnated blade. This cutting instrument allowed parallel-sided sections of reproducible thickness to be obtained. The saw also permitted the samples to be cut in a reasonable amount of time (~1 hour), and did not lead to cracking of the wafers during cutting. Previous attempts to cut the hard, brittle Nd-Fe-B samples with other saws had resulted in cracking of the wafer during the cutting process, or to cutting times which were unacceptably long.

The experimental setup used for the hydrogen permeation studies was designed and constructed by Abdul-Hamid [63]. The permeation cell consists of two cylindrical half-cells with a sample mounting assembly clamped in between, as shown in Figure 4.5 (a). The cell was machined completely out of Teflon® polytetrafluoroethylene (PTFE) sections.

Conical openings were machined through both rectangular slabs in the sample mounting assembly (Figure 4.5 (b)) in order to permit the metallic wafer to contact the electrolytes in

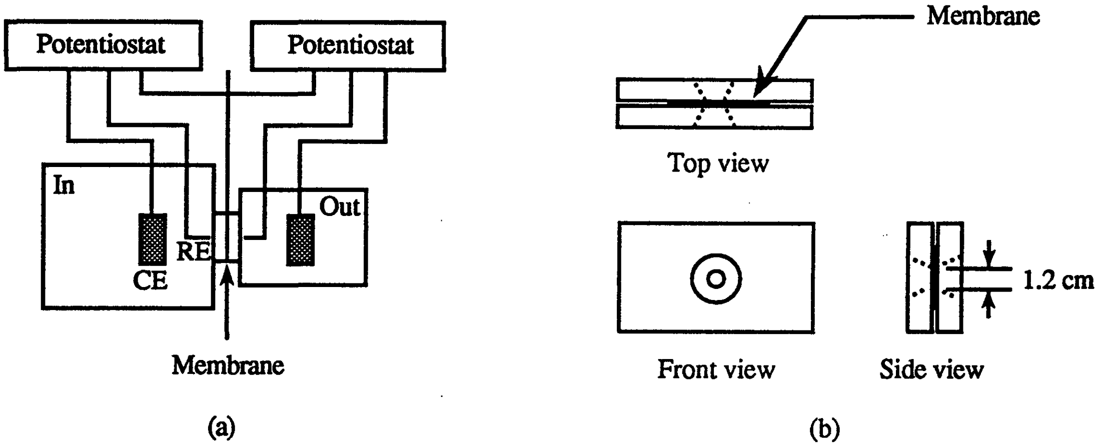

Figure 4.5 Schematic representation of (a) the permeation cell and (b) the sample mounting assembly.

the half-cells. The circular hole adjacent to the seating area of the sample was ~ 1.2 cm in diameter, which presented a complication for the present experiment. The cylindrical samples which the wafers had been sectioned from were only 0.6 cm in diameter, and the samples were thus too small for the existing openings in the permeation cell. In order to avoid the expense of machining a new sample holder, or of using a different permeation cell, the problem was solved using the sample arrangement described below.

After both sides of the sample had been polished to 1200 grit, two electrical contacts were made to the side of the wafer using the contact procedure described in Section 4.3.1. The electrical contact apparatus and a thin rim around the edge of each polished surface were masked off using electroplating lacquer. Small holes were cut in two polyethylene (PE) sheets of dimensions 5 cm x 5 cm x 0.07 cm. The sample and its attached electrical contact were placed between the two PE sheets and the sample was pressed into both of the circular holes. Silicone rubber adhesive was then applied in order to seal the gap between the sample and the hole in each sheet, leading to the final sample arrangement shown in Figure 4.6. Once the silicone had cured, the sample was clamped into the permeation cell and the

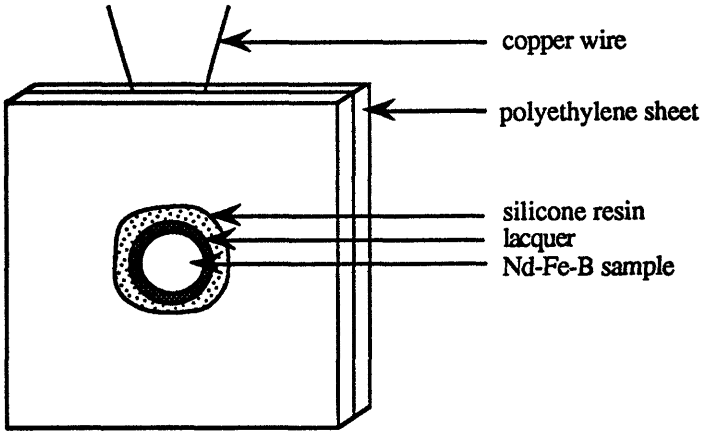

Figure 4.6 Schematic representation of the hydrogen permeation sample arrangement.

arrangement was verified to be leak-proof. The resistance of the polymeric materials to NaOH was subsequently verified by immersion testing.

4.3.8.1 Palladium Deposition

It was necessary to perform an additional step before utilizing the samples for testing. Since the output side of the membrane is anodically polarized in order to oxidize any permeating hydrogen, an active metal such as Nd-Fe-B will exhibit a very high corrosion rate if exposed to the electrolyte on the discharge side of the membrane. The anodic dissolution reaction will produce a large and likely unstable electron current, which will be superimposed upon the hydrogen permeation current. In order to avoid this problem, the output side of all Nd-Fe-B membranes was coated with a layer of palladium metal (~ 1 μm thick). The ability of palladium to passivate in NaOH will allow a low, stable background current to be established, from which the hydrogen current is easily distinguishable. Palladium also has an extremely high hydrogen diffusion coefficient, such that the thin coating will not act as a barrier for hydrogen transport through the membrane.

The palladium was deposited using a Materials Research Corporation Model 8620 RF sputtering system. An argon ion plasma is created in the chamber and is then directed at a palladium target to produce a sputtering effect. The membrane samples are coated by the sputtered Pd, with the process continued until a 1 μm coating has been deposited.
An important requirement of the deposition process was that the palladium coating had to be pinhole-free so that the Nd-Fe-B was not exposed to NaOH on the discharge side of the sample. Abdul-Hamid found that a 1 μm deposition thickness was more than adequate to produce a continuous Pd coating, using operating conditions which were essentially identical to those employed in this study [63]. It was also of critical importance that no palladium be deposited on the input side of the samples, in order to avoid the formation of Pd/Nd-Fe-B galvanic couples on this side of the membrane. The presence of Pd would likely change the electrochemical behavior of the input surface under certain conditions. Palladium was prevented from reaching the input side of the membrane by using Al foil to completely mask this side of the sample before it was placed in the sputtering chamber.

Hydrogen permeation tests were conducted using the following procedure. The test sample was first clamped into the permeation cell, and NaOH was added to the Pd-coated output side of the membrane. The output side was polarized to +0.5 V (SCE) in order to oxidize all incoming hydrogen. Once a stable passive current density was attained on the Pd-coated side of the sample, the test solution (NaCl or Na_2SO_4) was added to the other half-cell and the appropriate input condition established. The start time of the experiment was recorded and the current on the output side monitored in order to record the flux transient.

4.4 Microscopy

Electrochemical tests can provide a great deal of information to the corrosion scientist. A considerable limitation of electrochemical corrosion tests, however, is that the morphology (location) of corrosive attack can generally not be identified using these methods. Given the importance of identifying and understanding the corrosion morphology in the system under test, it is considered to be critical in most corrosion work to combine electrochemical testing with a microscopic analysis of the damage resulting from corrosive attack.

Although microscopic analyses would ideally be performed *in-situ* while the sample is corroding in the electrolyte, *in-situ* testing was prevented in this study by the formation of insoluble corrosion products on the surfaces of all Nd-Fe-B samples. In situations where *in-situ* experiments are precluded, an alternative process known as *ex-situ* analysis also allows the changes in corrosive attack to be followed with time. *Ex-situ* analysis consists of immersing test samples in the corrosive electrolyte for different periods of time and then removing them from the solution prior to viewing in the microscope; all experiments in this study were performed using the *ex-situ* method.

The Nd-Fe-B samples employed in the microscopic analysis were identical to those utilized for electrochemical testing (Section 4.1). Each sample was polished to a 1200 grit finish, cleaned in detergent solution, and degreased with acetone. The sample was immersed in the appropriate electrolyte for a predetermined length of time. At the end of the immersion period, the sample was removed and rinsed in deionized water. An effort was then made to remove the insoluble corrosion products formed during immersion. Insoluble corrosion products on the surface of the sample were generally removed by ultrasonic cleaning in deionized water. Corrosion products still occasionally obstructed the viewing process even after this cleaning step, but in general the sample surface was clear enough for adequate observation. It is not feasible to remove the corrosion products from Nd-Fe-B via acid pickling, because reliable inhibitors have not been established for this alloy system. If acid cleaning were used, subsequent microscopic investigation would produce ambiguous results, since it would not be clear whether the observed damage occurred during immersion in the test solution or during the acid cleaning step. An attempt to remove the corrosion products using cellulose acetate replica stripping was unsuccessful.

Immersion times for the microscopy samples were 15 minutes, 1 hour, 12 hours, 24 hours, 72 hours, 1 month, and 3 months. All samples were immersed at ambient temperature, and were oriented such that the polished surface exposed to the solution was placed in a vertical position, in order to facilitate a correlation with the electrochemical tests.

Several different types of microscopes were employed in the current study. Imaging of the surface was performed with a scanning electron microscope (SEM), and a confocal laser microscope was used to obtain quantitative surface topography information. A field emission SEM was used to attain images at high resolution, and an electron probe microanalyzer (EPMA) was employed to obtain compositional (chemical) information. Non-magnetized samples were utilized for all electron microscopy work.

Images of the corroded samples were acquired using a Cambridge Stereo Scan® scanning electron microscope (SEM) operating at an accelerating voltage of 20 kV. The instrument was used in secondary electron mode in order to permit the observation of topographic detail. Samples were generally coated with a thin layer of sputtered gold in an effort to reduce charging effects from incompletely removed corrosion products. Compositional analysis was occasionally performed using energy-dispersive x-ray spectroscopy (EDX).

Quantitative topographical information was obtained using a Lasertec 1LM11 confocal microscope. The 1LM11 is actually an optical microscope which employs a laser (HeNe, 632.8 nm) as a light source. The confocal microscope is capable of generating profiles of the attacked or corroded surfaces. The microscope is fitted with a motor which allows the lens system to translate up and down relative to the plane of the sample. The nature of confocal optics leads to a very small depth of field whereby light only reaches the detector when the sample is precisely at the focal length of the currently selected lens. During the translation process, the microscope will record the position of maximum light intensity for each point along a selected profiling line on the sample surface. Each maximum intensity point is then correlated to surface height, and a topographical profile is generated.

High resolution images were obtained using a JEOL 6300 field emission SEM. Such images were necessary because of the fine scale of the grains in the rapidly solidified alloys (80-100 nm). Samples were not coated with gold prior to viewing, as the gold islets which form can interfere with high resolution imaging. The instrument was operated at a low accelerating voltage (1 kV), in order to increase the surface sensitivity of the images.

Compositional information was obtained using a JEOL Superprobe® 733 electron probe microanalyzer (EPMA). The instrument was employed in backscatter mode, with an accelerating voltage of 15 kV. The standards utilized in the calibration of the instrument are shown in Table 4.1. The EPMA was not able to measure the composition of boron, due to the low atomic weight of this element. In order to reduce charging effects, all samples were coated with carbon (~25 µm thick) prior to placement in the specimen chamber.

Table 4.1 Standards used in the calibration of the electron probe microanalyzer.

Element	Standard	Chemical Symbol
Nd	Neodymium fluoride	NdF_3
Fe	Iron	Fe
Co	Cobalt	Co
O	Hematite	Fe_2O_3
Cl	Scapolite	$Na_4Al_3Si_9O_{24}Cl$

5. Corrosion Behavior of the Alloy

The work described in the following chapter was performed in order to obtain a comprehensive understanding of how the Nd-Fe-B alloy corrodes. The analysis was conducted using electrochemical methods (e.g. electrochemical impedance spectroscopy, potentiodynamic polarization) in conjunction with microscopic techniques such as scanning electron microscopy and confocal laser microscopy.

All tests were performed on industrially-produced Nd-Fe-B alloys, in order to ensure that the results of the study were as relevant as possible to actual service conditions. It should be mentioned, however, that the corrosion of the alloy could have been studied using an alternative method. The corrosion of a metal possessing a multiphase microstructure can be analyzed using galvanic corrosion methods (with the constituent phases of the alloy serving as the coupled metals) in order to simulate the microgalvanic cells which are operative on the corroding surface.

Such an analysis normally provides insight into the corrosion behavior of multiphase alloys, but these tests were believed to be of questionable utility in the current study. The identity of the Nd-rich phase is disputed in the literature, and it was not considered feasible to procure test samples which adequately represented the grain boundary phase. Strong consideration was given to fabricating "facsimile" grain boundary phase samples, but this alternative was ultimately rejected because of the expected difficulty of the fabrication task. In addition, it was believed that any results obtained using "facsimile" grain boundary samples would likely be of diminished significance due to the ambiguity surrounding the actual composition of the Nd-rich phase in the industrially-produced alloy. It was considered to be much more efficient and relevant to test the actual Nd-Fe-B alloy used in service.

5.1 Polarization Behavior of h.p. and d.u. Alloys

A preliminary investigation of the corrosion behavior of Nd-Fe-B can be performed by measuring its polarization behavior in relevant test solutions. The results will provide some basic but important diagnostic information about the corrosion of the alloy, as described in Section 4.3.4. A rapid determination of whether corrosion is occurring in the active state or in the passive state can be made using this technique. Polarization testing can often be used to qualitatively identify the important reactions occurring during the corrosion process (e.g. metal dissolution, oxygen reduction). The effects of magnetic flux and solution composition on the corrosion of the alloy can be rapidly assessed. Tafel extrapolation techniques can be used to obtain a preliminary estimate of the corrosion rate of the alloy.

It is emphasized that the results presented in Section 5.1 are meant to serve as a *preliminary* analysis of the corrosion behavior of Nd-Fe-B. It will be necessary to study the corrosion of the alloy in far more detail than can be obtained using the results of the polarization curves alone. A comprehensive analysis is contained in Sections 5.2 - 5.4.

Anodic and cathodic polarization curves were measured for h.p. and d.u. alloys in NaCl and Na_2SO_4. Two orthogonal planes of the d.u. magnets had to be tested because of the crystallographic and magnetic anisotropy exhibited by die upset Nd-Fe-B. To account for crystallographic anisotropy, one test plane was approximately perpendicular to the c-axis of the elongated $Nd_2Fe_{14}B$ grains (d.u. $\perp$ c) and the other plane was approximately parallel to the c-axis of the grains (d.u. $\parallel$ c). The selected test planes also accounted for the magnetic anisotropy of the d.u. alloys, as magnetic flux lines are perpendicular to the test plane of the d.u. $\perp$ c specimens and parallel to the test plane of the d.u. $\parallel$ c samples (Figure 2.5). As discussed in Section 4.1, all d.u. alloys examined in this study were tested in the magnetized condition, while all h.p. alloys were tested in the non-magnetized condition.

5.1.1 Anodic Polarization Behavior at 30°C

Anodic polarization curves for the h.p. and d.u. alloys (30°C) are shown in Figure 5.1. In order to enhance the clarity of these figures, regions of high anodic overpotential were not included in the plots (these regions are shown instead for the h.p. alloy in Figure 5.2).

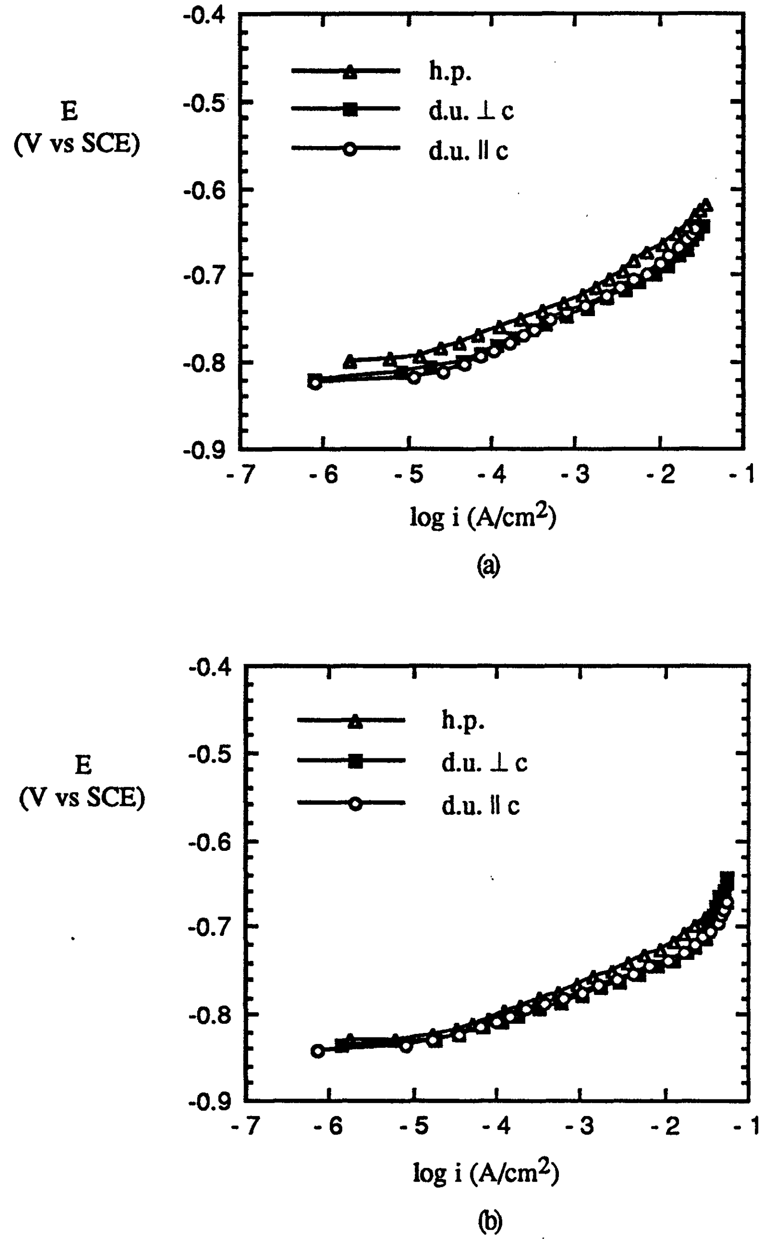

Figure 5.1 Anodic polarization diagrams for h.p. and d.u. alloys in (a) NaCl and (b) Na_2SO_4 at 30°C.

Nd-Fe-B was found to exhibit active (Tafel) corrosion at low anodic overpotentials in both test solutions, as shown in Figure 5.1. The strong dependence of current density on potential and the approximate linearity of the E-log i curve are both characteristic of metal dissolution occurring under charge-transfer control, as discussed in Section 4.4.1.

At higher anodic overpotentials, mass-transfer control was found to exist up to +1.5 V (SCE) in NaCl, as shown in Figure 5.2. A slight reduction in current density was observed at potentials noble to -0.2 V (SCE) in Na_2SO_4. Current density reductions at oxidizing potentials have been previously observed for Nd-Fe-B in various SO_4^{2-} solutions [48,54], but this limited passivation appears to be of little or no engineering significance.

In order for passivation to be useful, the alloy would have to exhibit a low passive current density (preferably below 10^{-5} A/cm^2), since a low i_{pass} corresponds to a low metal dissolution rate via Faraday's Law. The passive film ideally would not have to be induced by anodic polarization, but rather would be spontaneously stable at open-circuit.

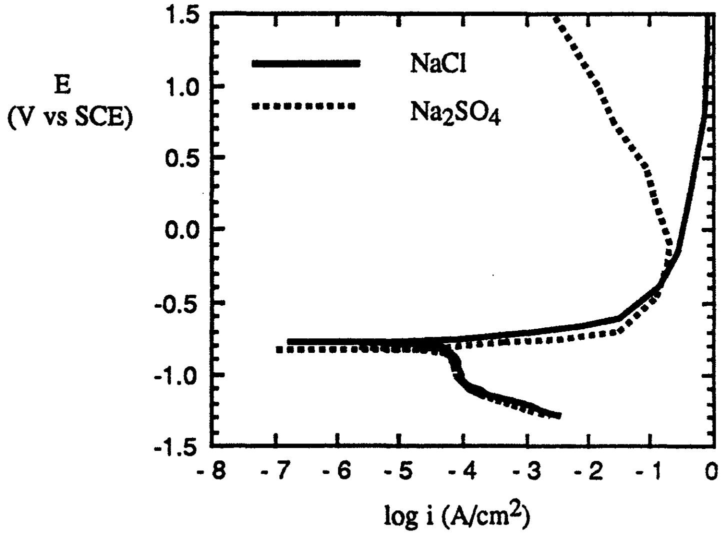

Figure 5.2 Anodic and cathodic polarization behavior of h.p. Nd-Fe-B in NaCl and Na_2SO_4 at 30°C.

5.1.2 Cathodic Polarization Behavior at 30°C

Cathodic polarization curves for the h.p. and d.u. alloys (30°C) are shown in Figure 5.3.

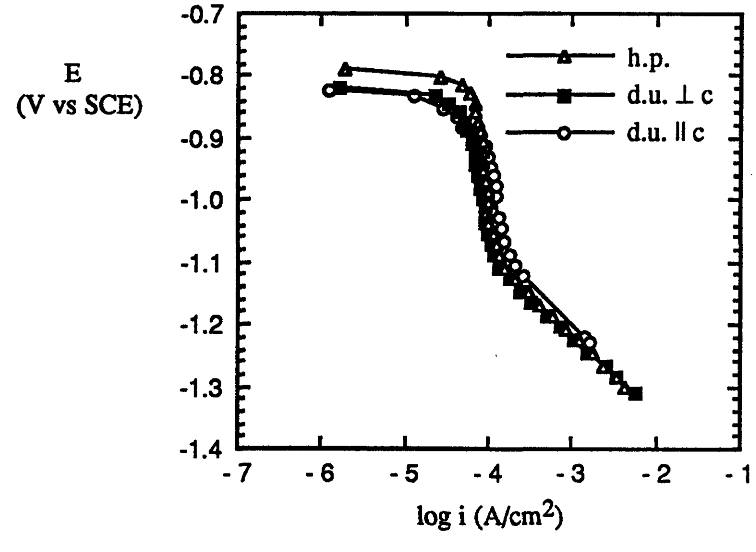

(a)

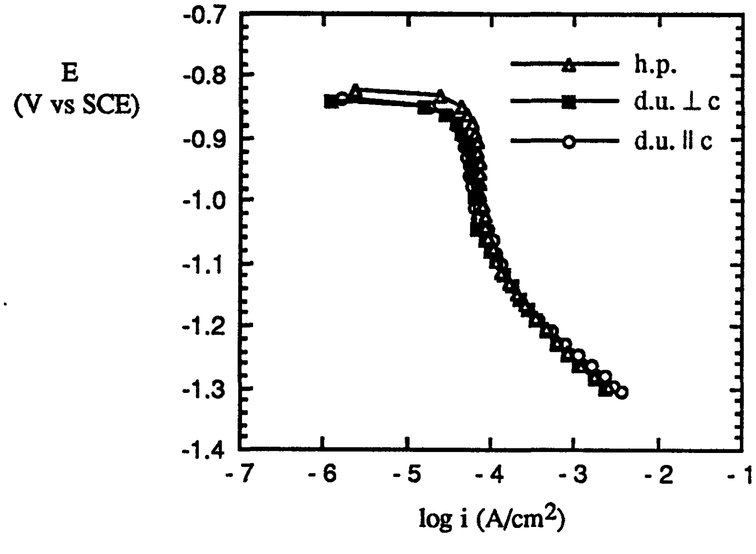

(b)

Figure 5.3 Cathodic polarization diagrams for h.p. and d.u. alloys in (a) NaCl and (b) Na_2SO_4 at 30°C.

At low cathodic overpotentials, the alloy was found to exhibit diffusion-limited oxygen reduction kinetics in both test solutions, as shown in Figure 5.3. The nearly vertical region of the E-log i curve is characteristic of processes which are under mass-transfer control, as discussed in Section 4.4.1. The observed i_{lim} values are typical for diffusion-limited oxygen reduction processes in aerated, non-agitated near-neutral solutions [64]. At higher cathodic overpotentials, the linear regions in Figure 5.3 correspond to the reduction of water to hydrogen (under charge-transfer control).

Electrochemical data from Figures 5.1 and 5.3 are shown in Table 5.1. The corrosion current density (i_{corr}) values were calculated by Tafel extrapolation (average of both anodic and cathodic tests). The i_{corr} values will be used to estimate metal loss rates in Section 5.1.10, and the β_a values to estimate metal loss rates from EIS data (Appendix 10.2).

Table 5.1 Average electrochemical data from polarization of Nd-Fe-B in (a) NaCl and (b) Na_2SO_4 at 30°C.

(a)

Alloy	E_{corr} (V)	i_{corr} ($\mu A/cm^2$)	β_a (V/decade)	i_{lim} ($\mu A/cm^2$)
h.p.	-0.794	57.7	0.042	95.4
d.u. $\perp$c	-0.823	58.6	0.046	89.1
d.u. $\parallel$c	-0.822	74.6	0.052	130.9

(b)

Alloy	E_{corr} (V)	i_{corr} ($\mu A/cm^2$)	β_a (V/decade)	i_{lim} ($\mu A/cm^2$)
h.p.	-0.824	54.2	0.034	87.8
d.u. $\perp$c	-0.839	41.7	0.033	68.0
d.u. $\parallel$c	-0.840	38.6	0.034	65.5

5.1.3 Anodic Polarization Behavior at 80°C

Anodic polarization curves for the h.p. and d.u. alloys (80°C) are shown in Figure 5.4. Regions of higher anodic overpotential were again removed in order to improve clarity.

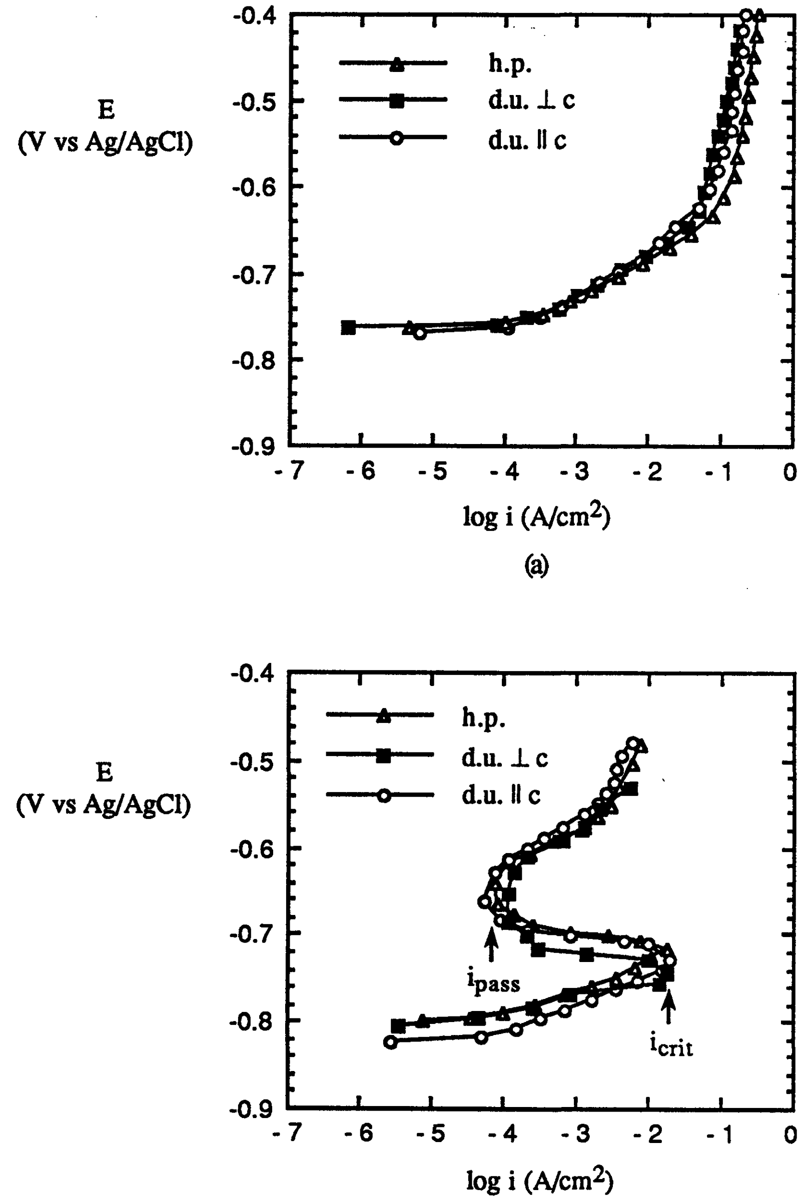

(a)

(b)

Figure 5.4 Anodic polarization of h.p. and d.u. alloys in (a) NaCl and (b) Na_2SO_4 at 80°C. The passive current density (i_{pass}) and the critical current density for passivation (i_{crit}) are indicated in (b).

Nd-Fe-B was found to exhibit active corrosion at low anodic overpotentials in both test solutions, as shown in Figure 5.4. At higher anodic overpotentials, mass-transfer control was found to exist up to +1.5 V (SCE) in NaCl, as shown in Figure 5.5. An active-passive transition was observed in Na_2SO_4 at 80°C (Figure 5.4 (b)), as discussed below.

Passivation was induced by anodic polarization at 80°C in Na_2SO_4, but the obtained passive film appears to be limited in its usefulness. A viable passive film should be stable at open-circuit and exhibit a low i_{pass}, as mentioned earlier. A low critical current density for passivation is also important, since i_{crit} dictates the amount of current which must be supplied by the cathodic reactant in order to form the passive film. Passivity should also be stable over a broad potential region, so that the passive film will resist oxidizing conditions.

The alloy exhibits active dissolution at open-circuit in Na_2SO_4. Both the passive current density (~ 100 μA/cm^2) and the critical current density for passivation (~ 20 mA/cm^2) are relatively high; the passive region is also very narrow (< 0.1 V). The corrosion rate of the alloy is substantial (~ 110 μA/cm^2), despite the presence of the active-passive transition.

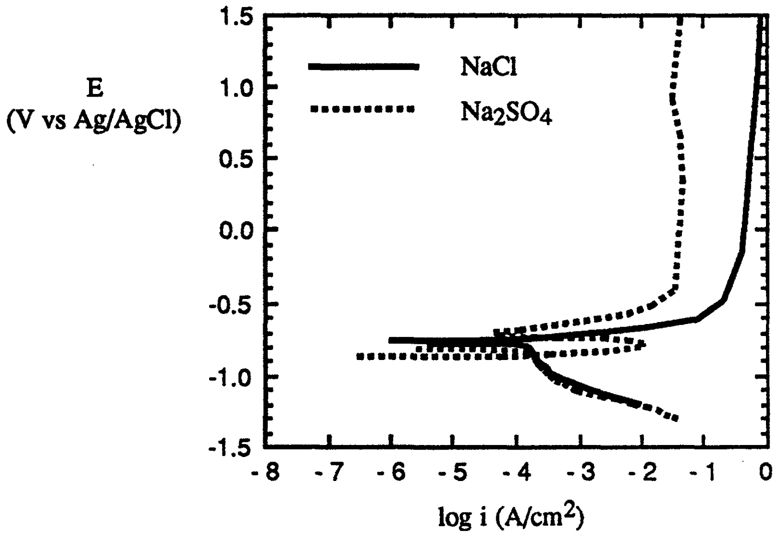

Figure 5.5 Anodic and cathodic polarization of h.p. Nd-Fe-B in NaCl and Na_2SO_4 at 80°C.

5.1.4 Cathodic Polarization Behavior at 80°C

Cathodic polarization curves for the h.p. and d.u. alloys (80°C) are shown in Figure 5.6.

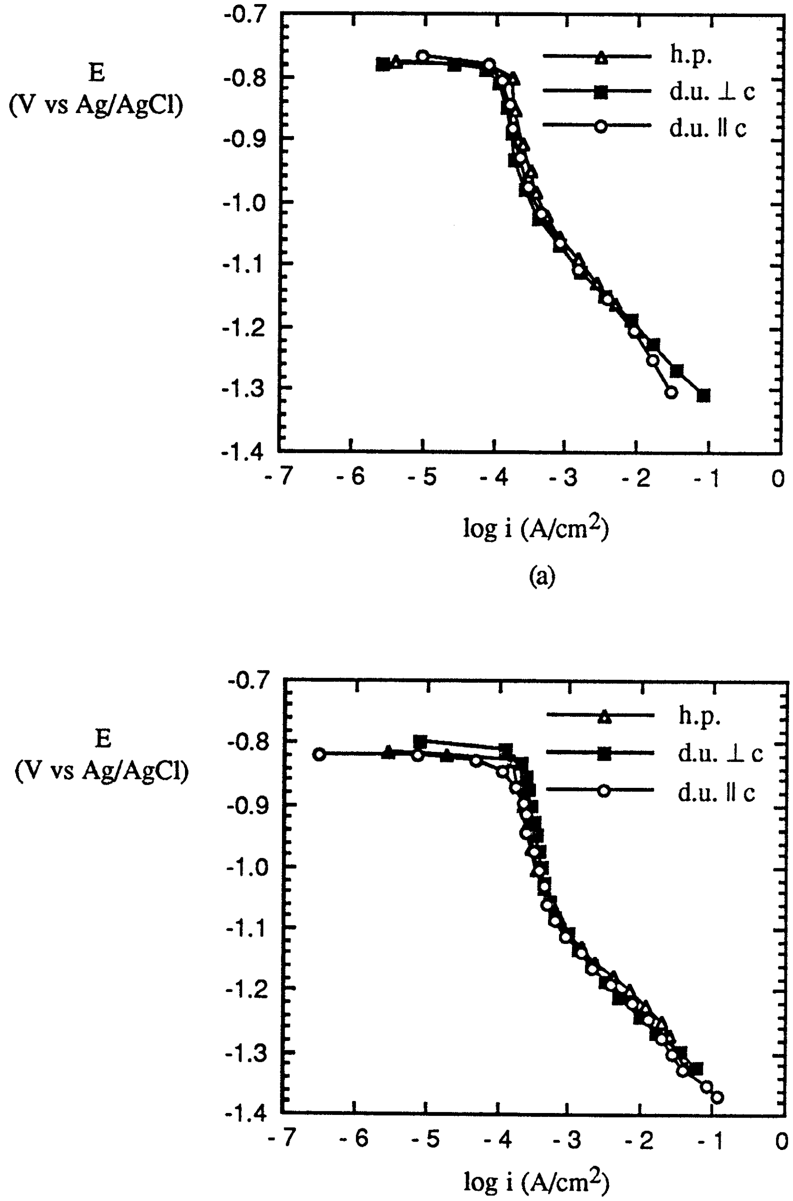

(a)

(b)

Figure 5.6 Cathodic polarization of h.p. and d.u. alloys in (a) NaCl and (b) Na_2SO_4 at 80°C.

At low cathodic overpotentials, the alloy was found to exhibit diffusion-limited oxygen reduction kinetics in both test solutions, as shown in Figure 5.6. The measured i_{lim} in these tests is higher than at 30°C, due to the effect of temperature upon the rate of oxygen diffusion to the surface. As a result, the predicted corrosion rate is higher at 80°C than at 30°C (126 $\mu A/cm^2$ as opposed to 58 $\mu A/cm^2$ for the h.p. alloy in NaCl).

At higher cathodic overpotentials, the observed linear regions again correspond to the charge-transfer controlled reduction of water to hydrogen.

5.1.5 Summary of Polarization Results

The results of the anodic and cathodic polarization measurements at both 30°C and 80°C are compatible with previous reports of poor corrosion resistance for the Nd-Fe-B magnet [47, 49,49a]. The inability of the alloy to passivate spontaneously indicates that it is corroding actively at open circuit. Under these conditions, the corrosion rate of the magnet is controlled by electrochemical reactions which are not related to passivation.

The most important reactions in the corrosion of Nd-Fe-B appear to be anodic metal dissolution under charge-transfer control and oxygen reduction under mass-transfer control. The overall rate-controlling reaction in the corrosion of Nd-Fe-B in all four test solutions appears to be the diffusion-limited oxygen reduction reaction. Due to the nearly vertical slope of the cathodic curves and the relatively low slope of the anodic curves, the cathodic reaction has a more substantial influence on the corrosion rate than does the anodic reaction. For example, if the oxygen access rate were to increase as a result of solution flow or the formation of a thin electrolyte film, the corrosion rate should increase due to rapid access of oxygen (the cathodic reactant) to the metal surface. This disproportionate influence of the cathodic reaction on the corrosion rate is known as cathodic control.

5.1.6 Effect of Solution Composition

The polarization behavior of h.p. and d.u. alloys at 30°C did not appear to be significantly affected by differences in solution composition (Figures 5.1 and 5.3). The limiting current density is slightly higher in the NaCl solutions than in the Na_2SO_4 solutions, owing to the difference in the solubility of oxygen in the two solutions. The salt content (in terms of weight percent) is higher for the 0.5M Na_2SO_4 solutions than for the 0.5M NaCl solutions (owing to the greater formula weight of Na_2SO_4), and the solubility of oxygen in a given solution is known to be inversely proportional to its salt content. At 80°C, the open-circuit behavior was not generally affected by solution composition, but the behavior of the material under anodic polarization was markedly different (Figure 5.4 (b)).

5.1.7 Effect of Magnetization

The nearly identical polarization behavior exhibited by the d.u. $\perp$ c samples and the d.u. $\parallel$ c samples (Figures 5.1, 5.3, 5.4, 5.6) indicates that the direction of the magnetic flux relative to the sample surface does not significantly influence the polarization behavior of Nd-Fe-B. In fact, the *presence* of a strong magnetic flux was found to have little effect upon the polarization behavior of Nd-Fe-B, as evidenced by the general similarity between the polarization diagrams for the h.p. (nonmagnetized) and d.u. (magnetized) samples. The microstructural changes which result from subjecting the h.p. alloy to the die upsetting process were additionally found to exert only a slight effect on the polarization of Nd-Fe-B.

The absence of a magnetic field effect on the samples tested in this study is consistent with theoretical expectations. Magnetic flux has been shown by Kelly [65] to exert a significant effect on the rates of electrochemical reactions occurring in *flowing* electrolytes, but this effect is not believed to apply to the quiescent (non-flowing) electrolytes utilized in this study. The alloy is not expected to be exposed to flowing electrolytes in service.

Magnetic fields can affect corrosion rates because of their ability to induce electrical potential differences according to Faraday's Law of Induction [66]. An electrical potential difference, if induced across the metal-electrolyte interface, would likely have a significant effect on the electrochemical reaction rates in the corroding system. The possible presence of magnetically-induced potential differences is therefore a significant concern in the corrosion of a system exposed to a magnetic field.

A magnetic field will typically induce an electrical field in the presence of relative mechanical motion, such as a physical translation of either the magnetic field or of the electrolyte containing charged (ionic) species. The change in the potential difference at a metal-electrolyte interface due to the presence of a magnetic field (ΔE_{mag}) is [65]:

$$\Delta E_{mag} = 2 \cdot B \cdot a \cdot v \tag{5.1}$$

where B is the magnetic flux density, a is a geometric factor, and v is the velocity of the flowing electrolyte. Equation [5.1] shows that an electrical field can be induced in the presence of charge movement. The movement of faradaic current through the metal-electrolyte interface would not be expected to induce a potential difference across the interface, however, since the induced field must act at right angles to both the applied magnetic field and the movement of charge. Magnetic flux should thus not affect the corrosion behavior of this particular system, owing to the absence of a flowing electrolyte. A potential difference can also be induced by changes in the magnetic field over time, again via Faraday's Law of Induction [66]. This particular mode of induction would not be expected to affect the corrosion of a permanent magnet, since the magnetic field output of such a material is expected to be very stable over time.

Another possible influence of magnetic flux on the corrosion rate of Nd-Fe-B is related to the types of insoluble corrosion products which form on the metal surface. One corrosion product which can form on the surface of a ferrous alloy is magnetite (Fe_3O_4). Due to its magnetic properties, a magnetite corrosion product could be tightly bound to the surface of a magnetized Nd-Fe-B sample. This attraction would take place only in alloys which have been magnetized. If magnetite were protective to the alloy, disparate corrosion rates might be obtained between magnetized and non-magnetized samples.

Magnetite was visually observed in the corrosion products at the end of anodic polarization tests (magnetite can generally be identified by its characteristic black color), but not in tests conducted at open-circuit with no external anodic polarization. Magnetite is not stable in the presence of oxygen, as it is readily oxidized to form a ferric corrosion product. It is likely that magnetite was temporarily stable after external anodic polarization, since the anodic dissolution products had not yet had time to oxidize to a significant extent. These corrosion products were found to gradually oxidize to the ferric state if allowed to remain at open-circuit after anodic polarization was removed. When the corrosion was *not* driven externally by the potentiostat, the corrosion products appeared to be in the ferric or oxidized state (although an underlayer of magnetite could conceivably have been present).

If magnetite were protective to Nd-Fe-B in terms of passivation, a noticeable decrease in current density should have been obtained at some point during the anodic polarization tests. The absence of such a current density decrease in the three test solutions besides Na_2SO_4 at 80°C indicates that magnetite is not protective to Nd-Fe-B, which suggests that the corrosion of Nd-Fe-B should not be affected by its presence on a magnetized sample.

5.1.8 Hot Pressed Alloys as Primary Test Samples

The results of the present study have provided a strong indication that corrosion behavior is essentially independent of magnetic flux, a conclusion which agrees with established theory regarding non-flowing electrolytes [65]. The corrosion behavior of the alloy is apparently also not affected by the processing of h.p alloys into d.u. alloys; a result which is not unexpected, since the same phases are present in both products (although the phases are isotropic in h.p. and elongated in d.u.).

In order to perform an in-depth analysis of the corrosion behavior of Nd-Fe-B in a reasonable length of time, a decision was made to use only one formulation of the alloy in the remaining investigations. The essentially identical electrochemical behavior of the h.p. and d.u. alloys in the work described in this section was used as a justification for this decision, as was the fact that the similarities in behavior are theoretically reasonable.

It was decided that h.p. alloys should be employed as the primary test sample in the remainder of the study. A significant benefit of utilizing h.p. alloysis that the isotropic nature of the h.p. alloys prevents two samples from being needed for each test condition. In other words, two times as many tests can be performed on h.p. samples as on d.u. samples in the same time period, since there is no need to test two orthogonal planes of the h.p. alloys. This decision was also influenced by the better availability of the h.p. samples, as it was judged that an insufficient number of d.u. samples were available to perform an in-depth analysis. Another major obstacle to using the d.u. samples as primary test specimens is related to the difficulty of characterizing magnetized specimens in an electron microscope. Magnetized specimens are known to affect the electron beam, which is especially problematic for a very strong permanent magnet such as Nd-Fe-B. It might therefore be difficult to attain the very high resolution needed to investigate intergranular corrosion, unless non-magnetized samples (such as the h.p. alloys) were employed.

It was believed that utilizing the d.u. samples would lead to significant limitations in terms of the number of tests performed, and the types of microscopic techniques available. The h.p. alloys offered no such limitations, and are thus utilized as the primary test sample in the remainder of the study.

5.1.9 Polarization Behavior of h.p. Nd-Fe-B at 23°C

It was necessary to conduct polarization testing at ambient temperature (~23°C), in order to facilitate an effective correlation to results of the EIS tests and microscopy described in Sections 5.2 - 5.5. In accordance with the foregoing discussion, only the h.p. samples were used to perform these experiments. The general characteristics of the polarization curves at 23°C were very similar to those obtained at 30°C. The only significant difference between the polarization behavior at the two temperatures is that the change in i_{lim} value for the diffusion-limited oxygen reduction reaction leads to a slightly lower corrosion current density at 23°C (39 $\mu A/cm^2$) than at 30°C (58 $\mu A/cm^2$). The i_{corr} value obtained at 23°C will be used in the following section to estimate the metal loss rate for the alloy.

5.1.10 Estimated Rate of Metal Loss

The corrosion current density (i_{corr}) can be estimated by extrapolating both the anodic and cathodic polarization curves to the corrosion potential. For h.p. Nd-Fe-B in NaCl at 23°C, for example, the average i_{corr} was estimated as 39 $\mu A/cm^2$. Faraday's Law can be used to convert this value into a penetration rate in either mils per year (mpy) or millimeters per year (mm/y) using the following equation [64]:

$$[5.2] \qquad \text{Penetration Rate [mpy]} = (0.129)\frac{i_{corr}\left[\frac{\mu A}{cm^2}\right] \cdot \text{atomic weight}\left[\frac{g}{mole}\right]}{\#\ \text{electrons transferred} \cdot \text{density}\left[\frac{g}{cm^3}\right]}$$

The effective atomic weight of Nd-Fe-B was estimated as 66 g/mole and the number of electrons transferred as 2.2, using weighted averages based on the standard alloy composition of 15% Nd, 77% Fe, and 8% B (at%). The density of h.p. samples is 7.6 g/cm^3. Using these parameters in equation [5.2], the rate of metal loss was estimated as 20 mpy (0.50 mm/y), assuming general corrosion to be operative.

The rate of metal loss for h.p. samples at 30°C was estimated as 29 mpy (0.74 mm/y) in NaCl and 27 mpy (0.69 mm/y) in Na_2SO_4, using the method outlined above. The rates of penetration at 80°C were calculated as 63 mpy (1.6 mm/y) in NaCl and 55 mpy (1.4 mm/y) in Na_2SO_4. The penetration rates rise with an increase in temperature due to the increase in the rate of oxygen transport to the metal surface, and are slightly lower in Na_2SO_4 than in NaCl due to the difference in oxygen concentration between the two solutions. Since penetration rates greater than 5-20 mpy are usually considered excessive for expensive alloys such as Nd-Fe-B [64], the estimated penetration rates indicate that corrosion control methods may be needed in order to improve the engineering viability of Nd-Fe-B.

No attempt was made in the preceding calculation to identify whether or not preferential corrosion was taking place. A significant limitation of polarization testing is that it does not provide information regarding the morphology of corrosive attack. If localized corrosion is taking place, the penetration rates calculated above are likely a significant underestimate of the actual metal loss rate of the alloy. In this case, it would be even more important to employ corrosion control methods than was previously stated. The morphology of corrosive attack is discussed in sections 5.2 and 5.3.

5.2 Corrosion Behavior of Nd-Fe-B at Short Times (≤ 1 hour)

The polarization studies described in Section 5.1 have provided a preliminary understanding of the corrosion behavior of Nd-Fe-B. In order to develop a more sophisticated understanding of the alloy's corrosion behavior, an in-depth analysis was performed using various electrochemical and microscopic techniques. Electrochemical impedance spectroscopy (EIS), cyclic anodic polarization, potentiostatic polarization, scanning electron microscopy, and confocal laser microscopy were utilized in this investigation, as described in Sections 5.2 - 5.4.

The work discussed in the remainder of this chapter was performed mainly at ambient temperature (~23°C), in order to provide an effective correlation to the results of EIS testing. EIS tests were conducted only at 23°C, since electrical noise was found to impede data acquisition if the temperature of the test solution was fixed by a thermostatic controller.

5.2.1 Electrochemical Impedance Spectroscopy (EIS) Testing

EIS testing is often performed to obtain both mechanistic information about corrosion processes and instantaneous corrosion rate data. EIS results are shown in Figure 5.7 for samples which were immersed in NaCl at open-circuit for 1 hour before testing was begun. Two distinct frequency regimes are visible in the Nyquist plot shown in Figure 5.7 (a). At frequencies greater than 0.2 Hz, a partially formed semicircle appears to be present. The appearance of a semicircle in a Nyquist plot is generally attributed to the presence of a resistance and capacitance in parallel, as discussed in Appendix 10.1.2. It can be initially postulated that the resistance and capacitance in question are associated with the metal dissolution reaction and the electrical double layer, respectively. The actual physical processes associated with these circuit elements are discussed in Appendix 10.2.

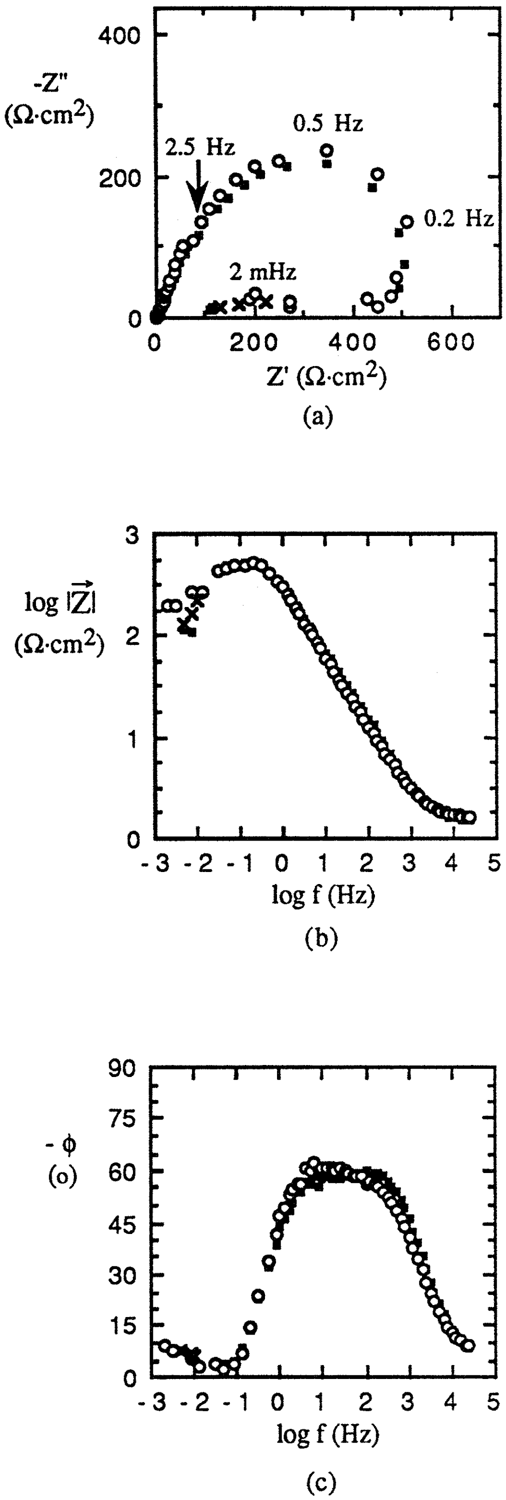

Figure 5.7 EIS data after 1 hour in NaCl. Data from three separate trials are included to show reproducibility. One trial (x) was started at 10 mHz to minimize changes in the sample during immersion.

At lower frequencies (below 0.2 Hz), the data are observed to curl under or "undercut" the semicircle. The undercutting feature in the Nyquist plot corresponds to the presence of a low frequency maximum in the Bode-magnitude plot (Figure 5.7 (b)). The physical processes which give rise to the low frequency data points are not apparent at this time. The physical significance of these points are discussed in Appendix 10.2.

The preferred method of analyzing EIS data is to utilize the equivalent circuit modeling process described in Appendix 10.1.2. A physically plausible equivalent circuit model is postulated, and the experimental data are then fit to the model in order to obtain quantitative estimates of parameters associated with the corrosion process. Analysis of the EIS data using equivalent circuit modeling is discussed at length in Appendix 10.2.

It is also relevant to *initially* analyze the EIS data qualitatively, in an attempt to correlate the obtained results to previous work reported by other investigators. Since certain features of EIS plots have been correlated to different physical phenomena by past researchers, a brief examination of the present experimental data may permit information to be obtained about the system under test. Such a comparative method will be utilized in the present section.

5.2.1.1 Comparison to Previous Work

Dawson and Ferreira [67,68] have previously reported EIS data exhibiting the undercutting (Nyquist) and low frequency maximum (Bode-magnitude) features in tests performed on 316 stainless steel in chloride-containing solutions, as shown in Figure 5.8. In this work, it was emphasized that these characteristic features were observed *only* when the stainless steel was polarized above its pitting potential (Figure 5.8 (a)), or was deliberately creviced (Figure 5.8 (b)). The presence of these features was therefore qualitatively correlated to the presence of localized corrosion. Comparison to the present EIS data suggests that pitting

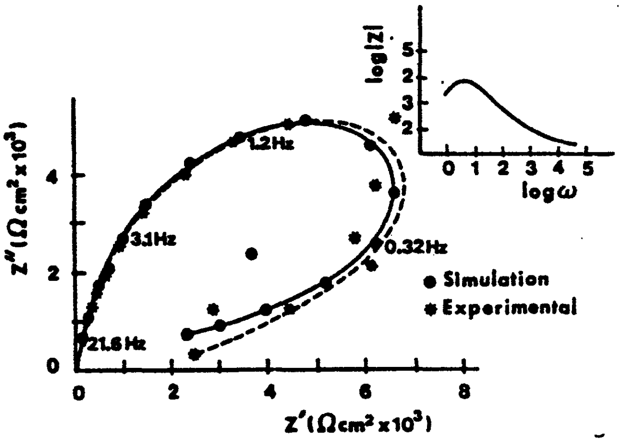

(a)

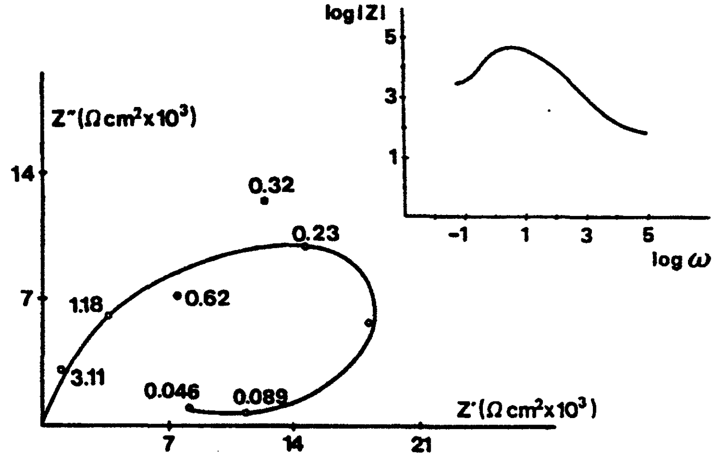

(b)

Figure 5.8 EIS data taken from the work of Dawson and Ferreira [67,68]. The data were obtained on 316 stainless steel electrodes in NaCl. The data in (a) were taken from an electrode polarized above its pitting potential, and the data in (b) from an electrode which was deliberately creviced.

or crevice corrosion may be occurring on Nd-Fe-B at open-circuit (NaCl). Complementary electrochemical techniques can be used to obtain additional information regarding this possibility, as described below.

5.2.2 Cyclic Anodic Polarization

Localized corrosion can be diagnosed electrochemically by the presence of hysteresis in a cyclic anodic polarization scan, as discussed in Section 4.3.4. If localized corrosion is occurring during the forward scan, the resulting compositional changes taking place within the occluded or localized cell will give rise to an increased current during the reverse scan. A cyclic anodic polarization diagram for Nd-Fe-B in NaCl at 23°C is shown in Figure 5.9. The hysteresis observed in the cyclic scan strongly suggests that localized corrosion is occurring on Nd-Fe-B at open-circuit after 1 hour of immersion. Hysteresis was also observed if the sample was held at open-circuit for only 15 minutes prior to testing. It should be noted that the presence of linear (Tafel) kinetics at low anodic overpotentials in the forward scan *is* consistent with localized corrosion, as such behavior has been observed in the past for many metal systems which exhibit localized corrosion [67].

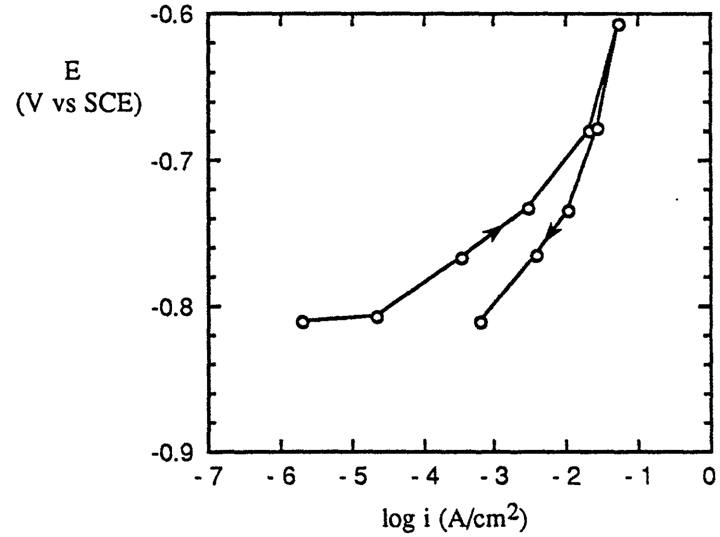

Figure 5.9 Forward and reverse anodic polarization in NaCl. The scan was reversed at -0.61 V vs. SCE ($\eta_a = 0.2$ V) in order to minimize the area increase which would result from continued anodic polarization.

5.2.3 Potentiostatic Anodic Polarization

Further confirmation of the presence of localized corrosion was obtained by holding the electrode at open-circuit for 1 hour and then stepping the potential directly from open-circuit to a potential in the anodic Tafel region of the forward scan. The resulting current is then monitored as a function of time. The selected polarization potential was -750 mV vs. SCE, since this potential allows substantial anodic polarization to be provided without causing significant IR drop errors. The results of the potentiostatic anodic polarization test are shown in Figure 5.10. Similar data were obtained if the sample was held for only 15 minutes at open-circuit prior to polarization.

The rising nature of the current density shown in Figure 5.10 indicates that the corrosive attack is intensifying with time. As discussed in Section 4.3.4, such behavior is usually attributed to increasing aggressiveness of the occluded pit or crevice solution as localized

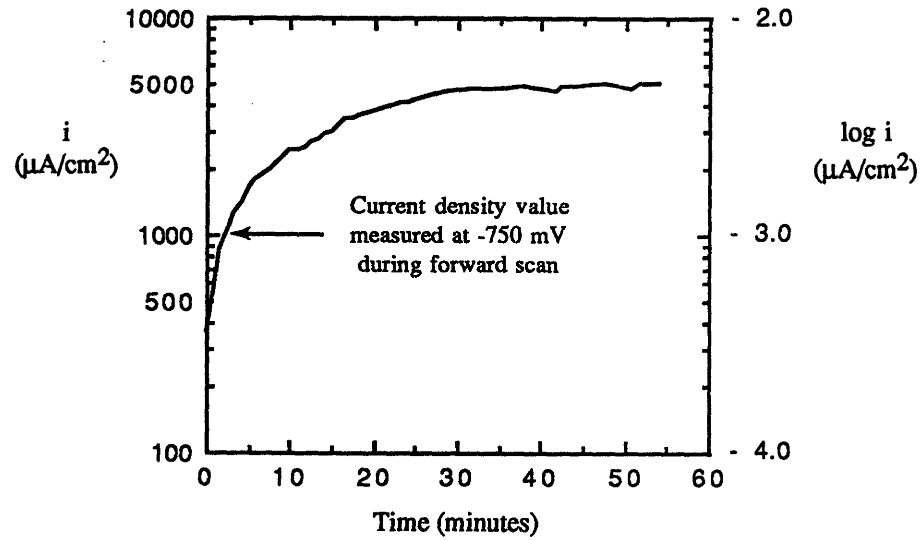

Figure 5.10 Potentiostatic anodic polarization in NaCl after 1 hour at open-circuit. The sample was polarized to -0.75 V vs. SCE ($\eta_a = 60$ mV).

corrosion propagates. It is clear that the anodic current density rapidly surpasses the value measured at -750 mV during the forward polarization scan, as indicated on Figure 5.10.

The results of EIS testing, cyclic anodic polarization, and potentiostatic anodic polarization therefore indicate that localized corrosion is likely occurring on Nd-Fe-B after short immersion times (15 minutes, 1 hour) in NaCl.

5.2.4 Microscopy

A microscopic analysis was performed in order to definitively evaluate whether or not localized corrosion was taking place, and also to determine the form of localized corrosion, if applicable.

Low magnification images of the corroded surfaces were obtained using a scanning electron microscope (SEM), as shown in Figure 5.11. Small depressions which resemble pits can be seen on the surface after only 15 minutes of immersion. Closer examination confirms that these depressions are indeed pits, as illustrated by Figure 5.12. Although the image shown in Figure 5.12 was taken after 1 hour of immersion, similar corrosive attack was obtained after an immersion time of only 15 minutes. Pitting was reproducible, as demonstrated by the presence of pits on several different test samples after short-term immersion. Nd-Fe-B surfaces were also investigated for evidence of crevice attack at short immersion times (15 minutes, 1 hour). Crevice corrosion was found to initiate only after 24-36 hours of immersion, and it is thus apparent that the electrochemical characteristics described in the previous sections are the result of pitting rather than crevice corrosion.

The SEM provides excellent image quality, and additionally allows pit width to be measured rather easily. The width of the pit shown in Figure 5.12 is approximately 7 μm.

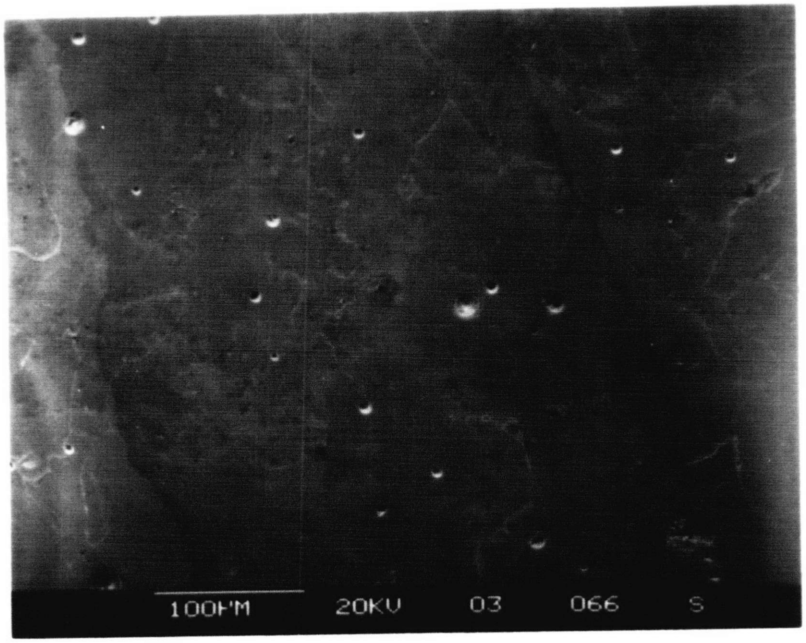
100ΜΜ
20KV
03
066
S

Figure 5.11 Low magnification SEM image of a Nd-Fe-B surface after 15 minutes of immersion (NaCl, 23°C).

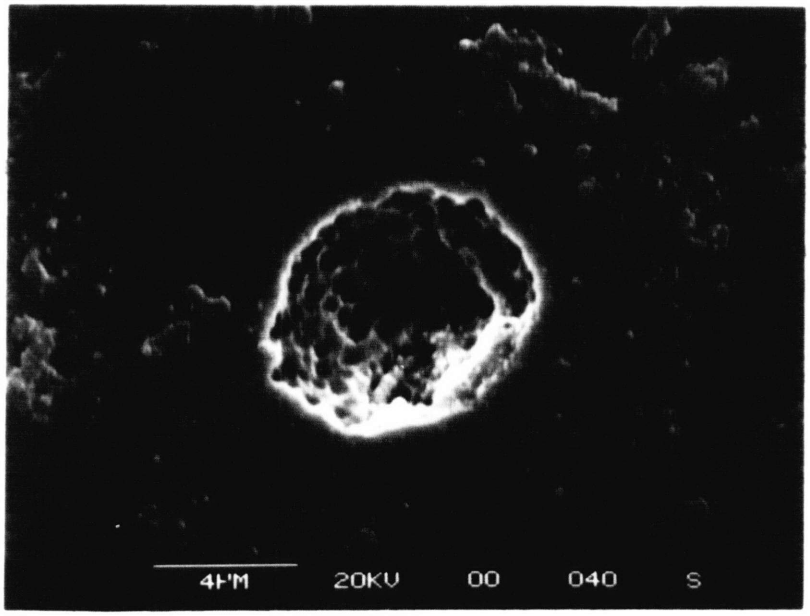
4ΜΜ
20KV
00
040
S

Figure 5.12 SEM image of a pit present on a Nd-Fe-B surface after 1 hour of immersion in NaCl at 23°C.

Important quantities such as the pit density can also be determined using SEM images; the measured pit density is discussed in Appendix 10.2. One of the main limitations of using the SEM to study pitting corrosion, however, is its inability to readily measure pit depths. This limitation was surmounted using the profiling ability of the confocal microscope.

Images of pits profiled after 15 minutes and 1 hour of immersion are shown in Figures 5.13 (a) and 5.13 (b), respectively. The solid horizontal line in both micrographs indicates the line across which the surface profile was taken. The second solid line visible in the photograph indicates the surface profile itself. In both micrographs, a depression in the profile is clearly associated with each pit, and the surface profile is relatively flat in the areas adjacent to the observed pit. The dashed cursors can be used to delineate the height of the profile (i.e. pit depth). The profiles shown in Figure 5.13 correspond to pit depths of 2.76 μm (15 minutes) and 3.38 μm (1 hour). These values represent the maximum pit depths measured on both samples.

A large number of pits (≥ 30) were profiled on both 15 minute and 1 hour samples using the confocal microscope. In order to avoid reporting a large number of pit depths for each immersion time, several pit depths were selected which were believed to approximately represent the actual pit depth distribution on the sample. A stipulation used in compiling the representative distribution is that the maximum pit depth measured on the sample was always included, since it is important to monitor the maximum penetration rate at different immersion times. Representative pit depth distributions were compiled for the 15 minute and 1 hour samples using the above procedure, which will also be utilized for all other immersion times analyzed in this study.

A plot of the representative pit depth distributions for both 15 minutes and 1 hour of immersion is shown in Figure 5.14.

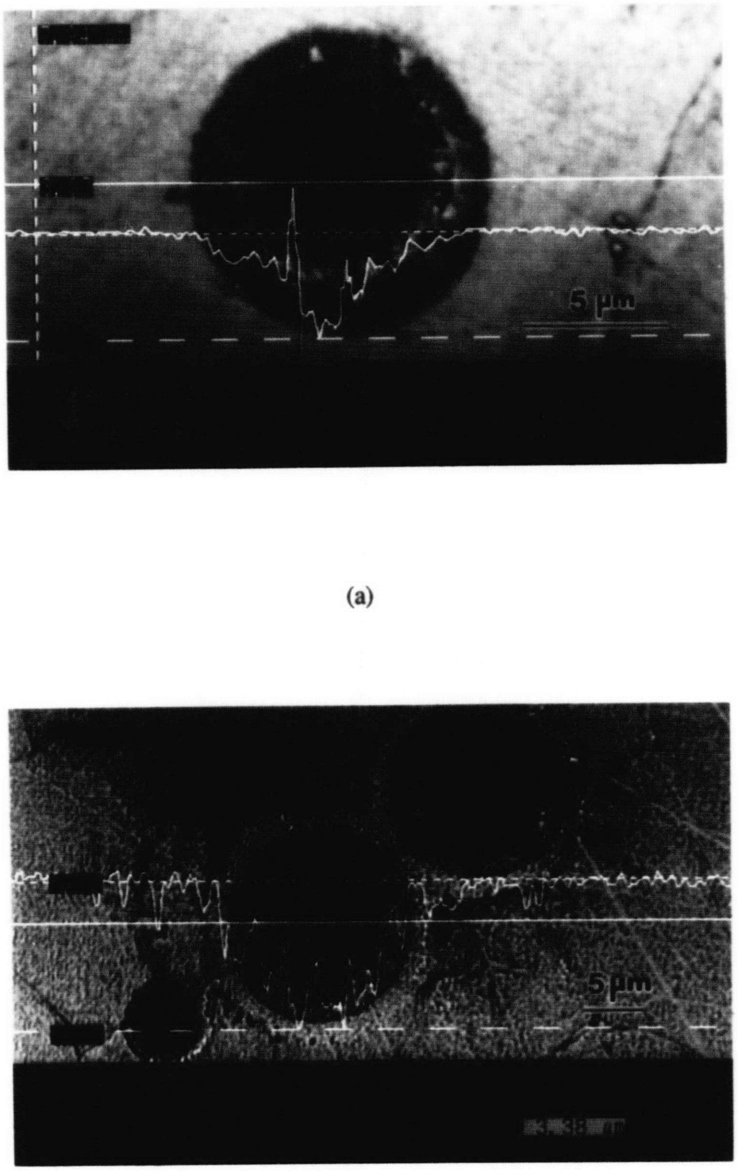

(a)

(b)

Figure 5.13 Confocal images of pits profiled after (a) 15 minutes and (b) 1 hour of immersion in NaCl at 23°C. The measured depth of the pits was 2.76 μm in (a) and 3.38 μm in (b). These values represent the maximum pit depth measured after 15 minutes and 1 hour, respectively.

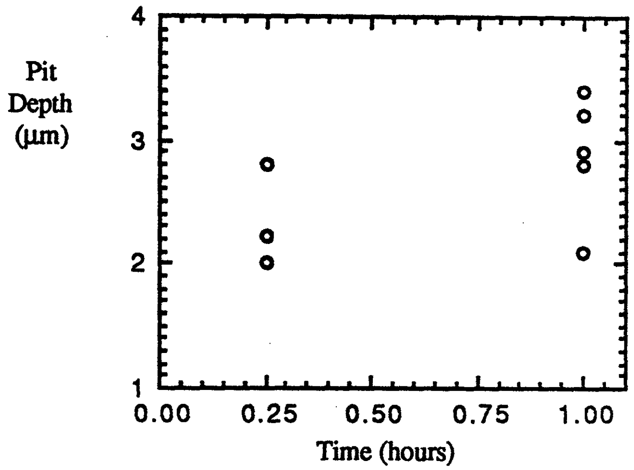

Figure 5.14 Representative pit depth distribution on Nd-Fe-B samples after 15 minutes and 1 hour of immersion in NaCl at open-circuit (23°C).

Pit propagation is clearly occurring between 15 minutes and 1 hour of immersion, as both the maximum and average pit depths were seen to increase during this time period. The rate of pit propagation appeared to be slowing with time during the hour, however, as the pit growth rate is much higher in the first 15 minutes after immersion than during the next 45 minutes. The effects of longer immersion time on pit propagation will be discussed in Section 5.4.

5.2.5 Corrosion Behavior in Na_2SO_4 at 23°C

The corrosion behavior of Nd-Fe-B was studied in Na_2SO_4 (23°C) using electrochemical and microscopic techniques similar to those used to investigate corrosion in NaCl.

EIS tests were performed after 1 hour of immersion in Na_2SO_4, and the results are shown in Figure 5.15. The diameter of the observed semicircle is larger in Na_2SO_4 than in NaCl, which indicates that the corrosion rate may be lower in Na_2SO_4 than in NaCl. The EIS data shown in Figure 5.15 otherwise display a strong similarity to the results obtained in

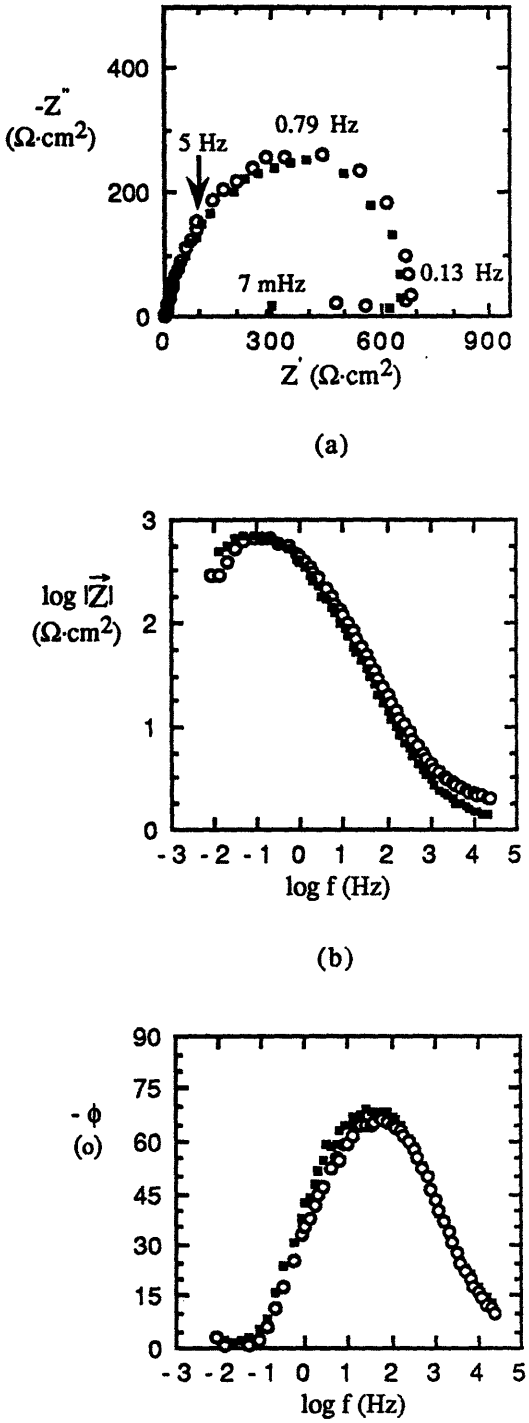

(a)

(b)

(c)

Figure 5.15 EIS data after 1 hour at open-circuit in Na_2SO_4. Data from two separate trials are included to show reproducibility.

NaCl. The presence of characteristic features previously correlated to localized corrosion (undercutting, low frequency maximum) indicates that localized attack such as pitting may be occurring in Na_2SO_4 as well as in NaCl.

Cyclic and potentiostatic anodic polarization tests were conducted in order to further investigate the possibility of localized corrosion in Na_2SO_4. The results of these tests are shown in Figures 5.16 and 5.17, respectively. Hysteresis is clearly evident in the cyclic polarization experiment, and the current density is observed to rise with time in the potentiostatic polarization test. The results of the cyclic and potentiostatic polarization tests indicate that pitting corrosion may be occurring at short immersion times in Na_2SO_4.

The confocal microscope was used to evaluate whether or not pitting attack was occurring on Nd-Fe-B surfaces immersed in Na_2SO_4. Pitting attack was found to be very evident on surfaces exposed to Na_2SO_4 after only 15 minutes of immersion. A confocal image and associated surface profile are shown in Figure 5.18.

Evidence that pitting attack occurs in Na_2SO_4 is noteworthy, since pitting in other alloy systems is normally associated with the presence of aggressive halide ions such as Cl^-. A possible explanation of why pitting attack may be occurring in Na_2SO_4 solutions as well as NaCl solutions is provided in Section 5.4.5.1.

Pits were found to be shallower in Na_2SO_4 than in NaCl after 15 minutes of immersion, as evidenced by the maximum pit depth of 1.39 μm measured for Na_2SO_4 (compared to 2.76 μm in NaCl). The lower attack rate is consistent with the higher diameter of the semicircle in the Nyquist representation of the EIS data (Figure 5.15 (a)), and also with the lower current density measured at the same anodic overpotential in the potentiostatic polarization tests (Figures 5.10 and 5.17). It is possible that the discrepancy in attack rates between

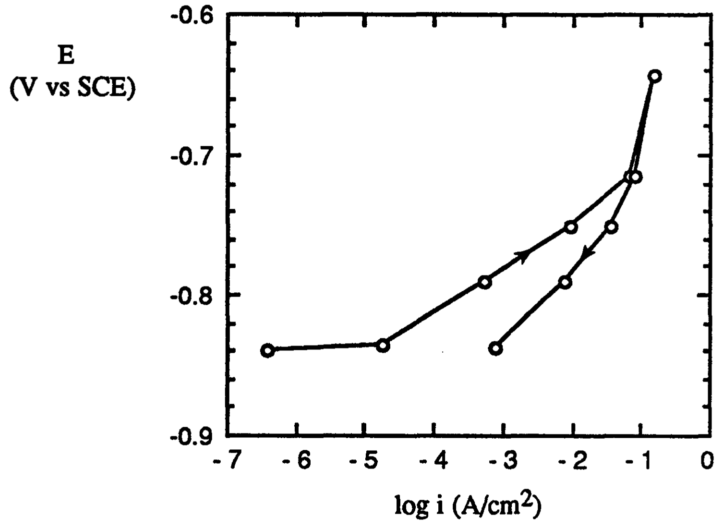

Figure 5.16 Forward and reverse anodic polarization in Na2SO4. The scan was reversed at -0.64 V vs. SCE in order to provide the same degree of polarization from E_{corr} before reversal as for NaCl.

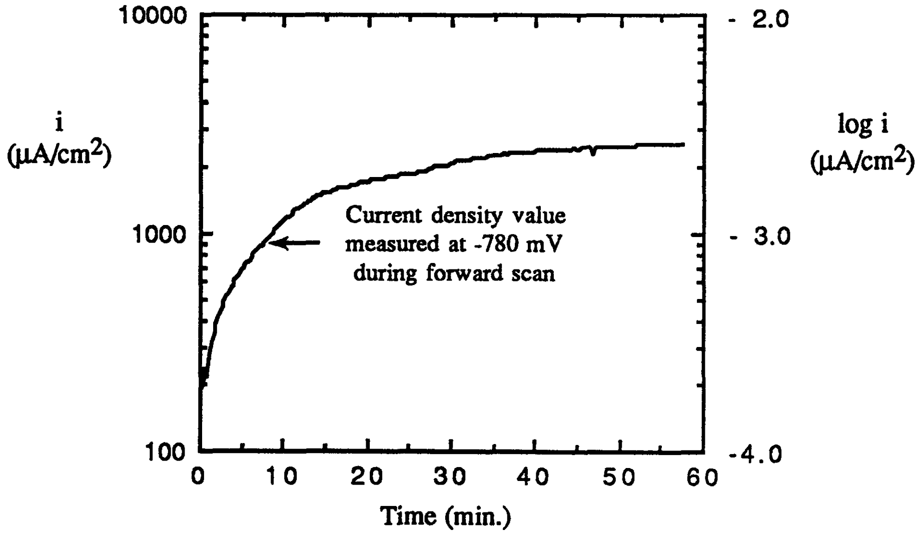

Figure 5.17 Potentiostatic anodic polarization in Na2SO4 after 1 hour at open-circuit. The sample was polarized to -0.78 V vs. SCE in order to apply the same anodic overvoltage (η_a = 60 mV) relative to the corrosion potential as for the test conducted in NaCl.

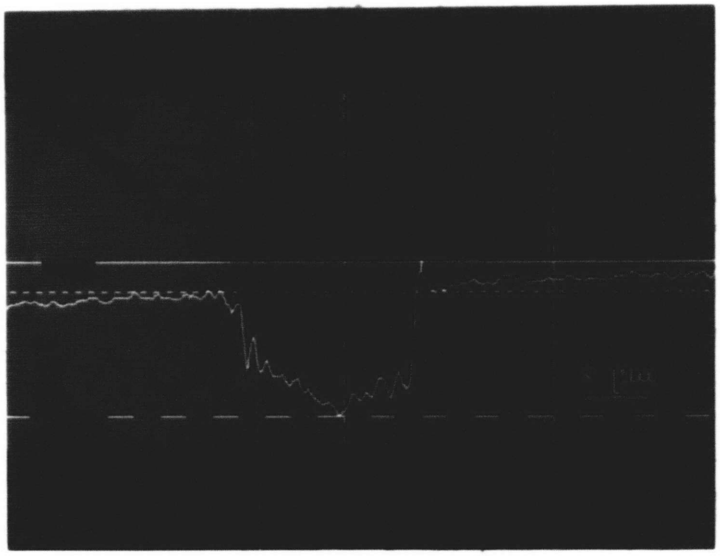

Figure 5.18 Confocal image of a pit profiled after 15 minutes of immersion in Na_2SO_4 at 23°C. The measured depth of the pit was 1.39 μm, which represents the maximum pit depth measured on the sample.

NaCl and Na_2SO_4 can be attributed to differences in the chemical conditions obtained within a growing pit in the two solutions. Such a notion qualitatively agrees with the results of Mankowski and Szklarska-Smialowska [69], who found that adding chlorides to a non-buffered solution resulted in an increase in hydrogen ion activity (i.e. a decrease in pH). The reduction in pH was attributed to the strong hydrolysis exhibited by species such as $FeCl_2$; since similar species are likely to be contained within growing pits in Cl^- solutions [69], the more aggressive (lower pH) solution created by strong hydrolysis may lead to a faster rate of pit propagation than is obtained in non-Cl- solutions.

5.2.6 Corrosion Behavior at 80°C

Microscopic examination of a sample immersed in NaCl at 80°C for 1 hour also revealed

evidence of pitting attack. The pits were found to be deeper at 80°C than at 23°C, as shown by the confocal microscope profiles in Figure 5.19. The maximum pit depth on this sample was 8.98 μm, which is significantly larger than the maximum depth observed in NaCl at 23°C. The fact that pitting corrosion was more rapid at 80°C than at 23°C can also be seen by comparing the representative pit depth distributions measured at both temperatures, as shown in Table 5.2. The increased rate of pitting corrosion is likely related to the more rapid diffusion rate of dissolved oxygen in the solution at 80°C than at 23°C. The electrons produced by the metal cations dissolving within a pit must be consumed by an accompanying cathodic reaction. Since the main cathodic reaction in the present metal-electrolyte system is diffusion-limited oxygen reduction (Section 5.1.5), it is expected that any increase in the access rate of dissolved oxygen might lead to an increased pitting rate.

Pitting was also observed to occur on Nd-Fe-B surfaces immersed in Na_2SO_4 at 80°C for 1 hour. Pit depth information was not obtained for the Na_2SO_4 samples.

Table 5.2 A comparison of the representative pit depth distributions in NaCl at 23°C and 80°C.

Temperature	Pit depths (μm)				
23°C	3.4	3.2	2.9	2.8	2.1
80°C	8.9	7.5	5.2	3.3	–

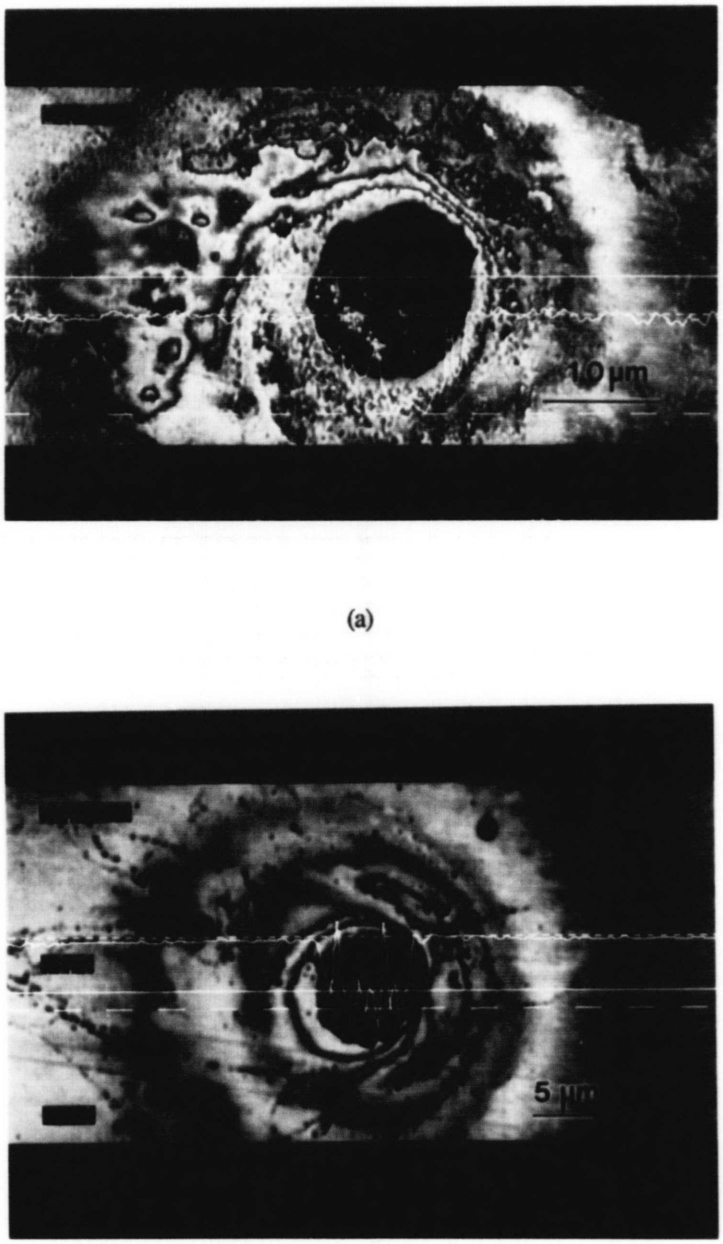

(a)

(b)

Figure 5.19 Confocal images of pits profiled after 1 hour of immersion in NaCl at 80°C. The measured depth of the pits was 8.06 µm in (a) and 8.98 µm in (b).

5.2.7 Implications of the Observed Pitting Attack

Nd-Fe-B has been shown to undergo pitting attack at open-circuit in NaCl and Na_2SO_4 at both 23°C and 80°C; pitting was found to initiate rapidly in all four of these test solutions. It is believed that pitting has not been previously reported for rapidly solidified Nd-Fe-B alloys. The ramifications of this type of attack in terms of its effect on the engineering viability of Nd-Fe-B will be discussed in Section 5.3.

It is important to note that this type of attack does not appear to be confined to a narrow set of electrolyte conditions, as pitting was observed in two different types of solutions and at two rather different temperatures. This result has important implications for the in-service behavior of the material, since Nd-Fe-B magnets are expected to be subjected to a relatively broad set of electrolyte conditions in practice.

Although the discovery of pitting at short immersion times is an important result, it is equally relevant to examine the effect of time on the dissolution morphology. A determination of whether or not the pits propagate over time will be made in Section 5.3.

5.3 Corrosion Behavior of Nd-Fe-B at Longer Immersion Times

The corrosion behavior of Nd-Fe-B at short immersion times has been described at length in Sections 5.1 - 5.2. It is relevant at this point to extend the analysis to include the effects of time. Although pitting has been established as a primary mode of corrosive attack at short times, the engineering utility of the material is ultimately just as dependent on pit propagation as it is on pit initiation. An analysis was therefore performed to determine whether or not pits propagate with time, and also to quantify the rate of pit propagation if applicable. A second objective of this investigation was to determine if any notable changes occurred in the corrosion behavior of the material over time.

The analysis was performed using electrochemical tests as well as *ex-situ* microscopic observation at immersion times of 1, 24, and 72 hours (and occasionally 6, 12, or 48 hrs.). Microscopy was additionally performed at immersion times of 1 month and 3 months.

To facilitate the completion of an in-depth analysis in a reasonable amount of time, one test solution was selected to serve as the primary electrolyte in the evaluation of the effects of time. More severe attack was evident in NaCl than in Na_2SO_4 in the short-time tests, and the corrosion behavior of the material in NaCl was thus believed to represent a worst-case condition which would be more critical to investigate than the corrosion behavior in Na_2SO_4 solutions. The work in this section thus deals exclusively with tests conducted in NaCl at ~23°C.

An investigation of intergranular corrosion is additionally discussed in this section. Intergranular attack has been proposed by several researchers as the main mode of corrosion in Nd-Fe-B [54], and a determination of whether or not this form of attack is occurring in rapidly solidified alloys was therefore considered to be important.

5.3.1 Anodic Polarization with Time

The anodic polarization behavior of Nd-Fe-B was measured after 24 and 72 hours of immersion at open-circuit, as shown in Figure 5.20. The material is corroding in the active state over this time period, which is very similar to the behavior obtained after 1 hour. Although insoluble corrosion products were observed to form on the surface of the samples during the three day immersion period, these products are clearly not protective to the metal in terms of passivation. Estimates of i_{corr} were obtained via Tafel extrapolation for 24 and 72 hours, but were not reported as useful data; the i_{corr} results are believed to be relatively inaccurate as a result of the area changes which occur during the corrosion of the sample.

The presence of hysteresis upon scan reversal provides a preliminary indication that pits may be propagating during the three day immersion time. Crevice formation often occurred at the metal/masking agent interface after about 24 hours, however, and it is thus possible that the hysteresis observed after 72 hours (or even after 24 hours) may be due to crevice attack rather than pit propagation.

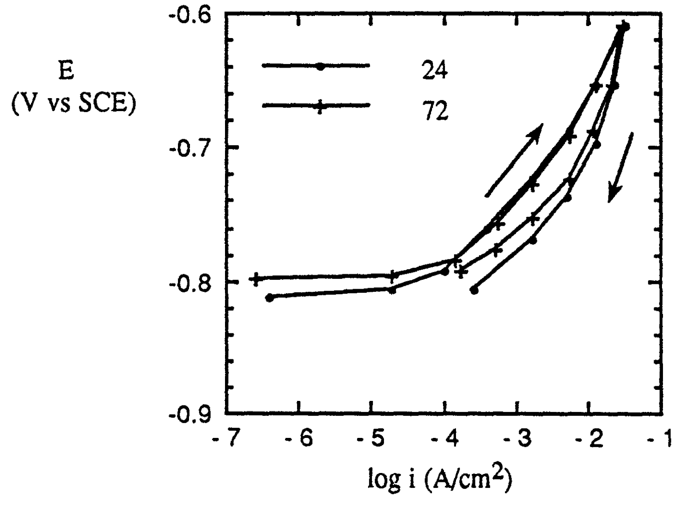

Figure 5.20 Cyclic anodic polarization of Nd-Fe-B in NaCl at 23°C.

5.3.2 Electrochemical Impedance Spectroscopy (EIS) with Time

The results of EIS tests performed after 24 and 72 hours of immersion at open-circuit are shown in Figure 5.21. Data from the 1 hour tests are included for comparative purposes.

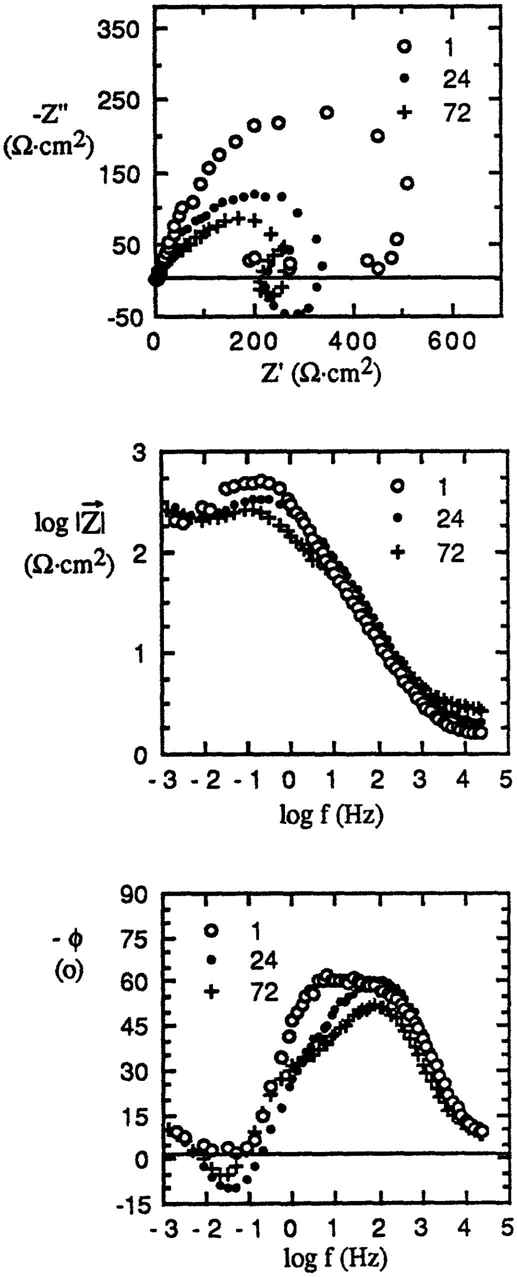

Figure 5.21 EIS data after 1, 24, and 72 hours of immersion at open-circuit in NaCl at 23°C.

In order that the results might be displayed more clearly, the EIS data have been replotted in the Nyquist representation, as shown below (Figure 5.22).

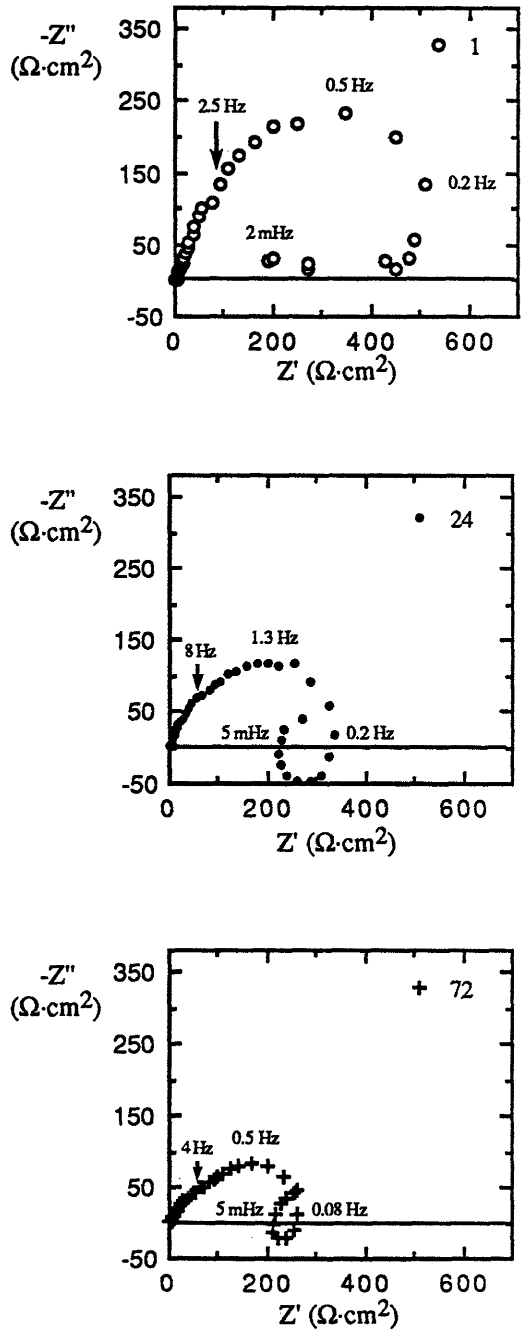

Figure 5.22 Nyquist representation of EIS data after 1, 24, and 72 hours in NaCl at 23°C.

The effect of time on the EIS data appears to be substantial. One apparent change is the marked difference in the low frequency appearance of the Nyquist plots in Figure 5.22. The low frequency "undercut" data points present after 1 hour of immersion have been supplanted after 24 hours by a small semicircular loop in the fourth quadrant of the plot (actually present even in 6 hour tests). Since the undercut points were correlated to pitting attack in Section 5.2, it is possible that their replacement by the fourth quadrant loop indicates that pitting has terminated during the first 24 hours of immersion. The change in form of the low frequency time constant is not readily interpreted, however, since the appearance of such a fourth quadrant loop has also been reported to coincide with the onset of stable pitting for 304 stainless steel (in 0.25M Na_2SO_4 + 100 ppm Cl^- at pH 1) [70].

Equivalent circuit modeling of the 24 and 72 hour EIS data is discussed in Appendix 10.2.6. A quantitative explanation for the apparent decrease in semicircle diameter with time is also provided in this Appendix (Section 10.2.6.1).

5.3.3 Cathodic Polarization with Time

The cathodic polarization behavior of Nd-Fe-B was measured after 24 and 72 hours of immersion, as shown in Figure 5.23. The alloy is seen to exhibit an oxygen diffusion-limited current density (i_{lim}) over this time period, which is very similar to the behavior obtained in the 1 hour tests. The fact that i_{lim} increases rather than decreases with time indicates that the insoluble corrosion products formed on the samples during the three day immersion period do not impede the transport of oxygen to the surface of the metal. The effects of corrosion products on oxygen access are important because the overall reaction rate is governed by the rate of oxygen arrival at the metal surface (as discussed in Section 5.1.5). The increasing nature of i_{lim} is believed to be related to an increase in surface area with time due to corrosive attack, which would initially appear to support the notion that pits are propagating with time. The pits in this study are likely to be deaerated (owing to the formation of corrosion product caps), however, and an increase of the pitted area with time is thus not capable of explaining the observed changes in i_{lim}. This result implies that the area increase may be occurring on the external metal surface between the pits. Surface dissolution may therefore be occurring in addition to the expected corrosive attack in pits.

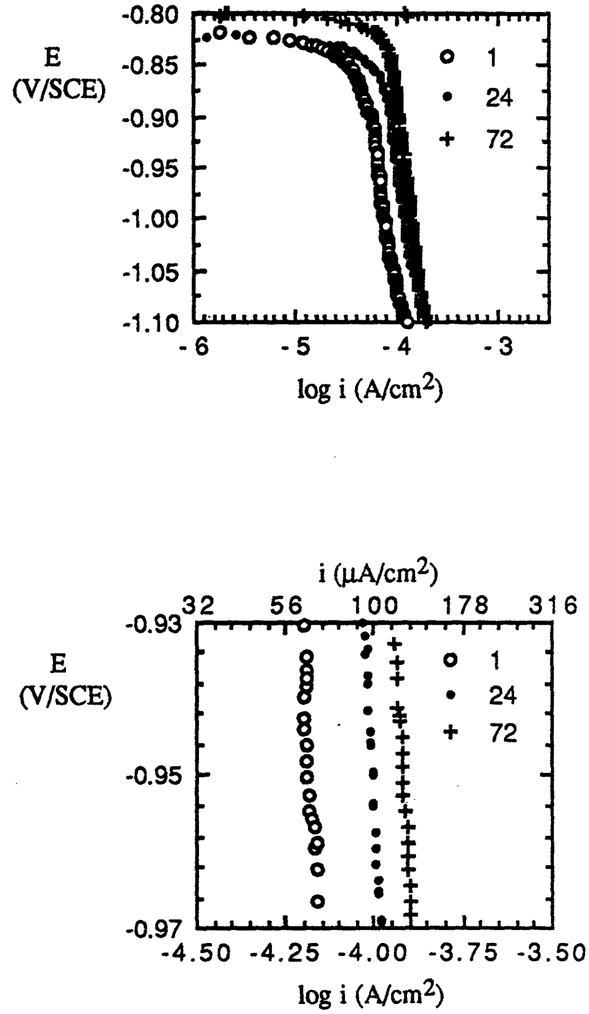

Figure 5.23 Cathodic polarization of Nd-Fe-B in NaCl at 23°C after 1, 24, and 72 hours of immersion. An expanded view is provided in (b) to emphasize the changes in i_{lim} with time.

5.3.4 Morphology of Attack

The electrochemical tests described in the preceding sections have provided quantitative insight regarding the corrosion behavior of Nd-Fe-B (NaCl, ~ 23°C) for immersion times up to 72 hours. In order to fully characterize the corrosive attack occurring during this time period, however, it was necessary to perform a comprehensive microscopic analysis. The goals of this analysis were to identify the types of corrosion taking place on the Nd-Fe-B surface and to measure the rates of the obtained corrosive attack; emphasis was placed on the evaluation of pitting (Section 5.3.4.1) and intergranular corrosion (Section 5.3.4.3).

5.3.4.1 Pit Propagation with Time

In Section 5.2, it was demonstrated that the primary form of corrosive attack at short immersion times (15 minutes, 1 hour) was pitting corrosion. The effect of time on pitting attack was investigated by subjecting Nd-Fe-B to microscopic examination after 12 hours, 24 hours, 72 hours, 1 month and 3 months of immersion in NaCl at 23°C. Microscopy was performed in order to determine whether or not pits propagate over time periods longer than 1 hour, and also to measure the rate of pit propagation if applicable.

Images obtained using the SEM and the confocal microscope will be presented in this section. Owing to the difficulty of providing individual images of a large number of pits on a given surface, selected representative pits will be shown for each immersion time.

5.3.4.1 (a) Immersion times up to 72 Hours

Examination of a surface immersed in NaCl for 12 hours reveals the presence of extensive pitting attack. An SEM image of a representative pit (12 hour immersion) is shown in

Figure 5.24. The width of the observed pit (~ 17.5 µm) is clearly larger than the width of the pit shown in Figure 5.12 (~ 7 µm), which was developed after 1 hour of immersion in NaCl. The increase in pit width between 1 hour and 12 hours of immersion provides a preliminary indication that pits may be propagating with time.

A more effective gauge of pit propagation can be obtained by comparing the pit depths measured on the 12 hour sample to pit depths previously reported for 1 hour of immersion. The maximum pit depth observed on the 12 hour sample was 8.81 µm, as shown by the confocal micrograph in Figure 5.25. The maximum pit depth measured after 1 hour was 3.38 µm, and it is thus apparent that significant propagation of at least one pit occurred between 1 and 12 hours of immersion.

Many pits were in fact observed to propagate during this time period, as demonstrated in Table 5.3, which is a comparison of the representative pit depth distributions for 1 hour and 12 hours of immersion. The representative pit depth distribution at 12 hours was compiled by the method previously described in Section 5.2.4.

Table 5.3 A comparison of the representative pit depth distributions for 1 hour and 12 hour samples.

Immersion time	Pit depths (µm)				
1 hour	3.4	3.2	2.9	2.8	2.1
12 hours	8.8	5.8	5.2	2.6	—

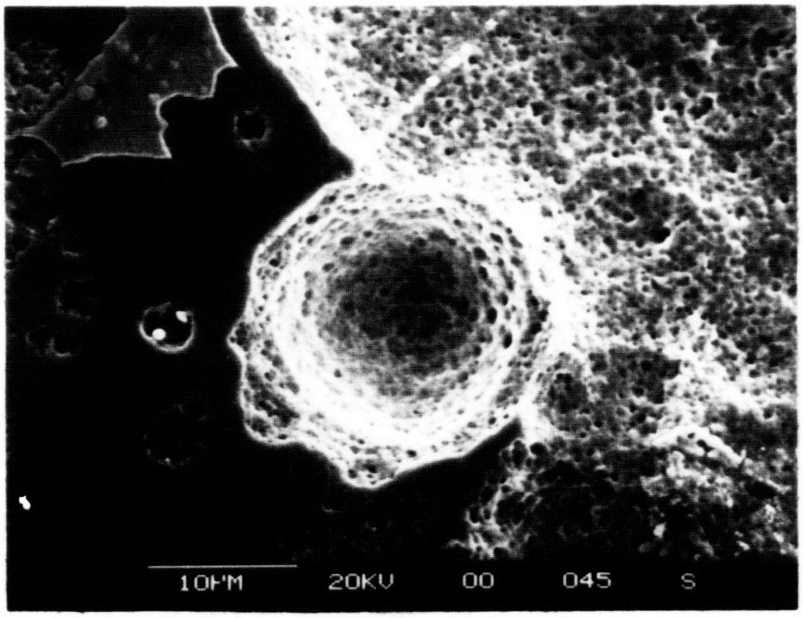

Figure 5.24 SEM image of a representative pit after 12 hours of immersion (NaCl, 23°C).

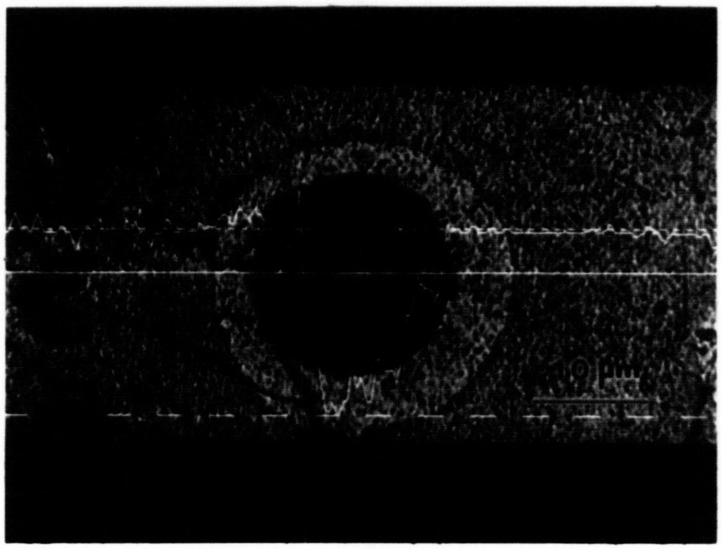

Figure 5.25 Confocal microscope image and profile of the deepest pit found on the 12 hour surface (measured depth is 8.81 µm).

Examination of samples immersed for 24 hours and 72 hours also revealed evidence of pit propagation. Confocal microscope profiles taken from 24 and 72 hour samples are shown in Figures 5.27 and 5.28. The width of the pits was observed to increase during the immersion period. Pit widths of approximately 24 μm and 44 μm were noted at 24 and 72 hours, respectively, according to Figures 5.27 and 5.28. Pit depths were also found to increase with time, as maximum depths of 12.8 μm and 21.4 μm were measured at 24 and 72 hours (note that the pit in Figure 5.27 was not the deepest pit profiled at 24 hours).

Representative pit depth distributions were compiled for the 24 and 72 hour immersions, and are plotted in Figure 5.26 along with the distributions for 0.25, 1, and 12 hours of immersion. The maximum penetration depth at all times is represented by the upper line. Figure 5.26 graphically displays the fact that pits are propagating with time during the 72 hour immersion period. The maximum pit depth is increasing with time, as is the average pit depth (not shown on Figure 5.26). The propagation rate appears to be approximately parabolic in nature, with the pit growth rate fastest at the shortest times shown.

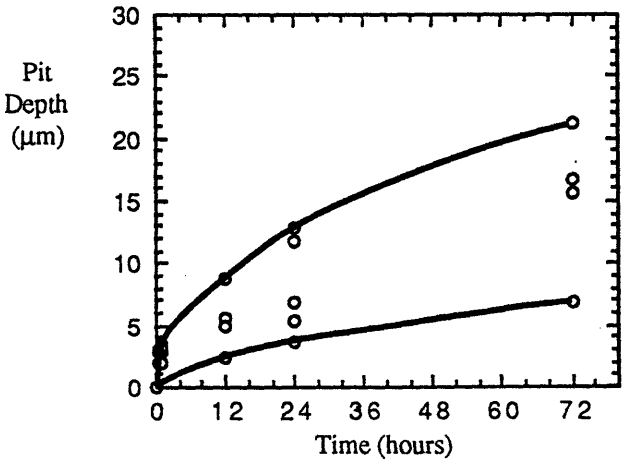

Figure 5.26 Representative pit depth distributions over a 72 hour time period. The upper line represents the maximum pit depth measured at each immersion time.

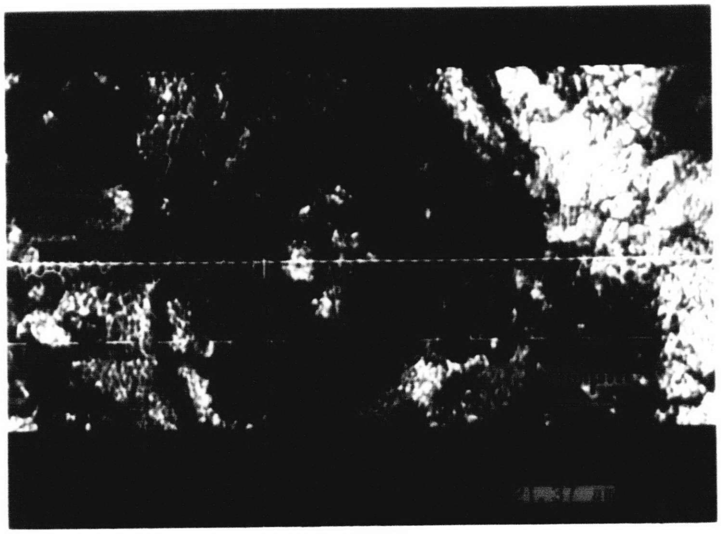

Figure 5.27 Confocal microscope image and profile of a pit on the 24 hour surface (measured depth is 11.65 μm).

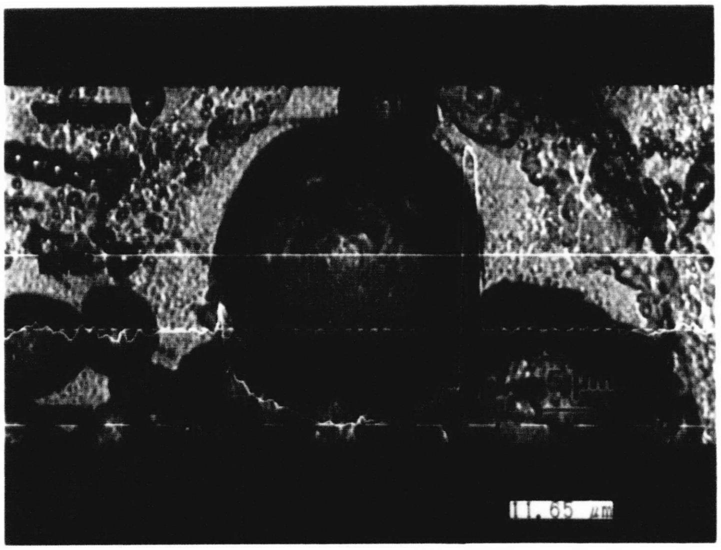

Figure 5.28 Confocal microscope image and profile of a pit on the 72 hour surface (measured depth is 21.37 μm).

Pits were observed to be nearly hemispherical in shape during the 72 hour immersion period. A pit width of 17.5 μm and a pit depth of 8.81 μm were measured in Figure 5.25 (taken after 12 hours of immersion), which corresponds to a depth-to-radius ratio of 1.007; this ratio is very close to the value of 1 expected for a perfect hemisphere. Similar data were obtained by examining Figure 5.27 (24 hours) and Figure 5.28 (72 hours), as shown in Table 5.4. Pits were generally found to be slightly shallower than perfect hemispheres.

Table 5.4 Depths, widths, and depth-to-radius ratios for pits shown in Figures 5.25, 5.27, and 5.28.

Immersion time (hrs.)	Width (μm)	Depth (μm)	Depth-to-radius ratio
12	17.5	8.8	1.007
24	23.8	11.6	0.975
72	43.8	21.4	0.977

The density of pits did not appear to significantly increase between 1 hour and 72 hours of immersion. In fact, some of the existing pits were not observed to propagate, thus leading to a decrease in the "active" pit density with time. It was difficult to accurately determine the active pit density at 12, 24, and 72 hours without profiling each and every pit on these surfaces; completely reliable pit density values were therefore not obtained at times greater than 1 hour. It is believed, however, that the pit densities at 12, 24, and 72 hours were reasonably close to the pit density value measured after 1 hour of immersion, since most of the pits formed during short-time immersion *did* appear to propagate over 72 hours. The fraction of inactive pits at 12, 24, and 72 hours was thus considered to be relatively low.

5.3.4.1 (b) Immersion times up to 3 Months

In order that the pit depth analysis would not be limited to a period of only three days, immersion times of 1 and 3 months were also utilized in this study. Pit depths were measured using the confocal microscope, and representative pit depth distributions were compiled. A small number of pits (~ 10) was used in the construction of the representative pit depth distribution, owing to the fact that much of the sample surface was obscured by corrosion products, making it difficult to accurately profile a large number of pits.

Confocal microscope profiles for two different pits on the 1 month sample are shown in Figure 5.29 (a) and 5.29 (b); the images correspond to pits with measured depths of 45.6 μm and 84.0 μm, respectively. The maximum measured pit depth at 1 month was 84 μm.

The images in Figure 5.29 are lower in quality than the confocal images previously shown (e.g. Figures 5.25), due to both corrosion product blockage and anodic dissolution of the surfaces between the pits (surface dissolution is discussed in Section 5.3.4.2). The image and profile are separated into two photographs in Figure 5.29 (b) because of the difficulty of discerning the surface profile atop the image.

A three month sample was also subjected to microscopic analysis. SEM images of the largest pit found on the sample surface are shown in Figure 5.30. This pit was found to be 215.4 μm in depth using the confocal microscope.

A plot of the representative pit depth distributions during the three month immersion period is shown in Figure 5.31. The maximum measured pit depths indicate that the pits are propagating with time, even after three months of immersion.

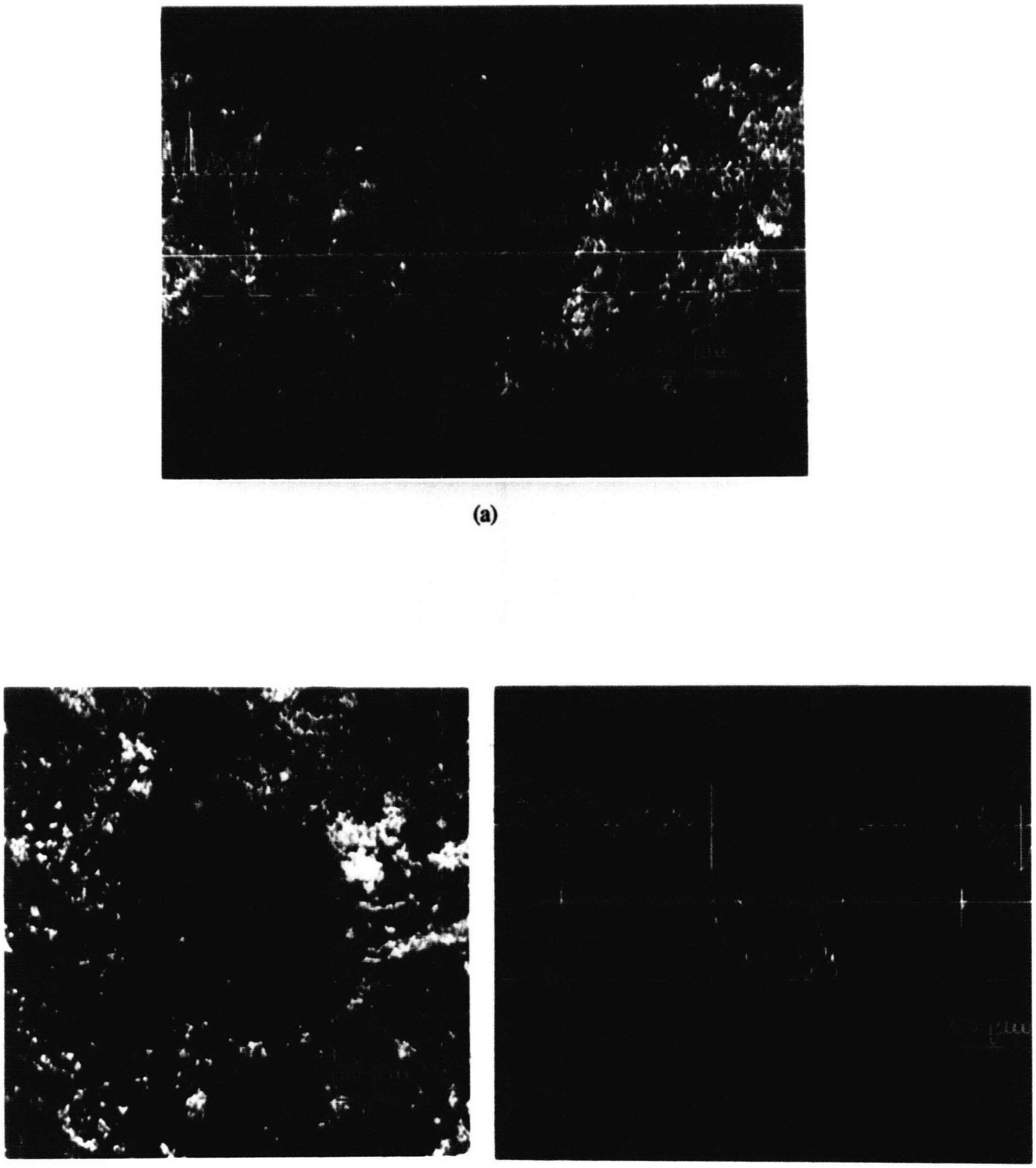

(a)

(b)

Figure 5.29 Confocal microscope images and profiles taken after 1 month of immersion. Measured profile depths were (a) 45.6 μm and (b) 84.0 μm.

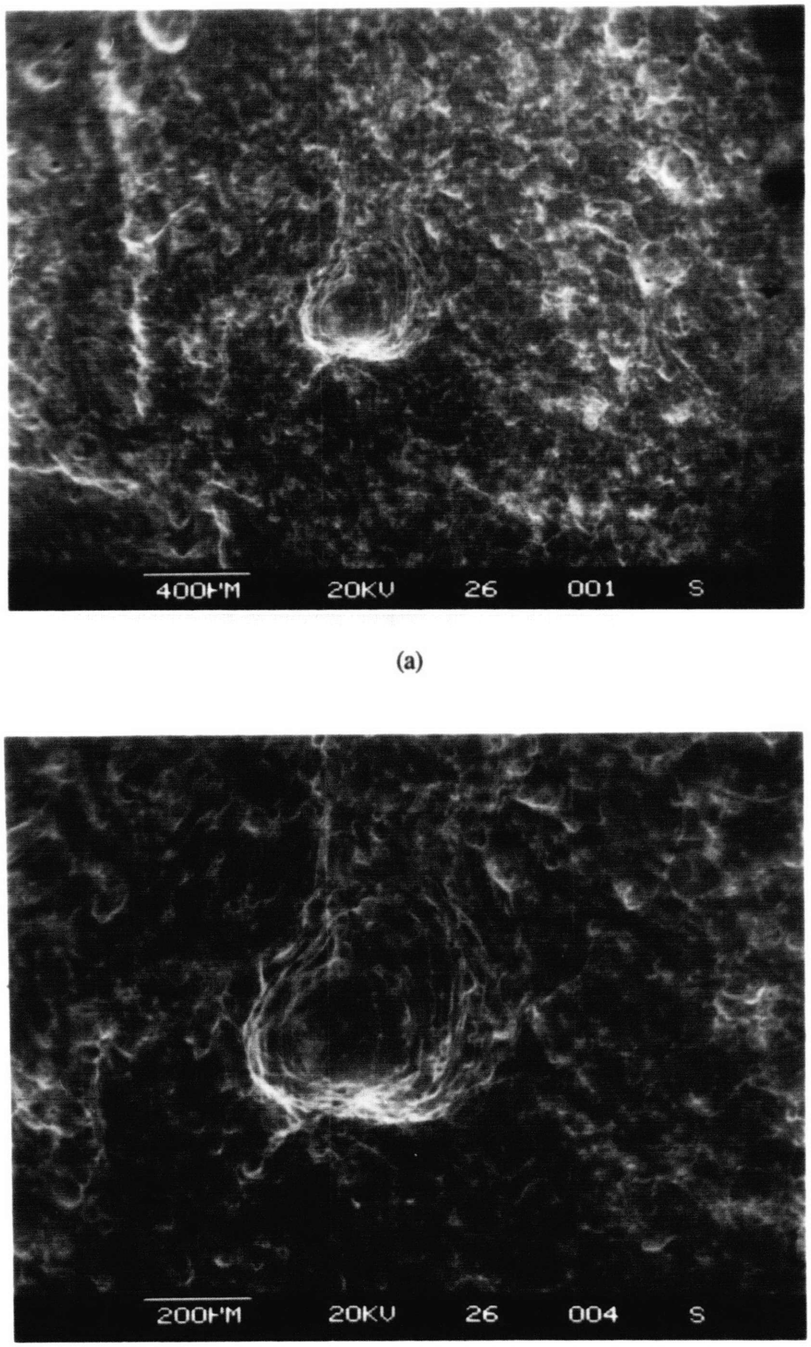
400µM 20KV 26 001 S
200µM 20KV 26 004 S

(a)

(b)

Figure 5.30 SEM images taken after 3 month of immersion, where (b) represents a higher magnification view of (a).

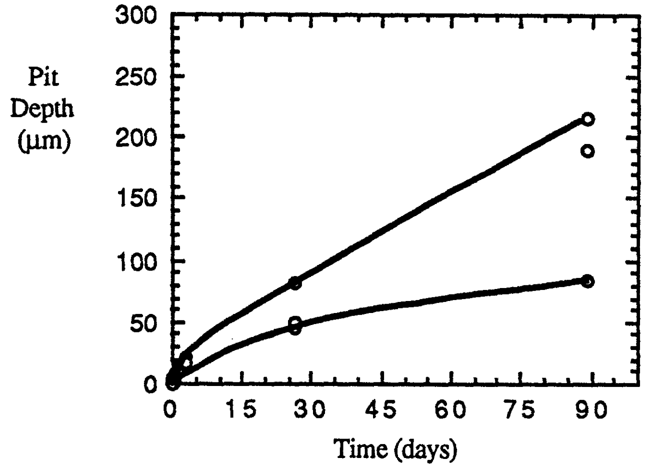

Figure 5.31 Representative pit depth distribution during a three month immersion period.

The approximately linear nature of the propagation of the maximum pit depth from 72 hours to 3 months allows extrapolations to be made. The estimated penetration during one year of immersion is approximately 0.9 mm, which is a relatively high metal penetration rate. The ramifications of such a penetration rate will be discussed in Section 5.3.5.

A compilation of pit depth distributions for all immersion times is given in Table 5.5.

Table 5.5 Representative pit depth distributions during 3 months of immersion.

Time	Pit depths (µm)				
15 minutes	2.8	2.2	2.0	–	–
1 hour	3.4	3.2	2.9	2.8	2.1
12 hours	8.8	5.8	5.2	2.6	–
24 hours	12.8	11.7	6.9	5.4	3.6
72 hours	21.4	16.8	15.6	6.9	–
1 month	84.0	50.0	45.5	–	–
3 months	215.4	190.2	85.3	–	–

5.3.4.2 Surface Dissolution

It was stated in the previous section that the quality of confocal microscope images taken after 1 month of immersion was found to be degraded by the presence of surface dissolution. Corrosive attack of the metal surface in the areas of the sample lying between pits was a definite characteristic of all samples examined in this study. Surface dissolution was clearly evident on the 12 hour sample, for example, as illustrated by the fact that the area above and to the right of the pit in Figure 5.24 has apparently undergone anodic dissolution. Surface dissolution can be more clearly observed in Figure 5.32, in which certain regions of the surface (in between the pits) have obviously suffered from corrosion. These attacked regions are visible as shallow depressions, some of which are marked by arrows. Evidence of surface dissolution can also be obtained by viewing the sample at lower magnification, as shown in Figure 5.33. The observed roughness of the surface in this photograph is a direct result of anodic dissolution of the metal surface. The confocal microscope is also capable of revealing surface attack, as shown in Figure 5.34 (this photograph was taken after 24 hours of immersion). The dark circular areas in Figure 5.34 are pits, while the irregularly shaped area marked by the arrow represents a region in between the pits which has undergone surface dissolution.

Surface attack was normally somewhat heterogeneous in nature. This type of attack was often found to occur to an uneven extent on the 12, 24, and 72 hour samples, as some areas of these specimens exhibited a greater amount of surface attack than other areas. At the longer immersion times, however, the surface dissolution eventually extended so that nearly the entire metal surface was covered, though some unattacked regions were present even at the longest immersion times. Evidence of surface dissolution on the three month sample is provided by Figure 5.30. The area around the pit in this micrograph clearly exhibits the rough, uneven characteristics associated with corrosive attack.

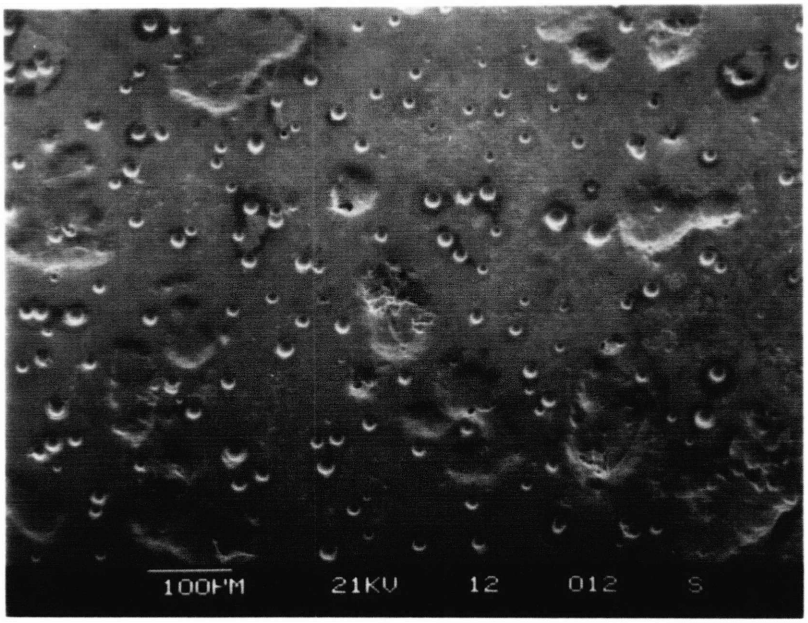

Figure 5.32 Dissolution of the surface between the pits, as observed on a sample which had been immersed for 12 hours in NaCl at 23°C. The regions marked with arrows correspond to the surface attacked areas.

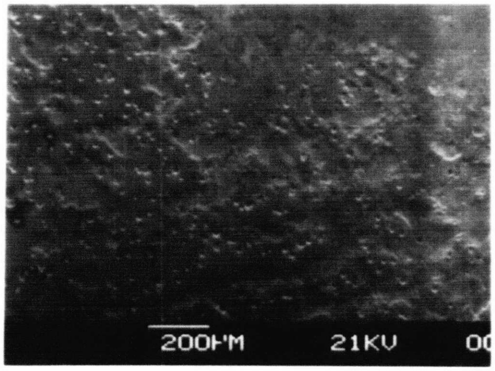

Figure 5.33 Dissolution of the metal surface, as shown at low magnification on sample immersed for 12 hours in NaCl at 23°C. The dissolution is illustrated by the obvious roughness of the metal surface.

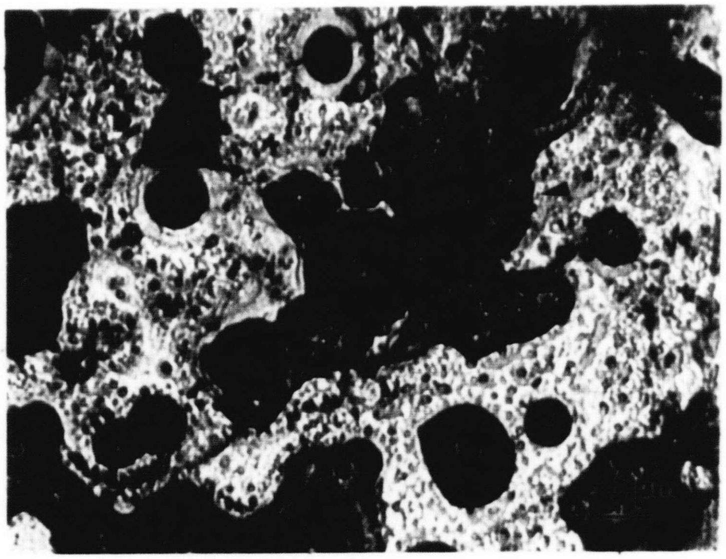

Figure 5.34 Surface dissolution as illustrated in the confocal microscope. The region which has undergone surface attack is the irregularly-shaped region marked by an arrow.

It was difficult to obtain quantitative depth measurements on the regions exhibiting surface attack, since these regions were typically too wide and shallow to fall withing the operating limits of the confocal microscope profiler. Qualitative determinations indicated, however, that the corroded surface areas were substantially shallower than pits. The irregular nature of the surface profiles in the regions adjacent to the pits in Figures 5.29 (a) and 5.29 (b) (1 month immersion) is believed to be related to the anodic dissolution experienced by the surface. According to these profiles, the surface attack appears to be only a few microns deep after 1 month of immersion. This observation was confirmed by moving the sample to a region where areas which had not undergone surface dissolution could be observed along with surface attacked areas. The confocal microscope was focused on the unattacked metal surface, and then on the bottom of regions which had undergone surface attack. The

attack depth could then be estimated by determining the amount of microscope translation necessary to alter the focus from one area to the other.

It is important to discuss the fact that the macroscopic roughening of the surface shown in Figure 5.33 was not clearly evident until about 12 hours of immersion had elapsed. Although observable surface dissolution was not present at short immersion times (15 minutes, 1 hour), evidence obtained using the confocal microscope indicates that the surface *was* corroding prior to the time when this type of attack could be readily detected in the SEM. Due to the particular type of optics used in constructing a confocal microscope, this instrument was found to be very sensitive to the intensity maximum generated by a highly reflective surface. For this reason, it was often difficult to obtain high-quality images of as-polished Nd-Fe-B surfaces. Imaging problems were not encountered when corroded samples were analyzed, however, even if short immersion times of 15 minutes or 1 hour were employed. Surfaces on the 15 minute and 1 hour samples were found to exhibit a significantly lower reflectivity than were the as-polished samples, suggesting that small-scale surface dissolution and accompanying surface roughening had occurred during the 15 minute or 1 hour immersion period. This dissolution eventually becomes readily visible at a later time, as shown by the surface attack evident in Figures 5.32 - 5.34.

According to the foregoing discussion, the metal surface appears to have been in the active rather than the passive state during its entire immersion period, which indicates that the metal does not form a protective (passive) film on its surface when immersed in NaCl at 23°C. The importance of this observation will become apparent in Section 5.4.5.1, when an attempt is made to identify the operative pitting mechanism in the Nd-Fe-B system. It should be noted that the presence of surface dissolution is highly unusual in a material exhibiting pitting attack, since the presence of pits is normally associated with the existence of a passive surface film.

The appearance of surface dissolution is additionally important because of its ability to explain the continuous increase in i_{lim} noted in the cathodic polarization tests (Figure 5.23). An increase in the area of the external metal surface is capable of explaining the obtained results, and the observed trend in i_{lim} can therefore be attributed to surface dissolution, since this type of attack results in a steady increase in the area of the metal surface.

5.3.4.3 Intergranular Corrosion

Intergranular attack has been proposed by several researchers as the main mode of corrosion in both sintered and rapidly solidified Nd-Fe-B alloys [54]. Definitive evidence of intergranular attack *has* been obtained [43,54], but only for Nd-Fe-B alloys produced by sintering. Experimental results indicating whether or not intergranular attack occurs in RSP alloys are currently not available. However, it has been conjectured that intergranular corrosion may also occur in RSP materials, since alloys produced by both rapid solidification and sintering techniques are known to contain a similar Nd-rich grain boundary phase. It is important to realize, however, that intergranular corrosion has been documented only for sintered Nd-Fe-B alloys which do *not* contain cobalt additions (i.e. Co-free magnets). The addition of 5% cobalt to sintered Nd-Fe-B has been found to dramatically reduce its susceptibility to intergranular attack [43]. It has been presumed that the observed reduction in attack is related to the formation of a Nd-Co intermetallic grain boundary phase (possibly Nd_3Co [44]). The improved intergranular corrosion resistance of Co-containing magnets suggests that the Nd-Co phase may be less electronegative than the Nd-rich grain boundary phase which exists in Co-free magnets [43].

The Nd-Fe-B samples employed in the present study are known to contain 2.5 wt% Co [58]. Although Co additions have been shown to reduce the susceptibility of sintered Nd-Fe-B to intergranular attack, it is not known *a priori* whether or not the same benefit will be obtained when Co is added to the RSP alloy. Owing to the substantial differences between rapid solidification processing and sintering, the metallurgical distribution of cobalt in Nd-Fe-B could obviously be very different in magnets produced by the two types of processes. It is possible, therefore, that the beneficial aspects of adding Co to sintered alloys might not be obtained in alloys produced by rapid solidification.

The preceding paragraphs have emphasized the fact that the process of intergranular attack in RSP Nd-Fe-B is clearly not well-understood. Available experimental evidence appears to be essentially nonexistent on this topic, and the existing discussion in the literature has been exclusively speculative in nature. A determination of whether or not intergranular corrosion occurs on the industrially-produced RSP samples was thus considered to be an important part of the present study. This task is believed to be especially relevant in view of the expected deleterious effects of intergranular corrosion on the magnetic properties of Nd-Fe-B. The undesirable effects of intergranular attack in a permanent magnetic material are described below, along with a quantitative estimate of the amount of corrosion expected if such attack were taking place in rapidly solidified Nd-Fe-B.

If the grain boundary phase in the alloy is undergoing preferential attack, grains would tend to fall out of the material once they are undercut by corrosion. It is believed that undercutting and subsequent fallout of grains can continue indefinitely due to the interconnection of the grain boundary phase; note that eliminating the interconnection of this phase would adversely affect the coercivity of the magnet. If preferential grain boundary corrosion were occurring, it would be qualitatively expected that the resulting metal loss and the associated magnetic flux loss would be substantial during long-term exposure to a corrosive environment. The effects of preferential grain boundary corrosion were quantitatively estimated by modifying the calculation in Section 5.1.10 in order to account for the presence of preferential grain boundary attack. The measured corrosion current, I_{corr} (determined via Tafel extrapolation) is normally assumed to be derived from the entire metal surface; this parameter is then divided by the nominally exposed area to determine the corrosion current density, i_{corr} (as was done in Section 5.1.10). The rate of intergranular attack was estimated in the present calculation by assuming that I_{corr} is derived solely from the corrosion of the grain boundary phase. The rationale for this assumption is shown schematically in Figure 5.35. In the event that intergranular corrosion is taking place, essentially all of the corrosion current should be emerging from the grain boundaries rather than from the entire surface. The intergranular corrosion current density, $i_{g.b.}$, should thus be determined by dividing the measured corrosion current, I_{corr}, by the estimated grain boundary area rather than by the nominal sample area.

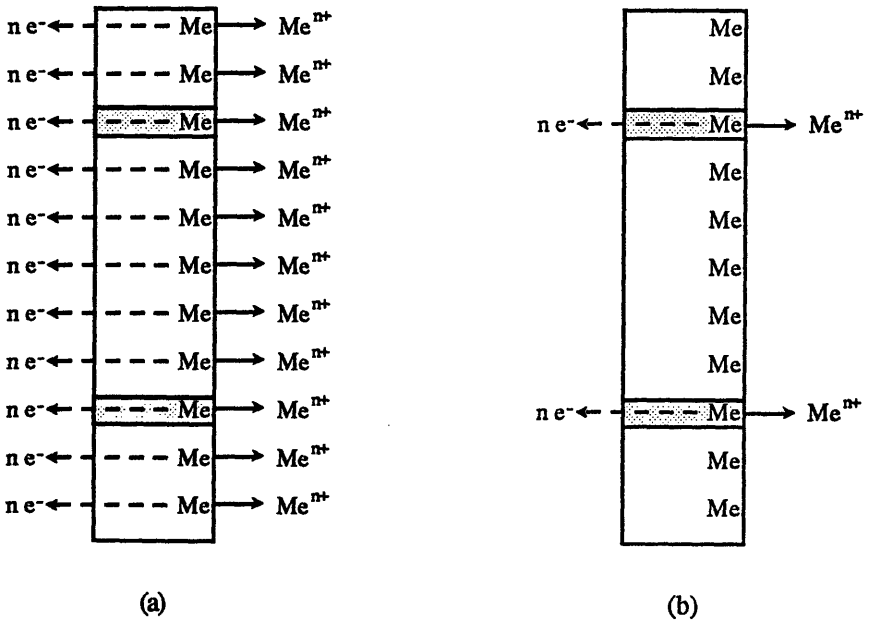

Figure 5.35 Schematic diagrams illustrating (a) general corrosion and (b) intergranular corrosion. Electrons are being produced all over the metal surface in (a), but only on a small portion of the sample area in (b). The symbols Me, Me^{n+}, and n e^- represent metal atoms, metal cations, and electrons, respectively.

The value of i_{corr} for Nd-Fe-B in NaCl at 23°C was previously given as 39 $\mu A/cm^2$ in Section 5.1.10. The ratio of grain area to grain boundary area was approximately 95 : 5, according to an estimated ratio cited in the literature [30]. In other words, 0.05 cm^2 of grain boundary area and 0.95 cm^2 of grain area are estimated to be present in a sample having a nominal surface area of 1 cm^2. The grain boundary corrosion current density, $i_{g.b.}$, can then be estimated using the calculation shown below:

$$[5.3] \qquad i_{g.b.}\left[\frac{\mu A}{cm^2\ [g.b.]}\right] = i_{corr}\left[\frac{\mu A}{cm^2\ [alloy]}\right] \cdot \frac{0.95\,[cm^2\ [alloy]]}{0.05\,[cm^2\ [g.b.]]}$$

The value of $i_{g.b.}$ was estimated as 741 μA per cm^2 of grain boundary area.

The revised corrosion current density ($i_{g.b.}$) was placed into equation [5.2] in order to determine the penetration rate associated with intergranular corrosion; several parameters had to first be estimated for the grain boundary phase. The density of the Nd-rich phase was estimated as 7.3 g/cm^3, the atomic weight as 118 g/mole, and the number of electrons transferred as 2.7. These values were calculated using weighted elemental averages based on an approximate grain boundary composition of Nd_7Fe_3, which is one of several compositions that have been estimated for the Nd-rich phase in the literature [29,45].

Equation [5.2] was then used to calculate the penetration rate as 573 mpy (14.5 mm/yr), which is clearly a very high value. It was assumed in this calculation that the undercutting of grains can continue indefinitely due to the interconnection of the grain boundary phase.

The foregoing calculation was designed to demonstrate how strongly preferential grain boundary attack would affect the overall metal loss rate; the magnitude of the calculated corrosion rates clearly show the detrimental effects of intergranular corrosion. The mass loss (or, alternatively, the volume loss) associated with grain fallout leads to a loss of magnetic flux. The percent flux loss for a given amount of metal loss obviously depends on the size of the initial magnet considered, but given the calculated penetration rates, the magnetic flux losses would be expected to be very large for almost any magnet considered. The expected degradation of magnetic properties which would result from such attack emphasizes the importance of determining whether or not intergranular corrosion is taking place in RSP Nd-Fe-B. The determination made in the present study is described below.

The calculation outlined above was capable of providing an estimate of the penetration rate which is expected to result from the intergranular corrosion of Nd-Fe-B. This calculation has an additional purpose, however, besides simply demonstrating the expected negative implications of grain boundary corrosion on magnetic flux. Since one of the measured parameters in the present study was the metal penetration rate as a function of time, indirect evidence indicating the presence or absence of intergranular corrosion can be obtained by comparing the measured and calculated metal penetration rates to one another. The comparison between measured and calculated quantities would have ideally been performed using weight loss rather than penetration rates, but the cracking of several test samples at relatively short times precluded the collection of accurate weight loss data. Performing the comparison using penetration rates was considered to be the best available alternative.

The maximum measured penetration depths have all been associated with pits in this study. Surface dissolution has been observed, but the depth of this attack has been shown in Section 5.3.4.2 to be far less that that obtained from pitting corrosion. The penetration depths measured by the confocal microscope can thus be compared to the penetration depths calculated for the same immersion time using the above calculation. If the observed corrosion is proceeding via intergranular attack, the measured and calculated penetration rates should be similar in magnitude. The actual comparison was made by superimposing the measured and calculated penetration rates, as shown in Figure 5.36. The calculated rates for both general and intergranular corrosion have been included on the plots, and the calculated rates after 72 hours and 89 days are additionally listed in Table 5.6.

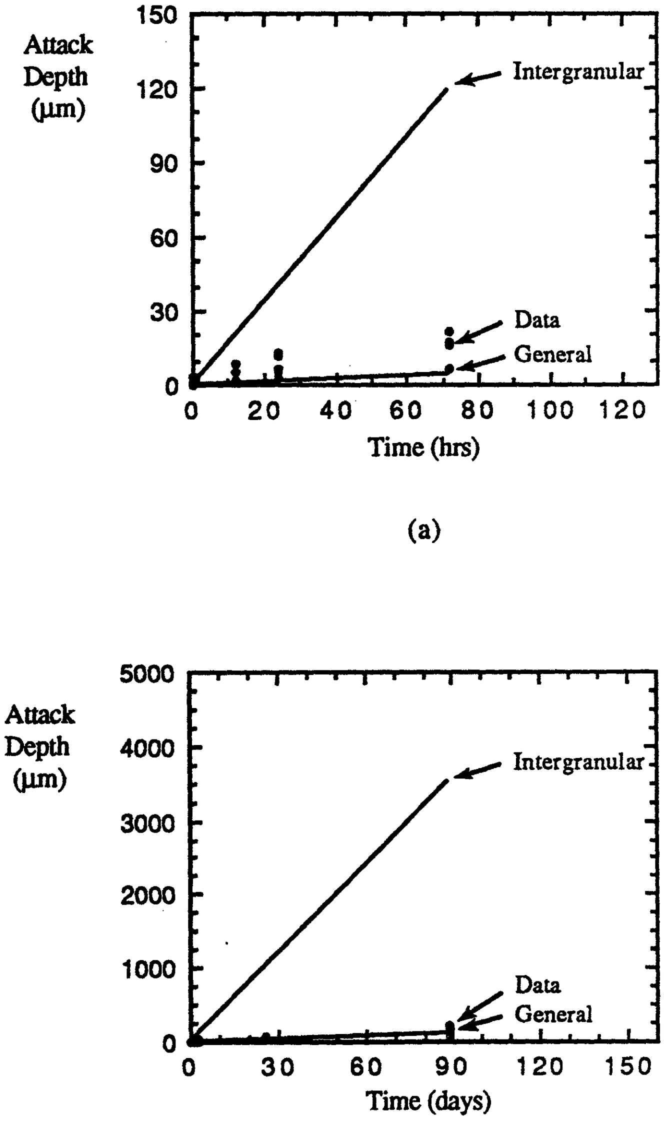

(a)

(b)

Figure 5.36 Calculated and measured penetration rates in Nd-Fe-B in NaCl at 23°C after (a) 72 hours and (b) 89 days.

Table 5.6 Calculated penetration rates for general and intergranular corrosion in NaCl at 23°C.

Type of Corrosion	72 hours	89 days
General	4.1 μm	121 μm
Intergranular	119 μm	3530 μm

The evident divergence between the measured and calculated penetration rates in Figure 5.36 provides substantial evidence that intergranular corrosion is not occurring on the RSP samples; the measured corrosion rates appear to be too low to correspond to intergranular attack. Although the comparison shown in Figure 5.36 provides important information in the attempt to determine whether or not intergranular corrosion is taking place, this evidence still must be considered indirect in nature. As such, it would be extremely useful if direct evidence could be obtained to supplement the argument outlined above.

Completion of a direct investigation of intergranular corrosive attack in rapidly solidified Nd-Fe-B (grain diameter 80 - 100 nm) is a relatively challenging task, however. Direct evidence of intergranular corrosion is normally obtained by analyzing a corroded surface using an SEM. Surfaces which have suffered from intergranular corrosion tend to have a characteristic appearance: grains normally appear in relief, creating a surface topography which has a height approximately equal to the grain diameter. This type of procedure was used in the evaluation of intergranular corrosion in sintered Nd-Fe-B (grain size ~ 10 μm) by Ohashi *et al* [43]. For RSP samples, however, such an investigation is hindered by the extremely fine $Nd_2Fe_{14}B$ grains (80-100 nm diameter) produced by rapid solidification. The small size of the grains precludes their resolution in a conventional SEM, and more sophisticated instruments must be utilized in order to perform such analysis. An additional complication in this work was related to the buildup of insoluble corrosion products during immersion, which can obstruct viewing of the sample surface in a microscope.

It might be initially thought that the presence of a Nd-rich corrosion product might indicate intergranular corrosion, but such an analysis neglects the possibility of preferential element dissolution (dealloying). An electrochemically active element such as Nd could actually dissolve from the $Nd_2Fe_{14}B$ phase more rapidly than Fe. An identification of the chemical composition of soluble or insoluble corrosion products therefore does not provide definitive evidence regarding the presence or absence of intergranular corrosion.

Direct evidence in this particular case can be most readily obtained using a high resolution scanning electron microscope. A JEOL 6300 SEM equipped with a field emission electron source was utilized, and the instrument was operated at an accelerating voltage of 1 kV in order to accentuate surface detail. A sample immersed for only 15 minutes (NaCl, 23°C) was utilized in an attempt to mimimize the blockage related to insoluble corrosion products.

If intergranular corrosion were taking place on the metal surface, the expected penetration depth after 15 minutes of immersion can be determined by referring to the penetration rate calculation above. The calculated depth of grain boundary corrosion after 15 minutes is 410 nm, which indicates that if intergranular corrosion is occurring, approximately 4 to 5 $Nd_2Fe_{14}B$ grains should have been undercut by the time the sample is removed from the corrosive solution. The purpose of this brief calculation is to demonstrate that the amount of intergranular corrosion taking place in 15 minutes should be sufficient for evidence to be available on the metal surface if this form of corrosion is indeed occurring.

When examining the corroded surface, it is important to look for topography commonly associated with intergranular attack, such as grains in relief with a characteristic size of

about 80 - 100 nm. Metal loss at the grain boundaries often also provides a good indication that intergranular corrosion is taking place, but the extremely small size of the grain boundary phase in RSP Nd-Fe-B (1-5 nm wide) indicates that this phase is unlikely to be resolved, even in the field-emission SEM. Surface topography associated with grains thus appears to be the most relevant indicator of the presence or absence of intergranular corrosion in this metal.

A high resolution micrograph of the surface of the 15 minute sample is shown in Figure 5.37. A few small islands of white corrosion product are visible in this area, but the bare metal surface is clearly visible in the remainder of the photograph. No evidence of any sort of 80 - 100 nm topography can be observed on the metal. In fact, the surface appears to be essentially featureless. The image shown in Figure 5.37 is thus consistent with the previous contention that intergranular corrosion is not occurring on the surface of rapidly solidified Nd-Fe-B.

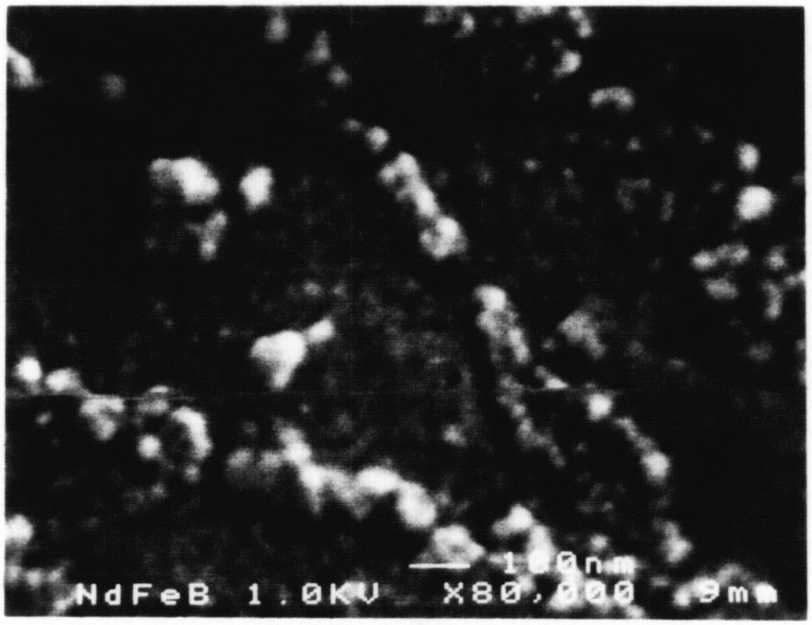

Figure 5.37 A high-resolution SEM image of a Nd-Fe-B surface which had been immersed for 15 minutes in NaCl at 23°C. An accelerating voltage of 1 kV was utilized to form the image.

The evidence presented in Figure 5.37 would be even more convincing if the ability of the microscope to clearly image 80 - 100 nm topography could be confirmed. The high resolution SEM *was* found to be capable of detecting such topography, as described below.

A different area of the same sample imaged in Figure 5.37 is shown in Figure 5.38. It is clear that Figure 5.38 corresponds to an area of the surface which is directly adjacent to a pit. The observed pit appears to be almost completely surrounded by insoluble corrosion products, except for a small area in the region just above and to the right of the pit. A high magnification view of the insoluble corrosion product is shown in Figure 5.39. The area from which Figure 5.39 was taken is indicated by an arrow on Figure 5.38; this arrow confirms the fact that Figure 5.39 was taken from a region which is completely covered by insoluble corrosion products. The high resolution micrograph of the corrosion products (Figure 5.39) reveals the presence of nodular topography, with nodule diameters which vary from about 40 to 110 nm.

The fact that the high resolution SEM was able to provide relatively good images of the corrosion product morphology indicates that the microscope *is* capable of detecting features which would be associated with intergranular corrosion in this fine-grained metal. The fact that such features are not observed on the metal surface itself strongly suggests that intergranular attack is not occurring. If this form of attack were taking place, grains should appear in relief on the surface of Figure 5.37. The corrosion product morphology in Figure 5.39 indicates that the absence of such topography in Figure 5.37 is not due to microscope limitations.

It is emphasized that the nodular surface in Figure 5.39 is characteristic of the corrosion product itself rather than of the metal; it would simply appear to be coincidental that the nodules happened to be ~110 nm or less in size. The fact that the nodular topography shown in Figure 5.39 is characteristic of incompletely removed corrosion products can be verified by moving to another area of the sample where the metal surface is visible without being blocked by corrosion products; the nodular topography is not apparent in these regions.

The results of the present study thus indicate that intergranular corrosion is not occurring on the surface of rapidly solidified Nd-Fe-B in NaCl at 23°C. This result can be attributed to the presence of cobalt in the alloy, as a previous report [43] indicated that Co additions are capable of minimizing intergranular attack in sintered Nd-Fe-B. Although the metallurgical distribution of Co in the RSP samples was not investigated in this study, it appears that the grain boundary phase(s) responsible for intergranular corrosion resistance in sintered Nd-Fe-B are also present in alloys produced by rapid solidification.

5.3.4.4 Inter-ribbon Attack

Another type of localized attack which should be considered in addition to intergranular corrosion is inter-ribbon attack. This form of localized corrosion is specific to materials which are produced by rapid solidification. Fragments of the rapidly solidified ribbons are metallurgically bonded together during the hot pressing process, as described in Section 2.2.3.2. The boundaries between the adjacent rapidly solidified ribbon fragments provide a possible pathway for localized corrosive attack. The complete interconnection of these boundaries throughout the material indicates the importance of considering such attack, as ribbons themselves could be undercut and fall out of the metal in a process similar to that of intergranular corrosion. Such a process could result in substantial mass loss and therefore magnetic flux loss. This type of attack has not been considered in the literature, mainly because most corrosion studies have employed sintered magnets, which do not contain ribbon boundaries. Inter-ribbon attack should not be overlooked, however, because if

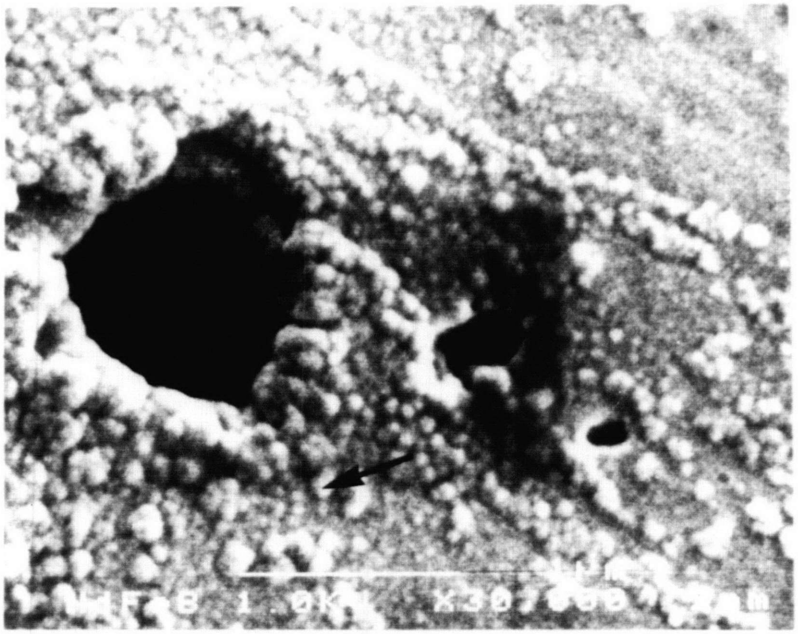
NdFeB 1.0KV X30,000

Figure 5.38 A high resolution SEM image of a sample which had been immersed for 15 minutes in NaCl at 23°C (1 kV). Note that arrow denotes the area which is imaged in Figure 5.39.

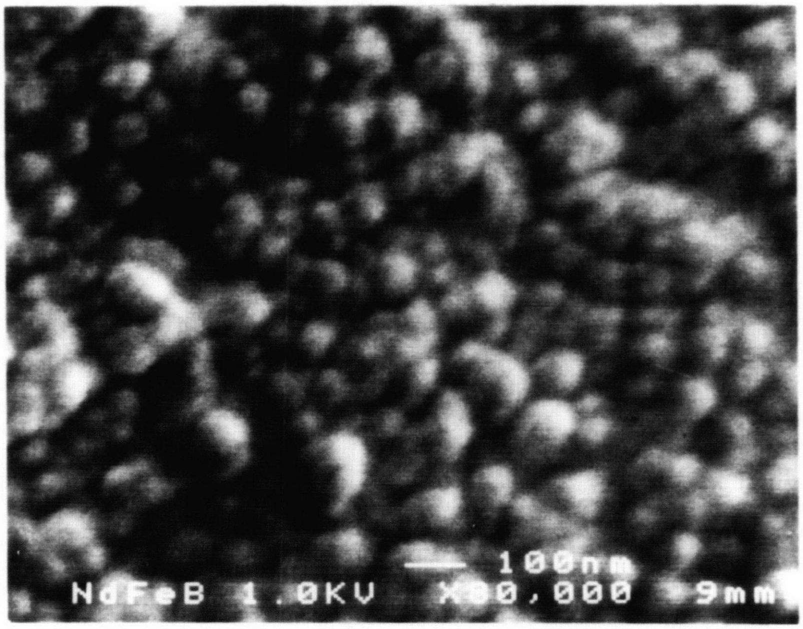
100nm
NdFeB 1.0KV X00,000 9mm

Figure 5.39 A high resolution SEM image of the morphology of incompletely removed corrosion products (1kV). The image was taken from the region marked with an arrow in Figure 5.38.

ribbons were to begin to drop out of the material due to preferential dissolution of the boundaries, this type of attack could conceivably cause a serious problem for the viability of the alloy. It is emphasized that in order to be truly damaging to the material, the entire ribbon boundary would have to corrode in a relatively even fashion. Attack of only part of the boundary would be far less problematic, as this type of attack would not be expected to lead to the undercutting and fallout of ribbons; it is the actual loss of the ribbons themselves from the metal surface which would result in a very large loss of magnetic flux. An image taken from a sample which had been immersed for 12 hours in NaCl is shown in Figure 5.40. Although a slight etch of the ribbon boundaries can be observed in this images, rapid, preferential attack of the boundaries was not found to occur in this material. Such attack would be expected to result in the presence of sharp ditches at the ribbon boundaries, which are not observed in Figure 5.40. Examination of surfaces at the longer immersion times (1 and 3 months) also did not reveal evidence of significant ribbon boundary attack.

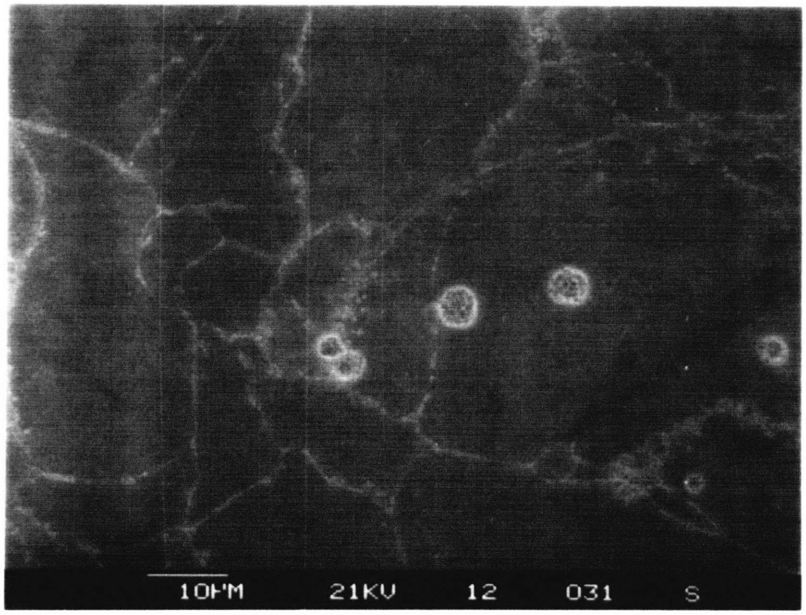

Figure 5.40 SEM image showing that a slight etch is present at the ribbon boundaries, but that significant inter-ribbon attack is not occurring (12 hours, NaCl, 23°C).

5.3.5 Summary of Rate and Type of Attack

Pitting corrosion was found to be the controlling form of corrosive attack in Nd-Fe-B at 23°C at both long and short immersion times; pitting is accompanied by relatively shallow surface dissolution at immersion times greater than about 12 hours. Intergranular corrosion is not believed to be a significant form of attack under these conditions, based on the results of calculations as well as direct observation of the corroded surface. It is relevant at this point to consider how the observed forms of corrosive attack would affect the ability of the material to perform its intended service function. If a particular material is to be used as tubing or piping, for example, the primary parameter of interest would be the rate of metal penetration. In fact, the relatively high penetration rate measured in this study would be a significant concern if the material were to be used for such an application, since sustained attack might lead to wall penetration and subsequent leakage. Nd-Fe-B is a permanent magnetic material, however, and its primary function is to supply magnetic flux to drive a magnetic circuit. This ability is much more closely related to the mass loss or volume loss of the material than to its penetration rate, since magnetic flux is directly proportional to the *volume* of metal present. Penetration rates have been reported much more extensively in this study than rates of weight loss, as a result of the cracking exhibited by several test samples. Cracking precluded the collection of acceptable weight loss data, and penetration rates therefore had to be utilized in order to facilitate comparisons between measured and calculated values (as in Section 5.3.4.3). At this point, however, the actual volume loss resulting from the observed corrosive attack should be estimated. It can be qualitatively stated that pitting attack should not be nearly as severe a form of corrosion for a permanent magnet as would intergranular attack, for example. Though both forms of corrosion can be associated with relatively high penetration rates, the mass loss resulting from the undercutting and subsequent fallout of grains on the metal surface would be expected to be much higher than the mass loss associated with pits. The metal loss resulting from pitting corrosion can still become significant, however, if pits continue to widen and deepen with time. The possibility that the estimated rate of metal loss may lead to corrosion concerns is increased by the fact that rare earth permanent magnets (such as Nd-Fe-B) are typically *thin* by design [48], which results in the utilization of magnets with a relatively high surface area to volume ratio. Such magnet geometry suggests that even the moderate metal loss normally associated with pitting may be capable of causing a magnet to lose a significant percentage of its magnetic flux over time. The effect of pitting corrosion on the volume of metal lost (and hence the magnetic flux lost) from the surface of Nd-Fe-B is considered below. The volume of metal lost due to pitting can be estimated by considering the width and the depth of the observed pits, along with the measured pit density on the metal surface. At a particular point in time, the average pit volume can be estimated from measured depth and width statistics; this value can then be multiplied by the corresponding pit density to obtain the total volume loss due to pitting at the given immersion time (the obtained value can be extrapolated if necessary).

The representative pit depth distribution at 72 hours will be used in this calculation. Since a pit density value was not directly determined for this immersion time, the value measured after 1 hour of immersion (1.05×10^4 pits/cm^2 of surface area; see Appendix 10.2) will be used instead. Even though not every pit on the 1 hour surface is still actively propagating at 72 hours, it was stated in Section 5.3.4.1 (a) that the fraction of inactive pits after 72 hours was considered to be relatively low; the 72 hour pit density is thus believed to be reasonably close to the pit density value measured after 1 hour of immersion (note that the rate of pitting is much more consistent at 72 hours than at 1 hour; an estimate collected for 72 hours is thus more amenable to extrapolation than an estimate obtained from 1 hr. data). The estimated volume per pit was determined by calculating the volume of each pit in the 72 hour representative pit distribution using a hemispherical approximation ($V = 0.667 \cdot \pi \cdot d^3$). These data were then averaged to obtain the approximate volume per pit on the surface after

72 hours (9.7 x 10^{-9} cm^3/pit). This value was multiplied by the estimated pit density and then extrapolated to 1 year of immersion to obtain the estimated volume loss per square cm of nominally exposed surface area. The calculated volume loss is 0.012 cm^3 per cm^2 of surface area in 1 year. A conversion of this value to magnetic flux density appears below.

The actual flux density output by a magnet is dependent on both its remanent magnetization (B_r) and the length of the air gap (L_g) in the magnetic circuit. B_r represents the upper limit of the flux density output, and the *maximum* flux density loss is thus equivalent to the loss in remanent magnetization due to corrosion (the *actual* flux density loss in each case would also be dependent on the L_g for the given magnetic circuit). The remanent magnetization (B_r) of Nd-Fe-B is 11.8 kiloGauss per cm^3 (Table 2.3), and the corresponding maximum loss in magnetic flux density is 143 Gauss per cm^2 of exposed surface area. Even though the total volume loss is readily converted to an absolute magnetic flux loss, it is believed to be more relevant to consider the *percent* magnetic flux loss. Use of the percent loss allows the obtained results to be more easily interpreted, since a given amount of flux loss may have serious consequences for the viability of one magnet and yet cause only a mild problem for another, depending on the initial flux output of the magnet in question. The percent magnetic flux loss is highly dependent upon the size (volume) and surface area of the magnet considered. Corrosive degradation is a direct function of exposed surface area. A given amount of corrosion-related flux loss will lead to a greater *percentage* of magnetic flux loss if the magnet considered has a relatively low total volume. The amount of corrosive degradation experienced by a permanent magnet is clearly dependent on both corrosion susceptibility *and* magnet geometry.

The geometry of a permanent magnet is expected to vary in size and shape depending upon the particular application in question. Information relating to the sizes and shapes used in actual practice was obtained from Magnequench® [19]. Magnet sizes were grouped into three general categories: small, average, and large. The surface area and volume was provided for each size category, and the percent flux loss was then calculated by using the surface area of the magnet to obtain the total estimated volume loss in 1 year; this value was then divided by the volume of the magnet considered to determine the estimated percent flux loss per year. The results of the estimates are shown in Table 5.7. Since the smallest magnet considered has a total surface area of 1.5 cm^2, the calculated value corresponds to a total estimated metal loss of 0.018 cm^3 in 1 year. The small magnet has a total volume of 0.125 cm^3, and the calculated percent volume loss (i.e. flux loss) in 1 year is thus equal to 14%; this value obviously represents a significant flux loss, which indicates that pitting corrosion *can* lead to a substantial rate of flux loss for relatively small magnets. Table 5.7 also indicates that the percent flux loss is markedly dependent upon the size and shape of the magnet considered (particularly upon the surface area/volume ratio). The observed deleterious effects of corrosion on smaller magnets is especially important in view of the fact that the size of Nd-Fe-B magnets is expected to decrease steadily over the next several years. In fact, the primary manufacturer of RSP Nd-Fe-B (Magnequench®) expects the magnets which are categorized as "small" in Table 5.7 to represent average size magnets in the relatively near future [19]. This trend towards miniaturization clearly has implications for the effects of corrosion on the viability of Nd-Fe-B; corrosion issues should become increasingly important as magnets become smaller and smaller with time.

Table 5.7 Estimated percent flux losses for various magnet geometries.

Magnet Size	Surface Area (cm^2)	Volume (cm^3)	% flux loss/ year
Small	1.5	0.125	14
Average	16.1	6.58	2.9
Large	38.7	39.5	1.2

The calculation presented above does not indicate that corrosion will be a problem for every Nd-Fe-B magnet placed into service, but it does indicate that the observed pitting attack *can* result in a considerable amount of flux loss. Such flux loss is expected to impede the intended function of Nd-Fe-B magnets in certain applications, especially when smaller magnets are to be used in a relatively aggressive environment (also note that since the rate of pitting attack was found to be substantially higher at 80°C than at 23°C after 1 hour, exposure at elevated temperatures may increase the flux loss associated with pitting).

The actual amount of pitting which can be tolerated will depend upon the geometry and the design requirements of the magnet considered. In order to judge the expected severity of pitting corrosion, factors such as the expected severity of the environmental conditions, the anticipated time of service, and the maximum amount of flux loss tolerable would also need to be considered. Another relevant consideration is the fact that the material will likely not be exposed to full immersion in service. Electrolyte is expected to be condensed on the surface during only part of the magnet's service life, and pits will thus be growing for only a fraction of the time during which the magnet is used. However, since most machines are typically required to last for 10 - 15 years or even longer, the complete time-of-wetness over such a time period is expected to be substantial even in the absence of full immersion.

In summary, the above estimate was not designed to provide an accurate gauge of the actual flux loss expected in service (this parameter would need to be determined on a case-by-case basis), but simply to determine whether or not the observed pitting attack *could* cause a problem from a magnetic flux loss standpoint. The answer to this question appears to be yes, and the flux loss resulting from the corrosion of Nd-Fe-B may be a significant concern in many corrosive environments, especially when relatively small magnets are utilized.

5.4 Sites of Pit Initiation

The presence of pitting attack on Nd-Fe-B in both NaCl and Na_2SO_4 solutions has been documented extensively in Sections 5.2 and 5.3. These results have provided a detailed description of *how* the Nd-Fe-B alloy corrodes in the environments of interest.

At this point, it is useful to try to extend the understanding of the Nd-Fe-B system by attempting to obtain some insight as to *why* the alloy corrodes in the manner described in Sections 5.2 - 5.3. Since the primary mode of corrosive attack in Nd-Fe-B is pitting, one way to examine the corrosion of the alloy in more detail is to identify the sites at which pits are initiating.

Identification of pit intiation sites may provide understanding regarding possible pitting mechanisms. Knowledge of the sites at which pits are initiating may also be relevant from an engineering point of view, as this information could provide valuable insight as to how pitting attack can be mitigated. The theoretical and practical importance of identifying pit initiation sites is discussed below, using the pitting of stainless steels as an example.

5.4.1 Importance of Identifying Pit Initiation Sites

Identification of sulfide inclusions as preferential pit initiation sites has provided insight into the operative pitting mechanism for stainless steels in Cl^- environments. At least three possible mechanisms are capable of explaining why pits might initiate at sulfide inclusions. Passive film formation may be more difficult at the sulfide-electrolyte interface than at the metal-electrolyte interface, resulting in a weak spot in the film that can lead to pit initiation.

The sulfide inclusion can also dissolve chemically or electrochemically in the solution, resulting in the production of species (such as H_2S) which can promote localized corrosive attack. Dissimilar coefficients of thermal expansion for the sulfide and the metal can lead to different shrinkage rates in the two phases during the cooling period after heat treatment. If the two phases tend to pull away from one another during cooling, a microcrevice can develop at the metal-sulfide interface. When the metal is exposed to an electrolyte, the solution contained within the microcrevice can undergo compositional changes which promote the initiation of localized attack, such as a decrease in pH or an increase in Cl^- concentration. This process occurs as a result of the restricted mass transport of dissolution products out of the crevice, as described in Section 4.3.4 and Appendix 10.1.1.

Pit initiation can therefore be attributed to either the *chemical* nature of the initiation site, as in the dissolution of the sulfide inclusion (e.g. to H_2S), or to the *physical* nature of the site, as in the formation of a microcrevice or a weak spot in the passive film.

Identification of pit initiation sites is important from an engineering viewpoint, since modifications in metallurgical processing may improve the resistance of the alloy to localized corrosion. Improved pitting resistance can be obtained in stainless steels, for example, by utilizing steel cleanliness procedures which minimize sulfur impurities.

5.4.2 Identification of Pit Initiation Sites in Nd-Fe-B

Samples which were immersed for short times (1 hour) were used in the determination of pit initiation sites, since these samples had been subjected to less corrosion damage than the longer time samples, and were thus more readily examined.

A determination of whether the pits initiate within grains or at grain boundaries was not attempted in this work. Pit initiation at grain boundaries is extremely difficult to detect in this alloy sysem, due to the fine scale of the grain boundaries, and also because the pit diameter is so much greater than the grain diameter (even after very short immersion times).

The confocal laser microscope was utilized at low magnification in an attempt to identify sites of preferential pitting attack, as shown in Figure 5.41. The black circles in these micrographs are pits (the dark circles around the pits in (b) correspond to incompletely removed corrosion product). The lines which appear to be etched correspond to the ribbon boundaries. These boundaries are the interface between adjacent rapidly solidified ribbon fragments which were bonded by the hot pressing process, as discussed in Section 2.2.3.2. The actual size of the ribbon fragments varies greatly as a result of the different amount of crushing undergone by each starting ribbon. It must be emphasized that the lines shown in Figure 5.41 are *not* grain boundaries, as the grains in this rapidly solidified material (80-100 nm diameter) are far too small to be observed in an optical microscope.

A strong association between the pits and the ribbon boundaries can be observed upon examination of the micrographs in Figure 5.41. There are six pits within the field of view in Figure 5.41 (a), and five of them appear to be located at ribbon boundaries (or, equivalently, at ribbon triple points). Of the five pits shown in Figure 5.41 (b), three appear to be located at the ribbon boundaries. One of the pits seems to be located within a ribbon, and the location of the remaining pit cannot be determined from the micrograph.

The association between pits and ribbon boundaries can also be observed in the SEM, as shown in Figure 5.42. All three of the pits present in this photograph appear to reside on a ribbon boundary or at a ribbon triple point. Although Figure 5.42 was taken from a different sample than that shown in Figure 5.41, a third sample was examined in the SEM in order to ensure that the observed association between pits and ribbon boundaries is a consistent phenomenon in this material. The results are shown in Figure 5.43.

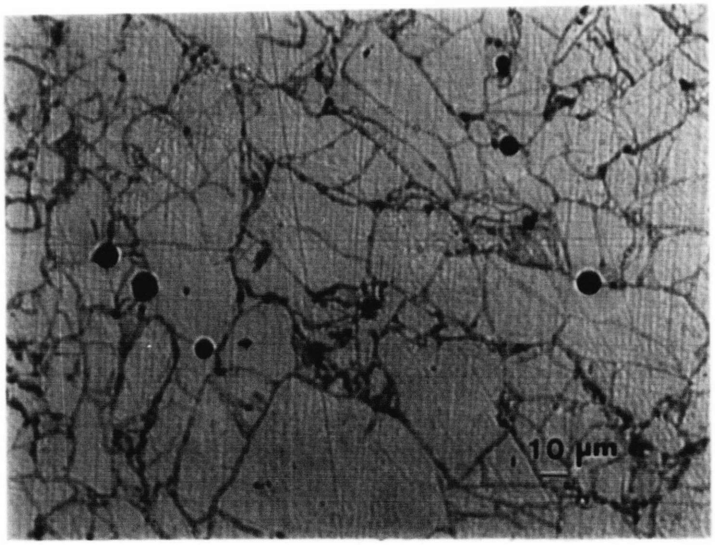

(a)

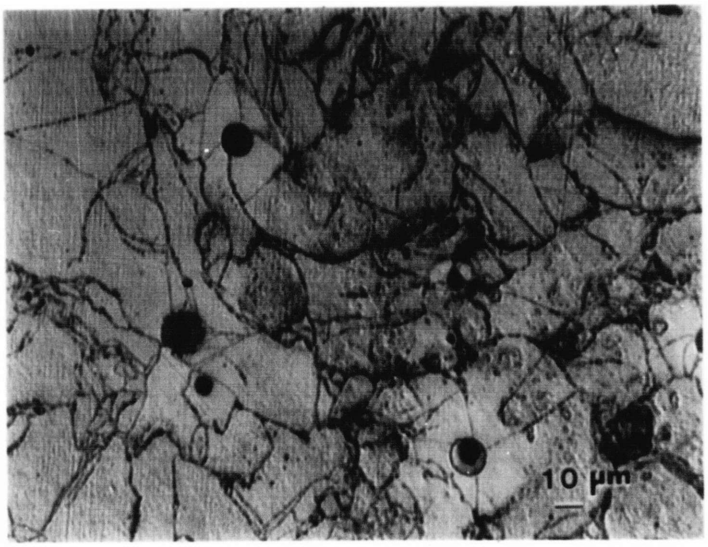

(b)

Figure 5.41 Confocal laser microscope image of Nd-Fe-B after 1 hour of immersion in NaCl at 23°C. The black circles are pits, and the lines are boundaries between adjacent rapidly solidified ribbons. Photograph (a) and (b) were taken from different regions of the same sample.

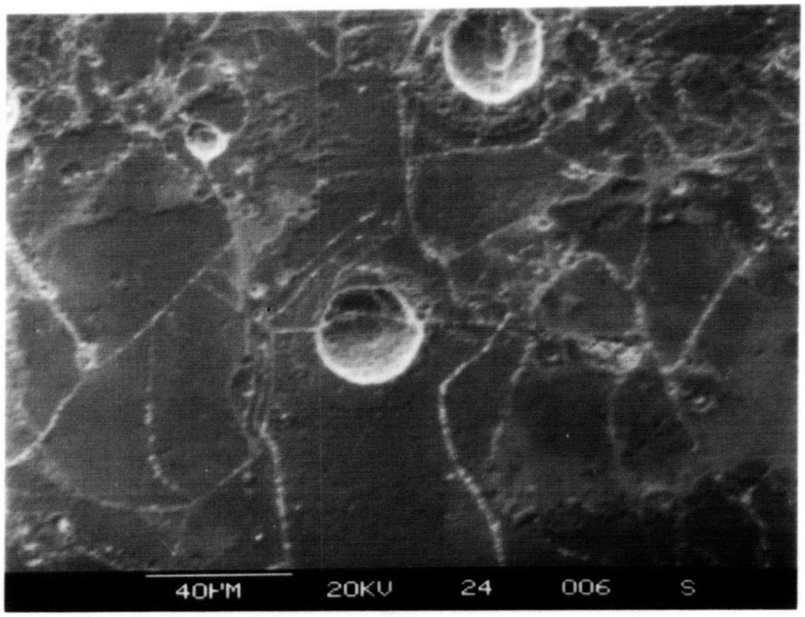

Figure 5.42 SEM image of Nd-Fe-B after 24 hours of immersion in NaCl at 23°C. This photograph was taken from a different sample than the one shown in Figure 5.58.

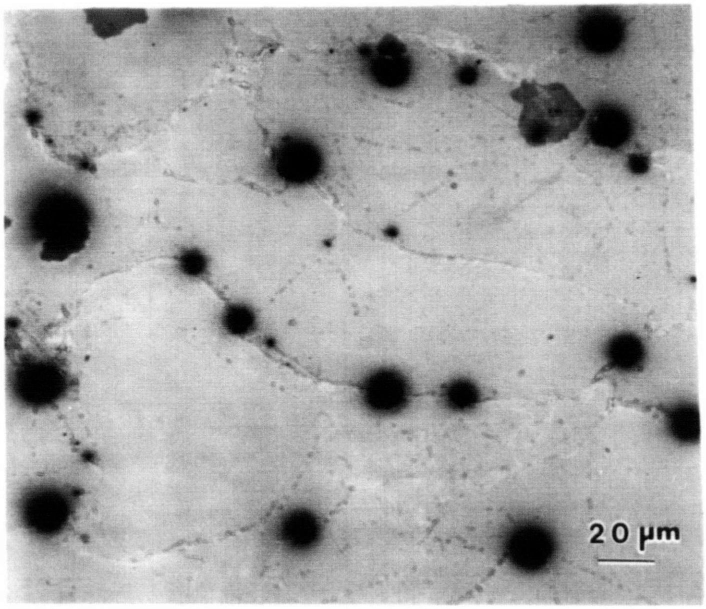

Figure 5.43 SEM (backscattered) image of Nd-Fe-B after 1 hour of immersion in NaCl at 23°C. This photograph was taken from a different sample than either the one shown in Figure 5.58 or Figure 5.59.

The ribbon boundaries are more difficult to discern in Figure 5.43 than in the previous micrographs, but careful examination reveals that twelve of the sixteen visible pits reside on the ribbon boundaries, one does not, and the location of the remaining three pits is unclear. The strong association between the pits and ribbon boundaries in three different test samples clearly suggests that the pits may be initiating preferentially at these boundaries within the Nd-Fe-B alloy.

As alluded to above, the association between pits and ribbon boundaries is not observed for each and every pit. In order to demonstrate the distribution of this association, areas with a lower percentage of pits residing on the ribbon boundaries are shown in Figure 5.44. Approximately nineteen pits are visible in Figure 5.44 (a). Although it is difficult to definitively classify the location of each pit in this micrograph, it appears that eight of the pits reside on the ribbon boundaries, five do not, and the location of the remaining six pits is ambiguous. Figure 5.44 (b) shows a region where only about half of the eleven pits in the field of view appear to lie on the ribbon boundaries.

Not all ribbon boundaries will be clearly visible in a given micrograph, and some of the pits which are considered not to lie on the boundaries may in fact reside on boundaries which are difficult to see. One possible source of ribbon boundary obstruction is the presence of insoluble corrosion products on the surface of the attacked metal. The blocking effect which can result from these products is especially problematic in the area surrounding a pit, since the residue from the corrosion product cap which covers the pit often leaves an opaque ring of insoluble corrosion products around the pit circumference. An example of this phenomenon is provided in Figure 5.45. Figure 5.45 (a) was taken at the same magnification (400 x) used in Figures 5.41 and 5.44. At this relatively low magnification level, it is difficult to tell whether or not the observed pit is located on a ribbon boundary. It appears that a light line may be present on either the right or the left side of the pit, but it

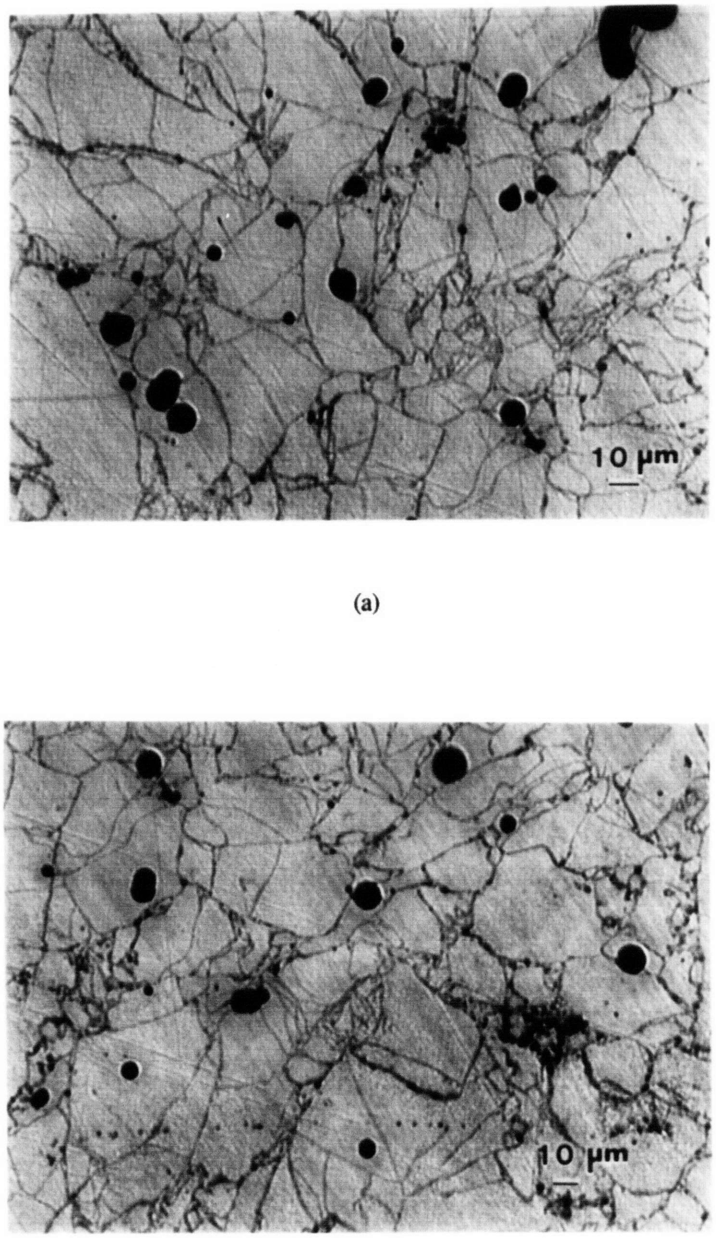

(a)

(b)

Figure 5.44 Confocal laser microscope image of Nd-Fe-B after 1 hour of immersion in NaCl at 23°C. Photographs (a) and (b) were taken from different regions of the same sample shown in Figure 5.58.

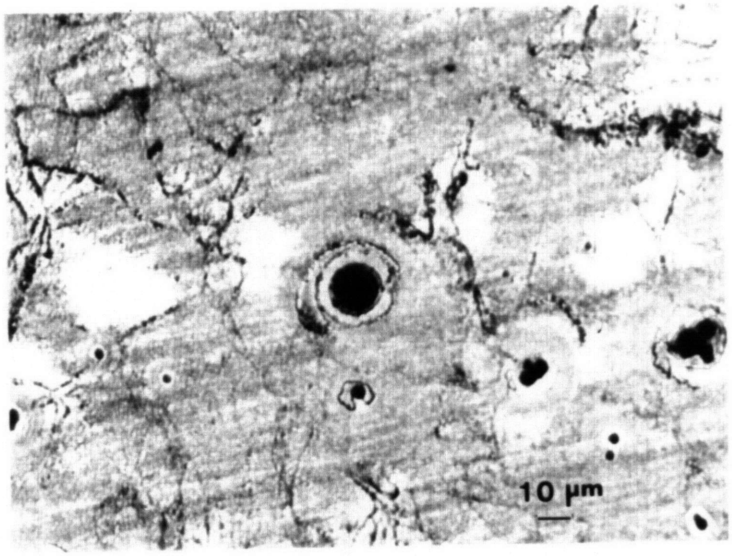

(a)

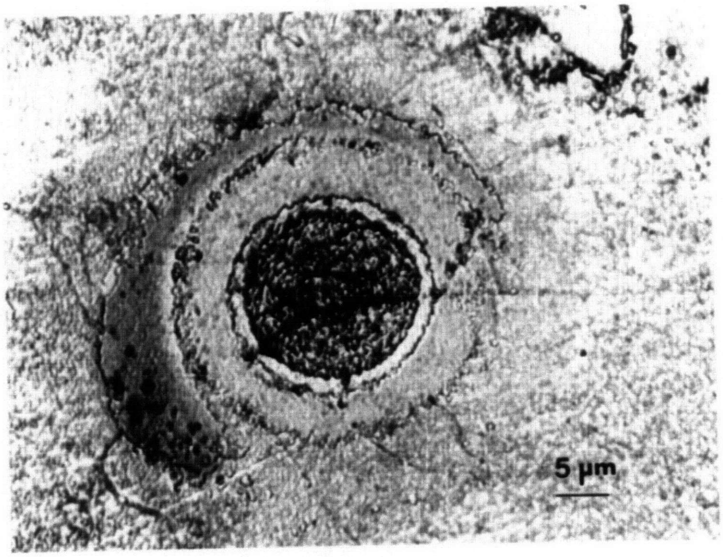

(b)

Figure 5.45 Two images of the same pit formed on Nd-Fe-B in NaCl at 23°C after 1 hour of immersion. Photograph (b) was taken at a magnification 4 times higher than photograph (a).

would be difficult to definitively conclude that the pit is located on a ribbon boundary based only on an examination of Figure 5.45 (a). However, a closer look at the same pit in Figure 5.45 (b) clearly indicates that the pit is located on a ribbon boundary. The ribbon boundary was difficult to see in Figure 5.45 (a) due to the corrosion product residue surrounding the pit, and also to the black color of the pit at lower magnification; note that an additional illustration of the large amount of corrosion product residue which can form around pits is shown in Figure 5.46. Since Figures 5.41, 5.44, and Figure 5.45 (a) were all taken at the same magnification, it appears that an even larger number of the observed pits could have been located on the ribbon boundaries than cited above. Close examination of several other pits which appeared to reside within the ribbons rather than at the ribbon boundaries showed that the situation described in Figure 5.45 was *not* occurring in every case. It must be emphasized that not all of the pits were observed to lie on the ribbon boundaries, even when viewed at relatively high magnification.

Although the observed pits were not all found to be located on the ribbon boundaries, the preferential association of pits and ribbon boundaries is evident from the micrographs shown in Figures 5.41 - 5.44. It appears that at least 36 of the 60 pits shown in Figures 5.41 - 5.44 reside on the ribbon boundaries or at ribbon triple points, which corresponds to 60% of the observed pits. This value is likely to be an underestimate of the actual degree of association between pits and ribbon boundaries, since some of the pits not considered to be located on the boundaries may have been incorrectly assigned due to corrosion product blockage.

The correlation between pits and ribbon boundaries is especially significant when it is considered that the ribbon boundaries make up only a small fraction of the total surface area shown in Figures 5.41 - 5.44. The preferential location of pits at the ribbon boundaries is clearly not a statistical phenomenon and must be considered significant. Since most but *not*

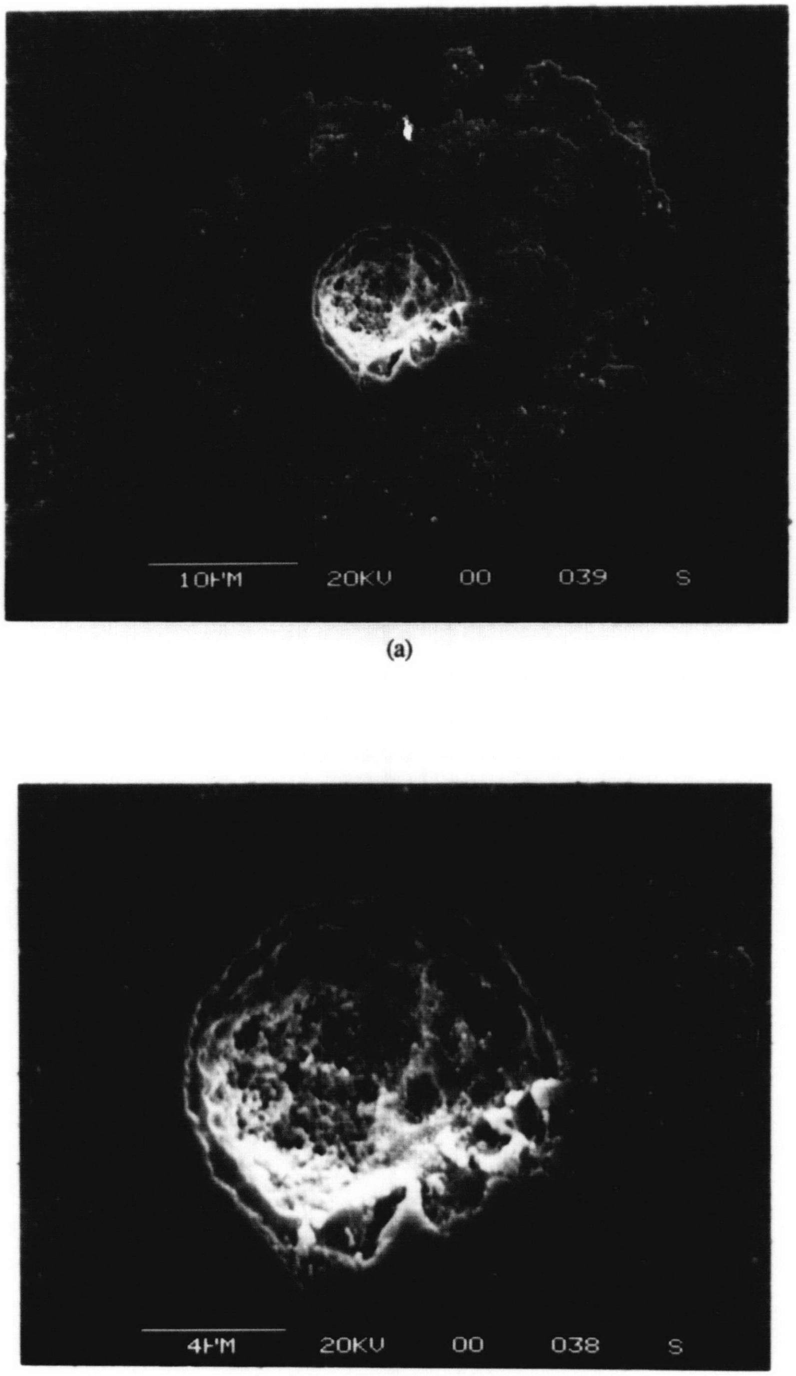
10µM 20KV 00 039 S
4µM 20KV 00 038 S

(a)

(b)

Figure 5.46 SEM photos (a) and (b) illustrating the presence of insoluble corrosion products around a pit.

all pits were observed to reside on ribbon boundaries, the relationship between the pits and the ribbon boundaries will be classified as preferential but not exclusive.

If the demonstrated association between the pits and the ribbon boundaries is not statistical in nature, then this phenomenon must be caused by a *chemical* or *physical* heterogeneity which exists preferentially (but not exclusively) at the ribbon boundaries. The heterogeneity must also exist within the ribbons themselves to a lesser extent, in order to account for the fact that some of the observed pits are not located on the ribbon boundaries. A microscopic investigation of some possible heterogeneities is discussed below.

5.4.3 Chemical Nature of the Ribbon Boundaries

It is quite possible that differences in the chemical composition of the ribbon boundaries relative to the ribbons (i.e. segregation or enrichment) might lead to the preferential initiation of pitting attack at these boundaries.

In order to examine the possible effects of alloy chemistry on pit initiation, electron probe microanalysis (EPMA) was utilized to look for chemical heterogeneities associated with the ribbon boundaries. The preferred method of comparing the composition of the ribbon boundary to the composition of the ribbons is to use an EPMA line scan, where quantitative elemental data are taken at discrete spatial intervals on either side of the boundary, as well as at the boundary itself. Analyses were performed for Nd, Fe, and Co because of their known presence in the alloy. Testing was conducted for chlorine, due to the effects of chlorides on pitting in many alloy systems; and was also performed for oxygen since this element is likely to be admitted to the system during processing. An analysis could not be performed for boron, due to its low atomic number, as previously discussed in Section 4.4. A typical line scan from an as-polished sample is shown in Figure 5.47.

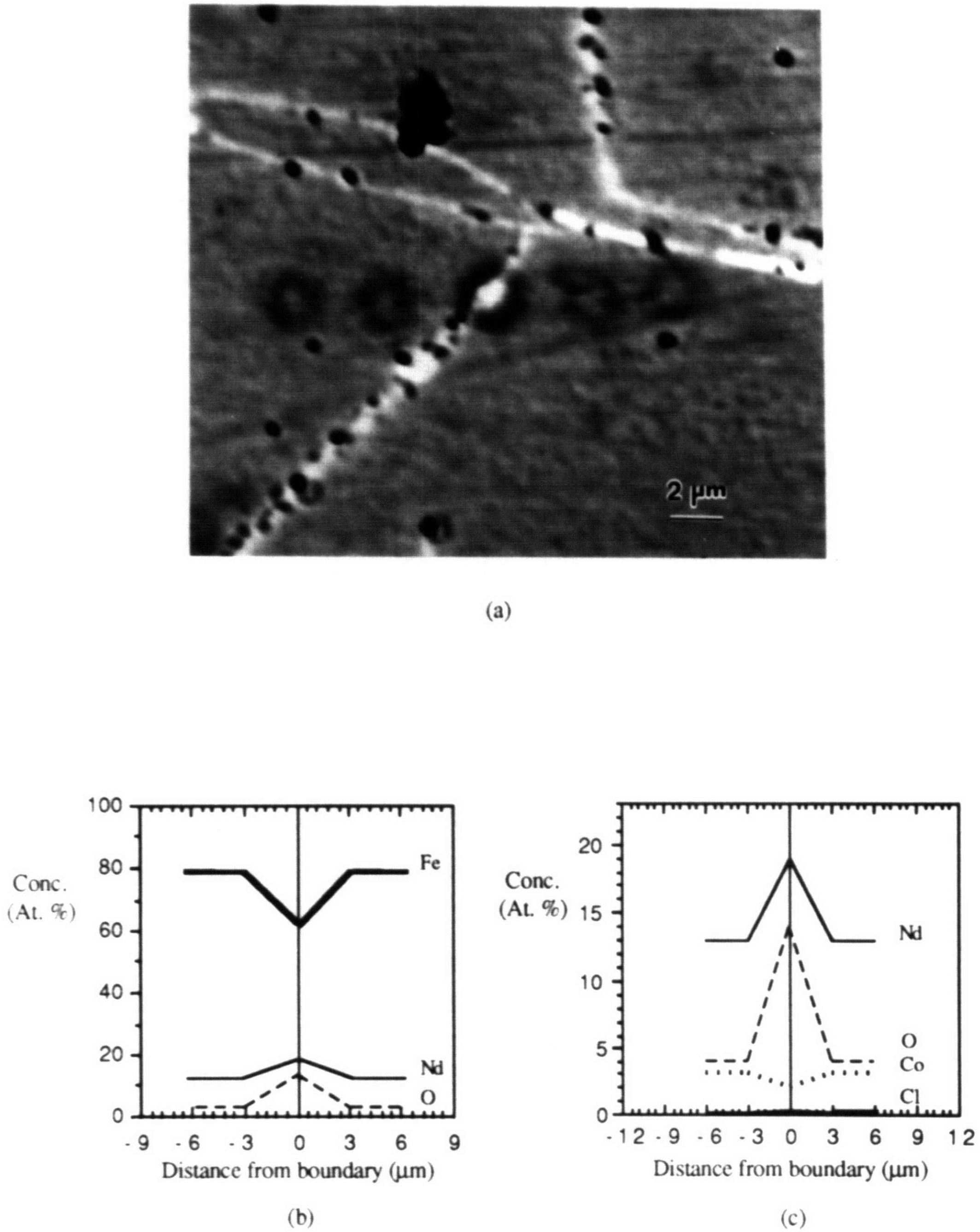

Figure 5.47 EPMA quantitative line scan across a ribbon boundary. The image shown in (a) indicates the locations of the analysis points. The obtained data are shown in (b) for Fe, Nd, and O. An enlarged view of the data for Nd and O is shown in (c), along with the data for Co and Cl.

The results of this scan indicate that chemical heterogeneities are definitely present at the ribbon boundaries. Nd and O were found to be enriched at the boundaries, while Fe was observed to be depleted (only slight changes were noted in the compositions of Co and Cl).

The actual degree of Nd and O enrichment is believed to be underestimated, since the sampling area (visible as the dot residing on the boundary in Figure 5.47 (a)) is clearly larger than the area of ribbon boundary analyzed. The measured data are thus diluted by signal derived from the ribbon itself.

Not every profiled ribbon boundary exhibited the same degree of heterogeneity, as some boundaries were found to be enriched in Nd by only 2-3 at%, as opposed to the 6 at% enrichment evident in Figure 5.47. The samples thus exhibited a distribution in the degree of heterogeneity present at the ribbon boundaries.

The white color of the ribbon boundaries in Figure 5.47 (a) is consistent with the data shown in Figures 5.47 (b) and (c); the light color is likely due to Nd enrichment. An element with a large nucleus (such as Nd) possesses a relatively high cross-section for electron scattering. Such elements generate a relatively high number of backscattered electrons, which causes areas rich in elements having a high atomic number to be light-colored. Boundaries which exhibited a lower degree of segregation than those profiled in Figure 5.47 (b) were not as light in color as the boundaries in Figure 5.47 (a).

Enrichment of an electroactive element such as Nd at the ribbon boundaries might initially seem to explain the preferential pit initiation at these sites. Galvanic corrosion could render the ribbon boundaries more susceptible to anodic dissolution than the ribbons, thus leading to pit initiation at the boundaries. Such an analysis presumes that Nd is present in its elemental state. The validity of this presumption is analyzed below.

According to the data shown in Figure 5.47 (b) and (c), the Nd concentrations were 19.4 at.% at the ribbon boundary and 12.8 at.% within the ribbons, giving an enrichment of 6.6 atomic % Nd. The oxygen concentrations were 13.3 at.% at the ribbon boundary and 4.2 at.% within the ribbons, giving an enrichment of 9.1 atomic % O. The Nd : O enrichment ratio is therefore 6.6 : 9.1, which corresponds to a ratio of 2.17 : 3. A second line scan performed across a different ribbon boundary in the same sample was found to exhibit a Nd : O ratio of 2.16 : 3. Since the stable oxide form of neodymium is the sesquioxide, Nd_2O_3 (Nd : O ratio of 2 : 3), it is strongly suspected that neodymium is present at the ribbon boundaries as neodymium (III) oxide.

The presence of Nd_2O_3 at the ribbon boundaries is consistent with the fact that after rapid solidification, each ribbon is able to oxidize at its free surface until the hot pressing process is completed. The observed distribution in the amount of Nd and O enrichment is likely due to differing amounts of oxidation undergone by each individual ribbon. The amount of oxidation exhibited by a particular ribbon would be related to its thermal history, degree of exposure to water (which is used as a cooling fluid in the process), and the time elapsed between solidification and hot pressing.

The interpretation that Nd is present in an oxide form, rather than as elemental Nd, is also supported by the observation that the ribbon boundaries themselves do not undergo uniform anodic dissolution all along the boundary length, as discussed in Section 5.3.4.4. If the ribbon boundaries consisted of elemental Nd, its electrochemical activity would likely lead to severe galvanic cell formation. The ribbon boundaries would then corrode evenly, and the ribbons themselves would eventually be undercut and drop out of the metal. It is emphasized that such attack would take the form of complete ribbon boundary dissolution (inter-ribbon attack), and not simply pit initiation at the ribbon boundaries.

5.4.3.1 Effect of Chemical Heterogeneities on Pit Initiation

It is relevant to explain how Nd oxide might or might not affect pit initiation. An oxide phase at the ribbon boundaries is unlikely to have a *chemical* effect on pit initiation, since Nd^{3+} is expected to be an electrochemically inactive species. Nd^{3+} has no thermodynamic tendency to dissolve anodically, since +3 is the preferred valence state for oxidized Nd.

In terms of physical effects, the oxide could conceivably nucleate pits due to incomplete coverage of a passive film. But as described in Section 5.3.4.2, there is no evidence that a passive film actually forms in this material under the test conditions. It is also conceivable that crevice formation could occur at the oxide/metal interface when the material is cooled at the end of the hot pressing process; no apparent separation between these two phases was noted during SEM observation.

5.4.4 Physical Nature of the Ribbon Boundaries

The physical nature of the ribbon boundaries was examined by studying as-polished samples using backscattered electron imaging in an SEM. As shown in Figures 5.48 - 5.51, a very clear physical characteristic of the ribbon boundaries is the presence of a large number of pores lying along the boundaries; pores are also located to a lesser extent within the ribbons themselves. Since these micrographs were obtained for the as-polished condition, the observed porosity is pre-existing and does not occur as a result of exposure to the corrosive environment. The fact that the black dots in these figures are pores rather than pits can be confirmed by examining the size of both features. The pores tend to be 1 - 2 μm wide or less, whereas the pits are generally 6 μm wide or more.

Pores are expected to be present in a hot pressed material. Hot pressed parts are typically

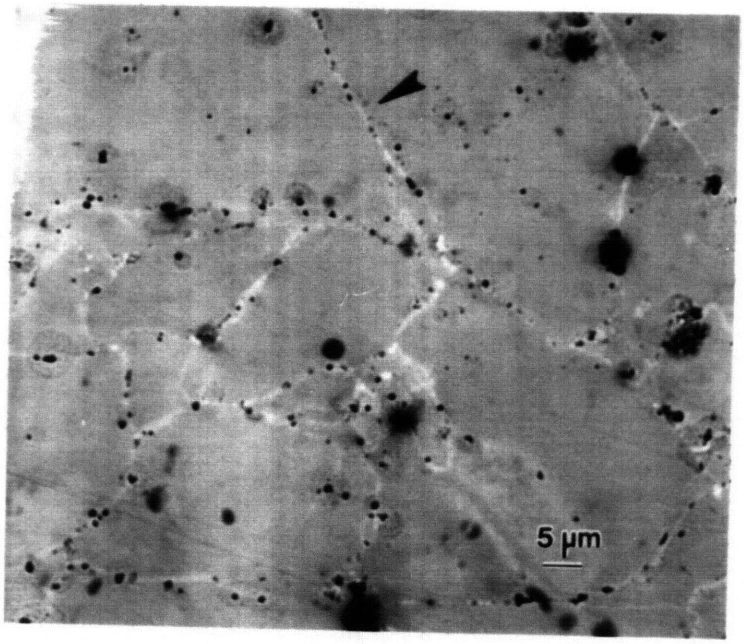

Figure 5.48 SEM image of an as-polished surface showing preexisting porosity, predominately at the ribbon boundaries.

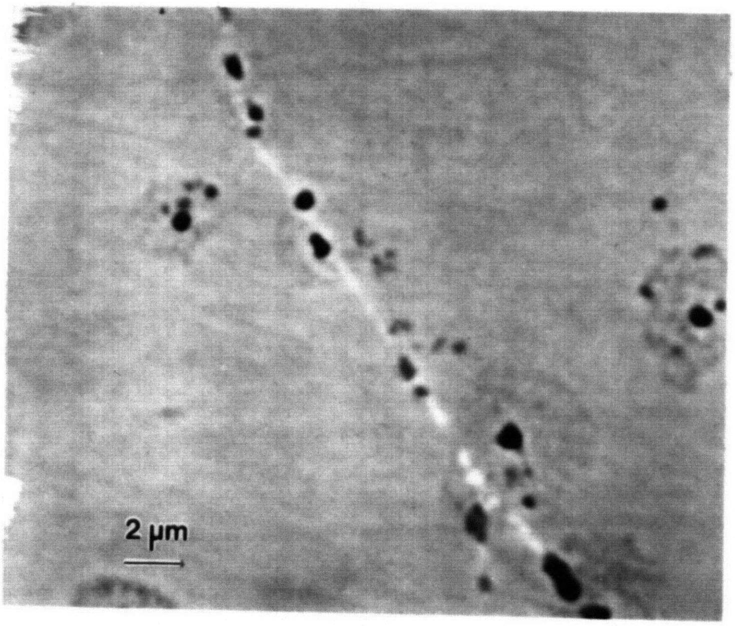

Figure 5.49 A magnified view of the the upper central portion of Figure 5.48.

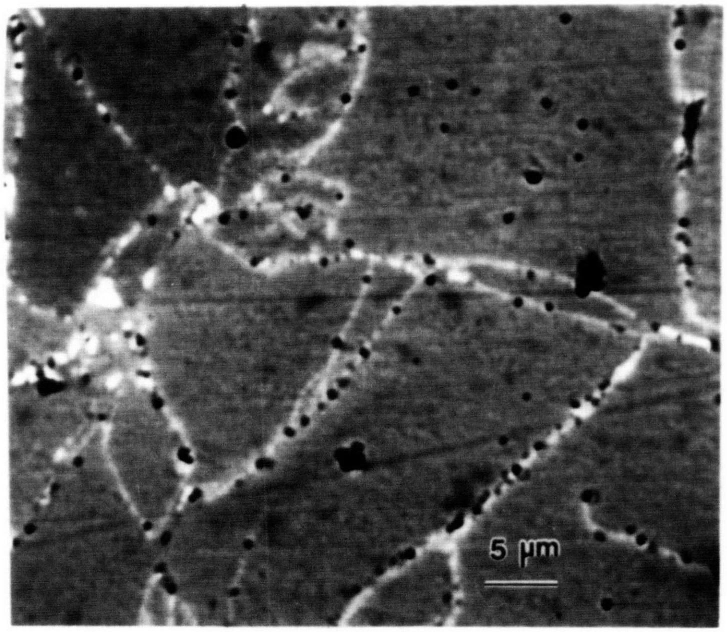

Figure 5.50 An SEM image of an as-polished sample, from a different region than Figures 4.48 and 4.49.

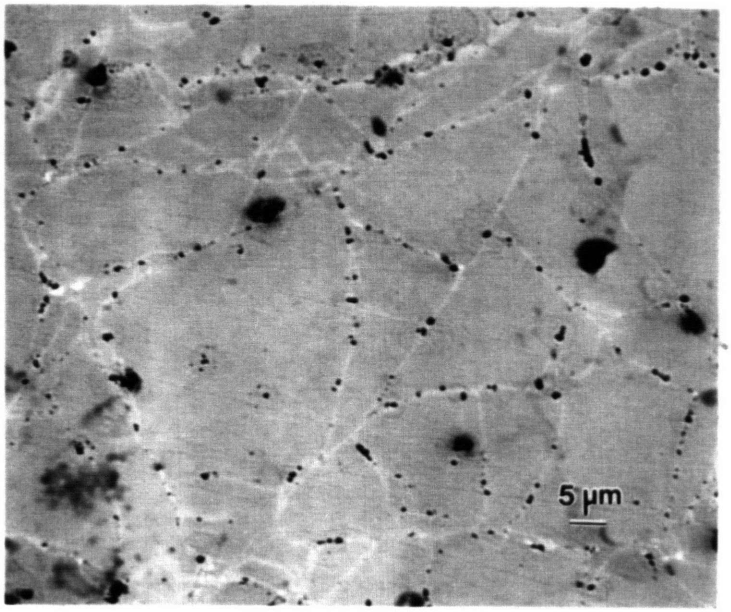

Figure 5.51 An SEM image of an as-polished region showing pre-existing pores.

porous because the precursor material inserted into the hot pressing die is rarely fully dense, as fully dense materials generally do not need to be hot pressed. Porosity results from incomplete bonding of the void spaces existing either between the separate particles of the precursor material, or within the precursor material itself. It is expected that pores should preferentially lie along the ribbon boundaries in rapidly solidified Nd-Fe-B because of the incomplete bonding between adjacent ribbon fragments during hot pressing, as discussed in Section 2.2.3.2. Pores are also located to a lesser extent within the ribbons. The intra-ribbon pores may be caused by argon gas entrapment in the descending molten alloy stream during rapid solidification, for example, or by shrinkage which occurs during the liquid-to-solid phase transformation.

Examination of Figures 5.48, 5.50, and 5.51 indicates that approximately 74% of the pores visible in these photographs appear to lie on the ribbon boundaries. This figure is clearly reminiscent of the approximately 60% of the pits which seem to reside on the boundaries. It is quite possible that the pre-existing pores may be involved in the pit initiation process.

5.5.5 Proposed Pitting Mechanism

In view of the preferential association between pits and ribbon boundaries, the appearance of preferential porosity on ribbon boundaries may have signficant implications regarding the mechanism of pitting in Nd-Fe-B. A possible pitting mechanism is discussed below.

A proposed pitting mechanism for the Nd-Fe-B alloy must be able to account for two characteristics of this system which are not typical of classical pitting: the occurrence of pitting attack in Na_2SO_4 as well as in NaCl solutions and the presence of surface dissolution in addition to pitting attack at long immersion times (Section 5.4). The proposed mechanism must additionally incorporate the fact that pit initiation has been shown to take place preferentially but not exclusively on the ribbon boundaries.

Formulating a reasonable explanation of the pitting attack observed in this system does not appear to be a simple task. Most of the accepted pitting theories described in the corrosion literature require the presence of an aggressive halide ion (such as Cl^-) which is capable of breaking down the passive film on the surface of the metal, thus initiating localized corrosion. Mechanisms in this category do not appear to apply to the present system, since pitting occurs both in the presence and in the absence of aggressive Cl^- ions.

Most accepted pitting theories additionally postulate the existence of a passive film on the surface of the metal. Since it appears that the surface of Nd-Fe-B is dissolving in the active state rather than in the passive state, as described in Section 5.3.4.2, mechanisms which rely on the existence of a passive surface film do not appear to apply to the present system.

Since many of the classical pit mechanisms do not seem to pertain to the system under study, it may be difficult to begin the procedure by trying to fit the available information to one of the established mechanisms. It may be more prudent to go directly to the experimental data in order to gain some insight into possible pitting mechanisms for this alloy. Information such as pit initiation sites may provide direction in the attempt to devise a viable pitting mechanism for this alloy system.

5.4.5.1 Hypothesis of Microcrevice Formation at Pores

The presence of pre-existing pores within the ribbons and especially at the ribbon boundaries has been established by Figures 5.48 - 5.51. It is relevant at this point to examine the question of how the pores might be acting as pit initiation sites.

It is conceivable that localized attack can initiate on a porous metal due to the formation of pore-related weak spots in a passive film present on the metal surface. However, such an explanation is not consistent with the view that the surface of Nd-Fe-B is in the active state rather than in the passive state. As discussed previously, mechanisms which rely on the existence of a passive surface film are likely unsuitable for application in this work.

A possible effect of porosity on pit initiation is that pores may be serving as microcrevice sites which can initiate localized corrosion. A small volume of electrolyte will enter each pore when the metal is immersed in the test solution. Restricted mass-transfer of anodic dissolution products out of the pores can lead to localized compositional changes within the pores, as discussed in Section 4.3.4 and Appendix 10.1.1. The pore solution may become more aggressive with time, and it is possible that the resulting concentration changes will lead to the initiation of a microcrevice in the form of a pit. The locally attacked areas would then appear visually like pits (owing to the approximately circular cross-sections of the pre-existing pores) but would have initiated as microcrevices. Such a mechanism has previously been postulated in other metal-electrolyte systems [71], and it was subsequently stated by Smialowska [72] that the notion of pit initiation via microcrevice formation at pore sites might be correct under certain conditions.

In order for the pore-microcrevice hypothesis to be plausible in the Nd-Fe-B system, the characteristics of the current pitting corrosion must be consistent with the characteristics of crevice corrosion; in other words, the observed pitting corrosion must actually resemble crevice corrosion in character. In fact, as shown in Table 5.8, the characteristics of the Nd-Fe-B system are actually more consistent with crevice corrosion than with pitting corrosion, as crevice corrosion is more likely to occur on non-passive metals and in Cl^--free solutions than is pitting corrosion. The notion that pits are initiating as microcrevices at pre-existing pore sites also qualitatively agrees with the rapid pit initiation observed in

Table 5.8 Likelihood of the occurrence of pitting and crevice corrosion under certain conditions [72].

	On non-passive metals	In chloride-free solution
Pitting Corrosion	Unlikely	Unlikely
Crevice Corrosion	Occasionally	Occasionally

this study (< 15 minutes), as crevice corrosion is known to initiate more rapidly than pitting corrosion [72].

It appears that microcrevice formation at pre-existing porosity is consistent with some of the observed characteristics of the present system. The possibility that pits are initiating by a microcrevice mechanism at pre-existing pore sites is referred to in the rest of this chapter as the pore-microcrevice hypothesis. Because of the apparent consistency of this type of pit initiation with the observed characteristics of the present system, the pore-microcrevice hypothesis will be subjected to further analysis, as discussed below.

The distribution of the proposed microcrevice sites (pores) appears to be capable of accounting for the observed distribution of pits, as approximately 74% of the pores and 60% of the pits were found to be located on the ribbon boundaries. The fact that a significant number of pits were *not* found to initiate on the boundaries is a potential obstacle to associating pit initiation with any particular characteristic of the ribbon boundaries. The presence of a substantial number of pores within the ribbons themselves, however, demonstrates that pores *are* able to account for both types of initiation sites.

A very important aspect of the pore-microcrevice hypothesis is its ability to rationalize the formation of pits on an active (rather than a passive) surface. Existing pitting mechanisms rely on the localized breakdown of a passive film, and are generally inconsistent with the presence of surface dissolution. The pore-microcrevice hypothesis does allow for surface dissolution, however. The entire metal surface is believed to be actively corroding, with the rate of local attack within the pores greater than the rate of attack at the surface, as a result of the concentration changes (within the localized solution) produced by restrictions on the mass transport of metallic cations out of the microcrevice. Alternative pitting mechanisms, in fact, do not appear to be capable of explaining why pitting would occur at all on an active surface such as Nd-Fe-B. In other words, it is not clear why corrosion would be localized on such a surface, unless a mechanism such as the pore-microcrevice hypothesis were operative. One of the strongest supports for the pore-microcrevice hypothesis is the fact that it can explain the appearance of pits on a material which is not believed to form a protective surface film; these two observations are often mutually exclusive.

The pore-microcrevice hypothesis is additionally capable of rationalizing the presence of pitting in Na_2SO_4 solutions. The concentration changes which are postulated to develop within the pores (thus leading to pit initiation) can occur in SO_4^{2-} solutions as well as in Cl^- solutions. The more rapid rate of localized attack observed in NaCl than in Na_2SO_4 can be attributed to the known fact that the intensity of crevice corrosion increases with increasing Cl^- concentration in the solution [73]. Pitting in SO_4^{2-} solutions is not readily explained by classical pitting mechanisms, since the SO_4^{2-} ion is normally not capable of initiating localized corrosion by breaking down a passive film.

Pitting in SO_4^{2-} solutions has been attributed in the past to the formation of an incomplete or discontinuous *air-formed* film on the surface of the metal prior to immersion in the test solution; attack is believed to occur at bare spots where the air-formed film does not cover the metal surface [72]. Localized corrosion thus results from the inhomogeneous nature of the air-formed film. This type of mechanism, however, inevitably results in short-term pitting corrosion which eventually becomes general corrosion (i.e. pits only propagate for a limited amount of time, and corrosion then becomes uniform in nature) [72]. Such attack is not consistent with the long-term pit propagation observed in the present study.

The information presented in the previous paragraphs seems to indicate that the pore-microcrevice hypothesis is consistent with the observed pitting corrosion. It is relevant at this point to consider how pores might be acting as sites of microcrevice formation.

The specific geometry exhibited by an occluded region is known to be a primary factor in the determination of whether or not the initiation of crevice corrosion will occur [74,75]. The likelihood of crevice initiation increases greatly as the size of the crevice mouth decreases and/or the depth of the crevice increases. The particular influence of crevice geometry on the initiation of localized attack is usually attributed to the effects of diffusion. Crevices with narrow openings, for example, would be expected to offer a significant hindrance to metal cations attempting to diffuse out of the local region. If the cations cannot readily diffuse into the bulk electrolyte, the concentration of metal cations will increase within the local region, leading to hydrolysis which will increase the aggressiveness of the localized solution; such a process may result in crevice initiation. In general, either a constriction at the mouth of the crevice or a very long diffusion path (or both) would be expected to be necessary in order for crevice corrosion to occur. An important test of the microcrevice hypothesis is a determination of whether or not such geometry can be produced at a pre-existing pore site.

Most of the pores in RSP Nd-Fe-B appear to be roughly spherical in nature, with an average diameter of about 2 μm or less (the spherical geometry likely results from the fact that this configuration represents the lowest surface energy state for a given pore). Such pores do not appear to be large enough to comprise what would be considered a "long" diffusion path; it is thus relevant to consider whether or not a constricted geometry could result from a pore which is spherical in shape. It is believed that such geometry *can* be produced from a spherical pore, as described below.

The h.p. and d.u. Nd-Fe-B magnets are fabricated to net shape via a machining or grinding treatment. Owing to the inherent porosity of this material, the surface of the magnet is expected to be porous at the conclusion of such a metal removal process. Each pore which intersects the newly formed surface will present a certain geometry to the surface, and thus to the electrolyte if the magnet is exposed to an aqueous solution. It is this geometry that will dictate whether or not a particular pore can initiate crevice corrosion, and it is therefore relevant to examine some different types of pore geometry which would be expected to result.

For each pore which intersects the surface after machining or grinding, the geometry of the pore presented to the electrolyte is governed by the amount of the pore which was removed by the machining or grinding treatment. If the machining process removes half of the pore, for example, a hemisphere will be presented to the electrolyte. If most of the pore is removed by machining or grinding, a shallow, bowl-shaped pore would be the result. If only the *very tip* of a particular pore were shaved off by metal removal, however, a pinhole-type opening will essentially be created, with a nearly full pore underneath the surface of the metal. The underlying pore would be connected to the electrolyte only through this "pinhole". Such geometry would perhaps be capable of serving as a crevice site, since the electrolyte and the pore would only be connected by a very small opening.

The actual geometry which would be expected to result from such a configuration is analyzed below.

If the tip of a pore has been removed by a machining or grinding treatment, the resulting "pinhole" should appear as a very small circular pore on an in-plane view of the machined or ground surface. Two micrographs of as-polished samples are shown in Figures 5.52 and 5.53. It can be seen that the larger pores are circular in shape with a diameter of about 2 μm or less, as stated above. Small pores do exist in each photograph, however, as marked by the letter "s". These small pores appear to be approximately 0.5 μm in diameter.

The size of a pore, as observed on a two-dimensional surface, is controlled by both the actual size of the pore and its plane of intersection with the surface. A pore which is smaller than 2 μm in cross-section can thus appear that way for two reasons: (a) it represents a larger pore which was cut at a point far from its center, or (b) it represents a smaller pore cut near its center. It is logical to believe that a pore size distribution exists in this material, since there appears to be no compelling reason why all pores should be the same size. Some of the pores marked "s" in Figures 5.52 and 5.53 may thus appear small in the micrographs because they actually are small pores.

It is also logical to believe that a certain fraction of the pores which appear small in cross-section represent larger pores whose tips have been removed by machining. A surface produced by machining will intersect thousands of pores in a typical sample, and a statistical distribution of intersection points indicates that a small fraction of these pores will be intersected by the machining treatment such that only their tips are removed.

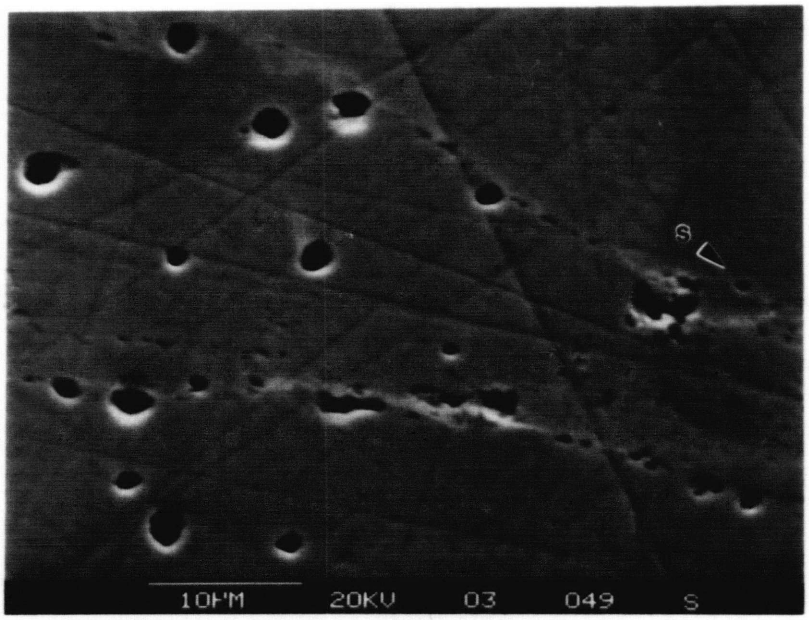
S
10µM
20KV
03
049
S

Figure 5.52 Secondary electron image of an as-polished Nd-Fe-B sample. The label "s" designates a small pore.

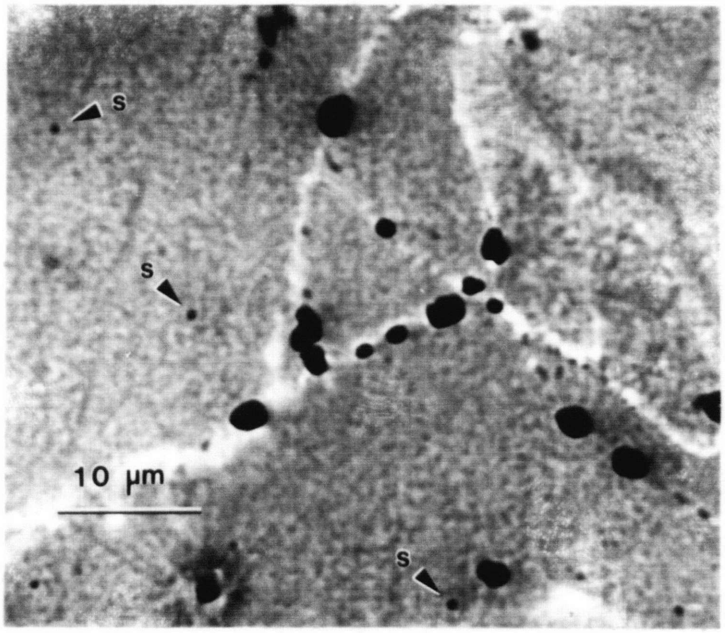

Figure 5.53 Backscattered electron image of an as-polished Nd-Fe-B surface. The label "s" designates a small pore.

It is instructive to assume for the moment that one of the small pores shown in Figures 5.52 or 5.53 is actually the tip of a larger pore (the larger pore in this case will essentially reside under the metal surface, except for the small "pinhole" connection). Since the average diameter of a large pore is approximately 2 μm and the cross-sectional diameter of the proposed "pinhole" is approximately 0.5 μm, the expected cross-sectional geometry of such an arrangement can be mapped in an attempt to qualitatively evaluate the type of geometric constriction obtained. Using the approximate measurements obtained from the micrographs in Figures 5.52 and 5.53, a schematic representation was constructed to represent the expected cross-section of a large pore whose tip had been removed by machining, as shown in Figure 5.54. The schematic was then rotated to the vertical position in order to provide an alternative view of the obtained geometry, as shown in Figure 5.55.

Figures 5.54 and 5.55 appear to indicate that a significant constriction *would* be formed by such a geometry. It is emphasized that the dimensions used in the construction of the schematics were estimates obtained from the micrographs shown in Figures 5.52 and 5.53.

It is important to qualitatively evaluate whether or not pores possessing the geometry shown in Figures 5.54 and 5.55 might be capable of initiating crevice attack. According to the pore-microcrevice hypothesis, the interior of the pores are corroding in the active (rather than the passive) state immediately upon immersion. In many crevice corrosion situations, the interior walls of the crevice are corroding at a passive current density (usually 1 μA/cm^2 or less). Since the pore walls in the present case are presumed to be in the active state, they will be corroding at the metal's corrosion current density, which has been measured as 39 μA/cm^2 in Section 5.1. A comparatively large number of metal cations per unit time should thus be formed within the occluded cell in the present work, leading to a rapid increase in the local concentration of metal cations. Hydrolysis will be strongly favored by such a

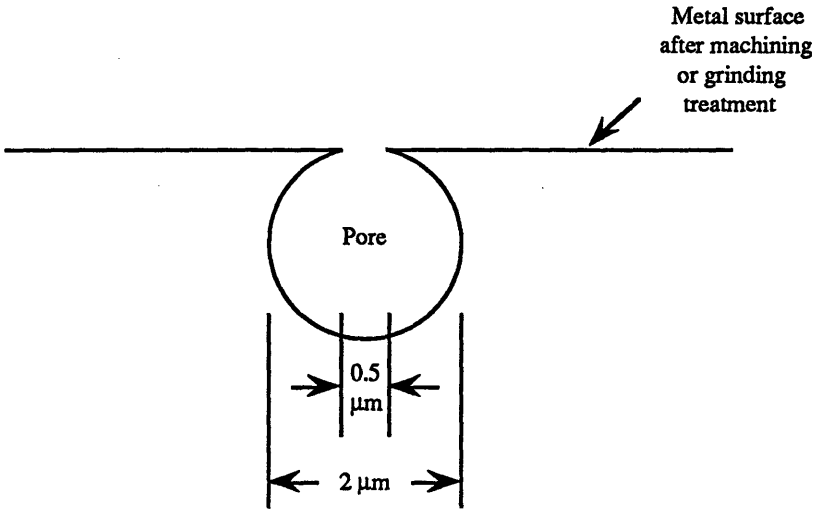
Metal surface after machining or grinding treatment
Pore
0.5 µm
2 µm

Figure 5.54 Schematic representation (drawn to scale) of a pore whose tip has been removed by machining. Dimensions were taken from the micrographs in Figures 5.52 - 5.53.

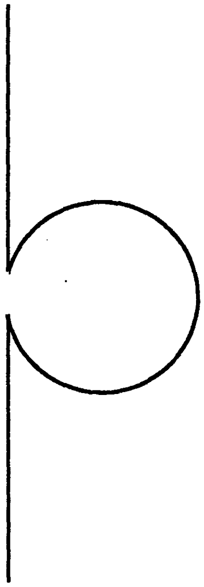

Figure 5.55 Vertical representation of the schematic shown in Figure 5.54.

state, and acidification would be expected to occur much more readily in the present case than if the pore walls were corroding in the passive state. When these expected concentration changes are coupled with the constricted geometry shown in Figures 5.54 and 5.55 (which should effectively reduce the rate of mass-transfer of metal cations out of the pore), it becomes apparent that such a pore configuration may be capable of serving as a site for microcrevice initiation.

Only a small fraction of the pores intersecting the machined surface would be expected to exhibit the geometry shown in Figure 5.54. The fact that the constricted geometry is predicted to be obtained by only a small fraction of the pores intersecting the machined surface is *not* considered to be a limitation or a drawback of the proposed initiation sites. In fact, the small fraction of pores which would exhibit the constricted geometry is in excellent qualitative agreement with the fact that the great majority of the pores on the Nd-Fe-B surface are *not* found to initiate pits. It can be seen that the proposed initiation sites are capable of not only answering the question of how constricted geometry can be formed by spherical pores, but are also capable of explaining how pores can serve as microcrevice sites without pits being initiated at every pore.

As discussed above, it is believed that a pore size distribution exists in this material. Many of the larger pores in Figures 5.52 and 5.53 are approximately 2 μm in diameter, but many pores with smaller diameters are also apparent on the metal surfaces. In Figure 5.49, for example, several pores which are approximately 1 μm in diameter are present in the top half of the image. A pore possessing a diameter of less than 2 μm in cross-section can actually be part of a larger pore which was cut at a point far from its center, as discussed above. It is believed, however, that many of these pores are simply not as large in size as the 2 μm pores.

It is relevant to consider how a pore which is smaller than 2 μm would affect the proposed microcrevice initiation sequence. Since several 1 μm diameter pores were shown in Figure 5.49, the smaller pore size will be assumed as 1 μm for the purposes of this analysis. It turns out that the smaller (1 μm diameter) pores would actually appear to form a more severe geometry and thus act as better crevice-forming sites than the 2 μm pores shown in Figures 5.44 and 5.45. An explanation of this point is given below.

Many of the smaller (1 μm) pores will intersect the machined surface, and it is statistically expected that a small fraction of these pores would have only their tips removed by machining; a certain percentage of the 1 μm pores would thus form the same type of constricted geometry shown in Figures 5.54 and 5.55. The primary difference between the constricted pores in Figures 5.54 and 5.55 and the constricted pores expected to form on smaller (1 μm) pores is their size. The 2 μm pores would be expected to have a longer diffusion path, which normally would be expected to increase the likelihood of crevice formation. However, the diffusion path is believed to be too short in either case to act as a significant barrier to mass-transfer. If the pore-microcrevice hypothesis is correct, it appears that the mass-transfer barrier would have to be associated with a geometric constriction rather than with a long diffusion path. Since the same type of constricted geometry can presumably form on 1 μm pores as on 2 μm pores, it is considered that the barrier to mass-transfer is not very different for the two pore sizes. The concentration of metal cations which can develop within these different pore sizes *can* be very different, however, as described below.

Using a spherical approximation, the internal surface area of a 2 μm pore will be 4 times larger than the internal surface area of a 1 μm pore. Since the amount of metal cations dissolved is directly dependent on the magnitude of the exposed area, four times as many cations should be produced within the 2 μm pore as within the 1 μm pore (assuming the same corrosion rate for both pore sizes). However, the key parameter from the standpoint of driving a hydrolysis reaction is the *concentration* of metal cations within the localized geometry. This parameter depends both on the total number of cations present within the local area, and on the volume of the occluded region. Using a spherical approximation, the volume of the 2 μm pores is found to be 8 times as great as the volume of the 1 μm pores. This result indicates that the concentration of metal cations within a 1 μm pore will be twice as high as the concentration developed within a 2 μm pore (note that this value is a slight overestimate because the shorter diffusion path and the higher cation concentration in the 1 μm pores would lead to a somewhat greater rate of metal cation diffusion out of the pore).

The above analysis indicates that, all other parameters being equal, the electrolyte within a smaller pore should contain a higher concentration of metal cations, and should ultimately undergo more severe hydrolysis than a larger pore with identical geometry; the smaller pores are then expected to serve as more effective sites for microcrevice initiation.

The strong hydrolysis exhibited by Cl^--containing solutions was mentioned in Section 5.2 as a rationale for the larger pit depths observed in NaCl relative to Na_2SO_4. For a solution which does not exhibit the same strong hydrolysis as NaCl (such as Na_2SO_4), the existing pore geometry would likely have to be more favorable for crevice initiation than it would be for NaCl. In other words, the metal cation concentration would likely have to be higher in Na_2SO_4 than in NaCl in order to produce the same degree of hydrolysis. It is possible that the metal cation concentration within a pore in Na_2SO_4 may only become sufficient to intiate localized corrosion if the pore volume is very small. It is therefore qualitatively reasonable that smaller pores may serve as the initiation sites in Na_2SO_4.

The microcrevices initiated at pores would resemble pits in shape, due to the general similarity between the proposed pore sites and pits. Pits will eventually tend to develop a hemispherical shape, presumably because of the fact that the corrosion product caps found atop the pits create a diffusion barrier; hemispherical shapes are associated with pit growth processes controlled by diffusion, according to Smialowska [72].

The pore-microcrevice hypothesis has been shown to be consistent with many of the seemingly ubiquitous features of the observed pitting corrosion. The intersection between pores and the machined surface has been postulated to result in a small fraction of pores which possess a constricted geometry. This postulated geometry is capable of explaining how microcrevices might initiate at pores sites, and can additionally rationalize the fact that most of the pores present on the surface of the metal are *not* found to initiate pits. Despite the large amount of persuasive evidence supporting the pore-microcrevice hypothesis, it is still not possible, based only on the above argument, to conclude that constricted pores are definitively serving as sites of microcrevice initiation.

It is believed that the microcrevice hypothesis should be evaluated both theoretically and experimentally. A theoretical study of the microcrevice formation can be accomplished by modeling the chemical and electrochemical conditions likely to exist within a constricted pore. An understanding of the prevailing conditions within these pores after 15 minutes of immersion in the test solution should provide a reasonable basis for determining whether or not the pores are likely to serve as initiation sites for localized corrosion. The microcrevice hypothesis can be evaluated experimentally by using improved hot pressing procedures to produce a fully dense (pore-free) starting material. Corrosion testing of this fully dense material can then be performed. It is hoped that the results of such experiments would conclusively prove (or disprove) the microcrevice hypothesis. Such experiments would also have the added benefit of indicating whether corrosive attack can be mitigated by using improved hot pressing procedures.

6. Environmentally-Assisted Cracking

Environmentally-assisted cracking (EAC) can be an important degradation mechanism for materials in many different applications. The cracking of a metallic member, for example, often represents a significant problem for an engineering structure. Cracking of pipes or tubes can lead to fluid leakage, or to a loss of system pressure which can result in costly plant shutdowns. Even though a permanent magnet is not expected to serve as a structural member or as a carrier of corrosive fluid, EAC can be a very significant mechanism of degradation for such a material. The generation and propagation of cracks in a magnet could lead to partial or total fracture of the metal. Such cracking would present a very serious problem for the engineering utility of a magnetic material, since a substantial loss in magnetic flux would be expected to result if large pieces were to crack and fall off of the bulk magnet. Several additional factors make EAC undesirable in a permanent magnet system. For example, it is unlikely that cracking would be preceded by any type of warning. In fact, cracking would probably not be detected until the component in which the magnet is used (e.g. a motor) was observed to fail. It is generally not possible to design for EAC, and expensive magnet replacement may be the only logical recourse after component failure.

EAC is a concern only for certain materials in specific environments. It is critical to determine if a material is susceptible to EAC under the expected conditions of exposure before placing it into service. During this investigation, Nd-Fe-B samples were observed to crack under certain conditions, which indicates that EAC *may* represent a significant in-service engineering consideration for this material. Such a concern is especially relevant in view of the fact that cracking has also been observed in salt spray tests conducted by Magnequench®, the primary manufacturer of RSP Nd-Fe-B [76]. The present chapter is thus concerned with a detailed evaluation of the EAC behavior of the Nd-Fe-B alloy.

6.1 Observation of Environmentally-Assisted Cracking (EAC)

A significant component of the present research project, which will be described in detail in Section 7.1, was the evaluation of sacrificial zinc coatings as a potential corrosion control method for Nd-Fe-B. The alloy was found to exhibit susceptibility to EAC during the zinc coating investigation, as discussed below.

In the zinc coating evaluation, the Nd-Fe-B alloy was either left at open-circuit to corrode freely, or was galvanically coupled to zinc. The open-circuit specimens are also referred to as uncoupled, in order to distinguish them from the samples coupled to Zn. As shown in Figure 6.1, cracking was much more rapid at the open-circuit potential than when the alloy was galvanically coupled to zinc. Both samples tested in the uncoupled condition cracked after 9 days in solution, one sample which was coupled to zinc cracked after 23 days in solution, and the other coupled sample had not cracked upon removal at 29 days. The extent of fracture in the open-circuit or uncoupled samples was also much more significant than for the coupled sample which did exhibit fracture, as shown in Figure 6.2.

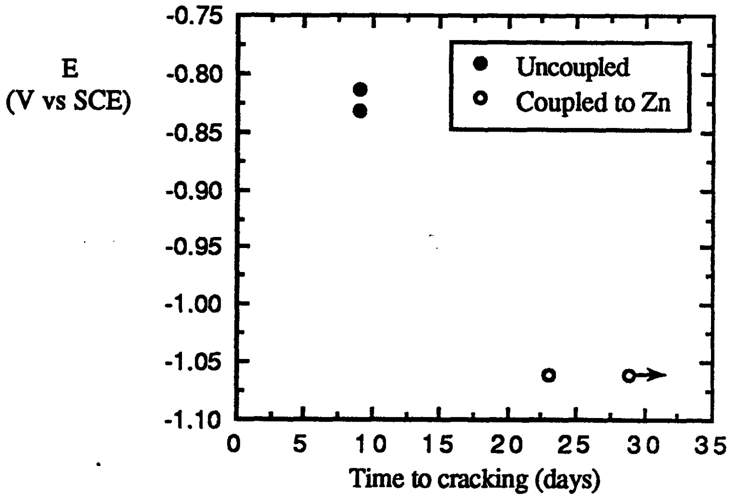

Figure 6.1 Rate of EAC of Nd-Fe-B (NaCl, 23°C) under two conditions: open-circuit (uncoupled) and coupled to Zn. The arrow represents a sample which had not cracked upon removal from the solution.

Both uncoupled samples were found to crack catastrophically into several fragments after 9 days of immersion (Figure 6.2 (a)). The damage suffered by the coupled sample which cracked after 23 days in solution was much less severe (Figure 6.2 (b)), as only a small fraction of the sample was lost due to cracking. The coupled sample which did not crack during 29 days of immersion is also shown in Figure 6.2 (b). The initial dimensions of the cracked samples were similar to the dimensions of this uncracked specimen. The samples shown in Figure 6.2 were believed to contain residual stresses from a machining treatment used to produce a common specimen diameter, as discussed in Section 6.4.2. The observed cracking could represent a substantial problem for the engineering utility of Nd-Fe-B, as cracking occurred rapidly and to a catastrophic extent under open-circuit (free corrosion) conditions. The observation of cracking in the absence of external polarization is important, since the magnet would be corroding at open-circuit in service. A further investigation of the observed cracking is clearly warranted.

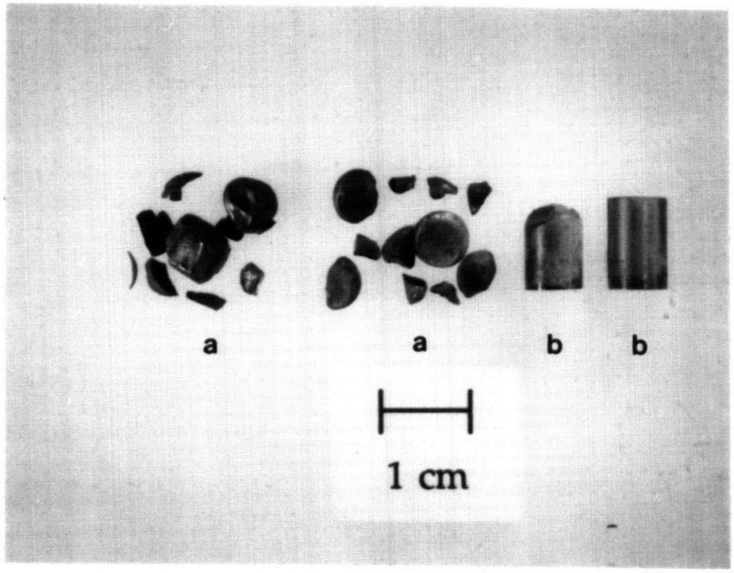

Figure 6.2 Extent of cracking exhibited by (a) uncoupled samples and (b) coupled samples after immersion in NaCl at 23°C. The uncoupled samples were removed (upon cracking) after 9 days in the test solution, and the coupled samples were removed after 29 days of immersion.

6.2 Mode of Environmentally-Assisted Cracking

An evaluation of the observed EAC should begin with an attempt to identify the operative mode of cracking in the open-circuit samples. If the mode of fracture can be determined, it may be possible to prescribe a course of action designed to mitigate cracking failures. Two primary modes of EAC can be defined: hydrogen-assisted cracking (HAC) (also known as hydrogen embrittlement), and a general type of anodic cracking defined by Wilde [77] as active path cracking (APC). Active path cracking includes such anodic EAC mechanisms as stress-corrosion cracking and corrosion product wedging .

The rate of cracking was higher for the Nd-Fe-B samples at open-circuit than for samples which were cathodically polarized (Figure 6.1). A comparison of the rates of both hydrogen production and anodic dissolution on both types of samples would initially *appear* to be capable of indicating whether HAC or APC is the likely cause of cracking in the open-circuit samples. Attributing a given failure to HAC or APC solely on the basis of hydrogen production and anodic dissolution rates is not recommended, however, since it has been demonstrated in the past that the operative mode of EAC *cannot* be conclusively determined using such evidence [77-78]. Comparing the rates of hydrogen production and anodic dissolution *will* provide a valid starting point for the HAC/APC analysis, though the mode of EAC must be determined using the hydrogen permeation method (Section 6.2.3).

Since hydrogen production is generally stimulated by cathodic polarization, less hydrogen is expected to be produced on the bulk surface of Nd-Fe-B at open-circuit than on the surface of coupled Nd-Fe-B. The rate of hydrogen production under both conditions can be estimated by the extrapolating the lower portion of the Nd-Fe-B cathodic polarization curve to both its corrosion potential (-0.825 V) and the galvanic couple potential (-1.05 V), as shown in Figure 6.3. According to Table 6.1, the quantities of hydrogen predicted to be generated are 0.6 μA/cm^2 at E_{corr} and 38 μA/cm^2 at E_{couple}.

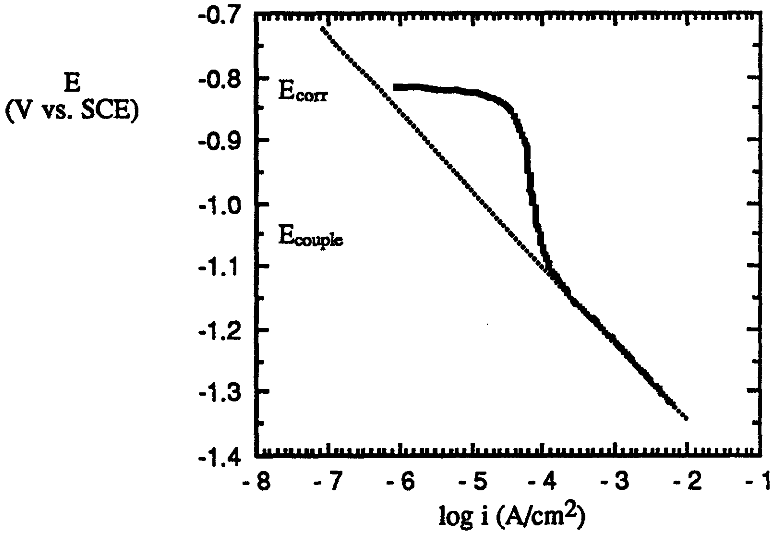

Figure 6.3 Cathodic polarization of Nd-Fe-B in NaCl at 23°C. The dashed line indicates the Tafel extrapolation of the portion of the curve corresponding to hydrogen reduction.

Table 6.1 Estimated hydrogen reduction current densities at various values of electrode potential.

E (V vs. SCE)	log i (A/cm^2)	i (μA/cm^2)
-0.750	-6.88	0.1
-0.825	-6.26	0.6
-1.050	-4.42	38.3
-1.250	-2.78	1673.4

The amount of anodic dissolution exhibited by both types of samples will be compared in Section 7.1. The open-circuit samples were found to corrode at a relatively rapid rate, but essentially no anodic dissolution was observed for the samples coupled to zinc.

Since the open-circuit samples were apparently subjected to more anodic dissolution and less hydrogen production than the coupled samples, it might *initially* seem that APC is the operative mode of cracking in Nd-Fe-B at open-circuit. A comparison of the rates of anodic dissolution and hydrogen production cannot be used to definitively conclude that APC is the controlling cracking mechanism in the open-circuit samples, however.

The primary shortcoming of the preceding analysis is that it neglects the large amounts of hydrogen which can be generated at E_{corr} (and at potentials anodic to E_{corr}) in cases where localized corrosion is present. The rate of hydrogen generation within a pit can be much greater than that predicted by the extrapolation of the cathodic polarization curve. Increased hydrogen production in pits is caused by a combination of metal cation hydrolysis and IR drop. The hydrolysis of metallic cations in an occluded corrosion cell (such as a pit) will lead to local acidification, as described in Section 4.3.4. The decrease in pH caused by hydrolysis will stimulate the production of hydrogen on the walls of the pit. Hydrogen production can also increase as a result of the IR drop which exists within a pit due to the anodic current (I) that flows through the pit electrolyte, which has a characteristic resistance (R). IR drop will cause the base of the pit to reside at a potential which is more cathodic than the measured surface potential, resulting in a greater driving force for hydrogen reduction. In some cases, the potential difference between the surface and the base of the pit is considerable [79], leading to substantial hydrogen production within the pit.

The possibility that significant amounts of hydrogen can be generated within a localized corrosion cell has important implications for the effect of electrode potential on the rate of hydrogen generation. Although it might appear to be counterintuitive at first, it is quite possible that the amount of hydrogen produced on a metal exhibiting localized corrosion may be greater than the amount of hydrogen produced on the same metal at more cathodic potentials. This possibility has been confirmed in several cases in the literature [77,80].

6.2.1 Hydrogen Production at Anodic Potentials: Literature Citations

Hydrogen permeation experiments performed by Shively et al [80] on 310 stainless steel have demonstrated the presence of significant hydrogen generation at anodic potentials in 8% HCl, as shown in Figure 6.4. In this context, the term anodic potential refers to E_{corr} and to any potential anodic to E_{corr}. All electrode potentials at which substantial anodic dissolution occurs will be referred to as anodic potentials for the remainder of Section 6.2. Conversely, the term cathodic potentials will be used to refer to potentials that are active to E_{corr}, at which little or no anodic dissolution is expected to take place.

In Figure 6.4, the hydrogen flux actually exhibits a minimum at a potential slightly cathodic to E_{corr}. The increase in hydrogen flux below (electronegative to) this minimum results from increasing cathodic polarization, and the increase in hydrogen flux above this minimum was attributed to the local generation of hydrogen within pits.

Substantial hydrogen generation has also been observed at anodic potentials by Gest and Troiano [81] on 7075-T651 Al alloys (3% NaCl), as shown in Figure 6.5. Similar data

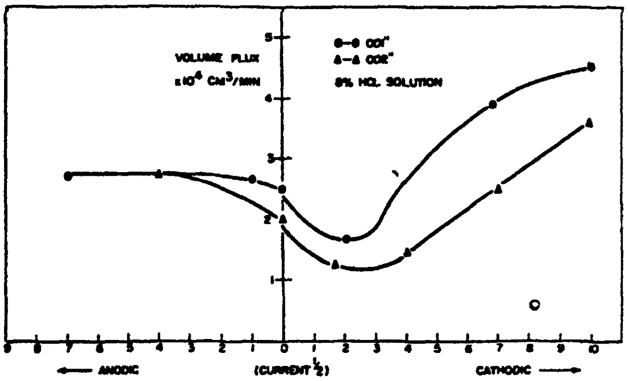

Figure 6.4 Flux of hydrogen through 310 stainless steel as a function of applied current in 8% HCl [80].

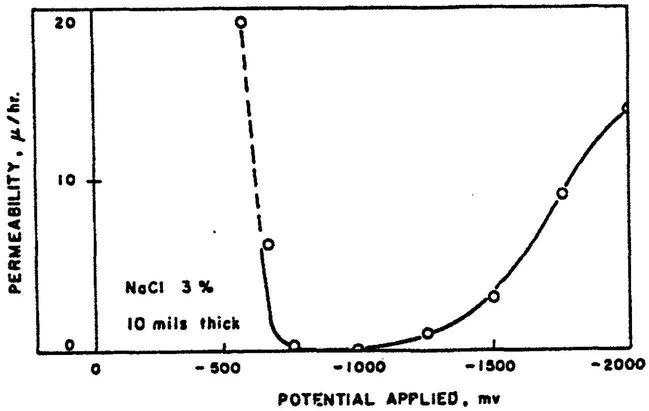

Figure 6.5 Hydrogen permeability through an aluminum alloy (7075 T-651) in 3% NaCl as a function of applied potential [81].

were acquired by Wilde [77] for 12% Cr martensitic stainless steel in 3% NaCl, and by Wilde and Kim [82] for 304 stainless steel (saturated LiCl at 146°C). The metal under test was found to suffer from pitting corrosion at anodic potentials in all three studies. In the work of Wilde [77], the addition of $K_3Fe(CN)_6$ (an oxidizing agent which is known to accelerate the rate of pitting in stainless steels) was found to significantly increase the rate of hydrogen production at anodic potentials on 12% Cr martensitic stainless steels. The correlation between pits and hydrogen generation at anodic potentials is supported by results obtained by Shively et al [80] on 310 stainless steel in 4% H_2SO_4. An increase in hydrogen flux was *not* obtained at anodic potentials in this solution (Figure 6.6), and the lack of such an increase was attributed to the absence of pitting in the H_2SO_4 solution.

The hydrogen production behavior of these materials suggests that cracking at anodic potentials can be caused by pitting-induced HAC as well as by an APC mechanism. The observed EAC at anodic potentials in several of the abovementioned studies [77,80] was believed to result from pitting-induced HAC rather than from APC.

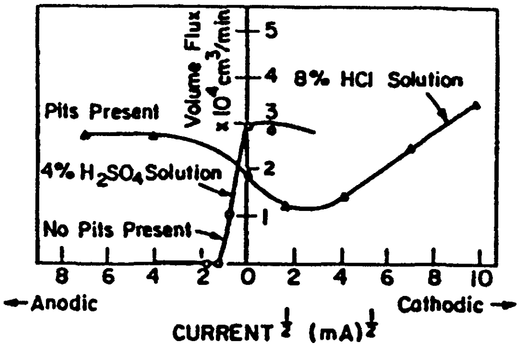

Figure 6.6 Hydrogen permeation through type 310 stainless steel as a function of applied currents in pitting and non-pitting environments [78,80,83]

It should be emphasized that the presence of significant hydrogen generation at anodic potentials can only lead to HAC if the metal itself is susceptible to hydrogen damage. The degree of sensitivity of a material to hydrogen embrittlement can be measured by evaluating its tendency to crack at cathodic potentials. Although Wilde and Kim [82] found high rates of hydrogen generation at anodic potentials for 304 stainless steel in saturated LiCl at 146°C, the material did not exhibit cracking at cathodic potentials. The mode of cracking at anodic potentials was therefore considered to be APC rather than HAC, despite the presence of substantial hydrogen in the metal lattice at these potentials.

The plot shown in Figure 6.7 was constructed by Wilde [77] in order to characterize the different types of EAC which can occur in the cathodic and anodic potential regimes. All cases of cracking at cathodic potentials were attributed to HAC, but the mode of EAC at anodic potentials is considered to be either APC or pitting-induced HAC, depending upon both the amount of hydrogen produced at the anodic potentials and the susceptibility of the material to hydrogen damage. A material exhibiting localized corrosion at anodic potentials is a possible candidate to exhibit pitting-induced HAC. The first step in assigning a failure to either APC or pitting-induced HAC is to determine the effects of potential upon cracking.

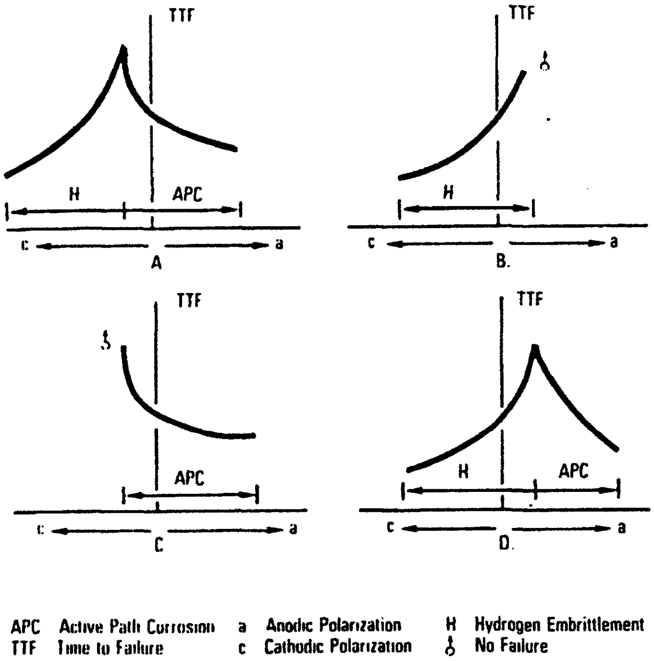
TTF
H
APC
c
a
A
B.
C
D.
APC Active Path Corrosion
TTF Time to Failure
a Anodic Polarization
c Cathodic Polarization
H Hydrogen Embrittlement
No Failure

Figure 6.7 Effect of anodic and cathodic polarization on the rates of environmentally-assisted cracking [77].

6.2.2 Effect of Potential on Cracking

In order to more clearly delineate the effects of electrode potential on the rate of EAC, testing was performed on Nd-Fe-B at two additional electrode potentials. A potential anodic to the corrosion potential was chosen (-750 mV), and a potential cathodic to the couple potential was also selected (-1250 mV). The specific values of potential were chosen such that the expected current (anodic or cathodic) was high enough to significantly drive the anodic or cathodic reaction, but not high enough to cause severe errors due to IR voltage drop. The obtained data are shown in Figure 6.8; the rate of cracking was found to be very rapid at both -750 mV and -1250 mV but minimized in the vicinity of E_{couple}.

The data of Figure 6.8 were replotted with the electrode potential on the horizontal axis in order to facilitate a correlation to Figure 6.7; the modified plot is shown in Figure 6.9.

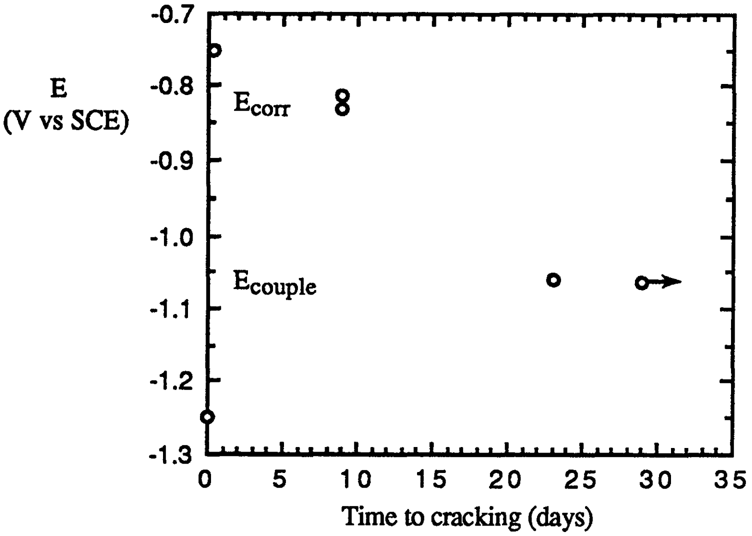

Figure 6.8 Effect of electrode potential on the rate of environmentally-assisted cracking.

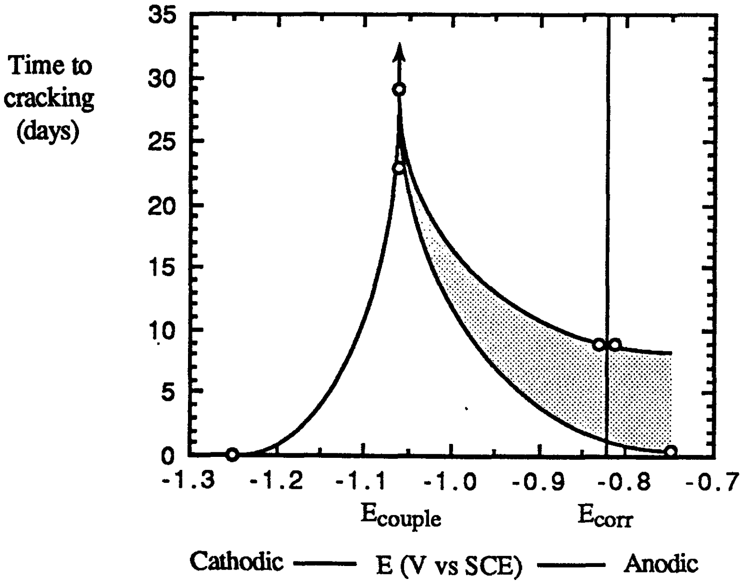

Figure 6.9 Effect of electrode potential on the rate of environmentally-assisted cracking. The data have been plotted with inverted axes for comparison to Figure 6.7.

The obtained data clearly correspond to case (a) in Figure 6.7. Wilde [77] presumed such cracking to occur by HAC in the cathodic regime and by either APC *or* pitting-induced HAC in the anodic region; the cracking observed in the present study is discussed below.

The rate of cracking was very rapid (~1.5 hours) at -1250 mV. A large amount of hydrogen was produced on the sample at this potential (as evidenced by vigorous bubble formation), but no apparent anodic dissolution occurred. The lack of apparent anodic dissolution in samples at -1250 mV (and the verified lack of anodic dissolution at E_{couple}) indicates that cracking at these cathodic potentials is unlikely to be proceeding by an APC mechanism. It appears that the sample held at -1250 mV failed as a result of HAC, as did the coupled sample which cracked after 23 days.

The rate of cracking was also very rapid (~10.5 hours) at -750 mV. The extent of anodic dissolution was substantial at this potential, as evidenced by the formation of insoluble anodic corrosion products within a few minutes of polarizing the sample. The rate of both anodic dissolution and EAC were lower at E_{corr} than at -750 mV. Enhanced anodic dissolution clearly corresponds to accelerated cracking, but it is not clear *a priori* whether the observed EAC can be attributed to APC or to pitting-induced HAC.

Pitting was verified to occur at E_{corr}, and is believed to occur at -750 mV, according to the potentiostatic polarization data presented in Figure 5.10. It is emphasized that the pitting-induced HAC mechanism at anodic potentials *is* consistent with the fact that the observed cracking rate is greater at -750 mV than at E_{corr}. Anodic dissolution is known to be a secondary but essential factor in pitting-induced HAC; more intense pitting (dissolution) gives rise to more severe local acidification and to greater IR drop, both of which increase the rate of hydrogen generation. Rapid anodic dissolution thus correlates to increased cracking rates via a pitting-induced HAC mechanism, as well as by an APC mechanism.

Nd-Fe-B was found to crack rapidly at cathodic potentials, and has previously been reported to be susceptible to hydrogen damage [49,49a]. It is emphasized that the susceptibility of Nd-Fe-B to hydrogen embrittlement, when combined with the pitting attack observed in the present study, raises the *distinct possibility* that the actual mode of fracture in Nd-Fe-B at anodic potentials is pitting-induced HAC rather than APC.

6.2.3 Determination of the Mode of EAC

The typical method of adjudicating between APC and HAC at anodic potentials is to utilize the hydrogen permeation technique described in Section 4.3.8. The input side of the metallic membrane is set to a given electrode potential and the hydrogen flux transient is then recorded. This technique allows the investigator to compare the amount of hydrogen generated (and subsequently absorbed into the material) at different values of potential. The permeation method was used to generate the data previously shown in Figures 6.4 and 6.5, and was also used by Wilde [77] to investigate cracking modes for a martensitic (12% Cr) stainless steel in a 3% NaCl solution, as shown in Figure 6.10. Since the amount of hydrogen generated at the anodic potential in the study of Wilde [77] was actually greater than at cathodic potentials, the observed EAC at anodic potentials was attributed by the author to pitting-induced HAC rather than to APC.

In most systems, the hydrogen permeation technique can be used to evaluate the mode of EAC without great difficulty, as samples can be cut from foil or sheet specimens and placed into the permeation cell after surface preparation has been completed. In the present study, however, testing was complicated by the fact that thin Nd-Fe-B specimens were not available. Nd-Fe-B wafers had to be cut from bulk sections, a process which was hindered by the repeated cracking of samples during sectioning. Even after a few thin samples were successfully cut, the small cross-section of the bulk material led to the production of wafers

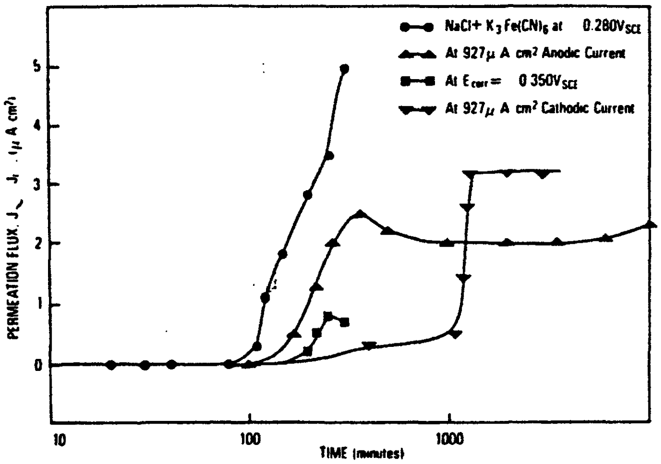

Figure 6.10 The absorption and permeation of hydrogen through a 12% Cr martensitic stainless steel in 3% NaCl at 25°C. Data were obtained using the hydrogen permeation technique [77].

which were not large enough to fit in the existing permeation cell. Nd-Fe-B wafers had to be sealed into thin polyethylene sheets using silicone resin in order that permeation testing could be performed. The entire sample preparation sequence is described in Section 4.x.x.

6.2.3.1 Results of Permeation Testing

The hydrogen permeation method was utilized in the present study to examine the effect of electrode potential on the amount of hydrogen absorbed into Nd-Fe-B. The input side of the membrane was set to one of the four conditions tested in the abovementioned cracking evaluation, and the flux transient was then recorded for each input condition.

Permeation tests were not conducted for the same length of time in all cases. The output side of the membrane tended to become ineffective at some point during the experiment, due to a sharp increase in the measured current density (which effectively ended the test by obscuring the hydrogen permeation current). Permeation transients were recorded until a current density surge occurred, and the experiment was then terminated. Fortunately, the measured current density increase was sharp enough that it could be readily distinguished from the typical hydrogen flux transient. The duration of the shortest experiment was limited to about 50 hours, while some tests were run for up to 11 days without failure.

The observed surges in current density were believed to be caused by solution ingress between the palladium coating and the silicone resin masking agent. Electrolyte which penetrates under this interface is capable of reaching the Nd-Fe-B base metal. The anodic dissolution current density on Nd-Fe-B at the output side potential (+0.5 V vs. SCE) is extremely high, and the exposure of the base metal under the masking agent would thus account for the observed increases in current density after extended immersion. This conjecture is supported by the observation of Nd-Fe-B corrosion products on the output surface after the removal of specimens for which a current surge had been observed. No evidence of Nd-Fe-B corrosion products was noted if samples were removed from the permeation cell prior to the occurrence of a current surge. Previous tests had additionally indicated that the effectiveness of the metal-silicone adhesion was often limited to a time period of a few days. The variation observed in the time to failure of this interface was likely related to differences in the quality of the application of silicone.

The results of the permeation tests are shown in Figure 6.11. As anticipated, the hydrogen flux is greatest for the cathodically polarized specimen (-1250 mV). A significantly lower hydrogen flux was observed if the input side of the sample was galvanically coupled to zinc. Since anodic dissolution does not occur under either condition (as shown for the E_{couple} samples in Section 7.1), the amount of hydrogen produced on the input side is proportional to the amount of cathodic polarization undergone by the surface. The behavior obtained for the -1250 mV and E_{couple} samples is thus qualitatively reasonable.

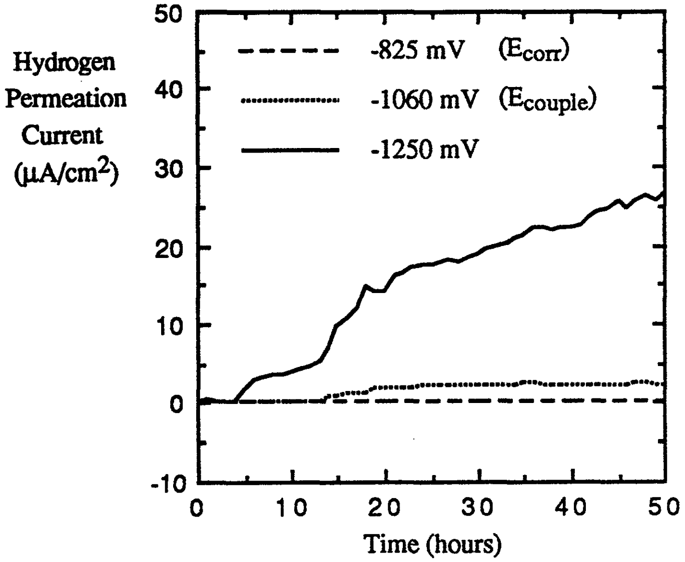

Figure 6.11 Permeation transients for three different input conditions (E_{corr}, E_{couple}, -1250 mV).

Prior to the performance of the permeation experiments, it was not clear what type of behavior would be obtained if the input side of the sample was allowed to rest at E_{corr}. Even though the bulk discharge of hydrogen ions is expected to be considerably less at E_{corr} than at E_{couple} (according to Table 6.1), the expected hydrogen generation within pits provided the significant possibility that the hydrogen permeation current might be greater for the freely corroding samples than for those coupled to zinc; such data have been previously shown for other metal-electrolyte systems in Figures 6.4, 6.5, and 6.10.

Large amounts of hydrogen were apparently *not* generated within pits on Nd-Fe-B at E_{corr}, as shown in Figure 6.11. No measureable hydrogen permeation current was detected for the E_{corr} specimen during the 50 hours of immersion shown in Figure 6.11. The E_{corr} test was actually run for 11 days without evidence of hydrogen breakthrough. Although data for -750 mV are not shown in Figure 6.11, this transient was found to be identical to that of the sample held at the E_{corr} over the 50 hour time period. Hydrogen breakthrough had not occurred after ~ 2 days in the -750 mV test, at which point a current surge occurred.

The substantial differences in hydrogen breakthrough times for different samples is likely due to the large variations in the hydrogen concentration gradients at the input side of the membrane. The amount of hydrogen produced within the pits is apparently quite small, or else the hydrogen concentration at the input side would have provided enough driving force to push the hydrogen through the membrane in less than 11 days.

The critical conclusion to be drawn from Figure 6.11 is that the amount of hydrogen produced at E_{couple} is clearly greater than the amount produced at E_{corr}. This result provides conclusive evidence that the cracking observed at open circuit does not result from pitting-induced HAC, and must therefore be attributed to some form of APC.

The APC/HAC evaluation is facilitated by integrating the permeation transient over the 50 hour time period to determine the amount of hydrogen passed through each membrane, as shown in Figure 6.12. The integrated hydrogen flux at each potential was then superimposed on the plot of cracking rate versus potential, as shown in Figure 6.13, in order to graphically demonstrate the relationship between hydrogen production and cracking rate. Figure 6.13 provides a very compact description of the rates and modes of cracking observed in the present study. Cracking at cathodic potentials (-1250 mV, E_{couple}) is attributed to HAC, while cracking at more anodic potentials (E_{corr}, -750 mV) can be ascribed to an APC mechanism.

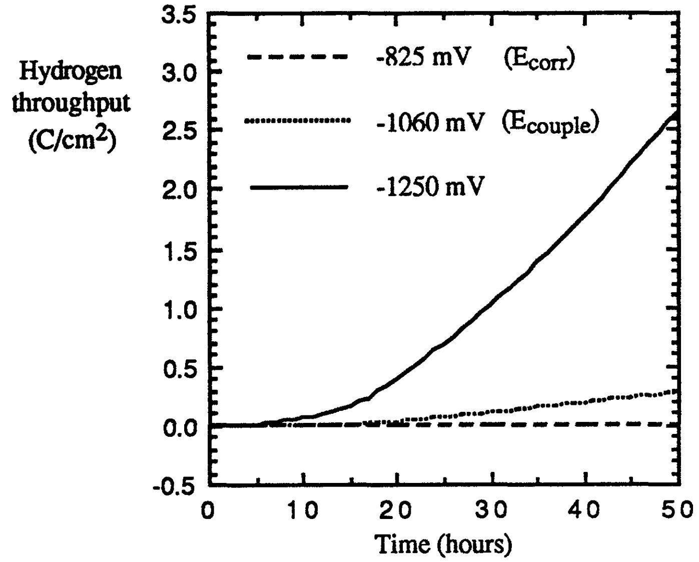

Figure 6.12 Cumulative hydrogen throughput for three different input conditions. The data were obtained by integrating the permeation transients shown in Figure 6.11 with time.

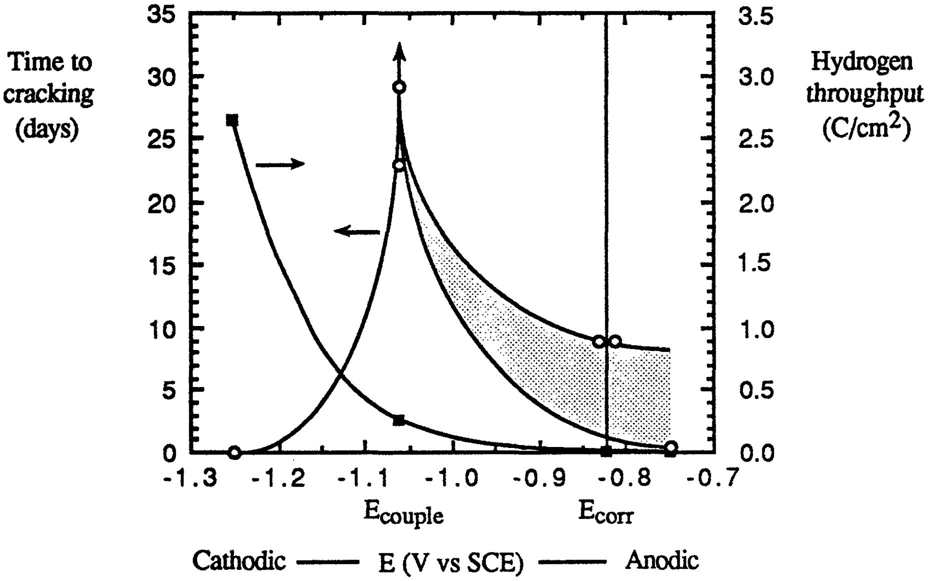

Figure 6.13 Effect of hydrogen on environmentally-assisted cracking of Nd-Fe-B, as shown by superimposing the time to cracking data (○) and the hydrogen throughput data (■).

6.2.4 Rationale for the Observed Behavior

The apparently low amount of hydrogen production on Nd-Fe-B at E_{corr} can be explained by estimating the degree of hydrolysis and IR drop expected to occur within growing pits.

The hydrolysis equilibria exhibited by both Nd and Fe indicate that an extremely low pH should not be expected to develop within pits. The equilibrium point of the reaction:

$$[6.1] \qquad Me^{n+} + n\,H_2O \Leftrightarrow Me(OH)_n + n\,H^+$$

depends upon the solubility product of the particular hydroxide in question. Consider a metal such as Al, which has an extremely low hydroxide solubility product ($K_{sp} \sim 10^{-32}$). The hydroxide phase associated with such a metal is very stable, which drives equation [6.1] strongly to the right in areas where $[Me^{n+}]$ is relatively high (e.g. within a pit). A relatively low pH should thus be produced in pits on Al; this theoretical observation is consistent with the large amount of hydrogen generated at anodic potentials on pitting Al in the work of Gest and Troiano [81]. The substantial hydrogen generation cited earlier for pitting stainless steels [77,80] is due to the strong hydrolysis of Cr. Pits in Fe are known to have a pH of ~ 3.5 [83], which is much lower than the pit pH values in Al or stainless steels; this effect results from the lesser hydrolysis of Fe compared to Al or Cr. The solubility product of Nd (~ 10^{-24}) [84] is also not nearly as low as the K_{sp} of Al or Cr.

It is qualitatively expected that large IR drops would not develop between pits and the external surface in Nd-Fe-B. A large IR drop is typically associated with a metal corroding in the passive state on its surface and in the active state within pits. Since the surface of Nd-Fe-B is believed to be corroding in the active rather than the passive state, there appears to be no viable means of sustaining large IR drops between the pit and the external surface.

6.3 Additional Topics Related to EAC

As previously mentioned, the present study was initiated in an attempt to evaluate the corrosion behavior of Nd-Fe-B and to devise a practical method of controlling its corrosion. When cracking was observed in several Nd-Fe-B samples, it was decided that an attempt to perform a preliminary evaluation of environmentally-assisted cracking should become an additional goal of the study (as stated in Chapter 3). It was not possible to study the EAC of Nd-Fe-B as thoroughly as desired, however, owing to the substantial time commitments required to fulfill the primary goals of the project. Time constraints dictated that only one particular aspect of EAC could be selected for detailed analysis. A definitive determination of the operative mode of EAC (i.e. HAC or APC) was judged to be the most critical issue relating to the cracking of Nd-Fe-B; efforts were therefore focused on an investigation of this topic, as described in the previous section.

Several other topics related to the EAC of Nd-Fe-B clearly merit further study, however. The effects of electrolyte anion, the path of cracks through the material, and the effects of residual stress on cracking are important factors worthy of more detailed analysis; the specific influence of anodic dissolution on the APC cracking process should also be considered. Although it was not possible to perform a detailed evaluation of these additional topics, some pertinent empirical results have been obtained. The present section contains these results, along with a brief discussion of each of the topics mentioned above.

It is emphasized that the cracking of Nd-Fe-B needs to be investigated in far more detail than was possible in the present work. Such an analysis is particularly important because of the fact that cracking associated with corrosion also been encountered by the primary manufacturer of RSP Nd-Fe-B [76]. Definitive plans are currently underway in the H.H. Uhlig Corrosion Laboratory to perform such a study, as discussed in Chapter 9.

6.3.1 Effect of Electrolyte Anion on EAC

To this point, all experiments related to the cracking of Nd-Fe-B have been conducted in NaCl solutions. Since cracking in other metal-electrolyte systems is often found to occur only in the presence of specific anions, it was considered important to determine whether or not Nd-Fe-B would exhibit cracking in solutions which do not contain Cl^- ions. A test sample was immersed in 0.5M Na_2SO_4 at open-circuit, in order to record the time to cracking (if applicable). The results of this experiment are shown in Figure 6.14, along with cracking data previously obtained in 0.5M NaCl at open-circuit.

Figure 6.14 illustrates the important result that cracking did indeed occur in Na_2SO_4. This observation indicates that cracking of the Nd-Fe-B alloy is not restricted to Cl^--containing solutions. The fact that cracking can apparently occur in either environment clearly has important implications for the practical utilization of Nd-Fe-B, since not all expected service environments will involve exposure to the Cl^- ion.

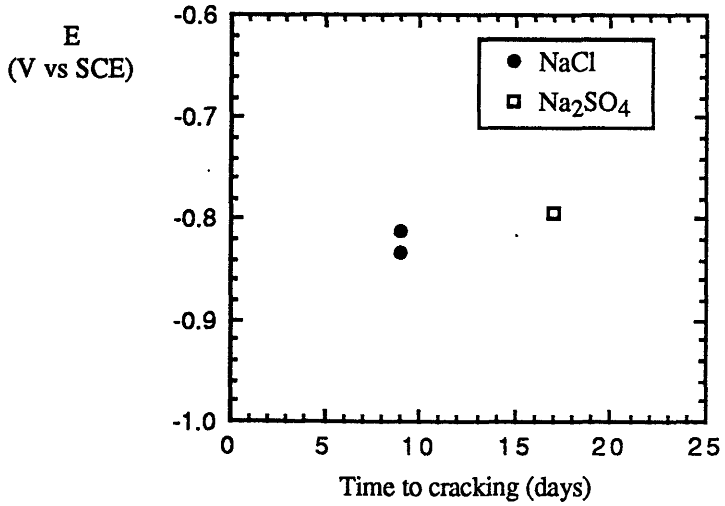

Figure 6.14 Effect of electrolyte anion on the rate of environmentally-assisted cracking.

Cracking did not occur as rapidly in the Na_2SO_4 solution as it did in the NaCl solution. The extent of the observed cracking was also less severe in Na_2SO_4, as the sample immersed in this solution did not exhibit the catastrophic fracture associated with the NaCl samples in Figure 6.2 (a). The extent of fracture in the Na_2SO_4 samples was actually quite similar to the partial cracking exhibited by the sample on the left in Figure 6.2 (b). The fact that cracking was more rapid (and more severe) in NaCl than in Na_2SO_4 provides a qualitative correlation to the anodic dissolution rates measured in Section 5.2, since the more rapid dissolution of the NaCl samples was found to result in a higher rate of cracking. The obtained results are therefore consistent with an APC cracking process, as expected.

6.3.2 Effect of Residual Stress

The Nd-Fe-B cracking tests discussed to this point were all performed using specimens which had been machined prior to testing. The cylindrical test samples were deliberately machined to a common diameter by means of centerless grinding. The importance of the machining treatment to the cracking of Nd-Fe-B is that such a process can lead to the generation of tensile residual stresses at the surface of the metal. It is relevant at this point to consider how a machining treatment can produce residual stresses at a metal surface.

Residual tensile stresses associated with machining are believed to result from the thermal changes associated with metal removal rather than from the process of metal removal itself. Metal removal processes tend to stretch out the surface atoms, which ultimately results in a state of residual compression at the surface of a worked metal. Evidence of such a stress state is shown in Figure 6.15, which is a plot of the residual stresses measured at the surface of hardened steel [85]. It can be observed that a gentle grinding process leads to the development of compressive residual stresses at the metal surface. This type of compressive stress state is only developed, however, if very slow metal removal rates are

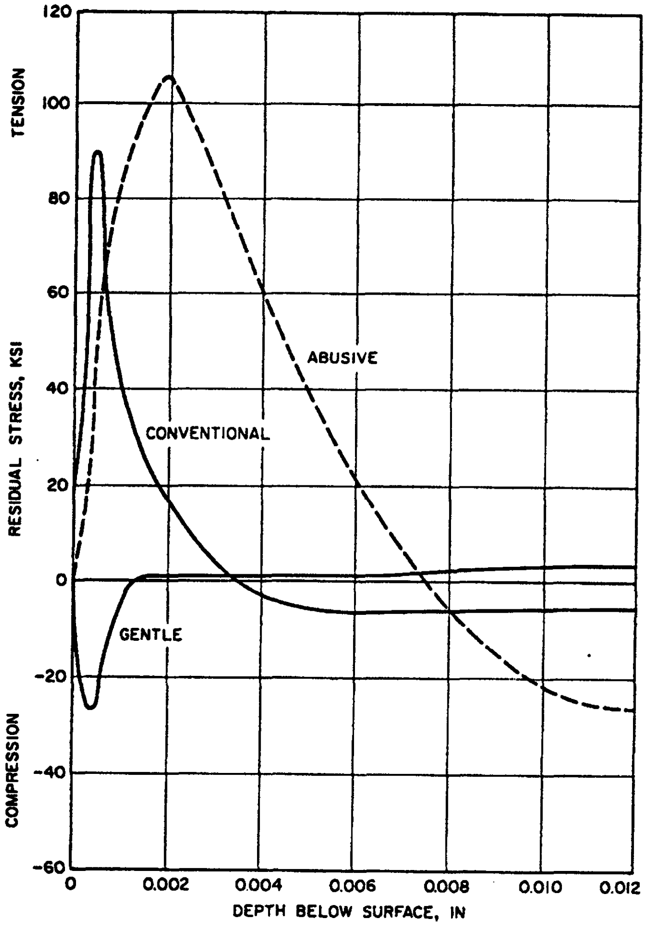

	GRINDING CONDITIONS		
	GENTLE	CONVENTIONAL	ABUSIVE
WHEEL	A46HV	A46KV	A46MV
WHEEL SPEED, FT/MIN	2000	6000	6000
DOWN FEED, IN/PASS	"LS"	0.001	0.002
GRINDING FLUID	SULF OIL	SOL OIL (1:20)	DRY

Figure 6.15 Residual stresses measured in a hardened steel which had been subjected to three different types of machining treatments; the treatments were classified as gentle, conventional, and abusive [85].

utilized, along with sharp cutting tools and an adequate supply of coolant (i.e. gentle grinding). Local heating of the surface tends to occur in the absence of such optimal grinding practices, and it is this heating which can lead to residual tensile stresses at the metal surface. When the grinding process is completed, the heated surface will cool and the surface atoms will thus attempt to contract. However, elastic constraint from the interior portion of the metal prevents full contraction of the surface, and the resistance to contraction leaves the surface in a "stretched" condition known as residual tension. Conventional grinding processes are often accompanied by such a thermal effect. If the shrinkage of the surface due to heating and cooling is of greater magnitude than the expansion of the surface due to mechanical deformation, the resulting stresses at the surface of the metal will be tensile in nature [85]. In practice, most conventional machining and grinding treatments result in the generation of tensile surface stresses, as illustrated in Figure 6.15. The development of tensile residual stresses is even more severe if abusive grinding practices are followed.

In the present study, a hexylene glycol-based coolant was used during machining. Several metal removal steps were utilized, with the first cut removing the most metal and the last cut resulting in the least amount of metal removed. The temperature profile at the surface of the metal was not recorded during machining, and no other information about the machining process was available. Since a concerted effort was not made to avoid surface heating, it is likely that the samples were subjected to a "conventional" grinding treatment.

Such an assertion is supported by the presence of cracking in the test samples, which were not externally stressed. The obtained results can only be explained if the machining treatment is presumed to have led to the generation of residual tensile stresses. Further proof of this conjecture was provided by testing several samples which had *not* been subjected to a machining process prior to immersion in the test solution.

As shown in Figure 6.16, the rate of cracking was much more rapid for the machined samples than for the specimens which were not machined. The only reasonable explanation for the observed results is that residual tensile stresses were generated by the

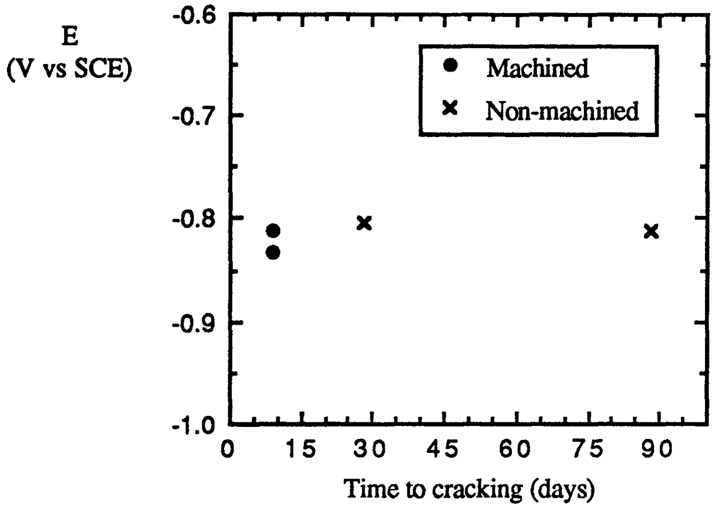

Figure 6.16 Effect of machining upon the cracking rate of Nd-Fe-B at open-circuit (NaCl, 23°C).

machining process. It should be noted that both types of samples were subjected to the same grinding, polishing, and cleaning process prior to testing, and that essentially no difference in corrosion behavior was detected between the two different types of samples.

Even though the cracking rate exhibited by the non-machined samples was substantially lower than that for the machined samples, the non-machined specimens did exhibit cracking during the test period. It is believed that the non-machined samples also contained residual stresses, as a result of the grinding and polishing treatment which was conducted in order to remove surface oxides prior to corrosion testing. The mechanical grinding process was carried out on standard silicon carbide grinding paper without water (i.e. dry). Although the metal removal rate (and thus the amount of surface heating) in such a process is expected to be much less than in a machining process carried out using cutting tools, the samples still sometimes became hot during coarse grinding. It is very likely that this heating resulted in the generation of residual tensile stresses according to the process described above.

It is known that the time required for corrosion-related cracking is very dependent upon the stress level in the material [86]. The apparent interpretation of Figure 6.16 is that both types of samples contained residual tensile stresses, but that the stresses generated by the machining process were greater than the stresses produced by the grinding and polishing sequence. These results indirectly indicate the importance of controlling residual stress formation in Nd-Fe-B magnets, which is a particularly relevant consideration in view of the fact that the h.p. and d.u. alloys are machined to shape prior to use.

It should be noted that an annealing treatment to remove or reduce residual stresses may have undesirable consequences for the magnetic properties of the alloy. If recrystallization is induced by annealing, the fine, single-domain grains produced by rapid solidification would likely be replaced by larger, multi-domain grains which may not provide the high coercive force normally expected of the typical RSP magnet.

Another possible source of residual stresses in a permanent magnet is magnetostriction. This phenomenon results from the fact that the magnetization process provides a driving force for strain in a ferromagnetic material, since an internal strain is associated with the alignment of magnetic domains. The relationship between stress and magnetization is demonstrated by the fact that when a tensile stress is externally applied to a specimen, the magnetization of the domains tends to become aligned parallel to the stress direction; when a compressive stress is applied, the domains tend to align transversely. This relationship is also observed when an unloaded specimen is magnetized, as the change in magnetization direction of each domain is accompanied by a largely elastic dimensional change. These elastic strains tend to give rise to compressive and tensile residual stresses within the material. Work was not performed to evaluate the level of stresses which could result from magnetostriction. It should be noted that the samples utilized in the present study could not have contained magnetostriction-related residual stresses, since the cracking experiments were conducted on non-magnetized samples. Additional residual stresses could conceivably have been imparted to the samples if they had been magnetized prior to testing.

6.3.3 Crack Path

The specific path followed by cracks in a fractured metal is an important parameter in understanding environmentally-assisted fracture. The information obtained from a crack path determination can often provide insight regarding the operative cracking mechanism, and can sometimes also assist in the mitigation of cracking failure. A discovery of intergranular fracture in a particular metal, for example, could conceivably lead to improved cracking resistance via modification of its grain boundary composition.

Experiments aimed at evaluating the path of APC cracks through Nd-Fe-B were not successful in the present study. Efforts to complete the crack path determination were hindered by the buildup of insoluble corrosion products on the crack faces. Corrosion products were found to block the fracture surface, thus rendering microscopic analysis ineffective. Despite the inability to complete these experiments in the present work, it is believed that a more diligent attempt to prevent corrosion product buildup on the crack faces (by improved post-cracking cleaning procedures, for example) might lead to the production of surfaces which can be used for crack path evaluation. Such surfaces must be examined in a high resolution scanning electron microscope in order to resolve the $Nd_2Fe_{14}B$ grains.

It is expected that a crack path analysis could be completed more readily for samples which cracked at E_{couple} or at -1250 mV than for samples immersed at E_{corr}, owing to the absence of anodically-formed corrosion products on these samples. However, these samples (E_{couple}, -1250 mV) were demonstrated in Section 6.2 to fail by HAC rather than by APC. Owing to the different cracking mechanisms exhibited by both types of samples, it appears that relevant information about the crack path in the open-circuit samples would not be obtained from an analysis of the cathodically polarized specimens.

The crack paths normally associated with brittle fracture are either transgranular in nature (cleavage) or intergranular. An additional crack path should be considered in rapidly solidified materials such as Nd-Fe-B, as it is possible that cracks could propagate along the ribbon boundaries in this material. Such a possibility is especially relevant in view of the fact that pits were found to initiate preferentially at the ribbon boundaries in Section 5.5, and also because the pits may be involved in the cracking process as sites of both intense local anodic dissolution and stress concentration (as discussed in the next section). In addition, the documented presence of a Nd_2O_3 phase at the ribbon boundaries (Section 5.4.3) indicates the existence of an interconnected brittle path at these boundaries.

The demonstration in Section 5.3.4.3 that intergranular attack is not the controlling mode of corrosion in rapidly solidified Nd-Fe-B suggests that cracking may not be intergranular in nature, but no other relevant crack path information was obtained in the present work. A crack path investigation will be an important part of the planned subsequent EAC study.

6.3.4 Effect of Anodic Dissolution on EAC

The effects of anodic dissolution on environmentally-assisted cracking can be divided into two general categories, depending on whether anodic dissolution is directly or indirectly involved in the fracture process. When cracking follows a preferred dissolution path in the material, it can be said that corrosion is *directly* involved in the cracking process.

Intergranular stress-corrosion cracking in metals which exhibit preferential grain boundary corrosion is an example of this type of cracking. The influence of corrosion on APC cracking can also be indirect in nature, as in cracking mechanisms which result from the wedging action of anodically formed corrosion products. Corrosion product wedging is an *indirect* result of corrosive attack, since the associated cracking is related to a by-product of the corrosion process (insoluble corrosion products), rather than to the actual dissolution of the metal itself. Both direct and indirect APC mechanisms will be discussed in this section.

6.3.4.1 Cracking which Directly Results from Anodic Dissolution

During cracking which occurs by a direct APC mechanism such as (but not limited to) stress-corrosion cracking, crack initiation is assumed to occur by anodic dissolution along pre-existing susceptible paths in the material [77]. For example, grain boundaries serve as the susceptible paths during the intergranular fracture of many different types of metals.

It is unlikely that intergranular corrosion is related to the APC cracking of rapidly solidified Nd-Fe-B, however, since intergranular attack has been demonstrated *not* to be a controlling mechanism in the corrosion of this alloy (Section 5.3.4.3). Since pits are the primary sites of intense local dissolution in Nd-Fe-B, it would appear that anodic cracking is more likely to be associated with pits than with than any other corrosion feature in the Nd-Fe-B samples. Surface dissolution was also shown to occur on Nd-Fe-B in Section 5.3.4.2, and it is conceivable that cracking could be related to surface attack rather than to pitting attack. The corrosion associated with pitting is more intense and more localized than the corrosion observed at the metal surface, however, and pits can additionally affect cracking by serving as sites of stress concentration. It is thus plausible to believe that APC cracking is related to pitting attack, as opposed to surface dissolution. The possibility that pitting corrosion is directly related to the observed EAC is consistent with the fact that anodic cracking has often been attributed to the presence of pitting in other alloy systems [87,87a]. An example of a material which exhibits pitting-induced cracking is carbon steel in either hot water or nitrate solutions [88].

In order to envision the possible relationship between crack initiation and the presence of pitting attack, it is useful to examine some of the processes associated with a growing pit. The pit surfaces in the present study are subjected to a relatively high rate of anodic dissolution at the time of cracking (9 days), as evidenced by the substantial rate of metal loss associated with the propagating pits. The surfaces of the machined samples are believed to reside in a state of residual tension (as discussed in the previous section), and the pits will therefore additionally serve as sites which concentrate the existing stress.

Two different cracking mechanisms can be envisioned by considering the possible effects of anodic dissolution and stress concentration on Nd-Fe-B. The first of these mechanisms relies on the initiation of cracks within a growing pit, with crack growth then leading to metal failure. In the second mechanism, the pit itself eventually grows to the point where it serves as the critical crack in the material. The possible mechanisms are discussed below.

It was stated above that both anodic dissolution and stress concentration are expected to be associated with the pits on Nd-Fe-B. It is known that the interaction between these two phenomena (anodic dissolution and stress concentration) can lead to crack initiation at the base of a propagating pit [87]; such crack initiation is often observed in stressed materials which exhibit pitting attack. Crack initiation can result from an undesirable synergism which occurs at the base of the growing pit. Tensile stress is known to increase the rate of anodic dissolution, and anodic dissolution is believed to be capable of altering the stress distribution at the pit base [89]. The synergistic combination of these factors may result in a severe condition of high local anodic dissolution and stress buildup at a particular area within the growing pit. If the conditions become excessively severe, a crack can be nucleated at the affected surface.

Once a crack has been nucleated within a pit, the crack can grow under the combined influence of anodic dissolution and stress concentration at the crack tip. Crack growth will continue until the length of the propagating crack becomes equal to the critical crack length in the material, at which point rapid and unstable fracture of the metal will occur.

Such a process is illustrated schematically in Figure 6.17, and is marked as mechanism 1. A crack can be initiated at the base of the pit at 9-x days owing to the combined influence of anodic dissolution and stress concentration. This crack will grow until its length equals a_1^*, the critical crack length in the material under the prevailing stress conditions; the metal will then fracture in a brittle manner. Since rapid, unstable cracking occurred after 9 days in the open-circuit Nd-Fe-B samples, the crack initiation process must occur at some time (9-x days) prior to the macroscopic fracture of the material. The initiated crack is presumed to grow to a critical length, a_1^*, during the subsequent x days, which results in fracture.

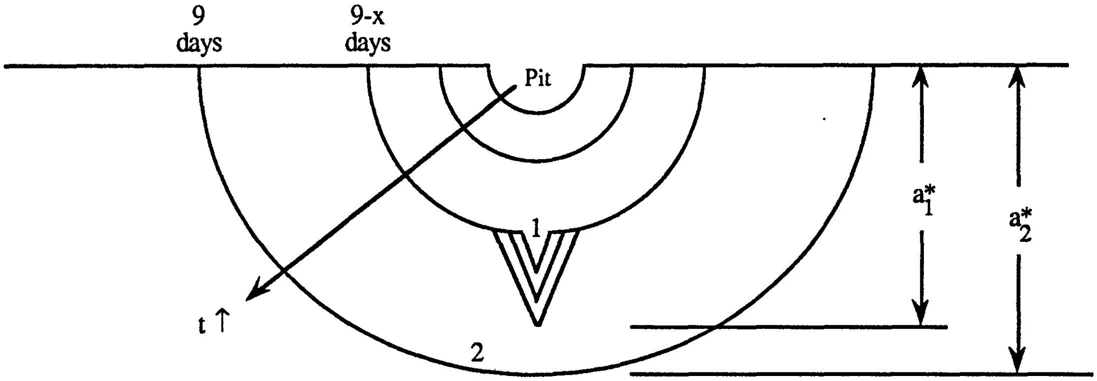

Figure 6.17 Schematic illustration of two mechanisms which could possibly lead to anodic cracking of Nd-Fe-B. Mechanism 1 relies on the initiation and growth of a subcritical crack. In mechanism 2, the growing pit itself serves as the critical flaw in the material.

It is also possible that the pits themselves act as critical flaws, and that rapid, unstable fracture of the material occurs without the initiation of a subcritical crack; this possibility is labeled as mechanism 2 in Figure 6.17. In this mechanism, anodic dissolution leads to sustained pit propagation, as above, but a crack is not initiated at the base of the pit. The pit instead continues to grow until the pit depth equals the critical crack length in the material. Fracture will occur once the pit depth reaches a_2^*. In order for mechanism 2 to lead to the observed fracture, the critical crack length in the material, a_2^*, must be less than or equal to the maximum pit depth measured after 9 days. Note that $a_1^* < a_2^*$, owing to the fact that an initiated subcritical crack is expected to be geometrically sharper than a hemispherical pit.

The optimal method of adjudicating between mechanisms 1 and 2 is to use a quantitative fracture mechanics evaluation to compare the maximum pit depth observed after 9 days to the critical crack length in the material. If the critical crack length is less than the measured depth of a 9-day pit, the metal would be expected to fail via mechanism 2.

On the other hand, if the critical crack length in the material is significantly greater than the maximum pit depth after 9 days, then mechanism 2 cannot result in the observed cracking. Mechanism 1 could then be operative, or an indirect APC cracking mechanism such as corrosion product wedging could be occurring.

It may be possible to quantitatively evaluate mechanism 2, since the flaw geometry and crack length after 9 days are known for this mechanism. Flaws were assumed to be semi-elliptical in nature, and the crack length at 9 days was estimated using the pit depth versus time plot shown in Figure 5.48; the maximum pit depth at 9 days was taken as 31 μm via interpolation. A quantitative evaluation cannot be performed for mechanism 1, since the geometry and length of the proposed subcritical crack are obviously not known. An attempt to evaluate the viability of mechanism 2 using Linear Elastic Fracture Mechanics (LEFM) is included as Appendix 10.5. The primary shortcoming of the LEFM analysis in the present study is that a definitive evaluation of mechanism 2 cannot be completed without knowledge of the stress level imparted to the samples by the machining treatment. Although the LEFM treatment in Appendix 10.5 does contribute to this study by providing quantitative insight into the cracking process, it was not able to conclusively evaluate mechanism 2 cracking.

Fortunately, it appears that a more simple method can be used to eliminate mechanism 2 as a cause of the observed cracking. Small, macroscopically visible chips were observed to be present on several of the machined samples used in the present study. The chipping of the samples presumably occurred during machining. Most of these chips were small in dimension, but were clearly greater than 31 μm in size. If the critical crack length in the material were indeed 31 μm (as required for the validity of mechanism 2), it would be expected that such surface discontinuities would have resulted in rapid cracking. The fact that such cracking was not observed appears to be inconsistent with the proposed mechanism 2. It thus appears that either mechanism 1 cracking or an alternative mechanism such as corrosion product wedging is responsible for the observed fracture.

It should be noted that the term "stress-corrosion cracking" was deliberately avoided when describing the anodic cracking exhibited by Nd-Fe-B. Although SCC is the primary cracking mechanism associated with anodic dissolution, the term SCC is typically used to refer to a specific type of cracking. SCC normally occurs in the presence of a passive surface film, and also takes place in the presence of specific anions. Both of these characteristics do not appear to be consistent with the behavior displayed by the present system. It is clear from the results of Section 6.2 that the open-circuit Nd-Fe-B samples failed by means of an anodic cracking mechanism, but it would be improper at this point to attribute the observed failures to classical SCC.

6.3.4.2 Corrosion Product Wedging

In addition to the direct form of APC cracking described above, anodic cracking can also occur in an indirect manner due to the wedging action exerted by insoluble corrosion products. It has been demonstrated [90] that insoluble corrosion products are capable of generating tensile stresses at the base of a cavity due to a wedging effect. The wedging process is known to result from the fact that corrosion products typically possess a greater volume than the metal from which they were formed.

The main factor necessary for the occurrence of corrosion product wedging (CPW) is metal dissolution which results in the formation of insoluble corrosion products. Insoluble corrosion products were present on the surface of the sample at the time of cracking, which suggests that CPW could be the operative cracking mechanism in the Nd-Fe-B alloy system. Such a possibility would be important since CPW, in addition to serving as a cracking mechanism, is also capable of providing its own stress. In fact, CPW may be capable of leading to cracking even in parts completely free of residual or applied stresses.

If the insoluble corrosion products form only on the metal surface, no wedging action can occur, and the presence of cavities within the metal surface is thus a second factor which must be present in order for CPW to occur. It is possible that either pits or grinding cracks could serve as potential locations for wedging action. The presence of corrosion products within pits was indirectly detected during SEM analysis by the fact that charging was observed at the bottom of pits on samples which had not been Au-coated. Grinding cracks were not found to be a primary feature of the Nd-Fe-B samples, but some chipping of the metal surface was observed to have resulted from machining; it is conceivable that corrosion within such cavities could result in CPW.

One piece of evidence which would initially seem to argue against CPW is the strong effect of machining (and presumably of residual stress) on the rate of cracking. This effect would seem at first to indicate that the stress formed by corrosion products is not a controlling factor in the observed cracking. In other words, if the main contributor to the stress is CPW, it would seem that residual stresses should not strongly affect the rate of cracking. It can be shown, however, that stresses are additive. In other words, the total stress on the corroding part could be represented as:

$$[6.6] \qquad \sigma_{total}(t) = \sigma_{applied} + \sigma_{residual} + \sigma_{cpw}(t)$$

where the applied stresses are equal to zero in this case. It can be assumed that the residual stresses in a given part are essentially constant during the experiment. The stress due to corrosion product wedging can increase with time owing to the continuted formation of insoluble corrosion products. Any stress created by wedging is added to the starting stress present in the material. The functional form of σ_{cpw} with time is not known, and has been represented by a linear function of time for illustrative purposes. Even if the stress generated by CPW in two different samples were identical, disparate cracking rates could still be observed because of the presence of differing residual stresses in the two specimens. The observed effect of machining on cracking rate thus does not rule out CPW as a cracking mechanism in this alloy system. Further information relating to the possible occurrence of CPW has not been obtained.

It should be clear from the foregoing analysis that a more comprehensive study is necessary in order to definitively determine the mechanism of anodic cracking in the Nd-Fe-B alloy system.

6.3.5 Importance of Controlling Corrosion to Minimize EAC

The results of Section 6.2 indicate that cracking is associated with the anodic dissolution process in Nd-Fe-B. As such, it is clearly important to develop methods which are capable of controlling the corrosion of this material in order to improve its resistance to EAC.

The results of the present section indicate that corrosion control methods capable of preventing the initiation and propagation of pitting corrosion should be targeted. Pits are very likely to be involved in the fracture process, whether APC cracking occurs by a direct anodic mechanism (e.g. by crack nucleation at the base of a pit), or by an indirect mechanism such as corrosion product wedging. Insoluble corrosion product formation in this alloy system is primarily dependent on the presence of pits, since much of the corrosion products formed on the metal result from anodic dissolution within pits. Any corrosion control method which is capable of reducing pitting attack may therefore also be successful in minimizing the observed anodic cracking.

The results of the present section also emphasize the importance of reducing the residual stress level of Nd-Fe-B magnets; the cracking time exhibited by the alloy appears to be highly dependent on the residual stress level, whether cracking occurs via a direct or an indirect anodic mechanism.

7. Corrosion Control Methods

In terms of the magnetic flux loss expected to result from corrosive attack, pitting corrosion is considered to be a less severe form of attack than intergranular corrosion, for example. Corrosive metal loss is still expected to be a problem for Nd-Fe-B in many environments, however. Permanent magnets are thin by design, and even the moderate metal loss associated with pitting can cause a magnet to lose a significant percentage of its flux over time, as was shown in Section 5.3.5. This concern is especially relevant if the material is to be used in a relatively aggressive environment. In addition to the metal loss (and accompanying flux loss) which results from anodic dissolution, the corrosion of Nd-Fe-B can also compromise the utility of the material by leading to anodic cracking.

Two modes of corrosive degradation can therefore be identified for RSP Nd-Fe-B alloys: metal loss and anodic cracking. Both degradation modes can lead to a loss of magnetic flux, and eventually to magnet failure if corrosion is not controlled. In particular, the elimination of pitting attack should be targeted in order to increase the resistance of Nd-Fe-B to both magnetic flux loss and anodic cracking.

In order to be considered viable, a corrosion control method must be able to reduce the corrosion of Nd-Fe-B to a tolerable level without interfering with the magnetic properties of the alloy. The method should also be cost-effective and easily integrated into processing.

Two corrosion control methods are described in the present chapter: corrosion control by sacrificial metallic coatings (Section 7.1) and corrosion control by ribbon boundary modification (Section 7.2). The latter method specifically attempts to minimize pitting attack by removing presumed sites of pit initiation.

7.1 Corrosion Control via Sacrificial Zinc Coatings

One of the primary goals of this research project was to improve the engineering viability of Nd-Fe-B by devising a practical, cost-effective method to control its environmental degradation. Emphasis was placed on developing a *practical* solution to the problem of Nd-Fe-B corrosion, one which could actually be utilized to protect the material in service. The results discussed in the present section indicate that the corrosion of Nd-Fe-B can be reduced to a negligible level through the use of sacrificial zinc coatings. Since zinc coatings are widely used in industry (in addition to being relatively inexpensive), this corrosion control method appears to fulfill the stated objective.

7.1.1 Limitations of Existing Corrosion Control Methods

As discussed in Section 2.3.5, Nd-Fe-B is currently protected using either epoxy coatings or nickel-base coatings. Both corrosion control methods have been found to provide adequate corrosion protection to the alloy as long as the coating itself remains intact. If the Nd-Fe-B base metal is exposed to the corrosive environment, however, neither epoxy coatings nor nickel coatings are capable of protecting it from attack. Since a coating is rarely perfect over its entire lifetime, the inability of an epoxy or a nickel coating to protect Nd-Fe-B once it has been compromised is a significant concern.

Base metal exposure can occur with any type of coating as a result of chipping or cracking of the coating material. Such damage can occur during service and is also a concern during handling between the application of the coating and the final installation of the material in its service environment [53]. Coating porosity can also lead to exposure of the base metal. Both epoxy and nickel coatings can additionally be compromised in practice by degradation methods specific to each type of material. Epoxy coatings are known to be permeable to water, and a base metal covered by epoxy is inevitably exposed to the corrosive electrolyte during its service life due to water uptake through the coating. Metallic coatings such as nickel will eventually be penetrated due to prolonged corrosion, though passivation allows nickel to corrode at a relatively slow rate. Degradation of both epoxy and nickel coatings have been observed under different environmental conditions, as discussed in Section 2.3.

Exposure of the Nd-Fe-B base metal to a corrosive electrolyte results in pitting attack, as described in Chapter 5, and can also lead to environmentally-assisted cracking, as discussed in Chapter 6. Exposure of Nd-Fe-B at breaks in a nickel coating is especially problematic, since nickel will act as a cathode and will therefore increase the degradation rate of Nd-Fe-B by galvanically stimulating the anodic dissolution of the alloy.

7.1.2 Rationale for Evaluating Zinc Coatings as a Corrosion Control Method

The zinc coating evaluation was initiated in an attempt to find a solution to the problem of Nd-Fe-B corrosion resulting from coating failure. It was hypothesized that corrosion of the Nd-Fe-B base metal could be minimized by using a bilayer combination of organic and zinc coatings. Zinc coating-organic coating systems are often used industrially to protect steel parts such as automotive body panels. Such coatings provide an excellent safety factor against coating penetration by offering three different levels of corrosion protection. The organic coating initially serves as a barrier layer. When this barrier is compromised due to absorption of electrolyte or to chipping of the organic coating, the zinc coating will provide barrier protection to the underlying metal. The corrosion rate of the zinc coating will be low, owing to the formation of sparingly soluble zinc corrosion products such as hydroxides, carbonates, and bicarbonates [91]. When the zinc coating is eventually penetrated, it will ideally provide sacrificial cathodic protection to the exposed base metal. It is well-known that zinc will provide sacrificial protection to carbon steels and many other

Fe-based alloys, but no information was available regarding its ability (or inability) to protect Nd-Fe-B. The apparent benefits of the protection scheme outlined above implied that it might be useful to evaluate the feasibility of protecting Nd-Fe-B using a sacrificial metallic coating (which is expected to be used with an organic overlay coating). Zinc coatings were selected for evaluation because of their low cost and ease of application.

7.1.3 Possible Limitations of Sacrificial Zinc Coatings

Sacrificial zinc coatings might represent a cost-effective corrosion control method for Nd-Fe-B, as described above, but their use may have previously been overlooked because of two potential limitations: incomplete protection and hydrogen damage.

Incomplete protection refers to the inability of a sacrificial metallic coating to fully prevent the corrosion of the base metal at breaks in the coating. Zinc coatings may be incapable of providing complete sacrificial protection to Nd-Fe-B, because neodymium is known to be an electrochemically active element. The anodic dissolution of Nd can occur at electrode potentials much more negative than the corrosion potential of Nd-Fe-B [24], and the cathodic polarization provided by the coating therefore may not be effective in reducing the corrosion of Nd. Although thermodynamic considerations indicate that zinc coatings may not be able to prevent the corrosion of Nd, the *rate* of Nd dissolution cannot be predicted on the basis of electrode potentials (i.e. thermodynamically). The degree of protection provided to Nd at breaks in the coating can thus only be determined by experimentation.

Hydrogen production will be galvanically stimulated on Nd-Fe-B at breaks in the coating (due to cathodic polarization), and the rate of Nd-Fe-B cracking could thus be accelerated by hydrogen uptake. Although hydrogen degradation has been observed [49] for Nd-Fe-B under strong cathodic polarization ($i_{cathodic}$ = 0.4 to 1.3 A/cm^2 in H_2SO_4 with pH 0 to 1), the relevance of these results may be limited due to the severe testing conditions employed.

Incomplete protection and hydrogen damage must be addressed in order to fully evaluate the ability of sacrificial zinc coatings to provide effective corrosion control to Nd-Fe-B.

It should be noted that corrosion control via zinc and/or organic coatings does not present an inherent problem for Nd-Fe-B from a magnetic standpoint, since these coating materials will not affect the magnetic field produced by the alloy. Effects of the coating on magnetic flux are not expected to be a limitation for the corrosion control of Nd-Fe-B, provided that the coating is not excessively thick. This point is discussed further in Section 7.1.7.3.

7.1.4 Results of Mixed Potential Theory and Galvanic Corrosion Testing

The barrier properties of both organic coatings and zinc coatings have been well-characterized in the past, and the current study thus focuses on evaluating the ability of a sacrificial zinc coating to provide cathodic protection to Nd-Fe-B once the zinc coating has been penetrated and a galvanic cell has been formed between zinc and Nd-Fe-B. An established technique for analyzing galvanic systems consists of utilizing the mixed potential theory, usually in combination with galvanic corrosion testing [91a-91e]. The methodology used to evaluate galvanic systems is discussed in Appendix 10.1.3.

Anodic and cathodic polarization tests were performed on both h.p. Nd-Fe-B and zinc in NaCl and Na_2SO_4 solutions at both 30°C and 80°C. The four polarization curves obtained in a given test solution were then superimposed on a common graph, as shown in Figure 7.1 (30°C) and Figure 7.2 (80°C). Figures 7.1 and 7.2 were constructed using units of amperes, since current (rather than current density) is conserved in galvanic systems.

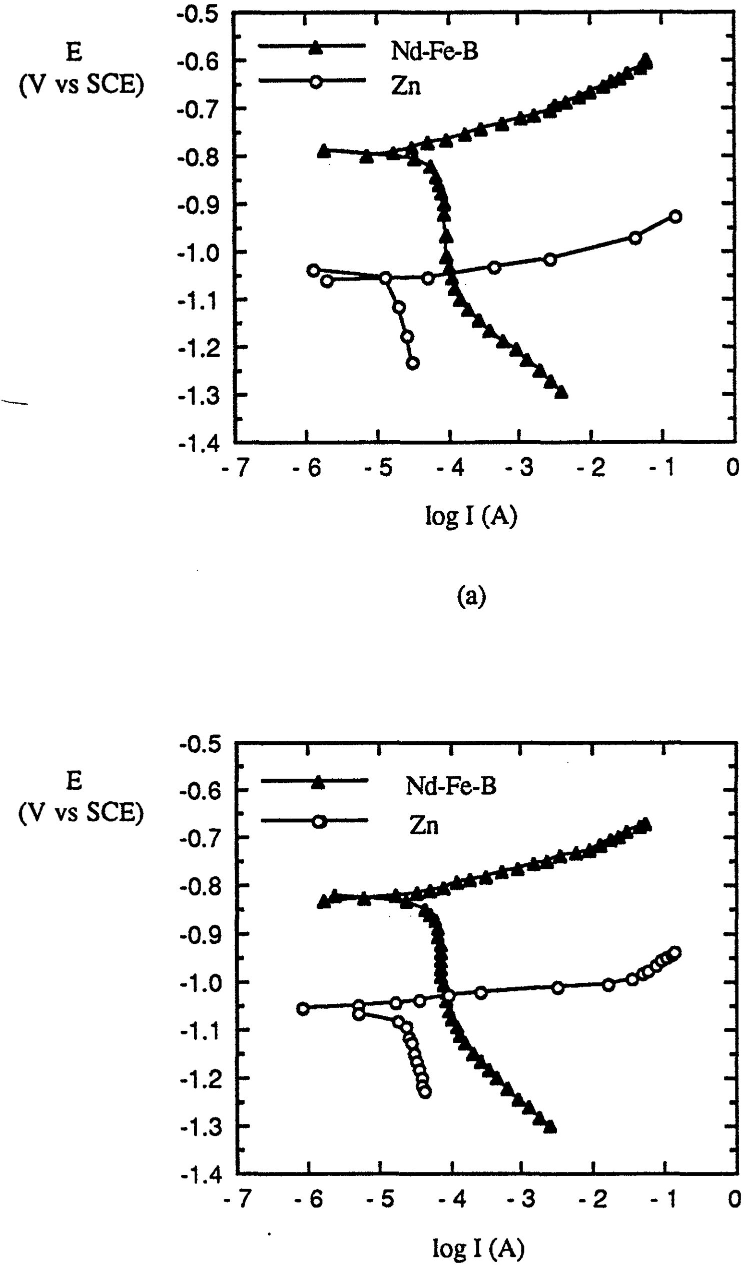

(a)

(b)

Figure 7.1 Anodic and cathodic polarization of Nd-Fe-B and zinc in (a) NaCl and (b) Na_2SO_4 at 30°C. The diagram corresponds to a Nd-Fe-B electrode with an area of 1 cm^2 and a Zn electrode of 1.8 cm^2.

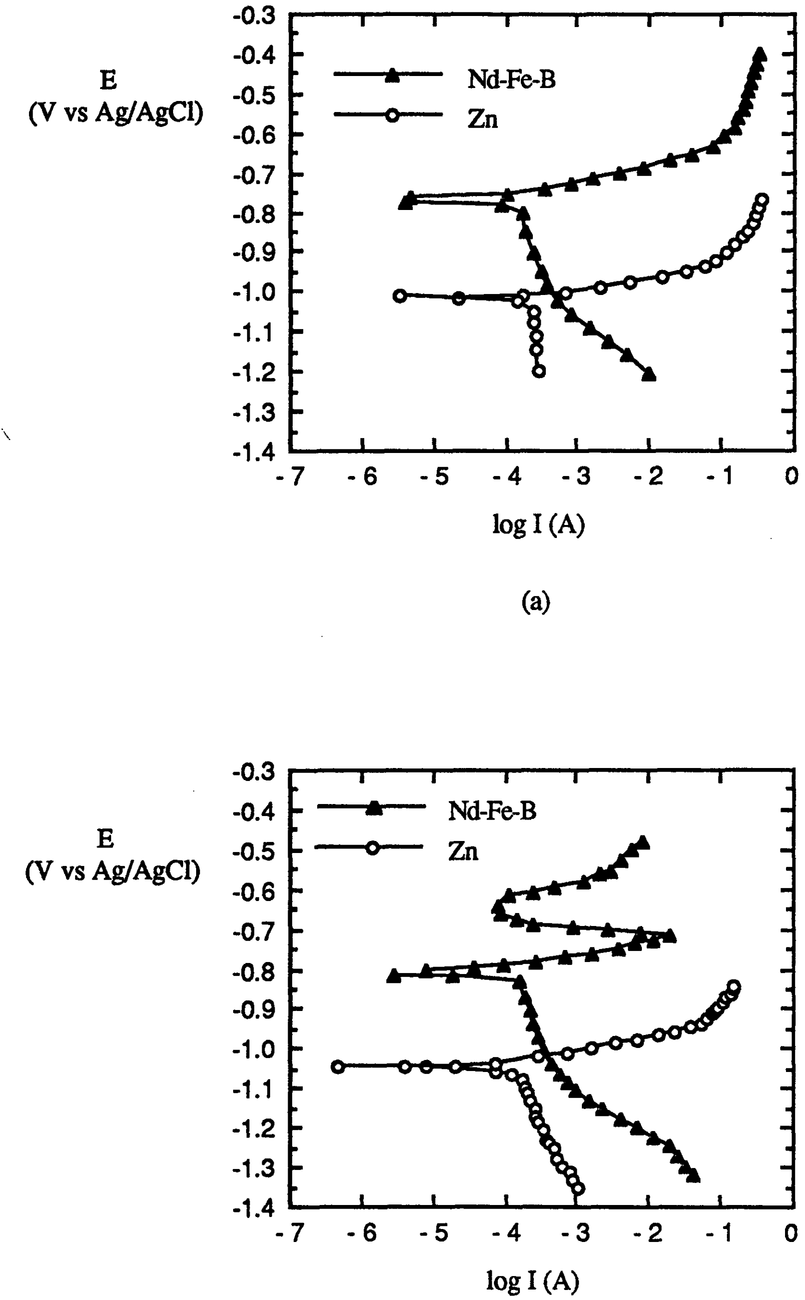

(a)

(b)

Figure 7.2 Anodic and cathodic polarization of Nd-Fe-B and zinc in (a) NaCl and (b) Na_2SO_4 at 80°C. The diagram corresponds to a Nd-Fe-B electrode with an area of 1 cm^2 and a Zn electrode of 1.8 cm^2.

The values of current shown in Figures 7.1 and 7.2 correspond to Zn electrodes of area 1.8 cm^2 and Nd-Fe-B electrodes of area 1 cm^2 (area ratio of 1.8 : 1). A coating : base metal area ratio greater than 1 : 1 was selected in order to simulate the ratio obtained when a small area of base metal is exposed to an electrolyte due to porosity, cracking, or corrosion of the coating metal; the exact area ratio utilized was based on available sample size.

According to the mixed potential theory, the intersection of the total oxidation curve and the total reduction curve is the predicted couple potential (E_{couple}) of the coating-base metal system. E_{couple} represents the common electrical potential to which both metals are polarized upon coupling. The reaction rate for each of the individual anodic and cathodic reactions in the system can be predicted by calculating its current density at E_{couple}. The anodic dissolution rate for the base metal (cathode) at E_{couple} can be predicted by extrapolating the linear or Tafel region of the Nd-Fe-B anodic polarization curve to E_{couple}, as previously shown in Figure 4.17. The anodic Tafel regime should ideally be extrapolated to a *measured* E_{couple} value, rather than to the E_{couple} value predicted by the mixed potential theory. In order to facilitate this process, the results of galvanic corrosion testing will be introduced prior to extrapolating the anodic Tafel region to E_{couple}. The dissolution rate of coupled Nd-Fe-B will then be predicted in Section 7.1.5.1.

Galvanic couples of zinc and Nd-Fe-B were immersed at 30°C and 80°C in NaCl and Na_2SO_4 solutions, using a Zn : Nd-Fe-B area ratio of approximately 1.8 : 1. Zinc was found to be the anodic member of the couple in all cases. The measured E_{couple} and $i_{g(c)}$ (the galvanic current density relative to the area of the cathode) are shown in Figure 7.3 (30°C) and Figure 7.4 (80°C). The galvanic current density is reported with respect to the area of the cathode (Nd-Fe-B), since the parameter $i_{g(c)}$ is relevant to the cathodic protection requirements of the Nd-Fe-B alloy. Average values of E_{couple} and $i_{g(c)}$ over the 20 hour test period are shown in Table 7.1.

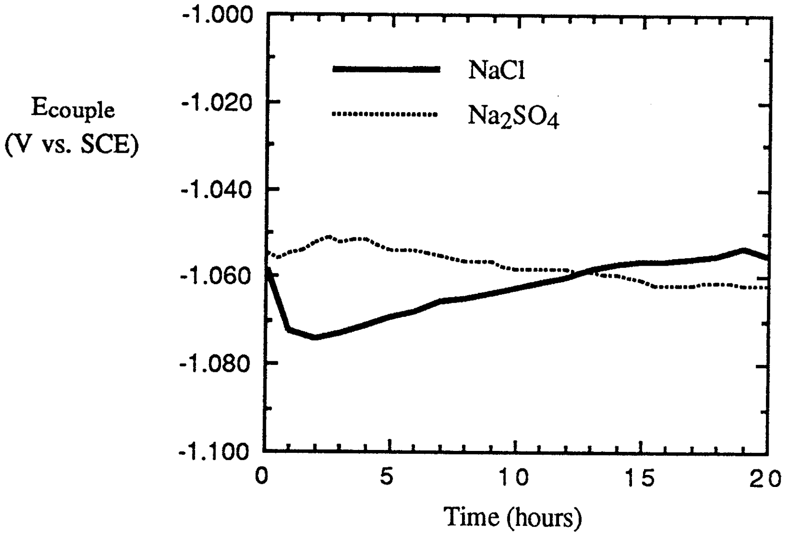

(a)

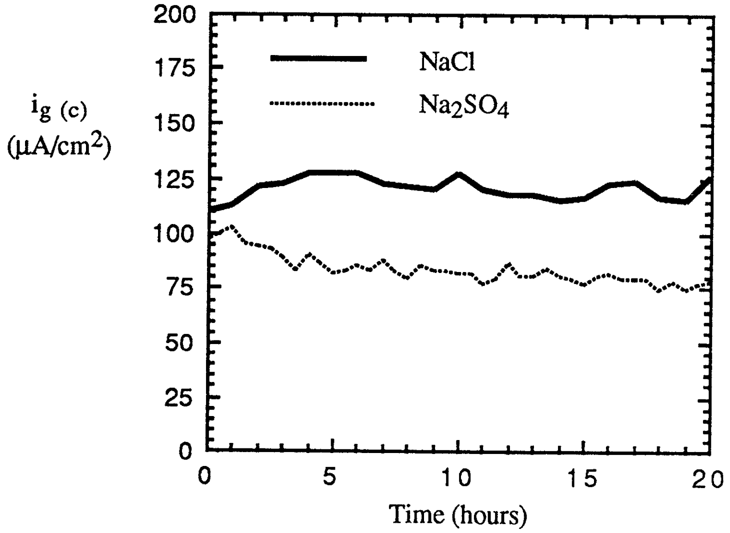

(b)

Figure 7.3 Results of galvanic corrosion testing for a Zn : Nd-Fe-B couple exposed at an area ratio of 1.8 : 1 at 30°C. Zinc was found to be acting as the anode in both NaCl and Na_2SO_4 solutions.

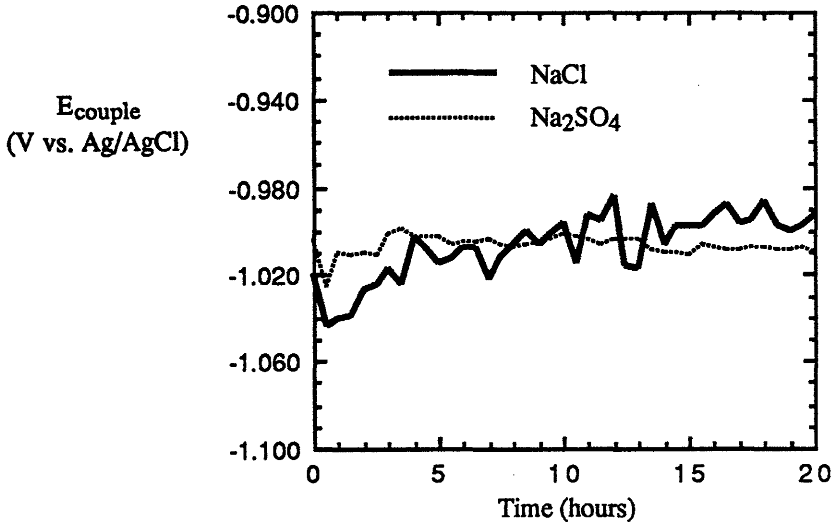

(a)

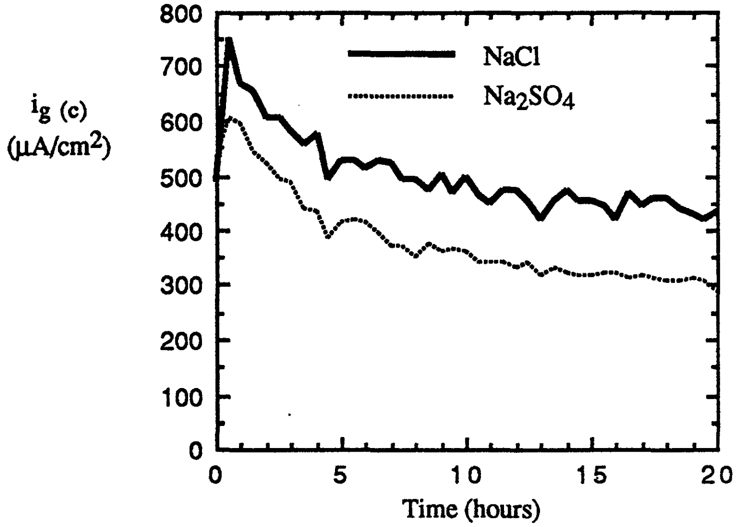

(b)

Figure 7.4 Results of galvanic corrosion testing for a Zn : Nd-Fe-B couple exposed at an area ratio of 1.8 : 1 at 80°C. Zinc was found to be acting as the anode in both NaCl and Na_2SO_4 solutions.

Table 7.1 Average data from galvanic corrosion testing at (a) 30°C and (b) 80°C.

(a)

	NaCl	Na_2SO_4
E_{couple} (V vs. SCE)	-1.063	-1.058
i_g (c) ($\mu A/cm^2$)	120	84

(b)

	NaCl	Na_2SO_4
E_{couple} (V vs. Ag/AgCl)	-1.007	-1.014
i_g (c) ($\mu A/cm^2$)	527	367

The magnitude of the galvanic current is higher in NaCl than in Na_2SO_4 at both 30°C and 80°C. This effect is believed to result from differences in the concentration of dissolved oxygen in the two test solutions. As discussed in Section 5.1.6, the Na_2SO_4 solutions used in this study have a lower dissolved oxygen concentration than the NaCl solutions, due to their greater salt content (in weight percent). An increase in the concentration of dissolved oxygen will allow the cathodic reaction on Nd-Fe-B to occur more readily, thus leading to a higher measured galvanic current. The galvanic current is substantially higher at 80°C than at 30°C in both types of solutions. This difference is believed to be related to the effect of temperature on the diffusion rate of dissolved oxygen. The oxygen diffusion rate is higher at 80°C than at 30°C, and the supply of cathodic reactant to the Nd-Fe-B electrode will thus be greater at the higher temperature. The increased supply of oxidant at 80°C should result in a larger value of i_g than at 30°C.

7.1.5 Preliminary Evaluation of Sacrificial Zinc Coatings

The first requirement for a sacrificial coating is that it must be electronegative to the material to be protected. Zinc is clearly active (electronegative) to Nd-Fe-B in all four test solutions, as shown by the corrosion potentials for Zn and Nd-Fe-B in Figures 7.1 and 7.2.

The metal to be protected must also be subjected to significant cathodic polarization upon galvanic coupling to the coating metal. The degree of polarization experienced by the base metal will be dependent not only upon the difference in corrosion potentials between the two metals, but also upon the relevant electrode kinetics. E_{couple} will approximately reside at the intersection of the lines corresponding to the anodic dissolution of Zn and the oxygen reduction reaction on Nd-Fe-B. Since the anodic dissolution reaction for Zn was found to exhibit significantly less polarization (dE/d(log i)) than the oxygen reduction reaction on Nd-Fe-B (Figures 7.1 and 7.2), the potential of zinc does not have to be driven very far in the oxidizing direction in order to supply the anodic current necessary for the stability of the couple. Measured E_{couple} values will thus be located near the corrosion potential of zinc, which is the preferred location for E_{couple} from a cathodic protection standpoint.

Galvanic coupling to zinc was found to be quite effective at imparting significant cathodic polarization (ΔE) to Nd-Fe-B. The alloy was cathodically polarized by more than 0.2 V upon coupling to zinc in all four test solutions, as shown in Table 7.2. For each solution, the value of ΔE was obtained by subtracting the measured E_{couple} value from the corrosion potential of Nd-Fe-B; these values ($E_{corr\ (Nd\text{-}Fe\text{-}B)}$, E_{couple}) are also provided in Table 7.2.

Table 7.2 Degree of cathodic polarization (ΔE) experienced by Nd-Fe-B upon coupling to zinc at (a) 30°C and (b) 80°C. Electrode potentials were measured versus SCE at 30°C and Ag/AgCl at 80°C.

(a)

	NaCl	Na_2SO_4
ΔE (V)	0.269	0.234
$E_{corr\ (Nd\text{-}Fe\text{-}B)}$	-0.794	-0.824
E_{couple}	-1.063	-1.058

(b)

	NaCl	Na_2SO_4
ΔE (V)	0.240	0.219
$E_{corr\ (Nd\text{-}Fe\text{-}B)}$	-0.767	-0.795
E_{couple}	-1.007	-1.014

Although the ability to impart cathodic polarization to the base metal is an important requirement for a sacrificial coating, the degree of polarization provides only a qualitative measure of the amount of protection provided by the coating. A quantitative prediction of the dissolution rate of Nd-Fe-B at E_{couple} can be obtained using the mixed potential theory.

7.1.5.1 Predictions of the Mixed Potential Theory

The process used to perform the mixed potential theory analysis is discussed in Appendix 10.1.3 (and is shown in Figure 10.14). The analysis was conducted for each solution by first using Tafel extrapolation to extend both the Nd-Fe-B anodic curve and the Zn cathodic curve over a large potential range. The anodic curves for both Nd-Fe-B and Zn were then summed over a range of potential values to give the total oxidation curve. The total reduction curve was determined by summing the cathodic curves for both Nd-Fe-B and Zn. A predicted E_{couple} value was defined by the intersection of the total oxidation and total reduction curve. The reaction rate for each of the individual anodic and cathodic reactions was predicted by calculating its current at E_{couple}, using areas of zinc and Nd-Fe-B of 1.8 cm^2 and 1 cm^2, respectively. In order to improve the accuracy of these results, the E_{couple} values measured in the galvanic corrosion experiments were utilized in the reaction rate determinations, rather than the E_{couple} values predicted by the mixed potential theory. Table 7.3 shows the predicted values of the anodic and cathodic reactions on both Nd-Fe-B and zinc, as well as the values predicted for E_{couple} and $i_{g(c)}$.

The predictions of the mixed potential theory can be utilized to develop an overview of the electrochemical situation at E_{couple}. The predominant anodic process is the dissolution of zinc. The cathodic reaction at E_{couple} is predicted to take place on both metals, with 70-80% occurring on Nd-Fe-B (Table 7.3). The main cathodic reaction is oxygen reduction, though the reduction of water to atomic hydrogen will also take place on both metals.

Table 7.3 Predicted values from the mixed potential theory analysis at (a) 30°C and (b) 80°C. All current values are reported in µA and galvanic current density values in µA/cm^2. E_{couple} values are given in volts with respect to either SCE (30°C) or Ag/AgCl (80°C).

(a)

	NaCl	Na_2SO_4
I_a (Nd-Fe-B)	0.000002	0.000044
I_c (Nd-Fe-B)	107	85
I_a (Zn)	132	110
I_c (Zn)	26	20
E_{couple}	-1.044	-1.028
i_g (c)	107	88

(b)

	NaCl	Na_2SO_4
I_a (Nd-Fe-B)	0.000380	0.000001
I_c (Nd-Fe-B)	464	383
I_a (Zn)	619	565
I_c (Zn)	186	119
E_{couple}	-1.004	-1.014
i_g (c)	449	415

The anodic current density on coupled Nd-Fe-B was predicted by extrapolating the anodic Tafel region of Nd-Fe-B to E_{couple}, as shown below in Figure 7.5 (NaCl, 30°C).

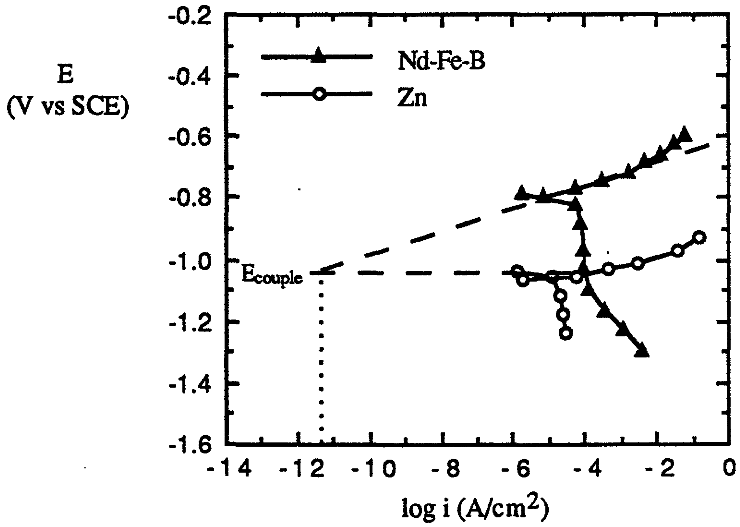

Figure 7.5 Extrapolation of the Tafel region of the Nd-Fe-B anodic polarization curve (NaCl, 30°C) to E_{couple}. The intersection with E_{couple} defines the predicted anodic dissolution rate for coupled Nd-Fe-B.

The anodic dissolution current on Nd-Fe-B at E_{couple} is predicted to be extremely low in all four test solutions, as shown in Table 7.3. The low values of the predicted currents are due to the relatively low anodic Tafel slopes measured for Nd-Fe-B, combined with the significant cathodic polarization which results from coupling. Deviations in $I_{a\ (Nd\text{-}Fe\text{-}B)}$ from one test solution to another are likely due to slight errors in estimating the anodic Tafel slopes; these errors are magnified by extrapolation over several decades of current.

By using the Faraday's Law calculation described in Section 5.1.10, the predicted anodic currents can be converted to penetration rates for samples with an exposed area of 1 cm^2. Three different types of corrosive attack were assumed to be operative in these calculations: general corrosion, pitting corrosion, and intergranular corrosion. General corrosion was considered in order to estimate the obtained penetration rate if the corrosion of Nd-Fe-B at E_{couple} were uniform in nature rather than localized. Pitting was considered because corrosion in this alloy system tends to take the form of pits, as described in Chapter 5. Even though it was demonstrated in Section 5.3.4.3 that intergranular corrosion does not occur on Nd-Fe-B at open-circuit, this form of attack was considered in order to verify that the predicted anodic currents on the base metal would lead to very low corrosion rates even if all of the anodic current at E_{couple} were derived from the grain boundary phase.

The various types of corrosion are accounted for by dividing the predicted anodic currents by the area associated with the specific type of corrosion considered. Dividing the predicted currents by the nominal surface area of 1 cm^2 yields the corrosion current density values associated with general corrosion. The pitted area was assumed to be 0.005 cm^2 on a nominal surface of 1 cm^2, based on an estimate of the pitted area fraction in Appendix 10.2. Intergranular corrosion was accounted for by dividing the anodic current by the expected grain boundary area. According to the estimate in Section 5.3.4.3, approximately 0.05 cm^2 of grain boundary area should be present on a nominal surface of 1 cm^2.

Calculated penetration rates are shown for all four test solutions in Table 7.4. All values were predicted to be less than 1 μm/yr (1 μm = 10^{-3} mm). The maximum penetration rate listed in Table 7.4 is for pitting corrosion in NaCl at 80°C; the predicted rate under these conditions was only 9.7×10^{-4} mm/yr, which corresponds to a negligible corrosion rate. The mixed potential theory analysis thus predicts that sacrificial zinc coatings should be capable of reducing the corrosion of Nd-Fe-B to a negligible level in all four solutions, even if the possibility of pitting or intergranular corrosion is considered.

The corrosion rates shown in Table 7.4 are also predicted to be negligible in terms of volume loss, weight loss, and magnetic flux loss. Even if general metal penetration was assumed to occur all over the entire 1 cm^2 sample to a depth of 1 μm, this attack would correspond to a volume loss of only 10^{-4} cm^3/yr and to a weight loss of 7.6×10^{-4} g/yr. The percent flux loss associated with such corrosive attack would obviously depend upon the initial size of the magnet considered. Sample calculations were performed for the cube-shaped magnets discussed in Section 5.3.5. Flux losses of 0.5% and 0.06% per year were calculated for the $(0.5\ cm)^3$ and the $(1\ cm)^3$ magnets, respectively. Magnetic flux losses are thus predicted to be negligible unless the magnet considered is extremely small.

Table 7.4 Predicted penetration rates for coupled Nd-Fe-B in mm/yr at (a) 30°C and (b) 80°C for various forms of corrosion.

(a)

	NaCl	Na_2SO_4
General	2.6×10^{-8}	5.6×10^{-7}
Pitting	5.1×10^{-6}	1.1×10^{-4}
Intergranular	5.1×10^{-7}	1.1×10^{-5}

(b)

	NaCl	Na_2SO_4
General	4.9×10^{-6}	1.3×10^{-8}
Pitting	9.7×10^{-4}	2.6×10^{-6}
Intergranular	9.7×10^{-5}	2.6×10^{-7}

7.1.5.2 Limitations of the Mixed Potential Theory Analysis

The utility of the mixed potential theory analysis is derived from its ability to make quantitative predictions about galvanic corrosion systems. The major limitation of this analysis, however, is the fact that its predictions must always be verified by further experimentation. Even though the fundamental viability of the mixed potential theory is well-established, it has not yet been verified that this analysis is valid in the present system.

The validity of utilizing the mixed potential theory as a basis for evaluating the Nd-Fe-B/Zn system is supported by the fact that it was able to accurately predict the values measured in the galvanic corrosion tests, as evidenced by comparing the measured values of E_{couple} and $i_{g(c)}$ in Table 7.2 to the predicted values in Table 7.4. As shown in Table 7.5, E_{couple} measurements were predicted to within 30 mV or less and $i_{g(c)}$ measurements to within 15% or less of the measured value for all four test solutions. Galvanic corrosion results thus provide preliminary support for the accuracy of the mixed potential theory predictions, but these predictions must still be supported by more definitive experimentation. Despite

Table 7.5 Deviations between measured data from galvanic corrosion testing and predicted data from the mixed potential theory at (a) 30°C and (b) 80°C.

(a)

	NaCl	Na_2SO_4
E_{couple} (V vs. SCE)	0.019	0.030
$i_{g\,(c)}$ ($\mu A/cm^2$)	11 %	5 %

(b)

	NaCl	Na_2SO_4
E_{couple} (V vs. Ag/AgCl)	0.003	0.000
$i_{g\,(c)}$ ($\mu A/cm^2$)	15 %	13 %

its useful predictive ability, the mixed potential theory is incapable of providing conclusive proof that the dissolution of Nd-Fe-B will be essentially negligible when coupled to zinc.

As discussed in Appendix 10.1.3, the mixed potential theory is also not capable of evaluating the susceptibility of the alloy to incomplete protection, alkaline damage, or hydrogen damage. It is important to evaluate incomplete protection and hydrogen damage owing to the electrochemical activity of Nd and to the known susceptibility of Nd-Fe-B to hydrogen damage under very high hydrogen reduction rates.

7.1.6 Evaluation of Sacrificial Zinc Coatings via Long-Term Immersion Tests

Long-term immersion tests were performed in order to evaluate whether the significant reduction in the Nd-Fe-B dissolution rate predicted to occur upon galvanic coupling to zinc would actually be obtained in practice. Immersion tests were also performed to determine whether incomplete protection, alkaline damage, and/or hydrogen damage would occur if Nd-Fe-B were subjected to cathodic polarization for an extended period of time. The test samples utilized in the long-term immersion experiments are described in Section 4.3.7. The long-term (1 month) immersion tests were performed exclusively in NaCl at ambient temperature (~23°C), due to the inconvenience associated with controlling the solution temperature with a thermostat for an extended period of time. Electrode potentials will thus be referenced to the saturated calomel electrode (SCE) for the remainder of Section 7.1.

Nd-Fe-B samples were either immersed at open-circuit or galvanically coupled to zinc. The open-circuit samples are also referred to as uncoupled in order to distinguish them from samples which were coupled to zinc. A Zn : Nd-Fe-B area ratio of 1.8 : 1 was used for the coupled tests in order to provide a correlation to the results discussed above.

7.1.6.1 Results of the Long-Term Immersion Tests

Electrode potentials of the Nd-Fe-B samples were monitored during long-term immersion. Average potential values were E_{corr} = -0.82 V and E_{couple} = -1.06 V for uncoupled and coupled samples, respectively. The potential of the coupled samples became slightly noble with time, but measured values were active to -1.04 V at all times during the 29 day test period. The measured bulk pH of all solutions was ~ 6.0 both before and after testing.

It was initially planned to evaluate the degree of protection provided by galvanic coupling to zinc by comparing the weight loss measured for Nd-Fe-B in both the uncoupled and coupled conditions. Weight loss testing was precluded by the cracking of several test samples, however, as discussed in Section 7.1.6.2. An attempt to obtain weight loss data by testing a second set of samples and removing them prior to cracking was unsuccessful. A small piece of each metal sample cracked off within 3-4 days of immersion, making the determination of weight loss due to corrosion ambiguous. The degree of protection could therefore only be evaluated by comparing the amount of insoluble and soluble corrosion products formed by both uncoupled and coupled samples. A third set of uncoupled samples was used in this determination, due to cracking of the original test specimens.

The uncoupled samples were found to be completely covered by an insoluble, rust-colored corrosion product in less than 5 days, as shown in Figure 7.6 (a). The coupled samples, however, exhibited no rust-colored products even after 29 days in solution, as shown in Figure 7.6 (b). As described in Section 7.1.7.1, the very thin white covering found to exist on the coupled samples is believed to be a zinc corrosion product which precipitated in the solution and settled onto the Nd-Fe-B samples. Although this product was too thin to be removed for conclusive analysis, the presence of zinc on the coupled Nd-Fe-B surfaces was verified by energy dispersive x-ray spectroscopy (EDX).

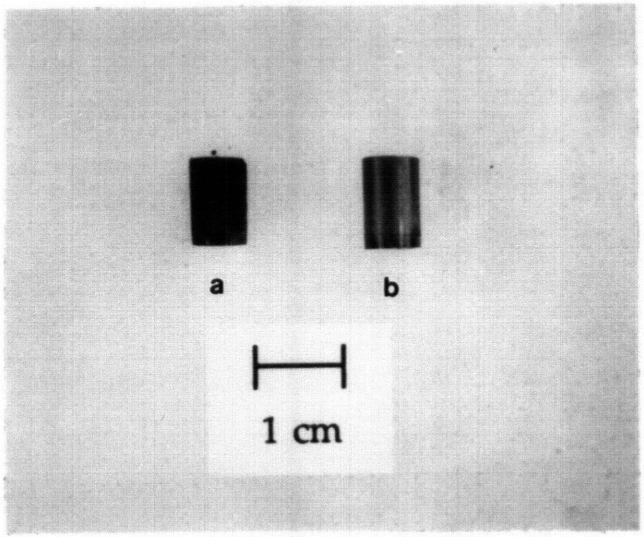

Figure 7.6 Nd-Fe-B samples which were (a) left at open-circuit (uncoupled) and (b) galvanically coupled to zinc (NaCl, 23°C). The uncoupled sample was removed after 29 days in solution and the coupled sample was removed after 29 days in solution. The dark, insoluble corrosion product on (a) is rust-colored.

The absence of any rust-colored insoluble corrosion product on the coupled samples after 29 days of immersion (Figure 7.6 (b)) indicates that the dissolution rate of Fe atoms may have been significantly reduced by galvanically coupling Nd-Fe-B to zinc. A reduction in the rate of Fe dissolution is consistent with the fact that cathodic polarization of Nd-Fe-B to E_{couple} moves the alloy into the immunity region of the Fe Pourbaix diagram [92], as shown in Figure 7.7 (a).

Cathodically polarizing Nd-Fe-B from E_{corr} to E_{couple}, however, does not move the alloy into the immunity region of the Pourbaix diagrams for either Nd or B (Figures 7.7 (b) and 7.7 (c)). A potential obstacle to protecting Nd-Fe-B using sacrificial zinc coatings is the possibility that both Nd and B could be dissolving at E_{couple}, even though the corrosion of Fe is thermodynamically prevented at this potential.

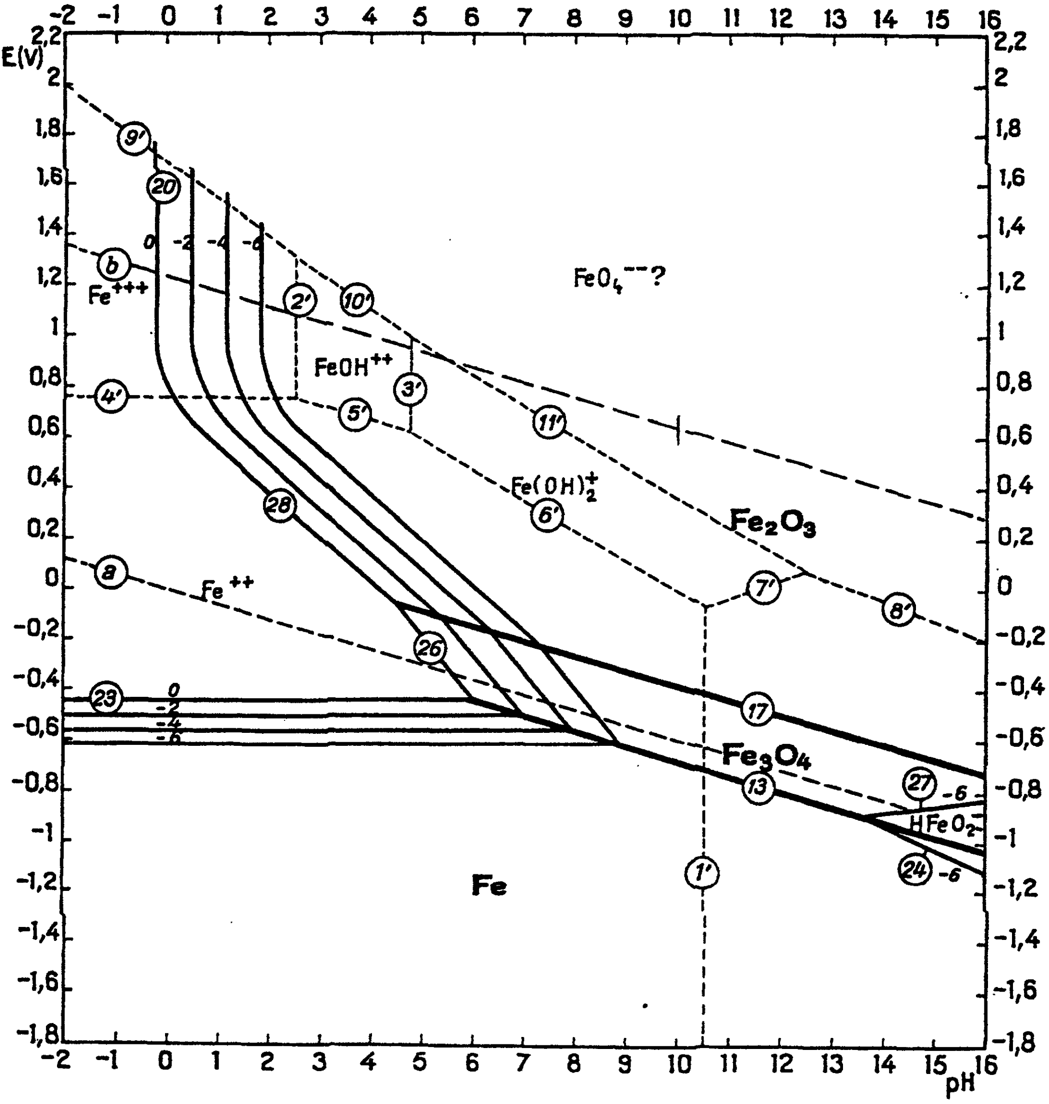

Figure 7.7 (a) Pourbaix diagram for Fe at 25°C. The average E_{corr} in the uncoupled tests (-0.82 V vs. SCE) corresponds to -0.58 V on the above diagrams, and the average E_{couple} (-1.06 V vs. SCE) corresponds to -0.82 V. The bulk pH was approximately 6.0 in both cases. Insoluble corrosion products appear in bold type and soluble corrosion products in standard type [92].

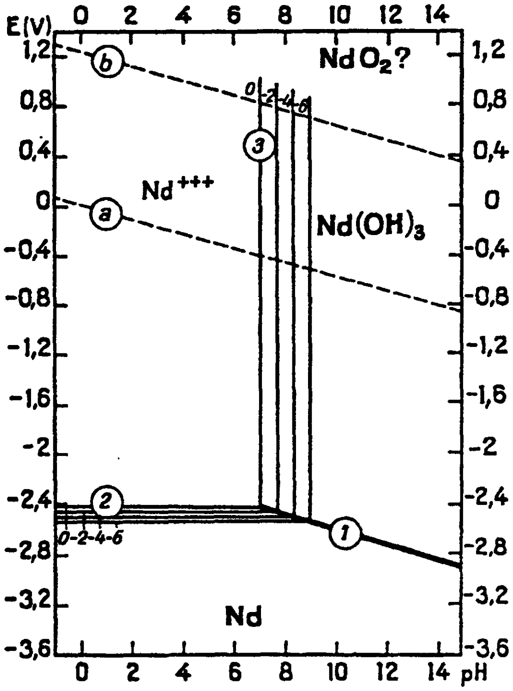

Figure 7.7 (b) Pourbaix diagram for Nd at 25°C. E_{corr} corresponds to -0.58 V on the above diagrams, and E_{couple} corresponds to -0.82 V. The bulk pH was approximately 6.0 in both cases. Insoluble corrosion products appear in bold type and soluble corrosion products in standard type [92].

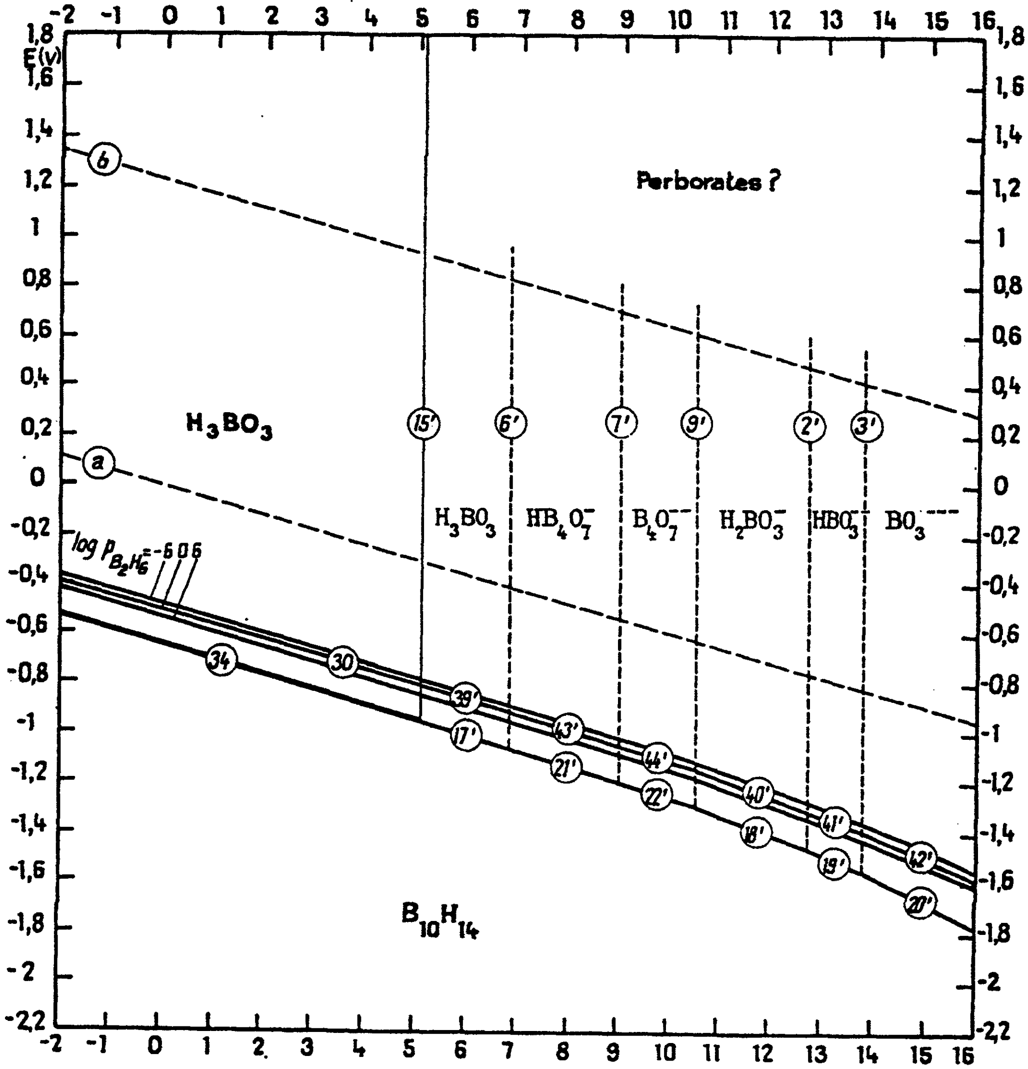

Figure 7.7 (c) Pourbaix diagram for B at 25°C. E_{corr} corresponds to -0.58 V on the above diagrams, and E_{couple} corresponds to -0.82 V. The bulk pH was approximately 6.0 in both cases. Insoluble corrosion products appear in bold type and soluble corrosion products in standard type [92].

The Pourbaix diagrams for Nd and B also indicate that an examination of insoluble corrosion products cannot be used to evaluate the anodic dissolution of Nd and B, since Nd-Fe-B is in the stability region of soluble Nd and B corrosion products at both E_{corr} and E_{couple}. The possibility of forming soluble Fe products at E_{corr} also exists, as shown in Figure 7.7 (a). It was therefore necessary to measure the amount of soluble Nd, Fe, and B corrosion products in solution.

Test solutions from both uncoupled and coupled experiments were quantitatively analyzed using inductively-coupled plasma atomic emission spectroscopy (ICP-AES), as shown in Table 7.6. Significant amounts of soluble Nd and Fe corrosion products were present after only 5 days of immersion in the solution containing the uncoupled sample. Conversely, the amount of soluble Nd, Fe, and B in the solution containing the coupled sample was below the detection limit of the spectrometer, even after 29 days of immersion.

The results of quantitative solution analysis provide conclusive evidence that the dissolution of Nd, Fe, and B was essentially prevented by galvanic coupling to zinc. Sacrificial zinc coatings appear to be capable of reducing the corrosion of Nd-Fe-B to a negligible level.

Table 7.6 ICP-AES solution analysis for coupled and uncoupled long-term immersion tests (NaCl, 23°C). The volume of test solution analyzed was 0.65 L and the exposed Nd-Fe-B area was 2.1 cm^2 in both cases. Uncoupled and coupled samples were removed after 5 and 29 days in solution, respectively.

Element	Uncoupled	Coupled
Nd	2.55 mg/L	< 0.10 mg/L
Fe	3.99 mg/L	< 0.05 mg/L
B	0.15 mg/L	< 0.05 mg/L
Zn	< 0.05 mg/L	20.30 mg/L

The marked reduction in the dissolution rate of Nd upon coupling (Table 7.6) indicates that the electrochemical activity of Nd should *not* be a barrier to the use of zinc coatings as a corrosion control method for Nd-Fe-B. The observed reduction in Nd dissolution can either be attributed to thermodynamic or kinetic factors, as discussed below.

When the Nd-Fe-B alloy is galvanically coupled to zinc, the anodic dissolution of Nd would be thermodynamically prevented only if E_{couple} (-1.06 V vs. SCE) were active to the equilibrium half-cell potential for Nd ($E_{Nd/Nd^{3+}}$). However, the standard potential of Nd is extremely electronegative ($E^{\circ}_{Nd/Nd^{3+}} = -2.67$ V vs. SCE), which indicates that the decrease in Nd dissolution upon coupling almost certainly cannot be attributed to thermodynamic considerations.

Since cathodic polarization of the Nd-Fe-B alloy from E_{corr} to E_{couple} is expected to reduce the anodic overvoltage (kinetic driving force) for the Nd dissolution reaction, it is possible that the corrosion rate of Nd could be kinetically reduced by coupling to zinc. This concept is discussed in Appendix 10.1.3, and is summarized by Equation [10.18], which shows that dissolution current is exponentially proportional to anodic overvoltage. Polarization from E_{corr} to E_{couple} can thus be qualitatively predicted to reduce the Nd dissolution current, since a Nd atom will have less driving force to corrode at E_{couple} than it has at E_{corr}. Kinetic considerations therefore may be capable of explaining the observed reduction in Nd dissolution upon coupling.

7.1.6.2 Environmentally-Assisted Cracking

Several Nd-Fe-B samples cracked unexpectedly during long-term immersion in the absence of external loading, due to the combination of residual stresses and environmental effects. Two uncoupled samples each cracked after 9 days in solution, one sample which was coupled to zinc cracked after 23 days in solution, and the other coupled sample had not cracked upon removal at 29 days, as shown in Figure 7.8.

The extent of cracking in the uncoupled tests was substantial, according to Figure 7.9 (a). Both uncoupled samples were found to crack catastrophically into several fragments after 9 days of immersion. The damage suffered by the coupled sample which cracked after 23 days in solution was much less severe, as shown in Figure 7.9 (b), as only a small fraction of the sample was lost due to cracking. The coupled sample which did not crack during 29 days of immersion is also shown in Figure 7.9 (b). The initial dimensions of the cracked

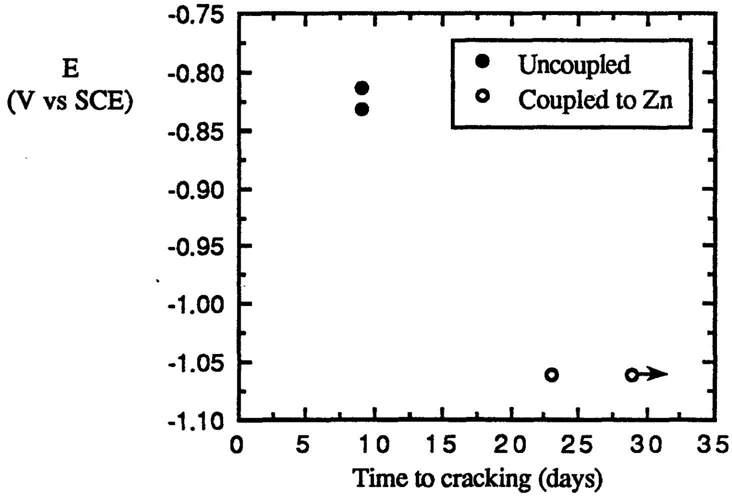

Figure 7.8 Rate of EAC of Nd-Fe-B (NaCl, 23°C) under two conditions: open-circuit (uncoupled) and coupled to Zn. The arrow represents a sample which had not cracked upon removal from the solution.

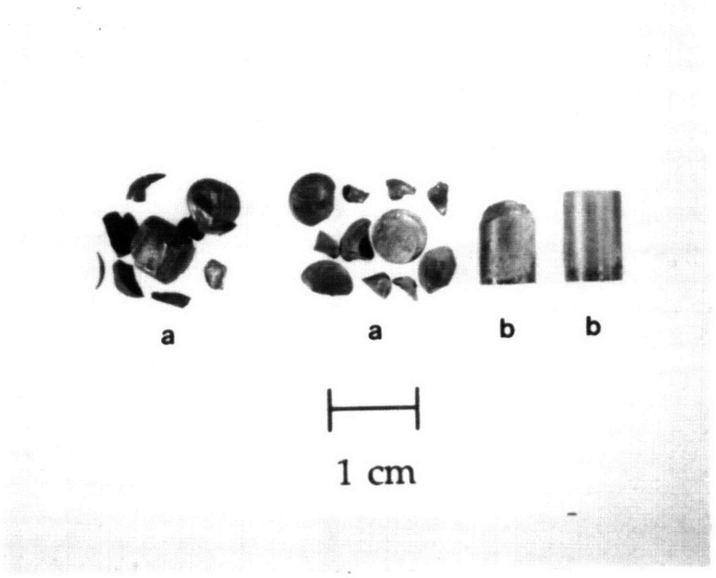

Figure 7.9 Extent of cracking exhibited by (a) uncoupled samples and (b) coupled samples after immersion in 0.5M NaCl at 23°C. The uncoupled samples were removed (upon cracking) after 9 days in the test solution, and the coupled samples were removed after 29 days of immersion.

samples were similar to the dimensions of the uncracked specimen. Cracking occurred in a brittle manner, as illustrated by the lack of plastic deformation observed (apart from a small shear lip at the end of the fracture surface). Brittle fracture was additionally indicated by the fact that each uncoupled sample was found to split into several fragments upon cracking, and also by the audible energy release which was found to accompany fracture.

One concern regarding the use of sacrificial zinc coatings as a corrosion control method for Nd-Fe-B is the fact that hydrogen production will be galvanically stimulated on the alloy at breaks in the coating. In the presence of an applied or residual stress, the rate of cracking of Nd-Fe-B could be accelerated by the resulting hydrogen uptake. Increased damage of Nd-Fe-B upon coupling was *not* found to occur, however, as galvanic coupling to zinc was found to reduce rather than accelerate the rate of cracking (Figure 7.8).

The increase in cracking resistance obtained upon coupling should be viewed in a comparative rather than an absolute sense, since cracking was not completely eliminated by coupling to zinc. Since the coupled sample which cracked during testing underwent essentially no anodic dissolution (Table 7.6), it apparently was damaged by hydrogen. The appearance of hydrogen damage upon coupling does not appear to be a barrier to the use of sacrificial zinc coatings, however, since both the rate and the extent of cracking were much less severe than in the absence of coupling.

The hydrogen reduction current density (i_H) predicted to occur at E_{couple} in this study is approximately four orders of magnitude less than the lowest i_H value measured by Bala and Szymura [49], who reported hydrogen damage to Nd-Fe-B under extremely high cathodic polarization ($i_H = 0.4 - 1.3$ A/cm^2). The i_H value at E_{couple} in NaCl at 23°C was estimated as 38 μA/cm^2, as shown previously in Table 6.1. The minimum i_H value employed in the work of Bala and Szymura was equal to 4×10^5 μA/cm^2. Since only one hydrogen atom is predicted to be produced at E_{couple} in the present study for every 10,000 hydrogen atoms produced on the samples of Bala and Szymura, their results do not appear to be pertinent to an evaluation of hydrogen damage on the base metal at breaks in the metallic coating.

It should be noted that the cause of fracture in the uncoupled samples was determined in Section 6.2 to be related to an anodic phenomenon such as stress-corrosion cracking or corrosion product wedging. Residual stresses were identified as the primary source of the stress which contributed to the observed cracking. It is believed that residual stresses were imparted to the samples during a machining treatment used to produce specimens with a common diameter. As discussed in Section 6.3.4.2, some stress could also have been provided by the wedging action of anodically formed corrosion products.

7.1.7 Practical Considerations

The results of long-term immersion testing indicate that sacrificial zinc coatings should be a feasible protection method for Nd-Fe-B. Before concluding that the protection scheme is fully viable, however, it is relevant to discuss practical considerations such as the rate of consumption of the Zn coating, and the possible effects of the coating on magnetic flux.

7.1.7.1 Coating Consumption

An important consideration in sacrificial coating corrosion control is the rate of coating consumption. The consumption rate for a sacrificial coating must be considered in terms of two distinct processes, depending on whether or not the coating has been penetrated. The zinc coating will initially act as a barrier layer, and will therefore be undergoing dissolution at its open-circuit potential if exposed to a corrosive environment. Under these conditions, a corrosion current density of 20 $\mu A/cm^2$ was estimated for zinc in NaCl at 30°C using Tafel extrapolation. This i_{corr} value corresponds to a coating corrosion rate which is relatively low, but not insignificant. Once the coating has been compromised (and Nd-Fe-B exposed), the zinc metal located in areas adjacent to the locally exposed Nd-Fe-B will be anodically polarized to the Zn/Nd-Fe-B couple potential. Polarization will increase the consumption rate of the coating. The anodic dissolution rate for zinc was predicted to be 73 $\mu A/cm^2$ at E_{couple} (NaCl, 30°C). These results suggest that the coating consumption rate may be a significant concern, especially in areas where the coating has been penetrated.

Although anodic dissolution does tend to limit the service life of zinc coatings, previous work indicates that the consumption rates estimated in the above calculations are larger than would actually be expected in practice. In near-neutral environments, the formation of a natural protective coating of zinc compounds (consisting of the hydroxide, carbonate, and basic carbonate of zinc) has been found to add significantly to the life of the metal in *both* the uncoupled and coupled conditions, without preventing Zn from providing cathodic protection to the base metal [93]. The anodic dissolution rates cited above were based on polarization tests conducted after 1 hour of immersion, and it is thus likely that insoluble Zn corrosion products did not have sufficient time to build up on the zinc electrodes during the tests. The calculated dissolution rates are liable to be a significant overestimate of the rates obtained in practice, since the formation of corrosion products on zinc was not considered.

The consumption rate of zinc coatings can *also* be reduced because of Zn corrosion product formation on the Nd-Fe-B cathode. The calculated zinc consumption rates are believed to be excessively high because the precipitation of Zn corrosion products on Nd-Fe-B was not accounted for in the calculations; support for this contention is provided below.

The galvanic current density was monitored during the long-term coupled immersion tests, in part because of the direct relationship of i_g to the amount of anodic dissolution occurring on zinc under coupled conditions. The results of this test are shown in Figure 7.10. The first measured data point in Figure 7.10 is 93 $\mu A/cm^2$, which is lower than the average galvanic current density calculated from the 20 hour tests conducted at 30°C (120 $\mu A/cm^2$). This effect is likely due to the temperature difference which existed between the two test solutions. The magnitude of the galvanic current is controlled to a great extent by the rate of oxygen transport to the Nd-Fe-B surface, and the faster oxygen diffusion rate at 30°C relative to 23°C would be expected to result in a greater measured value of galvanic current.

The observed decrease in the galvanic current density after 1-2 days of long-term immersion (Figure 7.10) suggests that coating consumption due to zinc dissolution will decrease significantly over time. The decrease in i_g can be attributed to the precipitation of insoluble $Zn(OH)_2$ on the Nd-Fe-B cathode. The oxygen reduction reaction is known to

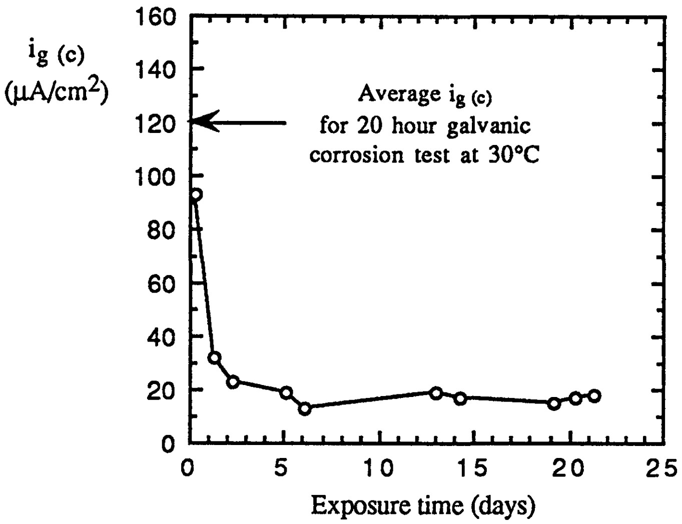

Figure 7.10 Galvanic current values measured during a long-term coupled immersion test (NaCl, 23°C).

occur on Nd-Fe-B at E_{couple}, and the hydroxyl ions produced by this reaction should lead to local alkalinization at the Nd-Fe-B surface. Increases in pH tend to lower the solubility of the corrosion products of zinc, and $Zn(OH)_2$ is thus often found to precipitate on the cathode of a galvanic cell which contains zinc as the anode [94,95].

White corrosion products were visibly observed to precipitate on Nd-Fe-B during the experiment. It is very likely that these corrosion products were zinc-based, since zinc was the only element found to exhibit corrosion in the coupled test cell (as shown in Table 7.6). EDX analysis additionally verified the presence of a zinc-containing solid on a coupled Nd-Fe-B sample after it had been rinsed and removed from the test solution.

$Zn(OH)_2$ is known to inhibit the oxygen reduction reaction on many metals [94,95]. The rate of zinc dissolution and the magnitude of the galvanic current are both closely related to the rate of oxygen reduction on the Nd-Fe-B surface, since the electrons produced by zinc dissolution flow through the ammeter circuit (registering as galvanic current) and are then consumed by the reduction of oxygen on Nd-Fe-B. Any decrease in the rate of the oxygen reduction reaction is expected to decrease both the magnitude of i_g and the rate of zinc dissolution. The precipitation of a cathodic inhibitor such as $Zn(OH)_2$ on Nd-Fe-B will decrease $I_{c\ (Nd\text{-}Fe\text{-}B)}$, thus leading to a decrease in both i_g and $I_{a\ (Zn)}$. The approximately steady-state value exhibited by the galvanic current after about 6 days indicates that the cathodic inhibition is relatively stable over time. The observed reduction in i_g after 1-2 days (presumably due to $Zn(OH)_2$ precipitation) corresponds to a decrease of nearly an order of magnitude, which supports the notion that the anodic dissolution rate previously calculated for coupled zinc is significantly greater than the rate likely to be obtained in practice. It is expected that the zinc dissolution rates calculated earlier in this section would be obtained for a short period of time, and would then decrease due to the formation of zinc corrosion products on both the zinc electrode and the Nd-Fe-B electrode.

7.1.7.2 Organic Coating Overlay

The life of a sacrificial zinc coating can be significantly extended by covering the metal with an organic coating (such as a paint), as discussed previously in this section. The organic coating serves as a barrier between the zinc and the electrolyte, and will therefore delay the exposure of the metal to the corrosive environment. The presence of the organic coating should extend the life of the zinc coating, and thus the life of the base metal, by delaying the onset of zinc corrosion.

7.1.7.3 Effect of Coatings on Magnetic Flux

A coating which is capable of controlling the corrosion of Nd-Fe-B yet interferes with its primary function as a permanent magnet would clearly be unacceptable. Fortunately, corrosion control of Nd-Fe-B via zinc and/or organic coatings does not present an inherent problem from a magnetic standpoint, since these coating materials will not affect the magnetic field produced by the Nd-Fe-B alloy. The only possible effects of such a coating on magnetic properties would result from the fact that magnetic flux decreases with the square of the distance from the magnet [1]. The magnetic field produced by Nd-Fe-B would thus be greatly diminished at the surface of a very thick coating. Coatings of 75 μm or more in thickness can be utilized, however, without adverse effects on the magnetic performance of Nd-Fe-B [19]. It is *also* important that the zinc coating not be excessively thin, since previous work has shown that the effectiveness of a zinc coating in controlling corrosion is essentially proportional to its thickness [93].

7.1.7.4 Methods of Application

Zinc coating application methods include hot-dip galvanizing, electroplating, metallization (thermal spray) and zinc vapor deposition. The possibility of hydrogen damage during electroplating indicates that this application method should be used with caution.

7.1.8 Summary of Protection via Sacrificial Zinc Coatings

The present study focused on evaluating the protection conferred to Nd-Fe-B once a Zn/Nd-Fe-B galvanic couple has been formed due to coating penetration. Quantitative solution analysis was used to demonstrate that the dissolution of Nd, Fe, and B was essentially prevented by galvanically coupling Nd-Fe-B to zinc in NaCl at 23°C. Galvanic coupling to zinc also reduced the rate of environmentally-assisted cracking of Nd-Fe-B. Sacrificial zinc coatings appear to be a viable, cost-effective corrosion control method for Nd-Fe-B.

7.2 Corrosion Control by Ribbon Boundary Modification

The benefits of minimizing pitting attack in the Nd-Fe-B system have been described in the introduction to Chapter 7. The flux loss experienced by the magnet due to pitting is expected to be a design concern under certain conditions; when the magnet has a high surface area to volume ratio and is to be used in a relatively aggressive environment, for example. Pitting has also been empirically correlated to the presence of environmentally-assisted cracking in the Nd-Fe-B system. An increase in the resistance of the alloy to pitting would therefore be expected to increase its viability from the standpoint of both metal loss and susceptibility to anodic cracking. The present section describes a proposed corrosion control method which may ultimately be capable of minimizing pit initiation.

As discussed in Section 5.4, the identification of sulfide inclusions as pit initiation sites in stainless steels [72] has led to improved pitting resistance through the use of cleaner metallurgical practices. It is believed that a similar methodology can be applied to the Nd-Fe-B system, since the ribbon boundaries have been identified (Section 5.4) as sites of preferential pit initiation. Ribbon boundary modifications can be attempted with the intention of improving the resistance of Nd-Fe-B to pit initiation. Such a corrosion control method may have several benefits. If a substantial reduction in pitting corrosion could be achieved, it might be possible to utilize the material in the uncoated state under certain conditions; in less aggressive environments, for example. It is likely that a more moderate increase in pitting resistance would be obtained, especially in view of the fact that not all pits were found to initiate on the boundaries. In this case, ribbon boundary modifications could be used to improve the resistance of Nd-Fe-B to pitting attack in situations where the base metal is exposed during service due to failure of the primary corrosion control method (e.g. a barrier coating). Such an improvement would be especially beneficial if the barrier coating employed cannot provide sacrificial protection to Nd-Fe-B (e.g. nickel, epoxy).

7.2.1 Densification of Nd-Fe-B

It was hypothesized in Section 5.4 that pre-existing porosity may be the characteristic of the ribbon boundaries which is responsible for preferential pit initiation. Pores may act as sites of microcrevice formation, with the resulting localized attack appearing in the form of pits. If the pore-microcrevice hypothesis is correct, it should theoretically be possible to drastically reduce the susceptibility of the material to pitting attack. Improved hot pressing processes can be utilized to collapse the existing pores, thus fully densifying the material.

Controllable processing parameters include temperature, time, and isostatic pressure. Moderate increases above the normal hot pressing temperature of 700°C are unlikely to induce phase transformations, but undesirable grain growth may become a problem as the temperature is elevated [96]. Large temperature increases should not be a prerequisite to densification in any case, as the material has sufficient plasticity at 700°C to accomodate the shape change associated with die upsetting. It is believed that an increase in the isostatic pressure (and perhaps also the pressing time) is more likely to yield the desired result. It is also possible that finer crushing of the starting ribbons might lead to a fully dense final product, if combined with one of the processing modifications describe above. The void size between the crushed ribbon fragments should decrease if finer crushing is utilized, and less adjustment of the hot pressing parameters may be needed to produce a fully dense part.

A possible drawback of the densification method is associated with the fact that standard hot pressing modifications are only capable of collapsing pores which are internal to the metal. Pores which exist at the free surface are restrained from collapse by the presence of the pressurizing gas, which enters the surface pores but not the internal pores. The pores residing at the surface are precisely the ones which may initiate pitting attack, and if the magnet is to be used directly after pressing (i.e. with no subsequent machining or grinding treatment), the surface pores will need to be collapsed if the process is to have any effect on corrosion resistance. Innovative processing modifications may need to be devised in order to heal the surface porosity in such cases. Fortunately, most of the h.p. and d.u. parts fabricated by RSP are pressed or upset to near-net shape, and then machined to net shape. If improved pressing practices can be used to collapse the internal porosity, the metal containing the surface pores would then be removed by machining, presumably leaving a pore free surface to be presented to the electrolyte in service.

The level of economic cost associated with modifying the hot pressing process should be considered. The additional expenditure needed to fully densify the material cannot be accurately determined, however, until the process is attempted by the manufacturer. The benefit received in return for the extra cost would be the increased pitting resistance of the alloy. If the associated cost increase were not prohibitive, all magnets could be processed to 100% density as part of a routine procedure. It is possible, however, that the additional processing costs may only be justified in certain cases. For example, customers who plan to use their materials in aggressive environments (and are thus concerned about corrosive degradation) may be willing to pay for the additional cost of processing modifications.

7.2.2 Prevention of Ribbon Boundary Oxidation

The ribbon boundaries in rapidly solidified Nd-Fe-B were observed to be enriched in Nd and O (and depleted in Fe). It is conceivable that the chemical heterogeneity of the ribbon boundaries may contribute to pit initiation, even though it was considered to be more plausible in Section 5.4 that pre-existing porosity was the cause of pit initiation.

In Section 5.4, the compositional inhomogeneities present at the boundaries were attributed to the oxidation of Nd at the free ribbon surfaces during processing. Prevention of Nd oxidation might thus contribute to pitting resistance by eliminating the chemical heterogeneity at the ribbon boundaries. It is expected, however, that it would be extremely difficult to produce oxide-free ribbon boundaries because of the strong tendency of Nd to oxidize in air. A calculation designed to evaluate this possibility appears below.

Nd oxidizes in air to form the stable sesquioxide (Nd_2O_3), as per the following reaction:

[7.1] $$2\ Nd\ (s) + \frac{3}{2} O_2\ (g) = Nd_2O_3\ (s)$$

The standard free energy of formation ($\Delta G^\circ_{formation}$) of Nd_2O_3 at 23°C is -138 kilocalories per gram-atom of oxygen [97], which is equivalent to -276 kilocalories per mole of O_2. The equilibrium oxygen partial pressure in the Nd/Nd_2O_3 system can be calculated using the following equation [98]:

[7.2] $$\Delta G^\circ_{formation} = R \cdot T \cdot \ln (P^{eq}_{O_2})$$

The calculated $P^{eq}_{O_2}$ is 10^{-203} atmospheres. This result indicates that the oxygen partial pressure would need to be kept below this value in order to prevent Nd from oxidizing at room temperature. It is unrealistic to believe that this condition can be attained within a rapid solidification manufacturing facility, even through the use of reducing or inert gas atmospheres. If pit initiation at the ribbon boundaries is related to neodymium oxide formation, this problem clearly would have to be mitigated using an alternative method.

The remarkably low value determined for $P^{eq}_{O_2}$ using equation [7.2] suggests that this calculation might be in error. In order to judge the accuracy of the obtained value, the equilibrium oxygen partial pressure was determined for another metal which also has a very strong tendency to oxidize in air (Ca), using an alternative method. An Ellingham diagram, which is a plot of $\Delta G^{\circ}_{formation}$ versus T, can provide rapid estimates of equilibrium partial pressure values using a nomograph which is attached to the diagram. The $P_{O_2}^{eq}$ value for the Ca/CaO system at 23°C was estimated as approximately 10^{-200} atmospheres, using the Ellingham diagram. The exact $P_{O_2}^{eq}$ value for Ca/CaO was subsequently calculated as 10^{-212} atmospheres, using equation [7.2] in conjunction with the known $\Delta G^{\circ}_{formation}$ for the Ca/CaO system (-289 k·cal/mole of O_2). Sharma [99] has stated that calcium is the only common metal capable of reducing Nd_2O_3, and the $P_{O_2}^{eq}$ value calculated for the Ca/CaO system is thus consistent with the known oxidation tendencies of these two metals.

7.2.3 Alternative Ribbon Boundary Modifications

The work described in Section 5.4 established a definite correlation between pit initiation sites and the boundaries between adjacent ribbon fragments. This correlation has been attributed to the presence of pores at the ribbon boundaries, and an appropriate course of action designed to address this issue has been recommended in Section 7.2.1. Even if the pore-microcrevice hypothesis is not the correct explanation for the preferential initiation of pits at the ribbon boundaries, this phenomenon can clearly be attributed to some tangible characteristic of the ribbon boundary. It is possible that a detailed study of this topic might elucidate other possible explanations for the observed tendency of pits to initiate at the ribbon boundaries; alternative ribbon boundary modifications might then become apparent.

7.2.4 Implementation of Corrosion Control Methods

The corrosion control methods described in this section are obviously only potential methods at this point, since no actual testing has been performed to verify or refute their effectiveness. As discussed in Chapter 9, it is planned to pursue the densification method, hopefully with the assistance of the primary manufacturer of rapidly solidified Nd-Fe-B.

7.2.5 Combination with Other Corrosion Control Methods

A particularly important benefit of the proposed ribbon boundary modification is that such a corrosion control method could be used in parallel with the zinc coating-organic coating protection scheme discussed in Section 7.1 to produce a Nd-Fe-B magnet with substantial resistance to corrosive attack.

It is believed that the use of ribbon boundary modification along with a zinc coating-organic coating bilayer would allow several levels of corrosion protection to be conferred to the alloy. The organic coating will initially act as a barrier layer which shields the zinc and the Nd-Fe-B base metal from the corrosive electrolyte. When the organic coating is eventually compromised due to solution uptake, the zinc layer will provide barrier protection owing to the formation of sparingly soluble corrosion products which allow it to corrode at a very slow rate. When the zinc coating is eventually penetrated due to cracking or prolonged corrosion, the zinc will provide sacrificial protection to the exposed Nd-Fe-B at breaks in the coating. When the protection at the breaks in the coating is finally exhausted due to the sacrificial consumption of zinc, ribbon boundary modifications (if effective) would then impart improved pitting resistance to the Nd-Fe-B substrate. It should be clear that such an approach to corrosion control is likely to be more successful than the simple reliance on one method (e.g. a barrier coating which cannot provide sacrificial protection).

8. Conclusions

1. Pitting attack was found to be the primary form of corrosion in rapidly solidified Nd-Fe-B alloys in NaCl and Na_2SO_4 solutions at both 23°C and 80°C. This form of corrosion has not been previously reported for RSP Nd-Fe-B. Pits were found to initiate within 15 minutes of immersion, and propagated to a depth of more than 200 μm within three months in NaCl at 23°C. Intergranular corrosion was not found to be a significant attack mode in rapidly solidified Nd-Fe-B. It had been previously believed by many researchers that intergranular corrosion was the primary mode of attack for this material.

2. Pitting is considered to be a less severe form of attack than intergranular corrosion in terms of the magnetic flux loss expected to result from corrosive attack during service. Flux loss is directly related to the volume of metal dissolved, rather than to the rate of metal penetration. Since pitting results in a high metal penetration rate but only a moderate loss in metal volume, the corrosion problems of the alloy are not as serious as they would be if intergranular attack were occurring. Corrosive metal loss is still expected to be a problem for this material in many environments, however. Permanent magnets are thin by design, and even the moderate metal loss associated with pitting can cause a magnet to lose a significant percentage of its flux over time. The actual amount of pitting which can be tolerated will depend upon the geometry and the design requirements of the magnet considered.

3. Pits were found to initiate preferentially but not exclusively at the boundaries between adjacent rapidly solidified ribbons in the material. Enrichment of both neodymium and oxygen was detected at the ribbon boundaries, as a result of oxidation of the free ribbon surfaces prior to hot pressing. Pores were also found to be located preferentially at the ribbon boundaries, as a result of incomplete

metallurgical bonding of the adjacent ribbons during pressing. It is believed that pit initiation is related to the pre-existing porosity within the material; pit initiation at pore sites is thought to occur by a microcrevice type of mechanism.

4. Environmentally-assisted cracking (EAC) of Nd-Fe-B was found to occur under free corrosion conditions in NaCl, and to a lesser extent in Na_2SO_4. Hydrogen permeation tests indicate that the fracture is related to an *anodic* cracking mechanism rather than to hydrogen embrittlement. It is believed that the observed EAC may be specifically related to the presence of pitting attack. The combination of localized anodic dissolution and stress concentration within a pit can conceivably lead to crack initiation and ultimately to fracture. Insoluble corrosion products formed as a result of metal dissolution within pits might also contribute to fracture by exerting a wedging action which creates tensile stresses at the base of cavities in the material.

5. Two modes of corrosive degradation can therefore be identified for RSP Nd-Fe-B alloys: metal loss and anodic cracking. Both degradation modes can lead to a loss of magnetic flux, and eventually to magnet failure if corrosion is not controlled. In particular, the elimination of pitting attack should be targeted in order to increase the resistance of Nd-Fe-B to both magnetic flux loss and anodic cracking.

6. It has been conclusively demonstrated that zinc coatings are capable of providing complete protection to Nd-Fe-B at breaks in the coating. A zinc coating-organic coating protection scheme thus appears to be a cost-effective corrosion control method which is able to provide both barrier and sacrificial protection to Nd-Fe-B.

7. It may be possible to produce a magnet with increased resistance to pitting attack by using improved processing techniques which result in full densification of the metal, as elimination of pre-existing porosity may remove the sites of pit initiation.

9. Recommendations for Future Work

The following areas have been identified as possible sources of future investigation:

1. *Evaluation of the Microcrevice Hypothesis.* In Section 5.4, it was postulated that pits might be initiating at pre-existing pores in the material via microcrevice formation. This hypothesis should be evaluated both theoretically and experimentally.

A theoretical study of the microcrevice formation can be accomplished by modeling the chemical and electrochemical conditions likely to exist within a pore. An understanding of the prevailing conditions within pores after 15 minutes of immersion in the test solution should provide a reasonable basis for determining whether or not the pores are likely to serve as initiation sites for localized corrosion. Plans to carry out such a modeling analysis are underway in H.H. Uhlig Corrosion Laboratory.

The microcrevice hypothesis can be evaluated experimentally by using improved hot pressing procedures to produce a fully dense (pore-free) starting material. Corrosion testing of this fully dense material can then be performed. It is hoped that the results of such experiments would conclusively prove (or disprove) the microcrevice hypothesis. Such experiments would also have the added benefit of indicating whether corrosive attack can be mitigated by using improved hot pressing procedures.

2. *Mode of Environmentally-Assisted Cracking.* In Section 6.2, it was conclusively demonstrated that fracture occurred by an anodic cracking mechanism rather than by a hydrogen-assisted mechanism. Given the potential importance of this degradation mechanism, further study aimed at investigating the specific type of anodic cracking which controls the behavior of Nd-Fe-B is clearly warranted. Ancillary topics related to the EAC

investigation include an analysis of the effect of electrolyte anion on the cracking behavior of Nd-Fe-B, as well as a determination of the controlling crack path during fracture. A comprehensive study of the EAC of Nd-Fe-B is being conducted in the Uhlig Laboratory, as a logical extension to this work.

3. *Evaluation of Residual Stress Production Methods*. The influence of residual tensile stresses on cracking behavior was qualitatively demonstrated in Section 6.3.2. Anodic cracking of Nd-Fe-B appears to depend upon the presence of both corrosive attack and residual tensile stresses in the magnet. Minimization of residual stresses should thus help to control cracking. A determination of the magnitude of stresses which can be produced by machining Nd-Fe-B would be valuable, as would an investigation of methods capable of reducing the amount of residual stress imparted to the alloy during machining.

4. *Practical Studies on Sacrificial Zinc Coatings*. It was conclusively demonstrated in Section 7.1 that zinc coatings can provide sacrificial protection to Nd-Fe-B at breaks in a zinc coating. Certain practical aspects of this corrosion control method were not investigated, however, such as the optimal coating application method, optimal thickness, and precoating preparation methods. Such parameters would all need to be determined before the coating could actually be utilized in service. It is also important to match the zinc coating to an appropriate organic coating in order to maximize the effective lifetime of the coating system.

10. Appendices

Appendix 10.1 contains a detailed introduction to some of the electrochemical techniques utilized in the present study. Appendix 10.1.1 describes the basics of potentiodynamic and potentiostatic polarization testing. Appendix 10.1.2 outlines the procedure for analyzing EIS data via equivalent circuit modeling. Appendix 10.1.3 demonstrates the process utilized in the analysis of galvanic corrosion systems; specific emphasis is placed on the evaluation of coating-base metal systems.

In Appendix 10.2, the equivalent circuit modeling technique is used to quantitatively analyze the EIS data collected in the present work.

Appendix 10.3 contains an explanation of the Kramers-Kronig transformations, which are used to evaluate the validity of EIS data in terms of their ability to be input to an equivalent circuit model. Appendix 10.4 provides the source code for the computer program used to perform the Kramers-Kronig transformations.

Appendix 10.5 consists of a quantitative analysis of the validity of considering pits as critical flaws in Nd-Fe-B, using Linear Elastic Fracture Mechanics as the analytical technique. The validity of using plane-strain conditions in the analysis is also confirmed in this section of the appendix.

10.1 Fundamentals of Electrochemical Methods

10.1.1 Potentiodynamic Polarization Testing

Determination of the polarization curve (current-potential relationship) for the metal-electrolyte system under study is a very basic and important test method in corrosion science. The experiment is typically performed using an instrument called a potentiostat, which functions by controlling the electrical potential of the test electrode and measuring the resulting current. A current-potential, or polarization curve is generated by scanning the electrode potential at a known rate and measuring the current as a function of potential. The electrode potential is known to have a substantial effect on the rate of electrochemical reactions. For example, polarization of the electrode to more electropositive (anodic) potentials generally increases the rate of oxidation reactions in the system while decreasing the rate of reduction reactions. These changes in rate are registered experimentally as changes in the cell current. The proportionality between reaction rate and current is derived from Faraday's Law, as described in Section 4.3.

The potential of the electrode under test (known as the working electrode) is controlled relative to a reference electrode such as a saturated calomel electrode. The potential of the reference electrode is essentially stable during the experiment. Current flow in the cell occurs in a circuit including the working electrode and an inert counter electrode, as shown in Figure 10.1. Current flow is both electrolytic and electrical. The electrolytic part of the circuit consists of the electrolyte between the working electrode and the counter electrode. The electrical part of the circuit consists of the metal electrodes, wire leads, and the potentiostat. The working electrode is actually part of two different circuits, a potential-controlling circuit and a current-measuring circuit. The potential-controlling circuit consists

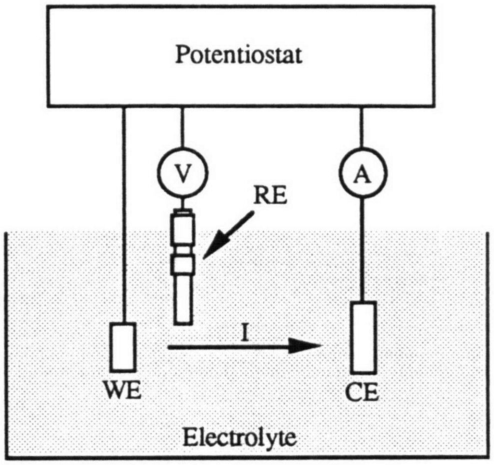

Figure 10.1 Schematic illustration of a potentiostat. The abbreviations WE, RE, and CE refer to the working, reference, and counter electrodes, respectively. The potential is controlled using a voltmeter (V) and the current measured using an ammeter (A).

of the working electrode, the reference electrode, and a high resistance voltmeter known as an electrometer. The current-measuring circuit includes the working and counter electrodes in addition to an ammeter. The potentiodynamic scan is normally begun from the corrosion potential (E_{corr}), which is also known as the open-circuit potential because no external current flows while the metal resides at this potential. The scan will proceed either in the anodic (electropositive) or the cathodic (electronegative) direction. As the scan proceeds, the difference between the corrosion potential and the potential enforced by the potentiostat is known as overpotential, which is designated by η, and is also referred to as overvoltage. When anodic polarization occurs, it can be said that an anodic overpotential, η_a, is being applied to the sample. Both anodic and cathodic polarization diagrams are normally measured for each metal-electrolyte system of interest. Polarization diagrams can provide an investigator with much important information. The presence or absence of passivation in a given metal-electrolyte system can be established using this method. For example, Figure 10.2 shows metals which are (a) passive at open-circuit, (b) passive only when anodic polarization is externally applied, and (c) active.

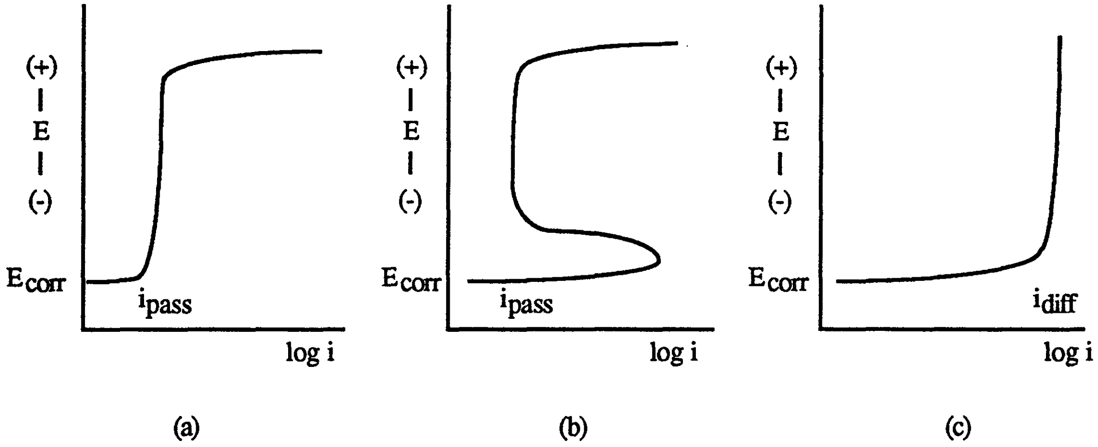

Figure 10.2 Schematic anodic polarization curves indicating (a) spontaneous passivation (b) active-passive behavior and (c) active behavior. The active metal will exhibit a vertical region when the rate of anodic dissolution becomes limited by the diffusion of metal ions away from the electrode ($i_{diff} >> i_{pass}$).

The important electrochemical reactions in a system can often be inferred from polarization diagrams, as different characteristic features of the curves can indicate the presence of certain types of reactions. For example, active anodic polarization behavior exhibiting a linear E-log i relationship in the vicinity of the corrosion potential (as in Figure 10.2 (c)) typically indicates that the rate of the metal dissolution reaction is being controlled by the rate of transfer of metal ions across the metal-electrolyte interface (charge-transfer control). Electrode potential changes tend to have a marked effect on the rate of electrochemical reactions controlled by interfacial charge-transfer, as discussed previously in this section. Since the nature of the functional relationship between current and potential in this type of reaction is logarithmic, an E-log i plot is linear for reactions under charge-transfer control.

Similarly, the controlling cathodic reaction can often be inferred from observing the cathodic polarization curve. In near-neutral solutions, the observed cathodic polarization behavior depends on the aeration conditions of the test electrolyte, and normally exhibits one of the forms shown in Figure 10.3 In deaerated near-neutral solutions, the main

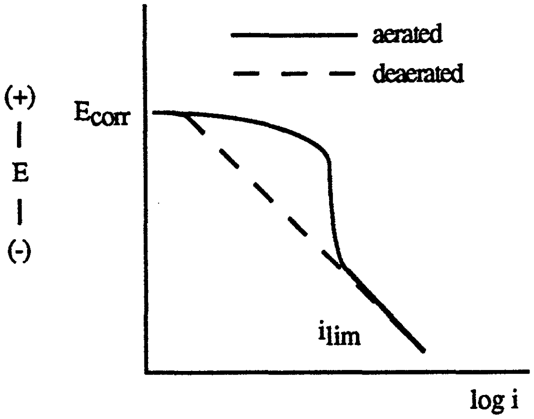

Figure 10.3 Typical cathodic polarization curves in near-neutral solutions. The diffusion-limited current density for the oxygen reduction reaction is labeled i_{lim}.

cathodic reaction tends to be the reduction of water to hydrogen. This reaction is typically under charge-transfer control, which can be inferred from the fact that its E-log i diagram is linear.

In aerated near-neutral solutions, however, a significant portion of the cathodic polarization curve appears to be vertical rather than linear. In this region of the curve, an increase in the degree of cathodic polarization has essentially no effect on the reaction rate. The rate of the cathodic reaction is controlled not by charge-transfer in this case, but by the rate of diffusion of oxygen to the electrode surface, a process which is not affected by changes in electrode potential. The cathodic reduction of dissolved oxygen atoms to hydroxyl ions is usually under mass-transfer control owing to the limited solubility of oxygen in aqueous solutions. The actual charge-transfer reaction (oxygen reduction) at the interface is assumed to occur much more rapidly than the rate of oxygen diffusion up to the surface. Since these two processes (mass-transfer and charge-transfer) must occur in series for the overall reaction to proceed, the slower step (mass-transfer) will control the overall process.

Polarization diagrams can provide other useful information in addition to identifying the types of reactions taking place on the corroding metal. The analysis of galvanic corrosion systems, for example, is greatly facilitated through the use of anodic and cathodic polarization curves, as described in Section 10.1.3. Another important use of polarization diagrams is that corrosion rates can be estimated from the current-potential relation using the Tafel extrapolation technique, as shown in Figure 10.4. In this technique, the linear (Tafel) region of each polarization curve is extrapolated until it intersects the corrosion potential (E_{corr}). This intersection provides a quantitative estimate of the corrosion current density, i_{corr}, in the system. The corrosion current density is a very important quantity since i_{corr} can be directly converted to the rate of corrosive metal loss via Faraday's Law:

$$\text{corrosion rate} = \frac{\text{weight loss}}{\text{time}} = \frac{m \cdot i_{corr}}{n \cdot F} \qquad [10.1]$$

where m is the atomic weight of the metal (g/mole), n is the number of electrons transferred in the dissolution reaction, and F is Faraday's constant (96,500 coulombs/equivalent).

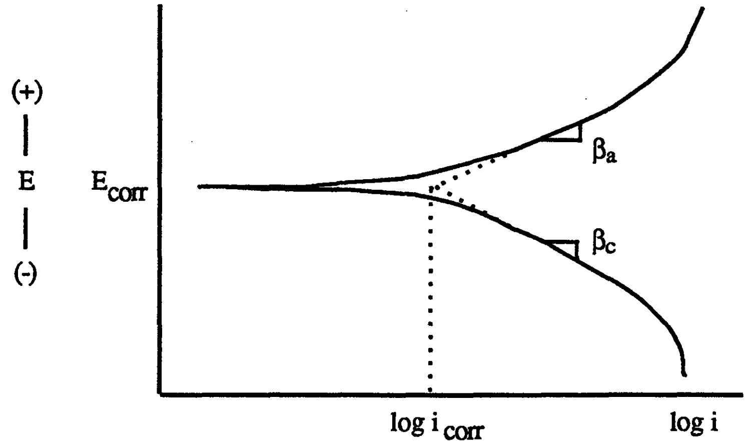

Figure 10.4. Use of the Tafel extrapolation technique to estimate i_{corr} from polarization diagrams. The quantities β_a and β_c are the Tafel slopes for the anodic and cathodic reactions, respectively.

10.1.2 Cyclic Anodic Polarization

Potentiodynamic anodic polarization tests can additionally be used to indicate the presence or absence of localized corrosion, if scan reversal (cyclic polarization) techniques are employed. By reversing the direction of the anodic scan at a predetermined potential value, the current densities measured in the forward and reverse polarization scans can be compared at a constant potential, as shown in Figure 10.5. The presence of higher current densities in the reverse scan (Figure 10.5 (a)) is known as hysteresis, which normally indicates that the rate of anodic dissolution has increased as a direct result of the corrosion process which took place during the forward scan.

The increase in current density is typically attributed to the compositional changes (such as acidification) which occur during corrosive attack in localized environments such as pits or crevices. As anodic dissolution proceeds within a local environment, the restricted mass-transfer out of the local area causes the concentration of metal cations to increase markedly

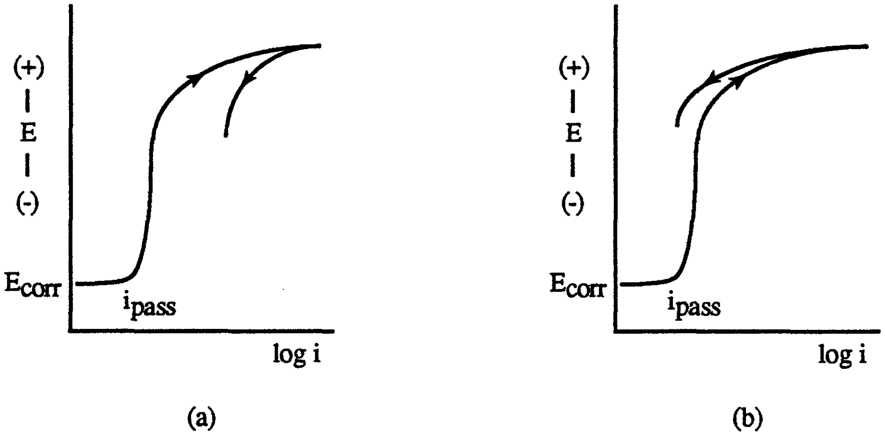

Figure 10.5 Cyclic anodic polarization scans (a) with and (b) without observed hysteresis.

within the localized or occluded region. Once the metal cation concentration reaches a certain critical value, the cations will react with water according to:

[10.2] $$Me^{n+} + H_2O \rightarrow Me(OH)^{(n-1)+} + H^+$$

The process represented by reaction [10.2] is known as hydrolysis. The production of H^+ ions via hydrolysis reactions will cause marked acidification to occur within the localized region. This acidification leads to the formation of an occluded electrolyte which is highly aggressive to the metal, and the rate of corrosive attack will therefore increase (causing a rise in the measured dissolution current). H^+ ion production additionally leads aggressive anions such as Cl^- to migrate into the acidified area due to electroneutrality considerations. The accumulation of such anions can also increase the rate of attack on the metal. Under conditions where hydrolysis occurs, the reverse scan actually takes place in a more aggressive electrolyte than does the forward scan, resulting in higher current. The local concentration buildup resulting from hydrolysis will not be readily diluted with time, due to the aforementioned mass-transfer limitations out of the local area. It should be noted that other processes, such as IR voltage drop into an occuded area, can also have a significant effect on the development of localized attack under certain conditions.

The accumulation of H^+ ions and aggressive anions does not occur to the same extent on the bulk surface as it does within an occluded cell. Unrestricted mass-transfer away from the surface tends to prevent large metal ion concentrations from building up, and the extent of hydrolysis is thus significantly less than within a localized or occluded area.

The absence of higher currents during a reverse scan (Figure 10.5 (b)) indicates that the increase in current with increasing potential during the forward scan was caused by an anodic process (such as oxygen evolution) which is unrelated to localized corrosive attack.

10.1.3 Potentiostatic Anodic Polarization

Potentiodynamic polarization tests were originally derived from a basic technique known as potentiostatic polarization. In this technique, the potential is held at a constant value and the dissolution current is monitored as a function of time. Information can be obtained not only from the actual value of the measured current but also from the changes exhibited by the current with time. If the measured current is relatively constant over time (Figure 10.6 (a)), for example, it is likely that dissolution is occurring in a film-free regime with the anodic reaction under charge-transfer control. Significant decreases in the current with time generally indicate that the metal is undergoing passivation, with the decrease in current corresponding to the formation of the protective film (Figure 10.6 (b)). The presence of localized corrosion can also be diagnosed using the potentiostatic anodic polarization method. An increase in current with time (Figure 10.6 (c)) usually indicates that a local electrolyte is becoming more aggressive over time due to hydrolysis, leading to an increase in the rate of corrosive attack and to a corresponding rise in the dissolution current, as described in Section 10.1.2.

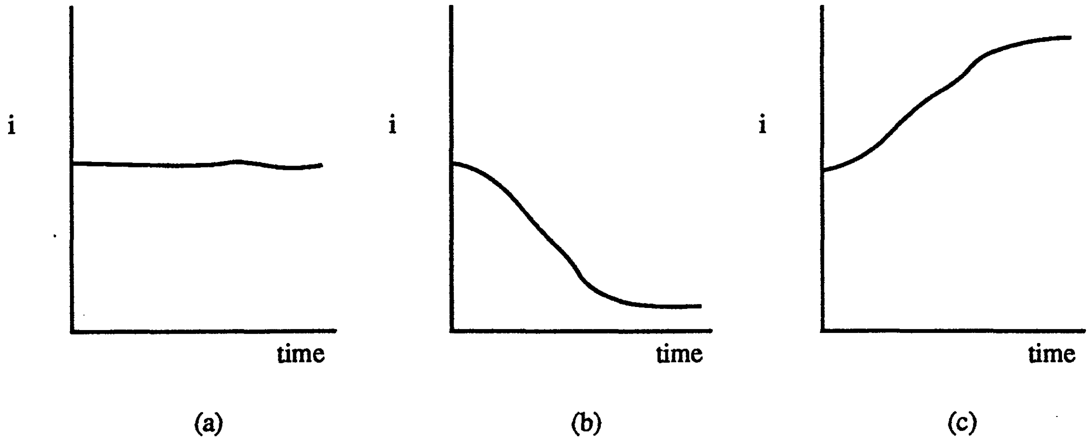

(a) (b) (c)

Figure 10.6 Potentiostatic anodic polarization tests where the material is exhibiting current-time behavior characteristic of (a) stable charge-transfer dissolution, (b) passivation, and (c) localized corrosion.

10.1.2 EIS Data Analysis via Equivalent Circuit Modeling

An initial evaluation of EIS data can be conducted by qualitatively comparing certain features of the obtained plots to previously reported data. For example, in Section 5.2, the undercut and low frequency maximum in the present EIS data were correlated to localized corrosion; this observation led to the in-depth analysis of pitting corrosion described in Chapter 5. Although a qualitative comparison to previous data can comprise a useful first step in obtaining information from EIS data, the preferred and more rigorous method of analysis employs an equivalent circuit modeling technique. An equivalent circuit is constructed for the electrochemical system under study, and the EIS data are mathematically fit to the circuit model in order to obtain quantitative values for the parameters which comprise the model. Because the model parameters are selected to represent particular physical phenomena in the electrochemical system, the quantitative values obtained by fitting can be correlated to physical processes in the corroding system. Mechanistic information and instantaneous corrosion rates can be obtained using this procedure. The primary drawback of the procedure is that the modeling procedure is rather intricate and difficult to perform correctly. A comprehensive procedure for modeling via equivalent circuits is provided in the present section. This procedure will be applied to the EIS data obtained in the present study in Section 10.2 of this Appendix.

10.1.2.1 Electrical Circuit Analogs

The preferred method of analyzing EIS data is to model the measured cell impedance using electrical analogs such as capacitors and resistors. Each electrical analog is chosen to represent a type of physical process believed to occur in the electrochemical system of interest. The circuit analogs are selected for their ability to impede alternating current in a manner that is similar to the way in which the actual process impedes alternating current.

All of the electrical analogs are linked together into a network, which serves as a model to represent the real electrochemical system. The network of circuit analogs is known as the *equivalent* circuit because a correctly devised network should impede alternating current (a.c.) in a manner that is equivalent to the way in which the actual electrochemical system impedes a.c. current.

Common electrical analogs used to analyze corroding metals are discussed below.

When a metal is immersed in a liquid electrolyte, it will invariably develop an excess or deficiency of electrons in a very thin surface layer next to the solution. The charge of this surface layer in the metal will be exactly balanced by the formation of an oppositely charged layer in the electrolyte adjacent to the metal such that $\sigma_m = -\sigma_{el}$, where σ_m and σ_{el} are the surface charge densities in the metal and the electrolyte, respectively. The layer of charge in the electrolyte will consist of oriented solvent dipoles and either positive ions (for an excess of electrons) or negative ions (for a deficiency of electrons), as shown in Figure 10.7. These two opposing layers of charge are known as the electrical double layer. When a sinusoidal perturbation voltage is applied to an electrochemical interface, the double layer tends to respond in a capacitive manner. Electrical double layers are thus typically represented as capacitors in equivalent circuit models. The impedance of a capacitor is:

$$[10.3] \qquad \vec{Z}_c(\omega) = \frac{1}{j\omega C}$$

such that the impedance of an electrical double layer will be dependent on the frequency of the perturbation voltage in addition to its capacitance.

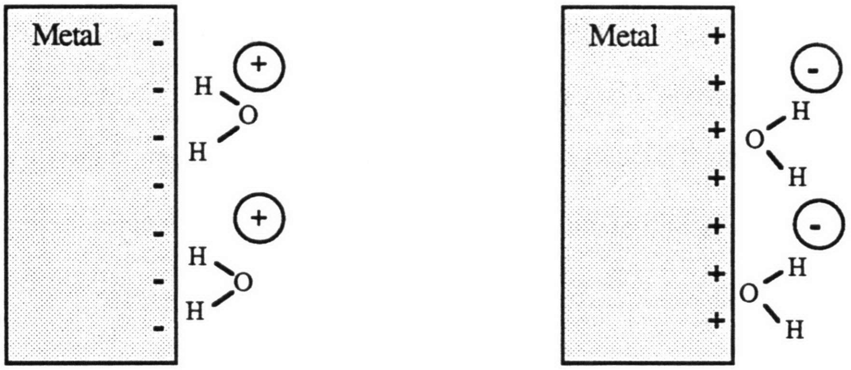

(a) (b)

Figure 10.7 Schematic representations of interfacial double layers for (a) an excess and (b) a deficiency of electrons on the metallic surface.

Faradaic charge-transfer reactions which occur across the metal-electrolyte interface, such as:

[10.4] $$\mathrm{Me} \rightarrow \mathrm{Me}^{n+} + ne^{-}$$

are typically modeled using resistors. The rate of any charge-transfer reaction is intimately linked to driving voltage (electrode potential), since an applied bias in the electropositive or anodic direction will cause an increasing oxidation current to flow across the interface. This direct relationship between applied potential and current is similar to that of an electrical resistor, as the current through a resistor is intimately related to the voltage across its terminals. Application of an opposing bias will cause current to flow in the opposite direction in both cases. Additionally, both faradaic current through the interface and electric current through a resistor are completely in-phase with an alternating current perturbation such as a sinusoid. The impedance of a resistor is:

[10.5] $$\vec{Z}_R(\omega) = R$$

which is independent of frequency. A critical difference between charge-transfer resistance and the resistance of a real electrical resistor is related to the potential range over which the current response is linear. The response of electrical resistors is linear over a very high range of applied potential, whereas the current in a charge-transfer reaction is only linearly related to the driving voltage over a very small potential range. Accordingly, the amplitude of the sinusoidal perturbation voltage used in the EIS experiments must be very small (< 20 mV) in order that charge-transfer reactions can be approximated using resistors. This point is discussed in detail in Section 10.1.2.6.

Components in the solution such as wire leads, the electrolytic solution, insoluble corrosion products, and the metal electrodes themselves tend to follow Ohm's Law ($I = E/R$) in response to a potential bias, and are therefore modeled as resistors in an equivalent circuit analysis.

Another important type of impedance often observed in EIS work is the impedance to mass-transfer in solution. The mass-transfer impedance is generally modeled using a linear electrical element known as the Warburg impedance, Z_W. The mass-transfer impedance cannot be easily related to a well-known circuit analog such as a capacitor or a resistor, and is described mathematically instead. The mass-transfer impedance at any given frequency is:

$$\vec{Z}_W(\omega) = \sigma\omega^{-1/2} - j \cdot \sigma\omega^{-1/2} \qquad [10.6]$$

where σ (the Warburg coefficient) is a complicated function of the diffusion coefficient and concentration of the diffusing species. It is important to observe that the impedance due to mass-transfer increases as the frequency of the perturbation voltage decreases.

The elements described above can be combined in series and in parallel to represent typical electrochemical systems. For example, a simple electrochemical system can be represented by a Randles circuit, as shown in Figure 10.8. The Randles circuit consists of a charge-transfer reaction occurring at an interface, which is modeled using a resistor designated R_t. The interface also has an associated double layer capacitance, C_d. The resistance of lead wires and electrolyte solution are collected together into an ohmic resistance element, R_Ω.

This circuit is capable of representing the simplest electrochemical system, a metal-electrolyte interface having only one electrochemical reaction occurring on its surface. The reaction is assumed in this circuit to be completely under charge-transfer control, since no provision has been included in the circuit for impedance due to mass-transfer.

An electrical circuit with a resistor and capacitor in parallel is referred to as an RC circuit (alternatively -R=C-) having only one time constant, τ (where $\tau = R_t \cdot C_d$ in Figure 10.8).

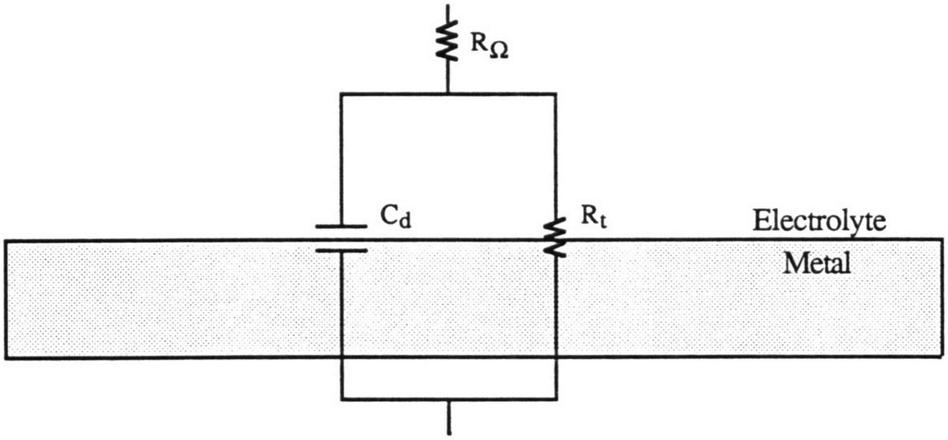

Figure 10.8 Typical Randles circuit representing an extremely simple electrochemical system.

The typical impedance spectrum resulting from the application of a sinusoidal excitation voltage to an -R=C- circuit can be observed using a wired test circuit consisting of real resistors and capacitors. The results of such an experiment are shown in Figure 10.9, with the data reported in the Nyquist, Bode-magnitude, and Bode-angle representations.

It is apparent from Figure 10.9 (a) that an -R=C- circuit produces a characteristic semicircular appearance in the Nyquist plot. The reason for the semicircular appearance is discussed below.

At high frequencies, the impedance of a capacitor is very low, as shown by equation [10.3]. The capacitor thus acts as a short-circuit so that essentially no current flows through the circuit branch marked R_t in Figure 10.8 at high frequency. The impedance to current flow at high frequency will therefore consist only of the ohmic resistance, R_Ω. At low frequencies, the impedance of the capacitor is very high. The capacitor then acts as an

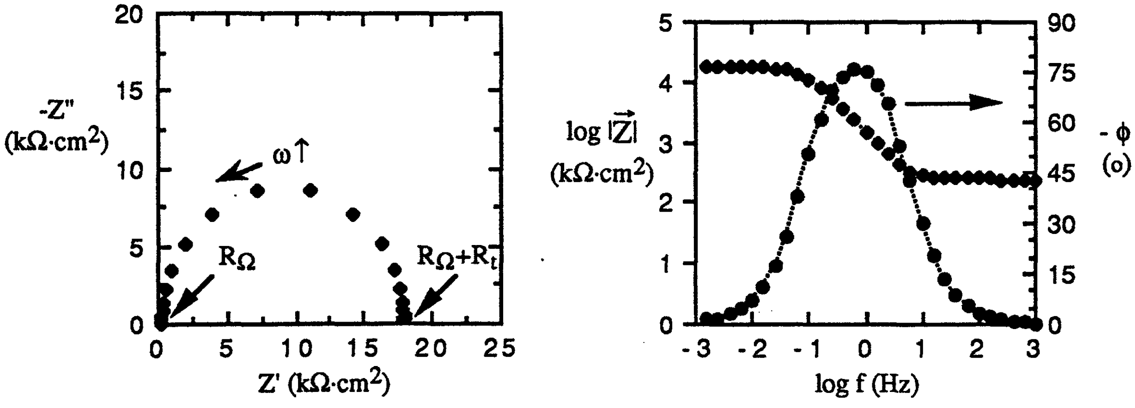

(a)

(b)

Figure 10.9 EIS data from a test circuit in the (a) Nyquist and (b) Bode representations. An -R=C- circuit was utilized with element values R_Ω = 0.243 kΩ, C_d = 100 μF/cm^2, R_t = 17.8 kΩ. Area taken as 1 cm^2.

open-circuit so that essentially all of the current flows through the R_t branch of the circuit as well as the R_Ω branch at low frequency. The impedance to current flow at low frequency therefore consists of $R_t + R_\Omega$.

The high frequency plateau in the Bode-magnitude plot is equal to R_Ω and the low frequency plateau is equal to $R_t + R_\Omega$. The phase angle ϕ is approximately 0° in both the high and low frequency regions, since the effective impedance to current flow is purely resistive. In the intermediate frequency regime, current passes through both the capacitive (C_d) branch and the R_t branch of the circuit, leading to impedance magnitudes between R_Ω and $R_t + R_\Omega$ and to phase angles between 0° and -90°C. When plotted in the Nyquist representation, the aforementioned data give rise to a semicircular pattern with the magnitudes of R_Ω and $R_\Omega + R_t$ indicated in Figure 10.9 (a).

Another notable aspect of Figure 10.9 is that even if the identity of the resistors and the capacitor used in this circuit were unknown, their values could be accurately determined by analyzing the impedance data using the methods described in the following sections. The determination of the values of analog circuit elements using the measured impedance data is the ultimate objective of analyzing experimental data from real electrochemical systems.

10.1.2.2 Equivalent Circuit Modeling Process

The *values* of the individual circuit elements representing the physical processes in the electrochemical system may be obtained through use of the equivalent circuit modeling analysis. In other words, the value of the capacitance (e.g. in μF) or the value of the resistance (e.g. in Ω) of each of the individual circuit analogs can be determined using the acquired experimental data in combination with a mathematical fitting procedure, which will be described in Section 10.1.2.5. Since each circuit element is associated with a specific physical process in the system, knowledge of the value of a circuit element can provide important information about the actual process represented by that element. For example, if a resistor representing a particular charge-transfer reaction is determined to have a very high value of resistance, the corresponding charge-transfer reaction would be considered to be kinetically sluggish. In electrical circuit terminology, the reaction has a very high resistance to charge-transfer. A low resistance value for the analog element would imply that the reaction which it represents is kinetically facile (i.e. has a low charge-transfer resistance).

One of the most important analog elements in corrosion science is the charge-transfer resistance (R_t) for the metal dissolution reaction. This resistance is often (but not in all cases) referred to as the polarization resistance, R_p. The value of this analog element is important because it is known to be inversely related to the instantaneous corrosion rate of the metal via the Stern-Geary equation:

$$[10.7] \qquad \frac{1}{R_p} = \frac{2.3\, i_{corr}}{\beta_c} + \frac{2.3\, i_{corr}}{\beta_a}$$

where β_a and β_c are the anodic and cathodic Tafel slopes. These quantities are obtained from the experimentally determined anodic and cathodic polarization diagrams as the slope of the E-log i curves (Figure 10.4). Equation [10.7] can be simplified under certain limiting conditions. If the cathodic reaction is under mass-transfer control, for example, as is often observed in aerated, near-neutral electrolytes, then $\beta_c \cong \infty$ and [10.7] becomes:

$$[10.8] \qquad i_{corr} = \frac{\beta_a}{2.3\, R_p}$$

The value of i_{corr} can be used to estimate the penetration rate or weight loss rate of the metal via Faraday's Law (equation [10.1]). In addition to estimating actual corrosion rates, EIS data can also be used to determine relative corrosion rates between two different samples or even on the same sample as a function of immersion time. Owing to the non-destructive nature of EIS testing (which results from the use of a small-amplitude perturbation), the corrosion rate can be monitored over time by following the changes in R_t for the metal dissolution reaction. An decrease in the diameter of the semicircle with time, for example, would indicate that the polarization resistance is decreasing, and thus the corrosion rate of the metal is increasing with time. A significant benefit of monitoring changes in corrosion rate using this method is that a new test sample is not required for each immersion time.

In view of the preceding discussion, it is clear that the objective of the modeling process is to determine the values of the *individual* analog elements in the equivalent circuit, which will then be related back to the different physical processes represented by these elements. The experimental setup, however, is only capable of measuring the *total* cell impedance, and a type of deconvolution procedure is therefore necessary in order to extract the required information from the experimental data. The deconvolution procedure consists of constructing a network of electrical circuit elements which are thought to represent the physical processes occurring during the corrosion of the metal, and then fitting this circuit mathematically to the experimental data. The model is called an *equivalent* circuit because if constructed properly, it should impede alternating current (over all frequencies) in the same way that the electrochemical system under study impedes alternating current.

10.1.2.3 Construction of the Equivalent Circuit Model

An electrochemical reaction cannot proceed without a charge-transfer reaction at the metal-electrolyte interface. Additionally, the reacting species must either diffuse up to the interface prior to reacting or must diffuse away from the interface after reaction (as in the case of metal cations during corrosion). Each electrochemical reaction must thus consist of a charge-transfer and a mass-transfer process in series, as shown in Figure 10.10. The impedance of a charge-transfer process is normally modeled using a resistor (R_t) and the impedance of a mass-transfer process is typically modeled using an impedance element known as the Warburg impedance (designated Z_W), as described in Section 10.1.2.1.

Each electrochemical reaction present in the system must be modeled using a circuit branch similar to that shown in Figure 10.10 in order to account for the possible effects of both mass-transfer and charge-transfer processes upon the impedance exhibited by the reaction. A double layer capacitance must additionally be included at each distinct metal-electrolyte interface in the system. Once all of the electrochemical reactions and capacitances in a system have been identified, a network of circuit elements can be assembled which effectively models the real metal-electrolyte system.

The procedure of constructing an equivalent circuit model for an actual electrochemical system (as opposed to the simple system represented by the Randles circuit) consists of using availiable information about the system under test in order to identify *all* physical processes which could possibly impede alternating current through the electrochemical cell.

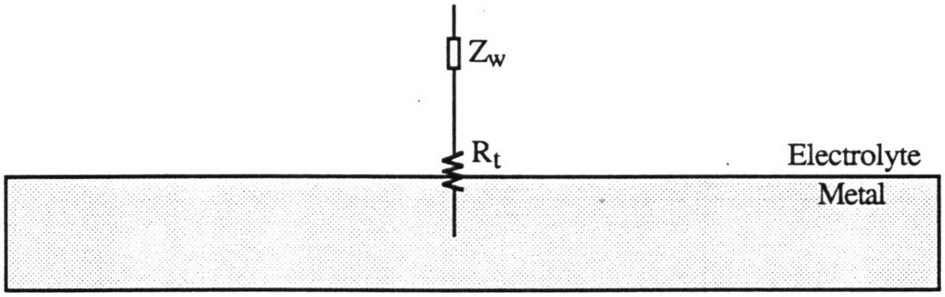

Figure 10.10 Series processes for electrochemical reactions. R_t represents the resistance to the charge-transfer process, and Z_W represents the impedance provided by mass-transfer.

Any corrosion system is inherently more complicated than the Randles circuit since at least one anodic and one cathodic reaction must be proceeding simultaneously on the surface.

An *initial* equivalent circuit model is constructed by devising an electrical network which incorporates analog circuit elements for each relevant physical process in the system. These elements are placed in parallel and series according to how the processes would respond to an applied electrical signal (such as a sinusoidal perturbation). For illustrative purposes, an initial equivalent circuit model for a very general corroding system has been constructed. This circuit model is shown in Figure 10.11 and is described in detail below.

A corrosion process occurring at open-circuit must consist of at least one anodic and one cathodic reaction on the surface of the metal. These reactions can either be under charge-transfer or mass-transfer control, and impedance elements for both types of processes must therefore be included in the initial equivalent circuit model. The anodic and cathodic branches should be placed in parallel, since the current applied by the potentiostat during the EIS experiment could flow *either* through the anodic branch of the circuit *or* through the

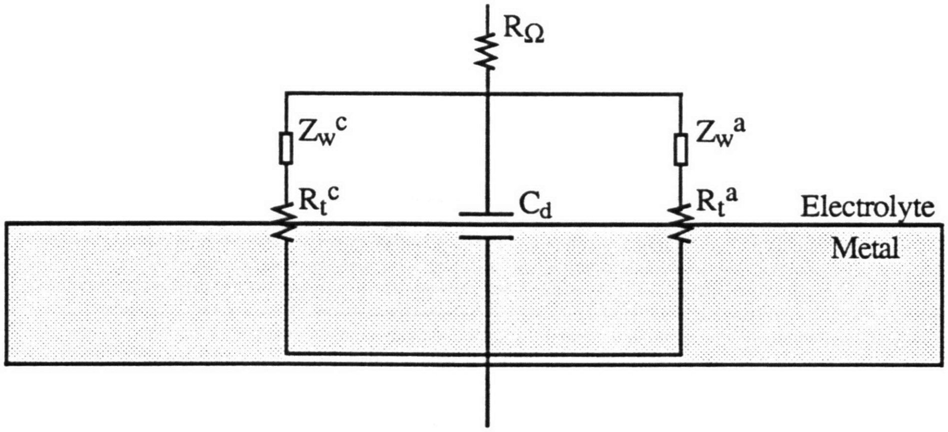

Figure 10.11 General equivalent circuit model for a corroding metal. Subscripts a and c refer to the anodic and cathodic electrochemical reactions, respectively.

cathodic branch of the circuit. It is also necessary to include a double-layer capacitance and an ohmic resistance element in the model circuit, since these processes will be present in the corrosion cell. Assembling all of these impedance elements together in a network results in Figure 10.11.

Note that Figure 10.11 is termed a general equivalent circuit model for a corroding metal, because it has not been constructed with regard to the location of corrosive attack or any other specific features of a given metal-electrolyte system.

10.1.2.4 Simplification of the Initial Equivalent Circuit Model

Once the initial equivalent circuit model has been constructed, standard electrical circuit simplification techniques can be used in order to eliminate elements which are unlikely to contribute markedly to the total impedance of the cell. Elements can be removed from the circuit model if physical evidence exists that their contribution to the total cell impedance is likely negligible. For example, a small resistance in series with a much larger resistance can be safely removed from the equivalent circuit, as it is unlikely to have a tangible effect on the total cell impedance. Circuits can be simplified using established series and parallel relationships for resistors and capacitors. For two resistors R_1 and R_2:

$$R_{series} = R_1 + R_2 \tag{10.9}$$

$$R_{parallel} = \frac{R_1 \cdot R_2}{R_1 + R_2} \tag{10.10}$$

Note that the mass-transfer impedance Z_w combines in series and parallel according to the rules governing resistors. For two capacitors C_1 and C_2:

[10.11] $$C_{series} = \frac{C_1 \cdot C_2}{C_1 + C_2}$$

[10.12] $$C_{parallel} = C_1 + C_2$$

The circuit reduction technique described above (as well as the construction of the initial equivalent circ relies on the availability of physical evidence about the system. Such information is often gathered using complementary electrochemical techniques or other methods such as microscopic analysis. The acquisition of such information will assist greatly in accurate equivalent circuit modeling.

At the end of the simplification process, the *final* equivalent circuit should consist only of elements which will significantly contribute to the total cell impedance. Numerical fitting is then used to fit this final equivalent circuit to the experimental data by a technique which is described in the following section. This fitting procedure determines the values of the individual impedance elements in the final equivalent circuit which are required to fit the experimental data. The values of the individual elements are then correlated to the associated physical processes in order to provide quantitative insight into the characteristics of each process, as described in Section 10.1.2.2.

10.1.2.5 Data Analysis Procedure

Once the final equivalent circuit has been constructed, the experimental data are used to calculate values of each circuit analog element via a numerical procedure known as complex non-linear least squares fitting (CNLS). The CNLS procedure operates by calculating the theoretical impedance spectrum of the model equivalent circuit and comparing this theoretical impedance at each frequency to the measured impedance at the same frequency.

The CNLS program will then iterate different values of the circuit analog elements and reperform the comparison. When the difference between the measured and calculated spectra reaches a minimum for a certain set of analog element values, this set of values is reported as the best fit for the data, given the input model. The quality of the fit is assessed by superimposing the measured data points and the points determined by the fitting routine.

Quantitative information is obtained from the fitting procedure about each analog element in the model, which is then related back to the physical process which that particular analog was intended to represent, as discussed in Section 10.1.2.2.

10.1.2.6 Requirement of Linearity

The analysis of EIS data using equivalent circuit models depends critically upon the linearity of the electrochemical response, as mentioned in Section 10.1.2.1. Modeling of the cell impedance using linear electrical circuit theory is only valid if the system responds linearly to the perturbation voltage, such that the current is directly proportional to the voltage ($i \propto E$). Electrochemical systems, however, are inherently non-linear in nature. For a typical charge-transfer reaction, the current is exponentially related to the electrode potential, such that $i \propto \exp(E)$. Despite this apparent incompatibility, the requirement of linearity can be met by an electrochemical system provided that the excitation voltage, $E(\omega)$, is sufficiently small to linearize the current-potential relationship. The exponential can be represented as a power series [100]:

$$\exp(E) = 1 + E + \frac{E^2}{2!} + \frac{E^3}{3!} + \frac{E^4}{4!} + \ldots \qquad [10.13]$$

At small values of E, the higher order terms of the exponential power series can be considered negligible, therefore:

[10.14] $$\exp(E) \sim 1 + E.$$

The implication of this equation is that the current-potential relationship is linear at very small values of the perturbation voltage via:

[10.15] $$i \,\alpha\, (1 + E)$$

In practice, the excitation voltage must be kept below ~ 20 mV rms to ensure that the linearity condition is fulfilled. Compliance with the linearity criterion can be evaluated using the Kramers-Kronig (KK) transformations, which are described in Appendix 10.3.

10.1.3 Galvanic Corrosion Testing

Galvanic corrosion techniques are employed when it is relevant to study the electrochemical properties of metals which are placed in electrical and electrolytic (ionic) contact with one another. In this work, galvanic corrosion testing was utilized to evaluate the feasibility of employing sacrificial zinc coatings as a corrosion control method for Nd-Fe-B. Galvanic corrosion properties are of interest as they relate to the Zn/Nd-Fe-B galvanic couples which are likely to form during service at breaks in the zinc coating. The detailed procedure used to evaluate corrosion control via sacrificial metallic coatings is described in this section.

10.1.3.1 Corrosion Control via Sacrificial Metallic Coatings

All metallic coatings initially function as barrier layers which protect the underlying base metal by isolating it from the corrosive environment, as shown in Figure 10.12 (a). Even though an effective metallic coating will generally corrode at a low rate owing to the formation of either a thin passive film or sparingly soluble bulk corrosion products, the

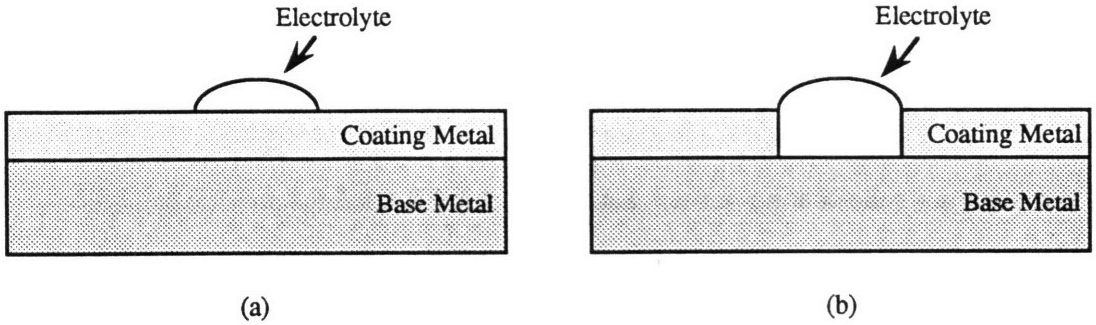

Figure 10.12 Metallic coatings which (a) act as an effective barrier layer and (b) permit base metal exposure due to coating penetration. A galvanic cell will be formed between the coating metal and base metal in (b).

base metal will eventually be exposed to the electrolyte as a result of prolonged corrosion of the coating. Base metal exposure can also result from cracking or porosity of the metallic coating. Under these conditions, the existence of both electrical and electrolytic contact between the base metal and the coating creates a bimetallic or galvanic cell between the two metals, as shown in Figure 10.12 (b). In any galvanic cell, the metal which is more electrochemically active (electronegative) will corrode preferentially, while the corrosion rate of the less active metal will be decreased. A coating made of an electrochemically active metal can thus protect the base metal from corrosive attack by functioning as the anode of an intentionally created galvanic cell. Electronegative metals such as zinc, aluminum, cadmium, or magnesium are therefore deliberately chosen to serve as sacrificial metallic coatings in practice. Since the barrier properties of these coatings have been studied extensively in the past, it is relevant to focus on the ability of the zinc coating to confer protection to the base metal at breaks in the coating. The actual process by which protection is conferred is discussed below.

The sacrificial coating metal serves as the anode of the galvanic cell formed between the coating metal and the base metal at breaks in the coating. The preferential corrosion of the coating metal produces electrons according to:

[10.16] $$Me_c \rightarrow Me_c^{n+} + ne^-$$

(where Me_c represents the coating metal). Sacrificial metallic coatings provide cathodic protection (CP) to the base metal by supplying it with the electrons which are generated by the galvanically-driven corrosion of the coating metal. The addition of electrons to the base metal will suppress its anodic dissolution reaction according to:

[10.17] $$Me_b \leftarrow Me_b^{n+} + ne^-$$

(where Me_b represents the base metal). The excess of electrons provided by the corrosion of the coating metal serves to reduce the rate of base metal dissolution by driving the equilibrium of reaction [10.17] from right to left according to LeChatelier's principle. The reduction in the rate of anodic dissolution on the base metal can alternatively be explained by the fact that the electron supply polarizes (alters the electrode potential of) the base metal in a negative (cathodic) direction from its corrosion potential. Cathodic polarization will retard the corrosion of a base metal which does not exhibit an active-passive transition, as shown graphically in Figure 10.13. The corrosion rate of the uncoupled base metal is I_{corr}. Note that current (I) rather than current density (i) must be utilized in the analysis of galvanic corrosion systems, since the metals in a galvanic couple can have exposed areas which are not equal. Cathodically polarizing the metal from E_{corr} to E' will reduce the anodic dissolution current on the base metal to I'.

The decrease in dissolution current upon cathodic polarization occurs because a more negative potential provides less *kinetic* driving force (overpotential) for the anodic metal dissolution reaction and thus reduces its rate according to the current potential relationship:

[10.18] $$I \alpha \exp(E-E_{Me}^{eq})$$

where E is the electrode potential of the base metal and E^{eq}_{Me} is its equilibrium oxidation/ reduction potential. As $(E_{corr} - E^{eq}_{Me}) > (E' - E^{eq}_{Me})$, the dissolution current will be greater at the corrosion potential than at the cathodically polarized potential E'.

Since the corrosion rate is proportional to the anodic dissolution current on the base metal according to Faraday's Law (equation [10.1]), cathodically polarizing the metal can lead to a substantial reduction in its corrosion rate. *Complete* cathodic protection can be conferred to the base metal if it can be cathodically polarized to a potential which is negative to E^{eq}_{Me} in the given solution. The metal is thermodynamically immune to corrosion at potentials negative to E^{eq}_{Me}, since the metal itself will be the equilibrium species in reaction [10.17]. The ultimate objective of cathodic protection is either to completely protect the base metal thermodynamically or to kinetically reduce its corrosion rate to a negligible level.

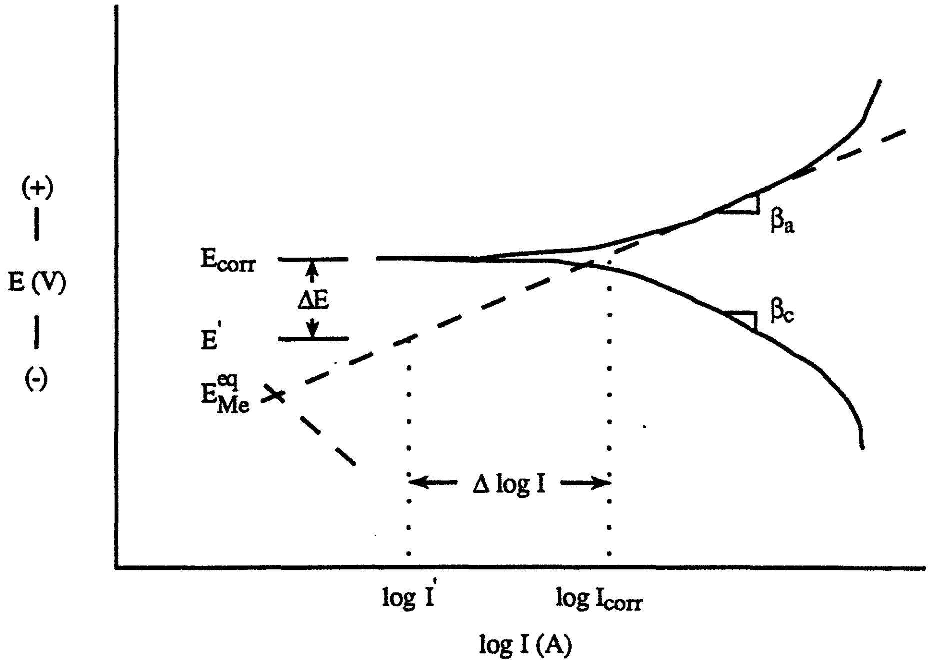

Figure 10.13 Principle of CP for a metal which does not exhibit an active-passive transition. An applied cathodic current polarizes the metal to E', thereby reducing its anodic dissolution rate from I_{corr} to I'.

10.1.3.2 Evaluation of a Coating-Base Metal System

Since CP is provided to the base metal at breaks in the coating by the galvanic interaction between the sacrificial coating and the base metal, the coating-base metal system can be evaluated by studying its galvanic properties. An established technique for analyzing galvanic systems consists of utilizing the mixed potential theory, usually in combination with galvanic corrosion testing.

The mixed potential theory [64] states that due to the law of charge conservation, the total rate of oxidation must equal the total rate of reduction during the corrosion of an electrically isolated metal or metallic system. Once the possible oxidation and reduction reactions in a system are accounted for, the "mixed" potential of the system can be defined as the potential where the total oxidation and reduction currents are equal (steady-state condition). The rate of each individual reaction in the system is then simply the rate of reaction at the mixed potential. In galvanic systems, the mixed potential is known as the galvanic couple potential (E_{couple}), which represents the common electrical potential to which both metals are polarized upon coupling.

The mixed potential theory is a very valuable tool in the analysis of galvanic corrosion systems. If two metals are immersed in the same solution but left uncoupled, each metal will reside at a different E_{corr}. If these two metals are now electrically connected (coupled), they cannot each remain at their original corrosion potentials. Electrically connected surfaces must be equipotential since metals are good electronic conductors, and electrons will therefore flow from the more electronegative metal (more negative E_{corr}) to the less electronegative metal. This electron flow will polarize both metals to a common electrode potential, E_{couple}, which resides between the two initial corrosion potentials. The more electronegative metal will be anodically polarized from its corrosion potential by the loss of electrons, which will increase its corrosion rate. The addition of electrons to the less electronegative metal will cathodically polarize it from its E_{corr}, which will retards its corrosion according to the argument outlined in Section 10.1.3.1.

The application of the mixed potential theory to a coating metal-base metal system can be analyzed using Figure 10.14. The anodic and cathodic polarization curves for both metals are measured and then summed over a range of potential values to give the total oxidation (Σ_{ox}) and total reduction (Σ_{red}) curves, respectively. The intersection of the total oxidation

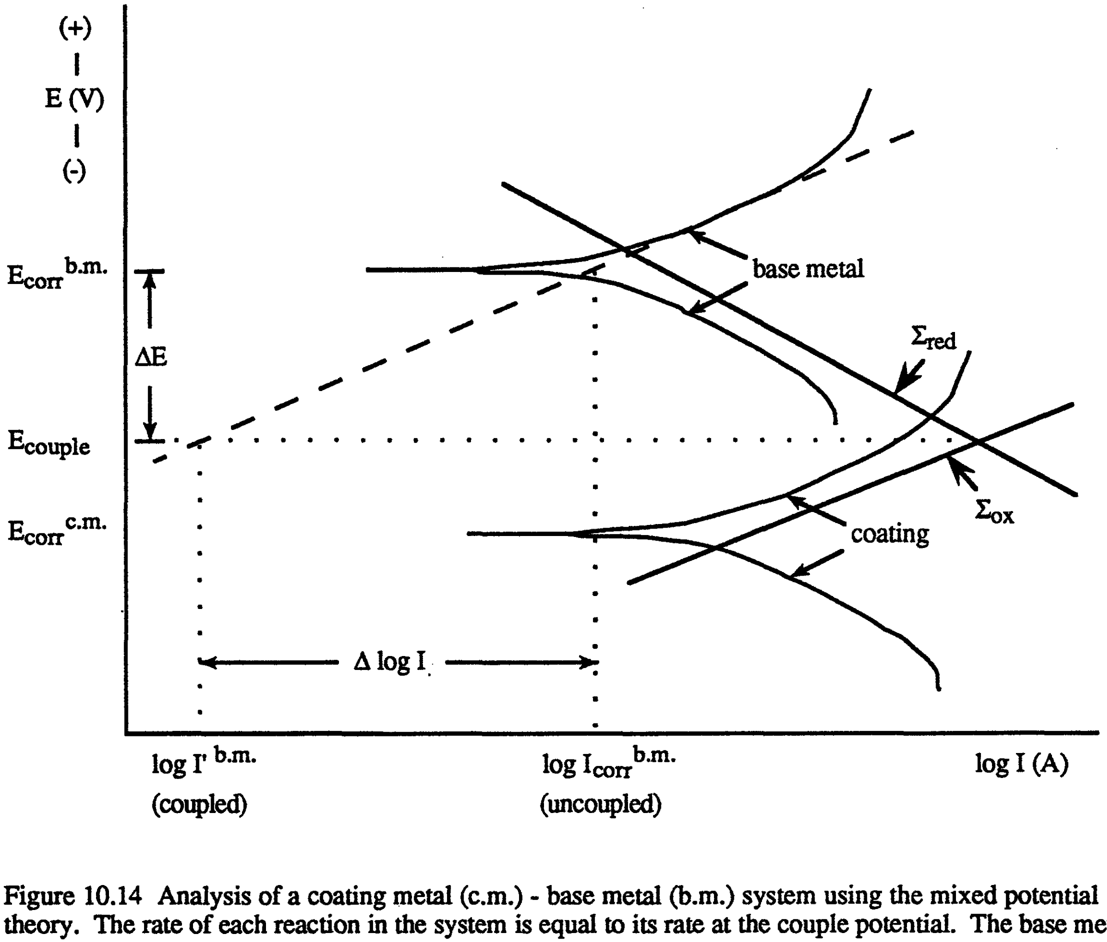

(+)
E (V)
(-)
$E_{corr}^{b.m.}$
ΔE
E_{couple}
$E_{corr}^{c.m.}$
base metal
Σ_{red}
coating
Σ_{ox}
Δ log I
log I' b.m.
(coupled)
log $I_{corr}^{b.m.}$
(uncoupled)
log I (A)

Figure 10.14 Analysis of a coating metal (c.m.) - base metal (b.m.) system using the mixed potential theory. The rate of each reaction in the system is equal to its rate at the couple potential. The base metal is cathodically polarized by ΔE volts upon coupling, which decreases its anodic dissolution rate by Δ log I.

curve and the total reduction curve is the predicted mixed potential (E_{couple}) of the coating-base metal system. The anodic dissolution rate of the base metal (cathode) at E_{couple} can thus be predicted if the value of the current for this reaction is known at E_{couple}.

It is not possible to directly measure the anodic current on the base metal at E_{couple}, however, since only cathodic currents can be recorded at potentials active (electronegative) to a metal's corrosion potential. In place of a direct measurement, the base metal anodic current at E_{couple} can be *predicted* by extrapolating the linear or Tafel portion of the base metal anodic polarization curve to the couple potential (as shown in Figure 10.14). The extrapolation is predicated on the fact that the anodic polarization curve provides the functional dependence of anodic current on electrode potential for the given metal. This measured relationship can then be used to predict the anodic current at any value of electrode potential. Although Tafel extrapolation is widely utilized in corrosion studies, this technique is useful only as a predictive tool since the dependence of anodic current on electrode potential was measured over a relatively short range, and thus *may* not be valid at all values of potential. It is generally accepted that any predictions made using this technique must be verified by further experimentation, as discussed in Section 10.1.3.4.

According to Figure 10.14, galvanic coupling to the coating metal is predicted to reduce the base metal anodic dissolution current from $I_{corr}{}^{b.m.}$ (uncoupled) to $I'{}^{b.m.}$ (coupled). The predicted base metal anodic current at E_{couple} can be converted to a penetration rate using Faraday's Law. In order for a sacrificial coating metal to provide adequate cathodic protection to a given base metal, the coating must be capable of cathodically polarizing the base metal to a potential at which its anodic dissolution rate is negligible.

A galvanic corrosion system can also be analyzed by electrically connecting the two metals and measuring both the magnitude and direction of galvanic current flow between them

(I_g), as well as the common potential to which both metals are polarized (E_{couple}). The primary advantage of utilizing this technique is that the system's E_{couple} is measured directly, rather than predicted as in the mixed potential theory analysis.

10.1.3.3 Evaluation of the Viability of a Sacrificial Metallic Coating

A sacrificial coating metal must be electrochemically active to the base metal. Conformance with this criterion can be evaluated by comparing the corrosion potential of the base metal ($E_{corr}^{b.m.}$) to the corrosion potential of the coating metal ($E_{corr}^{c.m.}$). The coating metal also must be capable of imparting significant cathodic polarization to the base metal upon galvanic coupling. This requirement can be evaluated by measuring the difference between $E_{corr}^{b.m.}$ and the E_{couple} value measured in the galvanic corrosion experiments. The mixed potential theory is then used to predict the actual decrease in base metal dissolution (and the resulting decrease in corrosion rate) which will result from cathodic polarization to the measured couple potential.

10.1.3.6 Requirement of Further Testing

An analysis based on the mixed potential theory can serve as an *indicator* of whether or not a sacrificial coating is likely to provide effective CP to the given base metal. Definitive experiments must be performed, however, before it can be *concluded* that the rate of base metal loss at E_{couple} is negligible. Long-term immersion tests can be employed in order to definitively evaluate the ability of a coating metal to protect a given base metal. Further testing is also important because the preceding analysis did not account for incomplete protection, alkaline damage, or hydrogen damage, as described below.

Incomplete protection refers to a situation in which cathodic polarization causes a slight but insufficient decrease in the corrosion rate of the base metal. The possibility of incomplete protection is especially relevant when the metal to be protected contains atoms of a very electrochemically active metal (such as Nd).

A consideration in the cathodic protection of any metal is its susceptibility to alkaline damage, as both the oxygen reduction and the hydrogen evolution reactions tend to increase the local alkalinity at the cathode (base metal). Metals which are susceptible to alkaline attack (such as aluminum, for example) may actually be damaged by cathodic protection.

Another serious form of degradation which can result from cathodic protection is hydrogen damage. Cathodic polarization of the base metal will increase the rate of reduction reactions on its surface. A common reduction reaction results in the production of hydrogen atoms:

[10.19] $$H_2O + e^- \rightarrow H + OH^-$$

The hydrogen atoms produced by [10.19] can diffuse into the lattice of the base metal and cause embrittlement, especially in hard metals with limited ductility (such as Nd-Fe-B).

Long-term immersion tests can be used to evaluate the susceptibility of a coupled base metal to incomplete protection, alkaline attack, and hydrogen damage.

10.2 Equivalent Circuit Modeling of EIS Data

The basis of equivalent circuit modeling of EIS data was described in detail in Section 10.1.2. The objective of the modeling procedure is to delineate the important individual processes in the overall corrosion reaction, and to obtain quantitative data which will provide insight into the characteristics of each process. An equivalent circuit model is constructed by identifying all of the physical processes which are expected to occur during the corrosion of the metal, and assembling analog elements for all of these processes into an electrical network. The model is called an *equivalent* circuit because if constructed properly, it should impede alternating current (over all frequencies) in the same way that the electrochemical system under study impedes alternating current. Numerical techniques are used to fit this equivalent circuit model to the experimental data. The fitting procedure determines the values (e.g. capacitance or resistance) of the individual impedance elements which are required to fit the experimental data to the equivalent circuit. The value of each individual element is then correlated to the particular physical process which it is intended to represent, in order to provide quantitative insight into the characteristics of that process. The most important analog element in corrosion studies is the charge-transfer resistance for the metal-dissolution reaction (R_t), which can be converted to i_{corr} using Equation [10.8]. The corrosion current density can then be converted to the rate of either metal penetration or weight loss via Faraday's Law.

Pitting has been shown to be the primary form of corrosion on RSP Nd-Fe-B. A detailed method for investigating pitting systems using EIS has been developed by Mansfeld *et al* [101]. These authors have advanced the notion that rates of pitting attack can be predicted on the basis of EIS data; such a procedure would clearly be very valuable in the analysis of systems exhibiting pitting. One objective of the modeling work in the present section, therefore, is to evaluate whether EIS data can accurately predict the measured attack rates.

10.2.1 Construction of the Model

The detailed construction of the initial equivalent circuit is begun by devising a schematic model of the electrochemical system under study. It is important to realize that the model should include *all* circuit elements representative of processes which might contribute to the total cell impedance. Three main groups of circuit elements must be included in the full model: those which represent the anodic reaction, the cathodic reaction, and the double layer capacitance(s). In order to construct a physically realistic equivalent circuit model, it is critical to consider not only the types of reactions present, but also their spatial location within the system.

The primary anodic reaction in all corrosion studies is metal dissolution, which will be represented by a charge-transfer resistance and a mass-transfer impedance in series, as in Figure 10.10. Microscopic analysis indicates that anodic dissolution in pits should be accounted for in the equivalent circuit model. Since the anodic reaction can occur either on the metal surface or within pits, two distinct anodic circuit branches must be included in the model.

The polarization curves in Figure 5.3 indicate that the main cathodic reaction in the system is the reduction of dissolved oxygen atoms to hydroxyl ions (OH^-). Pits are typically deaerated due to the formation of a semiporous corrosion product cap atop the pit, and the oxygen reduction reaction can thus be assumed to proceed almost completely on the surface of the metal, rather than within the pits. The reduction of water to hydrogen atoms is also predicted to occur at the corrosion potential, but since the current due to oxygen reduction is about 100 times greater than the current predicted for water reduction, this reaction will be neglected in the construction of the model. It should be noted that the actual amount of hydrogen generated can be somewhat greater than indicated above, due to local pH changes within the pits.

A capacitor will be used to represent the electrical double layer at the surface of the metal. It is additionally expected that a double layer capacitance would be associated with the interfacial region within the pits, since the composition of the electrolyte within the pits is likely to be significantly different than the composition of the electrolyte at the surface.

A system of notation was devised in order to allow the different impedance elements to be abbreviated in compact form. The impedance elements themselves were identified in accordance with the standard notation used in the electrochemical literature: ohmic resistance was designated R_Ω, charge-transfer resistance R_t, Warburg (mass-transfer) impedance Z_W, and double layer capacitance C_d. The abbreviations referring to the individual elements were then augmented using superscripts and subscripts in order to define the type and location of the reaction associated with the impedance. Superscripts refer to the type of reaction, where *a* represents an anodic reaction and *c* represents a cathodic reaction. Subscripts refer to the location of the reaction, where *surf* refers to processes occurring at the metal surface and *pit* refers to processes occurring within corrosion pits. Since resistances are strongly dependent upon the surface area through which current passes, the differing area of the pits and the external surface must be considered. In order to account for the effects of area, the parameter *F* will be used to represent the area fraction of the sample which is pitted, while *(1-F)* will represent the area fraction which is not pitted. The F notation has been adapted from work performed by Mansfeld *et al* [101] on the pitting corrosion of aluminum alloys.

An initial equivalent circuit model which takes account of all the possible reactions in the cell is shown in Figure 10.15. An explanation of the abbreviations used in the circuit model is shown in Table 10.1.

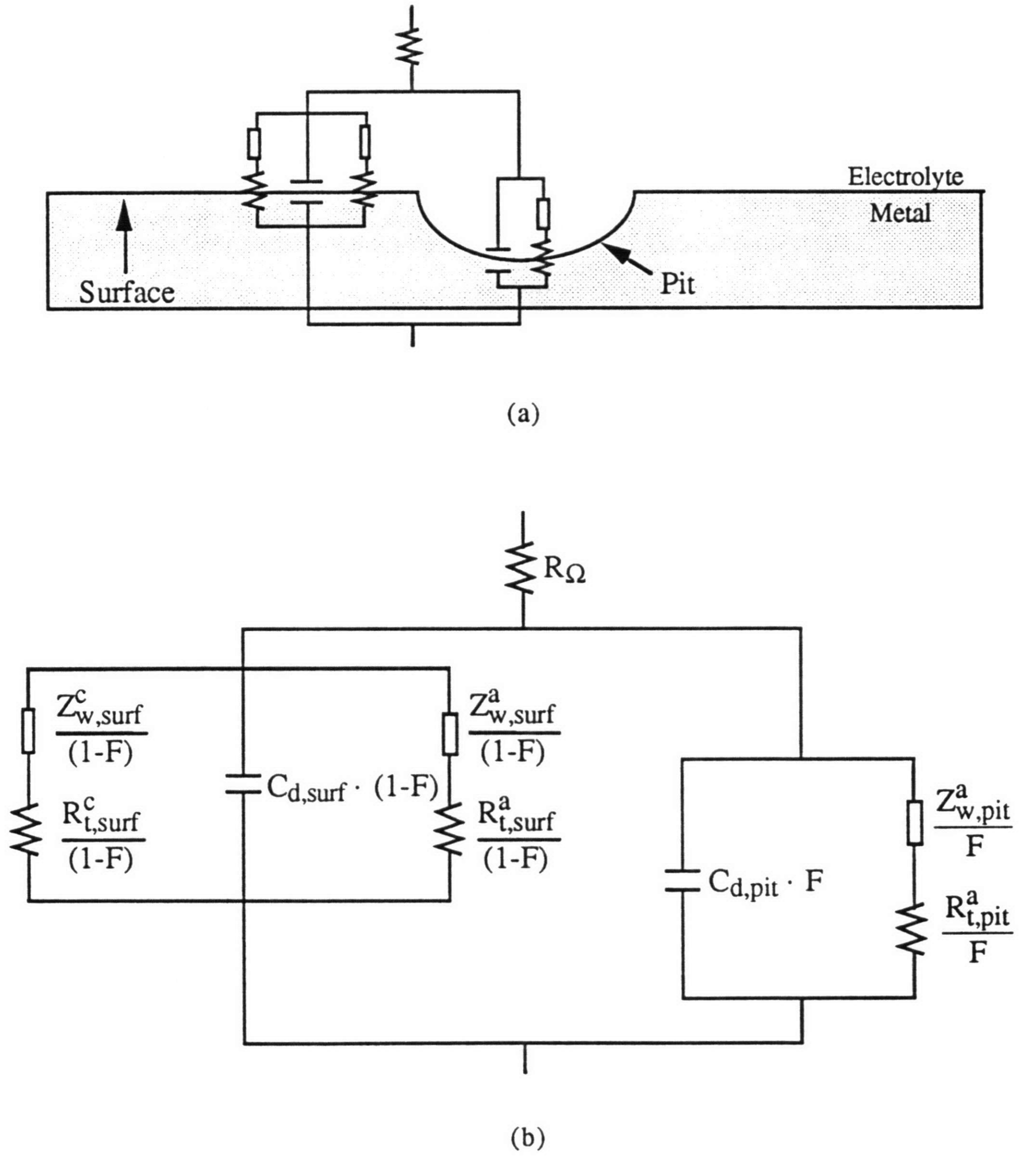

Electrolyte
Metal
Surface
Pit
(a)
R_Ω
$\frac{Z^c_{w,surf}}{(1-F)}$
$\frac{R^c_{t,surf}}{(1-F)}$
$C_{d,surf} \cdot (1-F)$
$\frac{Z^a_{w,surf}}{(1-F)}$
$\frac{R^a_{t,surf}}{(1-F)}$
$C_{d,pit} \cdot F$
$\frac{Z^a_{w,pit}}{F}$
$\frac{R^a_{t,pit}}{F}$
(b)

Figure 10.15 Initial equivalent circuit model showing all elements capable of contributing to the total cell impedance. The elements of the model are superimposed onto a schematic metal-electrolyte interface in (a). The meaning of each element is given in (b), and the abbreviations are described in Table 10.1.

Table 10.1 Abbreviations used in equivalent circuit modeling.

Abbreviation	Explanation
$\frac{Z^{c}_{w,surf}}{(1-F)}$	Mass-transfer impedance of the cathodic oxygen reduction reaction. Represents the diffusion of oxygen to the surface of the metal.
$\frac{R^{c}_{t,surf}}{(1-F)}$	Charge-transfer resistance of the cathodic oxygen reduction reaction. Represents the reduction kinetics for oxygen on the metal surface.
$\frac{Z^{a}_{w,surf}}{(1-F)}$	Mass-transfer impedance of the anodic metal dissolution reaction. Represents the diffusion of metal ions away from the surface.
$\frac{R^{a}_{t,surf}}{(1-F)}$	Charge-transfer resistance of the anodic metal dissolution reaction. Represents the kinetics for metal dissolution on the surface.
$\frac{Z^{a}_{w,pit}}{F}$	Mass-transfer impedance of the metal dissolution reaction in pits. Represents the diffusion of metal ions from the pit surface.
$\frac{R^{a}_{t,pit}}{F}$	Charge-transfer resistance of the metal dissolution reaction in pits. Represents the kinetics for metal dissolutions at the pit surface.
R_{Ω}	Ohmic resistance. Represents the resistance of lead wires, corrosion products, and uncompensated solution resistance.
F	Fraction of the surface area which is pitted.
(1-F)	Area fraction which is not pitted.
$C_{d,surf} \cdot (1-F)$	Capacitance of the double layer on the surface of the metal.
$C_{d,pit} \cdot F$	Capacitance of the double layer at the pit-electrolyte interface.

10.2.2 Simplification of the Initial Equivalent Circuit Model

Once the initial equivalent circuit model has been constructed, standard electrical circuit simplification techniques can be used in order to eliminate elements which are unlikely to contribute markedly to the total impedance of the cell. Circuits are simplified using series and parallel relationships for resistors and capacitors (equations [10.9 - 10.12]). Mass-transfer impedance elements combine according to the rules governing resistors.

The process of charge-transfer of the metal ions across the interface and the process of metal ion diffusion into the bulk electrolyte occur in series (as in Figure 10.10), such that for an anodic branch of the circuit:

$$Z^a_{branch} = R^a_t + Z^a_w \qquad [10.20]$$

which indicates that Z^a_{branch} will be controlled by the step exhibiting a higher impedance.

It is important to understand the correlation between the *impedance* of a given process and its *reaction rate*, a relationship which is indirectly illustrated by equation [10.20]. This equation indicates that the rate-controlling step in a series reaction is the step exhibiting a higher impedance, and since the overall rate in a series reaction is known to be controlled by the *slower* of the two steps in the reaction, a slow process can be associated with a high impedance. This correlation can be explained by considering that under the influence of a constant excitation voltage, the step having the slower reaction rate will permit less current flow than the step having the faster reaction rate, which corresponds to a higher impedance for the slower reaction (since $Z = V/I$).

Equation [10.20] can thus be simplified if evidence regarding the relative rates of the anodic charge-transfer reaction and the anodic mass-transfer reaction is available. Such information can be obtained from the anodic polarization curves shown in Section 5.1.

The anodic polarization curve in Figure 5.1 shows that the rate of the anodic reaction is exponentially dependent on the potential (E - log i plot is linear) in the vicinity of the corrosion potential. The appearance of this type of relationship indicates that the metal dissolution reaction is under charge-transfer control at the corrosion potential, as discussed in Section 10.1.1. Since the slow step is rate controlling and thus associated with a higher impedance, the impedance of the anodic charge-transfer reaction must be higher than the anodic mass-transfer impedance:

[10.21] $$\frac{R^{a}_{t,\,surf}}{(1-F)} >> \frac{Z^{a}_{w,\,surf}}{(1-F)}$$

[10.22] $$\frac{R^{a}_{t,\,pit}}{F} >> \frac{Z^{a}_{w,\,pit}}{F}$$

The impedance elements representing the anodic mass-transfer reactions will therefore not contribute significantly to the total cell impedance according to equation [10.20]. These two elements can be removed from the initial circuit model.

The cathodic process at the surface will similarly be evaluated using the equation:

[10.23] $$Z^{c}_{branch} = R^{c}_{t} + Z^{c}_{w}$$

in conjunction with the cathodic polarization curves. The cathodic curves shown in Figure 5.3 indicate that there is essentially no dependence of current on electrode potential in the vicinity of the corrosion potential (approximately vertical line). The appearance of this type of relationship indicates that the cathodic oxygen reduction reaction is under mass-transfer control at E_{corr}, as discussed in Section 10.1.1. The cathodic charge-transfer step is therefore more rapid than the oxygen arrival rate, such that:

[10.24]
$$\frac{Z^{c}_{w,\,surf}}{(1\text{-}F)} >> \frac{R^{c}_{t,\,surf}}{(1\text{-}F)}$$

Since the two processes are in series, the resistive element representing the cathodic charge transfer reaction is thus removed from the circuit model since it will not contribute significantly to the total impedance of the cell, according to equation [10.23].

The removal of the elements representing anodic mass-transfer and cathodic charge-transfer leaves the circuit shown in Figure 10.16.

The simplified circuit has one set of parallel resistors. Information on their relative values can be utilized in order to reduce the circuit even further, using:

[10.25]
$$R_{parallel} = \frac{\frac{R^{a}_{t,\,surf}}{(1\text{-}F)} \cdot \frac{R^{a}_{t,\,pit}}{F}}{\frac{R^{a}_{t,\,surf}}{(1\text{-}F)} + \frac{R^{a}_{t,\,pit}}{F}}$$

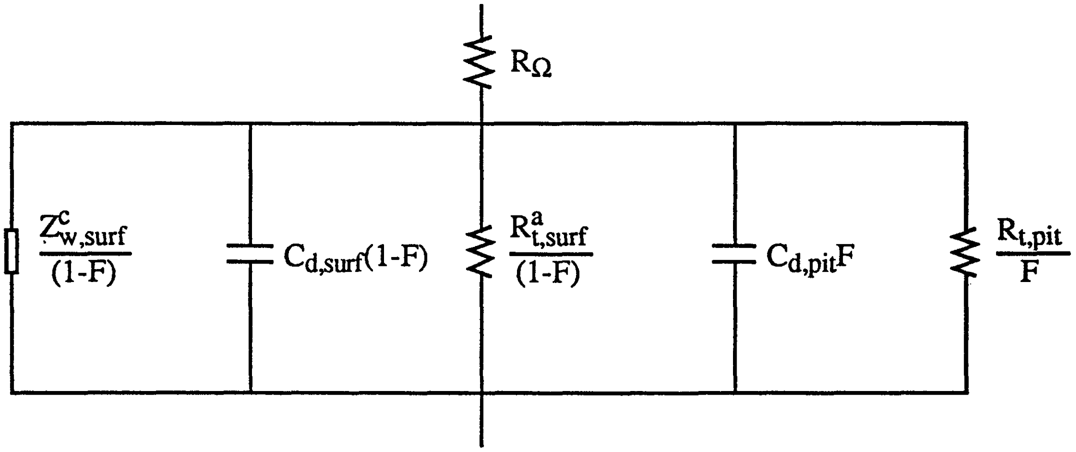
R_{Ω}
$\frac{Z^{c}_{w,surf}}{(1\text{-}F)}$
$C_{d,surf}(1\text{-}F)$
$\frac{R^{a}_{t,surf}}{(1\text{-}F)}$
$C_{d,pit}F$
$\frac{R_{t,pit}}{F}$

Figure 10.16 Intermediate equivalent circuit model, which has been reduced from the initial model using information from anodic and cathodic polarization curves.

The results of microscopic analysis clearly indicate that metal dissolution has occurred predominantly in pits after 1 hour of immersion. Since metal loss is related to current passed via Faraday's law, the magnitude of the anodic current through the pits must be significantly higher than that through the surface, as shown in Figure 10.17.

Since current always flows through the path of least resistance, it can be concluded that:

$$\frac{R^{a}_{t,\,surf}}{(1-F)} >> \frac{R^{a}_{t,\,pit}}{F} \qquad [10.26]$$

and the resistor representing the anodic charge-transfer reaction on the surface can then be removed from the circuit as per equation [10.25]. Note that equation [10.26] holds despite the fact that the area of the surface (1-F) is much greater than the area of the pits (F).

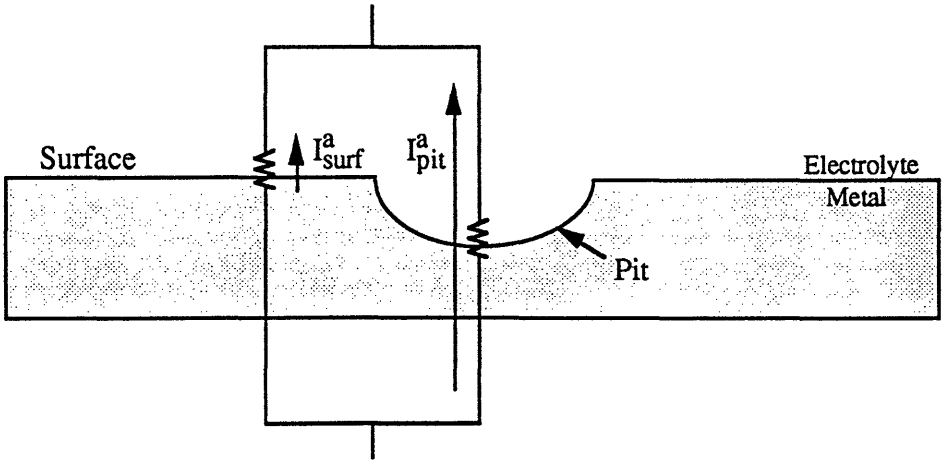

Figure 10.17 Current paths through the surface and through the pit. The arrow lengths indicate that the anodic current through the pit is much greater in magnitude than the anodic current through the surface.

No information appears to be available regarding the relative magnitudes of the double layer capactitances on the surface and in the pit. In the absence of such information, the two capacitances can be collected into a "parallel" capacitance for the purposes of simplification:

$$C_{\text{parallel}} = \frac{C_{d,\,\text{surf}}(1-F) + C_{d,\,\text{pit}}F}{C_{d,\,\text{surf}}(1-F) \cdot C_{d,\,\text{pit}}F} \qquad [10.27]$$

It is not clear whether one of these two capacitance terms will dominate the actual value of the parallel capacitance. The imprecise nature of this particular situation will preclude the assignment of double layer capacitance values to the surface and to the pit at the conclusion of the fitting procedure. This ambiguity should not present a substantial problem, since the main parameter of interest is R_t rather than either of the two capacitance terms.

The removal of the surface charge-transfer resistance and the consolidation of the two capacitance terms into a parallel capacitance results in the circuit shown in Figure 10.18.

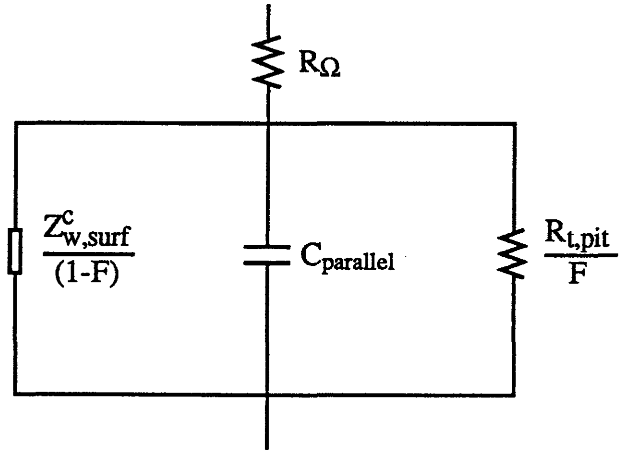

Figure 10.18 Intermediate equivalent circuit model which has been reduced from the circuit of Figure 5.4.3 using standard parallel resistor and capacitor relationships.

It is now relevant to assess the impedance due to oxygen mass-transfer and the impedance due to pit charge-transfer in terms of their contribution to the total impedance of the cell. It may seem unusual at first that these two processes have been represented in parallel, since under open-circuit conditions (with no applied electrical signal), these processes actually occur in series. A corrosion cell cannot operate without an electron sink (due to the principle of electroneutrality), and therefore any electrons produced by the dissolution of metal in the pits must be consumed by the reduction of oxygen on the surface. The overall process cannot occur unless both of these steps occur in sequence, which is characteristic of processes in series rather than of processes in parallel. The rate of the overall process is known to be controlled by the *slower* of the two individual steps, again indicating that these two processes are actually in series under open-circuit conditions.

Despite the fact that these two steps occur in series under open-circuit conditions, it is critical to realize that these processes occur in parallel as regards an *applied electrical signal.* In the presence of an applied signal, the potentiostat itself can act as an electron source or an electron sink. An anodic or cathodic reaction can therefore occur *alone* on an electrode surface if the metal is connected to a controlling potentiostat, contrary to the need for an accompanying reaction as at open-circuit. As the potentiostat forces current through the electrochemical interface, *either* the oxygen reaction *or* the metal dissolution reaction can occur. Such an "either/or" type of situation is characteristic of processes which are in parallel rather than in series. Since the slow step in a parallel reaction sequence is generally bypassed by reaction through the fast path, the faster of these two reactions would be expected to predominate in the equivalent circuit model.

According to equation [10.10], the total impedance of these two parallel branches is:

[10.28]
$$Z_{\text{parallel}} = \frac{\frac{Z^{c}_{w,\,surf}}{(1-F)} \cdot \frac{R^{a}_{t,\,pit}}{F}}{\frac{Z^{c}_{w,\,surf}}{(1-F)} + \frac{R^{a}_{t,\,pit}}{F}}$$

For information on the relative impedance of these two elements, the polarization diagrams must be consulted. The controlling reaction in a system can be inferred by noting which reaction has a greater slope in the E-log i plot. The more vertical the slope associated with the polarization behavior of a particular reaction, the more impact any change in the rate of this reaction will have on the overall corrosion rate. The polarization curves in Figures 5.1 and 5.3 therefore correspond to a situation known as cathodic control, where the rate of the overall corrosion reaction is controlled by the rate of the cathodic rather than the anodic reaction. The presence of cathodic control indicates that the rate controlling or slow step in the overall corrosion process *at open circuit* (no applied signal) is the mass-transfer controlled reduction of oxygen. Again, a slower step corresponds to a higher impedance. Since oxygen reduction is the slower of the two steps:

[10.29]
$$\frac{Z^{c}_{w,\,surf}}{(1-F)} >> \frac{R^{a}_{t,\,pit}}{F}$$

Using this relation, equation [10.28] simplifies to:

[10.30]
$$Z_{\text{parallel}} \cong \frac{R^{a}_{t,\,pit}}{F}$$

and therefore, the element representing the mass transfer impedance of oxygen diffusing to the surface can be removed from the circuit model. This removal is consistent with the notion that the faster reaction should be controlling in a parallel circuit. Elimination of this element from the circuit leaves the final equivalent circuit model shown in Figure 10.19.

According to the above analysis, only the elements included in the circuit of Figure 10.19 are expected to significantly contribute to the total cell impedance. This circuit will be used in the numerical fitting procedure which will be used to analyze the experimental data.

It may seem unconvincing that a simple -R=C- circuit has been obtained for a system with such a complicated initial equivalent circuit. It should be emphasized, however, that with the exception of the assumption made when simplifying the two parallel capacitors, all of the circuit simplifications performed above were based not on speculation, but on real information obtained either from microscopy or from polarization curves. The use of this information collected from other techniques makes the simplifications credible.

The circuit simplification which may be most difficult to grasp is the last one, where the impedance due to oxygen mass-transfer was removed from the circuit. This simplification is fortunately the easiest to verify. The impedance spectrum containing a significant mass-transfer element will have a characteristic line at 45° to the horizontal in the Nyquist plot. If an error was made in this step of the simplification, it will be detected immediately upon examination of the experimental data.

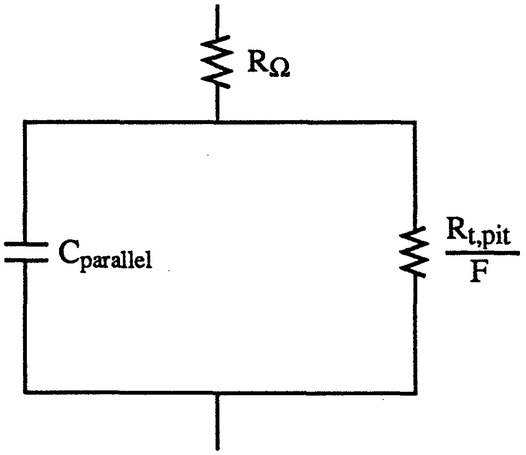

Figure 10.19 Final equivalent circuit model for Nd-Fe-B after 1 hour of immersion.

10.2.3 Analysis of the Experimental Data

The EIS data from a single experiment (NaCl, 1 hour immersion) are shown in Figure 10.20. Visual analysis of the impedance spectrum seems to indicate the presence of an incompletely formed semicircle in the Nyquist plot at frequencies higher than ~ 0.2 Hz. One or more time constants additionally appear to be present at low frequencies, corresponding to the undercut data points in the Nyquist plots.

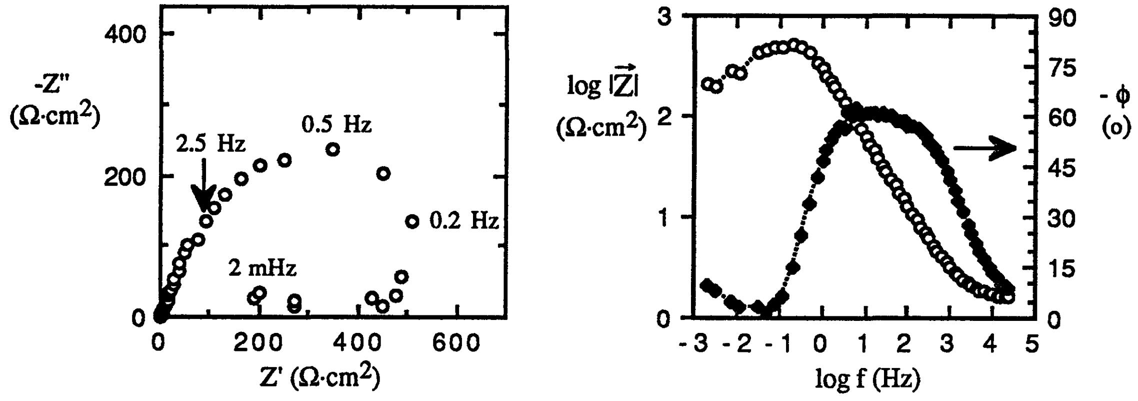

(a) (b)

Figure 10.20 EIS data in the (a) Nyquist format and (b) Bode format for Nd-Fe-B in NaCl at ambient temperature (~23°C) after 1 hour of immersion at open-circuit.

Semicircular Nyquist plots are typically modeled using a parallel combination of a resistor and a capacitor (an -R=C- circuit), as described in Section 10.1.2.1. The appearance of such a time constant is expected in this system, based on the modeling analysis described in the previous section. It appears, however, that the equivalent circuit shown in Figure 10.19 is incomplete, since it does not include any circuit elements which would seem capable of explaining the observed low frequency time constant(s). Physical processes which could lead to the appearance of the undercut data points must therefore be discussed.

The undercutting seems to indicate the presence of at least one low frequency time constant having a negative resistance value, since the observed decrease in the real component of the impedance with decreasing frequency cannot generally be explained using only positive resistance values. Extensive attempts to fit the data without using negative resistance elements were unsuccessful. Dawson and Ferreira [67] have modeled similar data using two low frequency time constants, one of which had a negative resistance. The physical understanding of such a time constant is unclear, however, as negative resistance means that current responds in phase with an opposing bias (Figure 10.21). Since the rate of a resistive process is typically increased by forward bias and decreased by negative bias, a negative resistance does not appear to correspond to a physically realistic situation.

The interpretation of the undercut data points does not appear to be physically realistic, and it therefore might be reasonable to examine the validity of these data points. It is known that each EIS data point will only represent valid impedance data if the system satisfied four separate criteria while the data point was being acquired. The four criteria are linearity, causality, stability, and a finite value of the impedance at low frequency. Owing to the questionable nature of the time constant(s) which would need to be postulated to fit

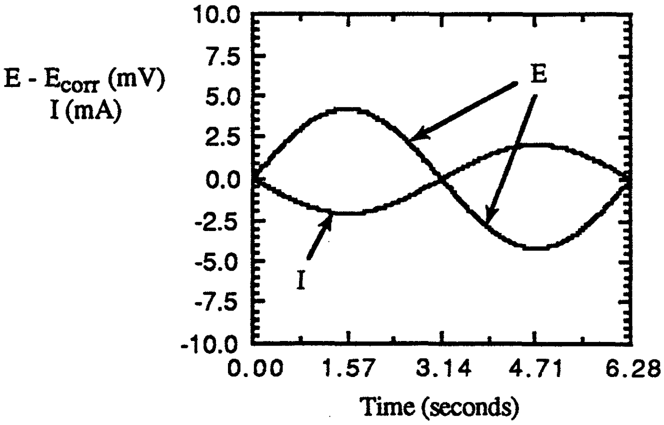

Figure 10.21 Simulated data for one cycle with a perturbation voltage of 3 mV rms, a resistive impedance with a magnitude of -2 Ω, and an angular frequency of 1 Hz (one cycle = 2π seconds).

these data, it seems possible that the undercut points do not represent valid impedance data which conform to these criteria. The fact that rapidly corroding metals often do not conform to the stability criterion at low frequency emphasizes the need for validation.

The low frequency data are also in question because Dawson and Ferreira [67] show a simulation rather than a fit for their plots which exhibit an undercutting feature. Normally, once data are accurately simulated using a particular circuit model, the investigator simply inputs the simulation parameters into the fitting program and allows the CNLS routine to fit the data to the given equivalent circuit model. An ability to simulate but not fit the data is an indication that some or all of the data points in the set do not constitute a valid impedance, since the data must conform to the criteria for a valid impedance in order to be *fit* using the CNLS program. When the data in the present study were initially analyzed, a similar problem was encountered. The circuit model of Dawson and Ferreira was capable of simulating the experimental impedance data shown in Figure 10.20, but the fitting program could not produce a reasonable fit to the data. It is possible that the invalid nature of the low frequency data prevented the fitting from being completed in both cases. Based on the ability to simulate but not fit the full data set, it can be hypothesized that part or all of the low frequency (undercut) data do not constitute a valid impedance according to the criteria outlined above.

10.2.4 Kramers-Kronig Transformations

The conformance of the experimental results to the four criteria which define valid impedance data can be evaluated using a set of mathematical relationships known as the Kramers-Kronig (KK) transformations. Although the general algorithm needed to perform the transformations has been outlined in the literature [102,103], the execution of the actual mathematical procedure is quite complicated. It appeared to be extremely relevant in this particular system to perform the validation procedure, however, and it was therefore judged worthwhile to expend the effort to construct a framework to perform the KK calculations. In order to perform the lengthy integrations associated with the transformations, a computer program was written in Microsoft QuickBasic®. The entire calculation procedure is described in detail in Appendix 10.3, and is also briefly summarized below.

The utility of the KK relations is derived from the fact that the real and imaginary components of a measured impedance are not truly independent quantities. In fact, Kramers [104] and Kronig [105] have shown that the real component of the impedance can be calculated at every measurement frequency if the imaginary component is known over a wide frequency bandwidth. The full set of calculations results in a freqency spectrum of transformed Z' data. A transformed -Z" frequency spectrum can similarly be calculated from knowledge of the real component of the impedance over a wide bandwidth. The output of the calculations are transformed data sets of Z' and -Z" as a function of the logarithm of the angular frequency, log ω, of the perturbation voltage (where $\omega = 2\pi f$). The transformed Z' and -Z" data sets can be compared to the measured data sets (Z' and -Z" vs. log ω). If the impedance data are completely valid according to the criteria descibed in the previous section, excellent agreement should be obtained between the transformed and measured data sets for both the real and imaginary components. The conformance of the data to the validity criteria can be judged by graphically superimposing the measured and transformed data sets, and by calculating the Average Error (AE) between the two sets [102]. It is possible that only certain data points in the complete set will represent valid impedance results which satisfy all four of the abovementioned criteria.

The measured and transformed data are superimposed in Figure 10.22. The conformance of the measured data to the transformed results is excellent at all frequencies above 0.2 Hz, at which point the measured and transformed data sets begin to significantly diverge.

The average error of these data sets are 5.2 (Z') and 6.4 (-Z"). Most of this error is related to the divergence of the low frequency data from the transformed results, and all data points below 0.2 Hz were thus removed from the data set. The results are plotted in Figure 10.23.

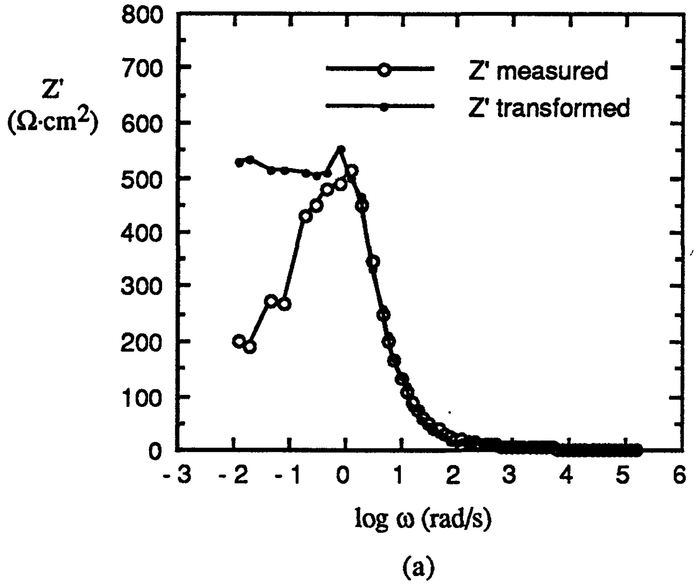

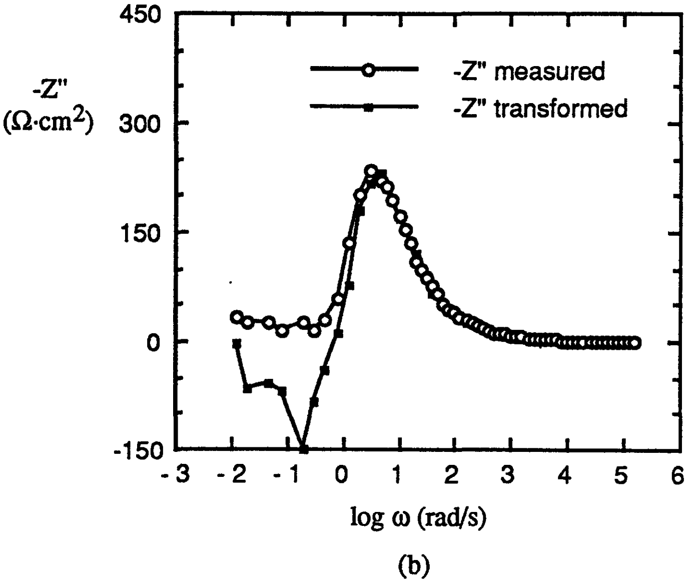

Figure 10.22 Kramers-Kronig transformations of (a) the real component and (b) the imaginary component of EIS data for Nd-Fe-B in NaCl at 23°C. Data were taken after 1 hour of immersion at open-circuit.

Note the excellent graphical agreement between the measured and transformed data sets in this figure. Upon removal of the low frequency data points, the average error values decrease from 5.2 to 0.6 (R → I) and from 6.4 to 1.5 (I → R), as shown in Table 10.2.

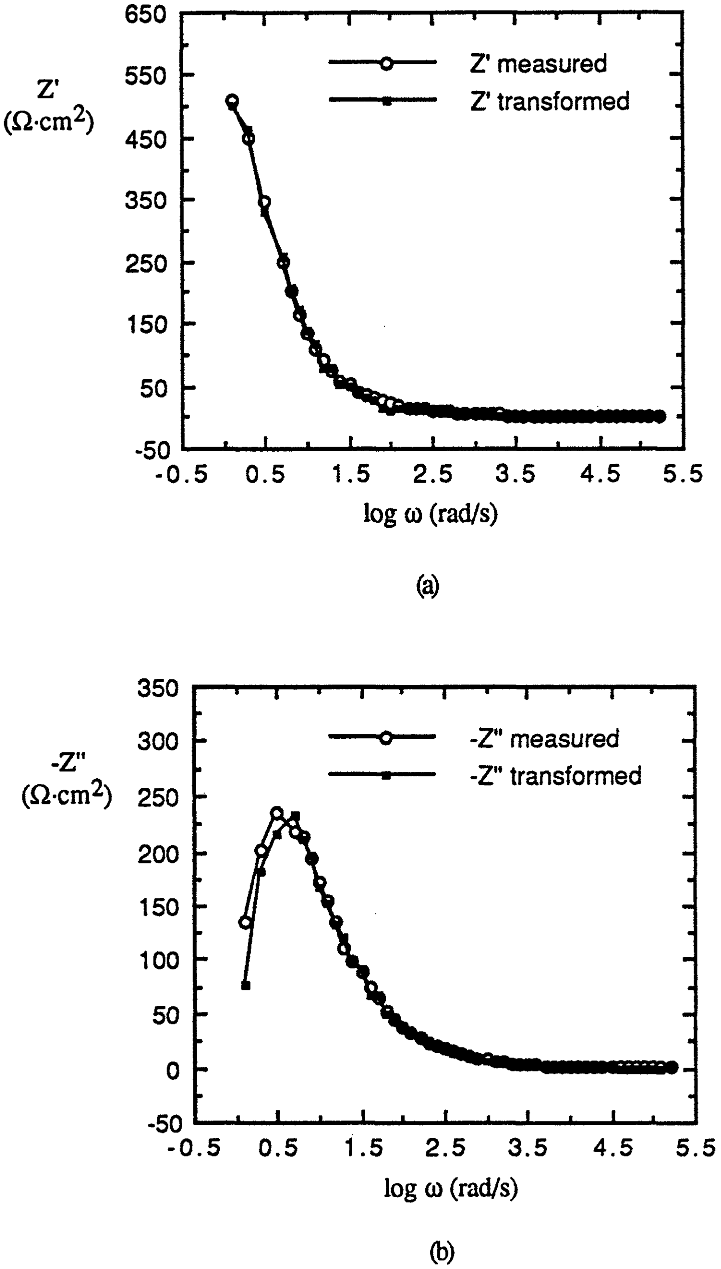

Figure 10.23 Kramers-Kronig transformations of (a) the real component and (b) the imaginary component of the EIS data shown in Figure 10.22 after removal of non-conforming data.

Table 10.2 Average Error (AE) for the full data set shown in Figure 10.22 and for the modified data set shown in Figure 10.23.

	Full data set	Modified data set
Imaginary-to-Real	5.2	0.6
Real-to-Imaginary	6.4	1.5

It is not coincidental that the nonconforming data correspond exactly to the data points which gave rise to the undercutting feature in the Nyquist plots and did not appear to be represented in the final equivalent circuit of Figure 10.19. The failure of these points to constitute a valid impedance helps to explain why physically realistic analog elements could not be devised to account for these data.

The consequence of the nonconformance of these data points is that they should not be utilized when fitting the data to the final equivalent circuit model. It is likely that these data points violated the stability criterion for a valid impedance, as low frequency data which are nonconforming due to instability are not uncommon in rapidly corroding metal systems. Relatively long acquisition times are often required to obtain low frequency data points, and it is possible that changes in the metal-electrolyte interface could occur during the test, especially if the metal is corroding rapidly or undergoing localized attack. In the present study, most of the EIS data points were acquired in 15-30 minutes, but approximately 10-12 hours were needed to acquire the remaining points at frequencies below 0.2 Hz. The acquisition times are longer at low frequency due to increased perturbation cycle times, greater ambient electrical noise, and higher cell impedance. The stability criterion is apparently satisfied during the first part of the experiment and then is violated at some point during the sweep (at approximately 0.2 Hz for the test represented in Figure 10.20).

There are several different reasons why the stability criterion might be violated. The fact that the real part of the impedance (Z') is observed to decrease with time in the undercut region implies that either a decrease in the charge-transfer resistance of the sample or an increase in the corroding area could be occurring during the test. Since such changes would be essentially permanent in nature, it would then be expected that the minimum Z' value measured at the end of the 1 hour test (~ 200 $\Omega \cdot cm^2$) would be the maximum value measured in a test performed immediately after the first experiment. When such a test was conducted, however, the maximum Z' value was 440 $\Omega \cdot cm^2$, which indicates that the undercut points cannot be attributed to decreases in R_t or increases in area. It is possible that the undercut data could be related to changes in the corrosion potential of the sample during the test period. EIS tests were conducted by measuring the sample's E_{corr} after 1 hour of immersion and then applying this d.c. potential back to the cell along with the a.c. sinusoidal perturbation. If the E_{corr} is absolutely stable over the 10-12 hour period, the a.c. signal will cycle at a mean value equal to the actual E_{corr}. However, if the E_{corr} were to drift during the experiment, then polarization to the initial 1 hour corrosion potential would be effectively providing a d.c. offset overpotential to the sample. It has been reported [xx-xx] that corrosion potential drift can lead to the collection of invalid low frequency data.

The "invalid" nature of the undercut data points does not mean that these data are spurious. The term valid is used in a very specific sense, meaning that the data points are not valid inputs to a linear electric circuit model. The data points are still useful in other respects; as a signature of localized corrosion, for example. A rational explanation is believed to exist regarding the nature of these low frequency data points, and this explanation (although not explored further in this study) is likely to be related to the process of localized corrosion.

10.2.5 Fitting of the Experimental Data to the Final Circuit Model

The EIS data for NaCl are shown in Figure 10.24 (Nyquist representation), with the nonconforming data removed. All data points included in this figure are valid in the impedance sense, and will thus be fit to the final circuit model shown in Figure 10.19.

When an attempt was made to fit the data to an -R=C- circuit, a problem was encountered because the data in Figure 10.24 do not correspond to a perfect semicircle. The observed semicircle can actually be described as both depressed and skewed; where the depression is manifested as a slight flattening of the semicircle, and skewing refers to the fact that the angle between the high frequency end of the semicircle and the x-axis is less than 90°.

Deviations from a perfect semicircular shape are very common in corroding systems, and are typically attributed to the presence of a distribution about the mean time constant, τ_{RC}. A distribution of time constants gives rise to semicircle depression, and a time constant distribution which is not symmetric about τ_{RC} will result in skewing of the semicircle. Time constant distribution is usually ascribed to the presence of a heterogeneous or imperfect surface (such as a metal-electrolyte interface which is not perfectly flat). Surface roughness

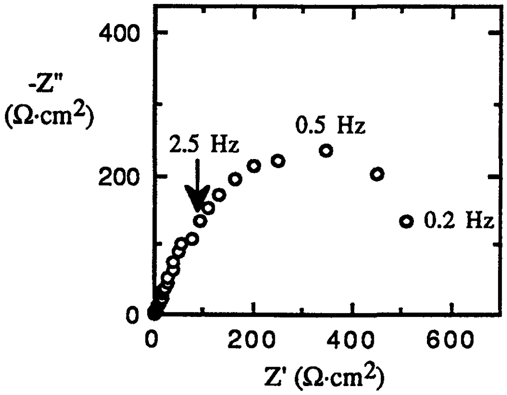

Figure 10.24 EIS data for 1 hour, NaCl with nonconforming points removed.

is considered to be a primary cause of time constant distribution in corrosion studies. It is believed that the time constant distribution observed in the present study may be related to the fact that the corroding surfaces (pits) are curved rather than flat.

EIS data exhibiting time constant distribution are generally modeled in two different ways. The most common method involves the use of mathematical functions which have been empirically devised to fit data which exhibit depression and/or skewing. Two mathematical parameters, α and β (which represent the degree of depression and the degree of skewing, respectively) are placed into the fitting routine to account for the observed depression and skewing. The experimental data can then be fit to the following equation [106]:

$$[10.31] \qquad |Z| = \frac{R}{\left(1 + (j \cdot \omega \cdot R \cdot C)^{\alpha}\right)^{\beta}}$$

If α and β are both equal to one, equation [10.31] represents the governing relation for data exhibiting a perfect semicicle. Empirically-derived fitting functions such as equation [10.31] are utilized to improve the fit to the data, and thus increase the accuracy of the circuit model values obtained by fitting.

A more sophisticated method of analyzing data exhibiting depression or skewing is to use transmission line modeling [107]. This type of modeling attempts to elucidate the cause of depression or skewing, and may thus be capable of providing in-depth information about the corroding system. The primary drawback of the transmission line approach is that it is extremely complicated, and cannot be performed without considerable effort. Despite the possible benefits of using transmission line modeling, the most relevant parameters of interest in this study were obtained much more easily and rapidly through the use of the empirical function described by equation [10.31].

The conforming EIS data (NaCl) were mathematically fit using the CNLS routine, and the results are shown in Figure 10.25. Data from the fit are provided in Table 10.3.

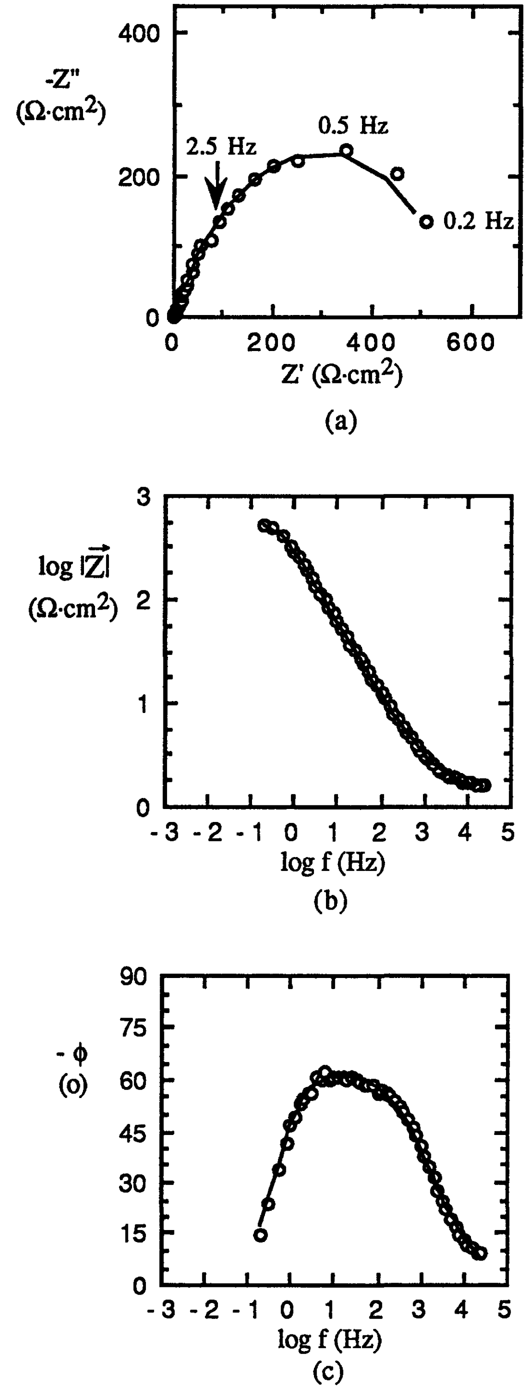

Figure 10.25 EIS data (NaCl, 1 hour) after the removal of data points which did not conform with the KK transformations. The line superimposed on the data indicate the fit obtained using the CNLS routine.

Table 10.3 Parameters obtained from the CNLS fit shown in Figure 10.25 (NaCl, 1 hour).

Analog Element	Element Value	Units	% error in fit
R_Ω	1.4	$\Omega \cdot cm^2$	1.1
$R_{t,pit}/F$	541.3	$\Omega \cdot cm^2$	1.1
$C_{parallel}$	637.9	$\mu F/cm^2$	1.3
α	1.0	—	0.0
β	0.7	—	0.2

The obtained values of α and β confirm the notion that a time constant distribution exists in the present system, and also indicate that the actual distribution is very asymmetric in nature. The fundamental reason for the asymmetric distribution is not apparent.

The low value obtained for the ohmic resistance parameter is consistent with the expected electrolyte resistance between the working electrode and the tip of the reference electrode. The resistivity of the NaCl solution is approximately 22 $\Omega \cdot cm$ and the distance between the two electrodes was 1-2 mm, which gives rise to an expected value of 2.2 - 4.4 $\Omega \cdot cm^2$. A low ohmic resistance value also indicates that a resistive film did not build up on the surface of the Nd-Fe-B electrode during the 1 hour immersion in NaCl.

The "parallel capacitance" element was constructed earlier in this section to represent the parallel combination of the double-layer at the bulk metal surface and the double-layer at the pit surface. The double-layer capacitance of a typical metal-electrolyte interface is 10 - 40 $\mu F/cm^2$ [108], and the capacitance value shown in Table 10.3 (637.9 $\mu F/cm^2$) is therefore much higher than expected. The capacitive element in this case clearly does not correspond to a double-layer capacitance.

Abnormally high capacitance values have been reported for various metal-electrolyte systems [109,110]. As shown in Table 10.4, abnormal capacitances were observed mainly on iron-based alloys in near-neutral solutions. The similarity between the present system (Fe-based, near-neutral) and the systems for which anomolous capacitance values have been reported in the past appears to suggest that the cause of this phenomenon might be common to all of these systems. A theory regarding the fundamental reason for the large capacitance values has not been formulated, however, and the obtained data therefore cannot be readily explained. The observed capacitance values seem to indicate the presence of an element in the system having an extremely high dielectric constant or a very low thickness, but the physical phenomenon exhibiting these characteristics has not been identified.

Table 10.4 Capacitance values for ferrous metals in various test solutions after short immersion times (< 5 hours [109,110]

Metal	Solution	C ($\mu F/cm^2$)
304 SS	0.25M Na_2SO_4 (pH 1) + 100 ppm Cl^-	105
4340 steel	0.5M Na_2SO_4	1700
4340 steel	0.5M Na_2SO_4 + 0.01M $NaNO_2$	400
4340 steel	0.5M Na_2SO_4 + phosphonic acid/fatty amine mixture	500
4340 steel	0.5M NaCl	1240
4340 steel	0.5M NaCl + 0.01M $NaNO_2$	550

Ambiguities regarding the time constant distribution and the nature of the primary capacitive element in this system should not present a serious barrier to the utility of the present work, since the ultimate objective of EIS modeling in this study (and in most corrosion studies) is to obtain the charge-transfer resistance for the metal dissolution reaction. Once R_t has been obtained from the EIS data, the Stern-Geary relationship shown in Equation [10.8] ($i_{corr} = \beta a/2.3 \cdot R_t$) can be employed to calculate the instantaneous corrosion current density (i_{corr}) for the system under test. Faraday's Law can then be used in order to convert i_{corr} to a metal penetration rate, according to the calculation outlined in Section 5.1.10.

Before a conversion can be made to i_{corr}, however, $R_{t,pit}$ must be isolated from $R_{t,pit}/F$. This parameter ($R_{t,pit}$) can be extracted by estimating F, the area fraction of the sample which is pitted. The process used to estimate F is summarized below.

The estimate of F is obtained by dividing the total pitted area by the total surface area. The total pitted area corresponds to the number of pits present on the metal times the average area per pit, and the total surface area refers to the nominally exposed sample area (which can be measured using calipers). Since it is not practical to analyze the entire surface of a metal, several different regions can be selected for analysis. The process of estimating F is initiated by determining the pit density (the number of pits per unit surface area) on the metal after 1 hour of immersion in NaCl. The pit density was estimated by counting the number of discernible pits in a low magnification micrograph, and then dividing this number by the total visible surface area. Data obtained from several micrographs were used to determine an average pit density. The second parameter which must be determined in order to estimate F is the average area per pit. The confocal microscope was used to measure the depth and width of a number of different pits on samples which had been immersed for 1 hour. The area of each pit was then calculated using a hemispherical approximation ($A = 2\pi r^2$), and the pit areas were averaged to obtain the approximate surface area of a typical pit. The ratio of pitted area to total bulk surface area is then obtained by multiplying the pit density times the area per pit, according to:

$$F = \frac{\text{pit area}}{\text{surface area}} = \left(\frac{\text{\# of pits}}{\text{surface area}}\right) \cdot \left(\frac{\text{pit area}}{\text{pit}}\right) \qquad [10.32]$$

This ratio is equal to F, the area fraction pitted. The pit density was estimated as $1.05 \cdot 10^4$ pits per cm^2 of surface area, and the area per pit as $4.4 \cdot 10^{-7}$ cm^2 per pit. The value of F was then estimated as approximately 0.005 after 1 hour of immersion in NaCl at 23°C.

An $R_{t,pit}/F$ value of 541.3 $\Omega\cdot cm^2$ was obtained from fitting (Table 10.3). The estimate of F determined above (0.005) allows the pit charge-transfer resistance, $R_{t,pit}$, to be determined as approximately 2.7 $\Omega\cdot cm^2$. This value can then be input into the Stern-Geary equation along with the βa value measured in Section 5.1 (0.042 V/decade), in order to estimate the corrosion current density. An i_{corr} value of 6800 $\mu A/cm^2$ was calculated using this procedure. Faraday's Law was subsequently used to convert this value into a penetration rate of approximately 9.8 μm/hour. The penetration rate estimated from the EIS data can be compared to the penetration rate determined in Section 5.2. The maximum pit density was measured as 3.4 μm after 1 hour of immersion in NaCl. This comparison indicates that the EIS calculation was capable of correctly estimating the order of magnitude of the observed penetration rate. Mansfeld *et al* [101] have advanced the notion that EIS data, in combination with the modeling methods and estimate of F described above, can be used to accurately predict metal penetration rates in pitting systems. The results of the present study indicate that such a method may not be viable in all systems, as the calculated penetration rate is in error by approximately 190%.

The low accuracy of the penetration rate calculation is likely related to the difficulty of accurately estimating F. Several different factors are believed to contribute to the relative inaccuracy of this estimate. For example, the estimate of F assumes that the pit density is relatively constant over the entire metal surface, a situation which did not appear to exist for Nd-Fe-B. The number of pits in various photographed regions of identical surface area were often found to differ by a factor of two or more. Even though the pit density value used to estimate F was an average taken from several micrographs, it is difficult to believe that this value accurately reflects the exact average pit density on the metal surface. A second problem in estimating pit density is that counting the number of pits in a given micrograph is more difficult than it might initially seem. Low magnification photographs were used in order to include as large an area as possible, and the pits can be quite small in these images. It is believed that errors may have been made in the determination of the number of pits present in each photograph used to estimate the pit density. Finally, the value determined as the average area per pit is likely in error as well. Due to the variation in the depths and widths of the observed pits, an extremely large number of pits would need to be profiled in order to generate a very accurate value for the average pit area.

It is conceivable that the parameter F could be estimated more accurately if an extremely diligent effort were made to minimize the errors described above. Such an effort might then result in a calculated penetration rate which more accurately reflects the real rate of penetration in the metal. However, a primary objective of using the Mansfeld analysis to estimate pit depths is to avoid the time-consuming labor of measuring the pit depths manually. Use of the EIS method to estimate pit depths did not appear to result in a large time savings, and more importantly did not achieve the desired accuracy for Nd-Fe-B. More accurate predictions are likely feasible for metals exhibiting more uniform pit densities. The analysis of Mansfeld *et al* [101] is believed to be very valuable from a scientific standpoint in any case, and can certainly form the basis for understanding EIS data in a system which is exhibiting pitting.

10.2.6 Modeling of the EIS Data with Time

In addition to the EIS data analyzed above (obtained after 1 hour of immersion), results were also collected for samples which were immersed for 24 and 72 hours prior to EIS testing. The results of these experiments were previously shown in Figures 5.35 and 5.36. Two substantial changes in the EIS spectra occur over time: the change in character of the low frequency time constant from an undercut appearance to a fourth-quadrant loop, and the apparent decrease in semicircle diameter with time. The present section attempts to discuss both of these factors, with primary emphasis on the changing semicircle diameter because of the possible effects of this parameter on the corrosion rate of the metal.

The appearance of a fourth quadrant loop is very common in corrosion studies. Although the loop occurs in the quadrant normally associated with inductive behavior ($\phi > 0$), the time constant is typically referred to as a "pseudo-inductive" loop rather than an inductive loop. Real electrochemical systems generally do not contain physical processes which exhibit truly inductive behavior [111]. The loop is instead typically attributed to an adsorption process, which is believed to give rise to a negative capacitance value under certain circumstances [111]. Although the physical significance of a negative capacitance is not exactly clear, a process exhibiting such properties would be capable of producing the acquired spectra without the necessity of postulating the existence of an inductive component in the electrochemical system.

When subjected to the KK transformations discussed in Section 10.2.4, the data in the pseudoinductive loop were found to transform correctly, as shown in Figure 10.26, which is consistent with previous citations for this type of data [112]. It should be noted that the two lowest frequency data points did not transform particularly well, and were thus removed from the data shown in Figure 10.26 prior to CNLS fitting.

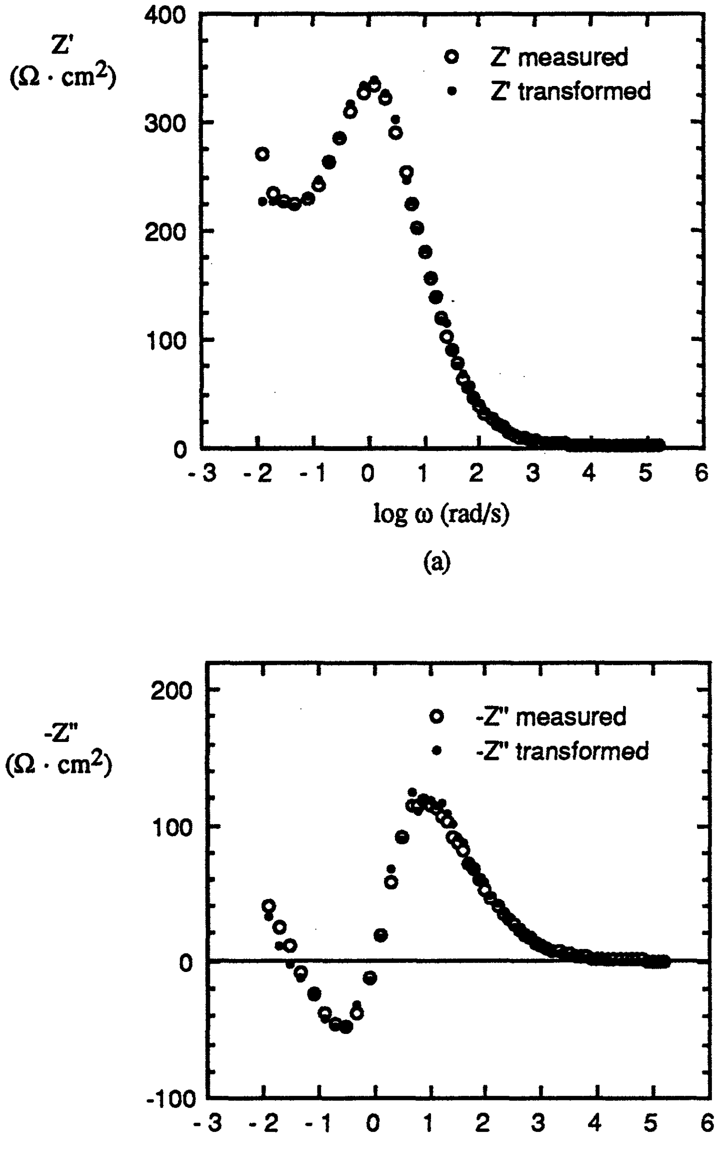

(a)

(b)

Figure 10.26 Kramers-Kronig transformations of (a) real and (b) imaginary EIS data collected after 24 hours of immersion in NaCl (23°C). The average errors were (a) 0.8 and (b) 2.3.

When construcing a circuit model for immersion times greater than 1 hour, it is necessary to include elements which give rise to the pseudoinductive loop. All data exhibiting such a loop were modeled using the circuit shown in Figure 10.27. Two time constants were

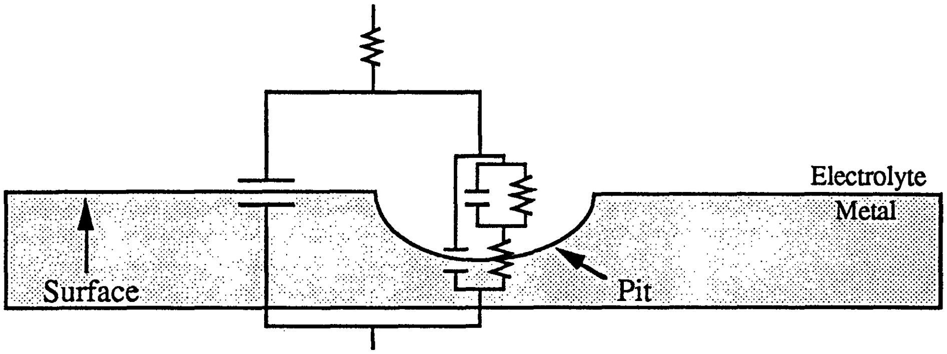

Figure 10.27 Equivalent circuit used to model the data exhibiting a pseudoinductive loop at low frequencies. The circuit elements are as labeled in Figure 5.xx, with the addition of R_{ads} and C_{ads}.

present in this circuit, one associated with the charge-transfer semicircle (R_t, $C_{parallel}$) and one associated with the pseudo-inductive loop (R_{ads}, C_{ads}). It should be noted that Figure 5.35 (c) indicates that a third time constant may be emerging at 72 hours (possibly related to crevice formation), but the data still were more accurately fit to a 2 time constant model.

As discussed in Section 5.3.4, most (but not all) of the anodic dissolution over the 72 hour period is still occurring within pits, and the resistor representing the anodic charge-transfer reaction is therefore located at the pit surface. The capacitance associated with the surface and pit can be collected into a parallel capacitance term, as described in Section 10.2.2. An -R=C- time constant was included to represent the adsorption reaction. The associated circuit branch was placed at the pit surface, since the adsorption process appears only after time has elapsed, and changes in the electrolyte with time occur mainly within pits.

The assumption that an adsorption reaction is taking place was based not on physical evidence, but rather on previous interpretations of similar data in the literature [111]. It is not at all certain that adsorption is taking place in the present system, nor is it clear which species are adsorbing on the surface if adsorption is in fact occurring. This assumption was utilized because it appears to be the only credible way to interpret the data.

The data were fit to the circuit model of Figure 10.27. Fit lines are superimposed on the 24 hour data in Figure 10.28, and the data obtained from fitting are shown in Table 10.5.

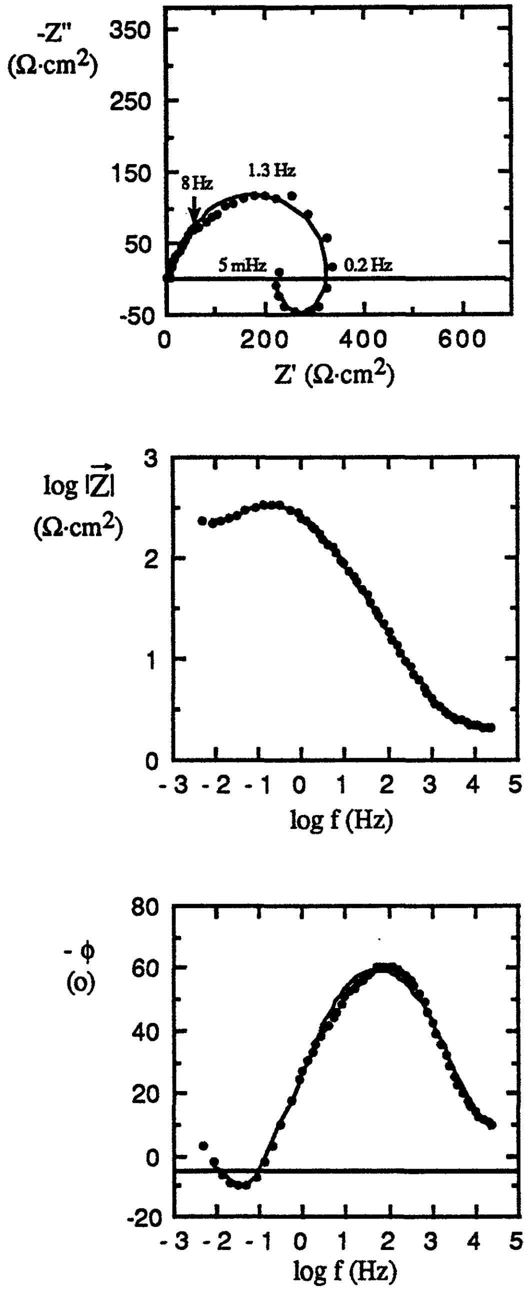

Figure 10.28 EIS data from 24 hour test with CNLS fit. The lines indicate the CNLS fits to the data.

Table 10.5 Parameters obtained from CNLS fit to 24 hour data.

Analog Element	Element Value	Units	% error in fit
R_Ω	1.8	$\Omega \cdot cm^2$	2.5
$R_{t,pit}/F$	362.4	$\Omega \cdot cm^2$	1.5
$C_{parallel} \cdot F$	503.4	$\mu F/cm^2$	2.6
α	0.7	—	0.5
R_{ads}	-138.8	$\Omega \cdot cm^2$	2.5
C_{ads}	-17400.0	$\mu F/cm^2$	4.4

Fitting the data to the model circuit shown in Figure 10.27 facilitates the extraction of the primary parameter of interest, the charge-transfer resistance in the pit ($R_{t,pit}/F$). This parameter was also determined for immersion times of 6, 12, and 48 hours (the form of the data for these tests was similar to the 24 and 72 hour tests). The obtained $R_{t,pit}/F$ data are shown as a function of time in Figure 10.29.

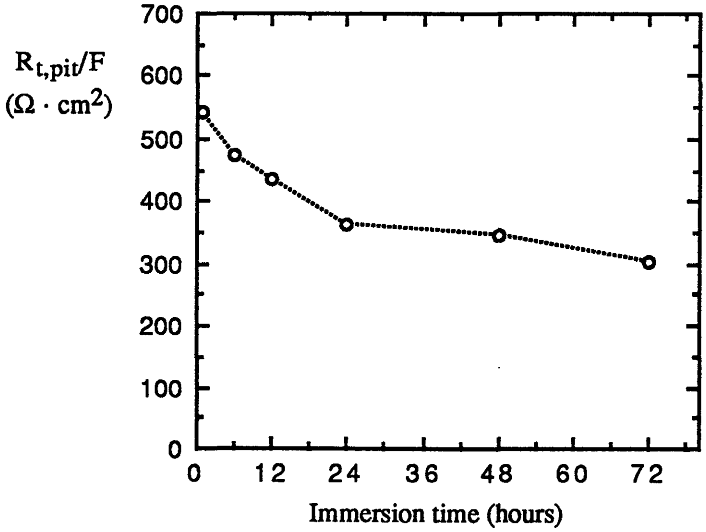

Figure 10.29 $R_{t,pit}/F$ at immersion times from 1 hour to 72 hours (NaCl, 23°C).

The decrease in $R_{t,\,pit}/F$ with time (Figure 10.29) correlates directly to the other temporal change in the Nyquist plots (besides the appearance of the pseudoinductive loop), which is the decrease in semicircle diameter with time. The most obvious explanation of the decreasing trend in $R_{t,pit}/F$ is that the rate of pitting is likely increasing with time, leading to a lower charge-transfer resistance and a higher metal attack rate. This interpretation is consistent with the auto-catalytic nature of the concentration changes occurring within pits.

Closer scrutiny reveals that changes in area with time may also be capable of accounting for the behavior observed in Figure 10.29. The EIS data were plotted using the *nominal* area of the sample for all three data sets, but the true area is unlikely to be constant during pit propagation. If the pits grow with time, the area of each pit must be consistently increasing. Since resistance is inversely related to the area through which current flows, the resistance to current flow will decrease as pitting propagates even if the rate of the actual metal ion dissolution reaction is unchanged. Mathematically, such an area increase would lead to a rise in the value of F, and the actual pit charge-transfer resistance ($R_{t,pit}$) might not be decreasing at all. The viability of this hypothesis will be quantitatively analyzed in below, using pit data obtained at 12, 24 and 72 hours of immersion.

10.2.6.1 Effect of Pit Propagation on $R_{t,pit}/F$

The parameter $R_{t,pit}/F$ was found to decrease with time, as shown in Figure 10.29. It was mentioned above that the decreasing nature of $R_{t,pit}/F$ could be due either to a decrease in resistance with time (likely due to an increasing dissolution rate), or to an increase in the corroded area with time. The *rate* of pit propagation was found to decrease with time during the 72 hour test period, as evidenced by the fact that the second derivative of the maximum penetration depth line in Figure 5.26 is negative. The decreasing nature of $R_{t,pit}/F$ apparently cannot be attributed to an increase in the corrosion rate with time. It is possible, however, that an increase in the dissolution area might be capable of accounting for the observed trend in $R_{t,pit}/F$, owing to the measured increases in both the depth and width of pits with time. Since resistance is inversely proportional to the area through which current flows, increases in pit area can lead to reductions in the measured value of $R_{t,pit}/F$ even if the actual charge-transfer resistance within the pit ($R_{t,pit}$) is not decreasing with time.

A precise calculation which accounts for the effects of changing pit area can only be made if accurate estimates of pit density are available for 12, 24, and 72 hours of immersion. Completely reliable pit density values are not available for times greater than 1 hour, however, as discussed in Section 5.4.4.1 (a). Even though a strictly accurate calculation of $R_{t,pit}$ with time cannot be made without pit density values for 12, 24, and 72 hours of immersion, a less precise calculation was performed by assuming that the pit density is essentially constant over the 72 hour time period (i.e. equal to the 1 hour pit density estimated in Section 10.2.5); an error is introduced by the fact that this assumption does not account for pits which do not propagate over time.

The purpose of the calculation is to estimate the possible effects of increasing pit area on the measured charge-transfer resistance, using the changing pit area as an indicator of increased area through which current flows. In this calculation, all pits were assumed to be nearly hemispherical, and the pit depth data shown in Figure 5.26 were used in conjunction with the formula for the area of a hemisphere ($A = \pi \cdot d^2$, where d refers to pit depth) to construct a representative pit *area* distribution at each immersion time. Average pit areas were then calculated from the representative area distributions. The average pit area (in cm^2) was multiplied by the assumed pit density in order to obtain the parameter F; the $R_{t,pit}/F$ value was then converted to $R_{t,pit}$ (in $\Omega \cdot cm^2$ of pit area) in order to estimate the resistance to charge-transfer within the pits at each immersion time. Results are shown in Figure 10.30.

It is clear that when the increases in pit area with time are considered, the polarization resistance within the pit is seen to increase rather than decrease with time. This trend is consistent with the observed data in Figure 5.26. The above calculation, though not strictly accurate, is capable of demonstrating that the increase in the area through which current flows *is* sufficient to account for the decrease in R_t with time. It is very likely, therefore, that the decreasing nature of $R_{t,pit}/F$ in Figure 10.29 can be attributed to area increases with time, especially in view of the fact that the alternative explanation of decreases in resistance with time are not consistent with measured pit depth data.

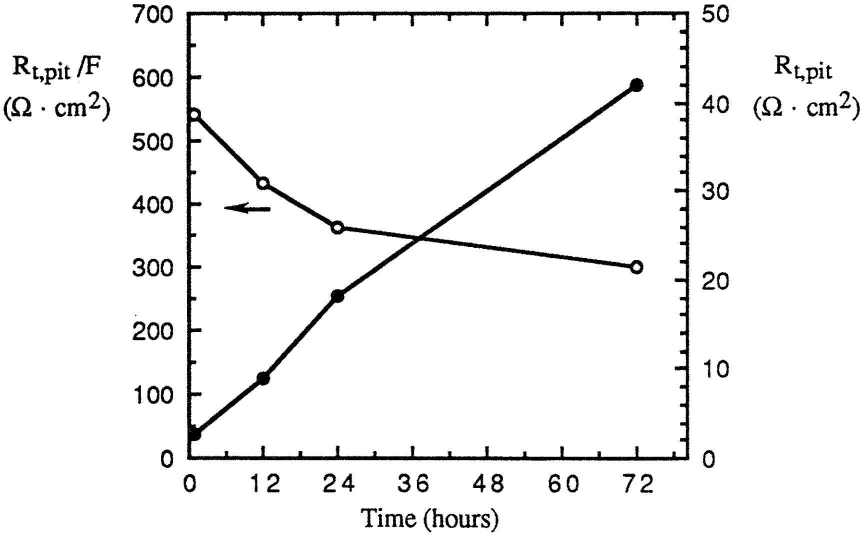

Figure 10.30 Changes in the charge-transfer resistance associated with the pit, both before (open circles) and after [filled circles] the data were corrected for increases in pitted area with time.

The decreasing nature of $R_{t,pit}/F$ with time was attributed above to increases in the pitted area with time. It is relevant to note that the observed trend in $R_{t,pit}/F$ *could* conceivably be related to surface attack. The fact that the area of surface dissolution increases with time to eventually cover nearly the entire sample indicates that corrosion of the surface could provide increasing area through which current can flow. This increase in the area through which anodic current flows could possibly result in a decreasing resistance with time. However, owing to the relatively shallow nature of the surface attack relative to the measured pit depths, the majority of the anodic current is still flowing through the pits even at longer immersion times; it is thus believed that the impedance response will be dominated by anodic dissolution in the pitted areas. This explanation can be described using the terminology introduced in Section 10.2.2. Since most of the anodic dissolution is occurring in the pits rather than at the surface, equation [10.26] is expected to hold, such that the charge-transfer resistance at the surface is still much greater than the charge transfer resistance at the surface; this notion is especially true as the pitted area increases and the resistance to current flow through the pits decreases. It should be considered that some anodic current must pass through the surface in order to account for surface dissolution, but it is believed that the amount of anodic current flowing through the surface is still far less than the amount flowing through the pits, even at longer immersion times.

10.2.7 Comments on the Results of EIS Modeling

The EIS modeling procedure was not capable of generating accurate penetration rate data for the system under study. Significant benefits have nevertheless been obtained from this analysis. The equivalent circuit modeling process forces the investigator to ponder all of the processes involved in the corrosion process as discrete steps, and therefore contributes to the overall understanding of the system. Use of the modeling process additionally prevents an investigator from misinterpreting EIS data. For example, many researchers simply take the R_t value determined by CNLS fitting, divide by nominal area and report the result as the corrosion rate of the metal. An integrated approach, using microscopy, complementary electrochemical techniques, and careful modeling can prevent such errors from being committed.

The EIS modeling also represents the major scientific aspect of the present work. This study has predominantly been focused on applied research, and the inclusion of material which is more fundamental in nature tends to prevent the work from focusing exclusively on practical concerns. EIS is an important technique in the analysis of corroding systems, and it is believed that this work has contributed to EIS knowledge in general, as well as to the understanding of the corrosion of Nd-Fe-B. For example, the effect of changing area on impedance response is believed to be an important consideration in analyzing EIS data for corroding metals which is often overlooked in practice. The results reported in the present study should focus attention on this particular issue in the interpretation of EIS data.

10.3 Kramers-Kronig Transformations

Quantitative analysis of electrochemical impedance spectroscopy (EIS) data relies on a modeling process which is derived from linear electric circuit theory, as described in Appendix 10.1.2. In order to utilize such a modeling process with confidence, it is necessary to determine whether or not each experimentally acquired data point constitutes valid impedance data within the framework of linear circuit theory. Impedance data must satisfy four criteria in order to be considered valid: linearity, causality, stability, and finite value of the impedance (or admittance) at zero frequency; as defined below.

Causality means that the response of the system is due only to the perturbation applied, and does not contain significant components from spurious sources. Linearity implies that the perturbation and response of the system are described by linear differential equations, which requires a low voltage perturbation to be used (as described in Section 10.1.2.6). Stability means that the system must be stable, in the sense that it returns to its original state after the perturbation is removed. Either the impedance or the admittance ($1/\vec{Z}$) must be finite-valued at both $\omega \rightarrow 0$ and $\omega \rightarrow \infty$. The impedance must also be a continuous and finite-valued function at all frequencies between 0 and ∞ [102].

The conformance of the experimental results to the four criteria which define valid impedance data can be evaluated using a set of mathematical relationships known as the Kramers-Kronig (KK) transformations, as described in Section 5.3. The utility of the KK relations is derived from the fact that the real and imaginary components of a measured impedance are not truly independent quantities. The real component of the impedance (Z') can be calculated at every measurement frequency if the imaginary component of the impedance (-Z") has been measured over a wide frequency bandwidth [104,105]. The measured imaginary component ($-Z''_{meas}$) is examined as a function of the logarithm of angular frequency, log ω, and the measured imaginary data set is represented as $(-Z''_{meas}, \log \omega)$.

The imaginary-to-real transformation $(-Z''_{meas}, \log \omega) \rightarrow (Z'_{trans}, \log \omega)$ results in a frequency spectrum of transformed real data $(Z'_{trans}, \log \omega)$. The real-to-imaginary transformation can also be performed, in order to convert the measured real data set $(Z'_{meas}, \log \omega)$ to a transformed imaginary data set $(-Z''_{trans}, \log \omega)$. The output of the calculations are transformed data sets (Z'_{trans} and $-Z''_{trans}$ vs. log ω), which can be compared to the measured data sets (Z'_{meas} and $-Z''_{meas}$ vs. log ω). If the impedance data are completely valid according to the criteria described above, excellent agreement should be obtained between the transformed and measured data sets for both the real and imaginary components. The conformance of the data to the validity criteria can be judged graphically by superimposing the measured and transformed data sets, and quantitatively by calculating the Average Error (AE) between the two data sets [102]. It is possible that only certain data points in the complete set will represent valid impedance results which satisfy all four of the abovementioned criteria.

The use of the KK transforms to evaluate the actual impedance data generated in this study was described in Section 10.2. The present section will focus on delineating the exact steps utilized in performing the transformations. The procedure will be outlined for the $-Z''_{meas} \rightarrow Z'_{trans}$ transformation. The form of the $Z'_{meas} \rightarrow -Z''_{trans}$ transformation is similar, though a slightly different equation is used in the actual transformation. Appendix 10.4 contains the source code for the computer program which was used to actually perform the imaginary-to-real transformation.

10.3.1 Kramers-Kronig Transformation Procedure

An overview of the entire sequence used to perform the KK transformations is shown in Figure 10.31. A general description of the KK procedure appears on the following page.

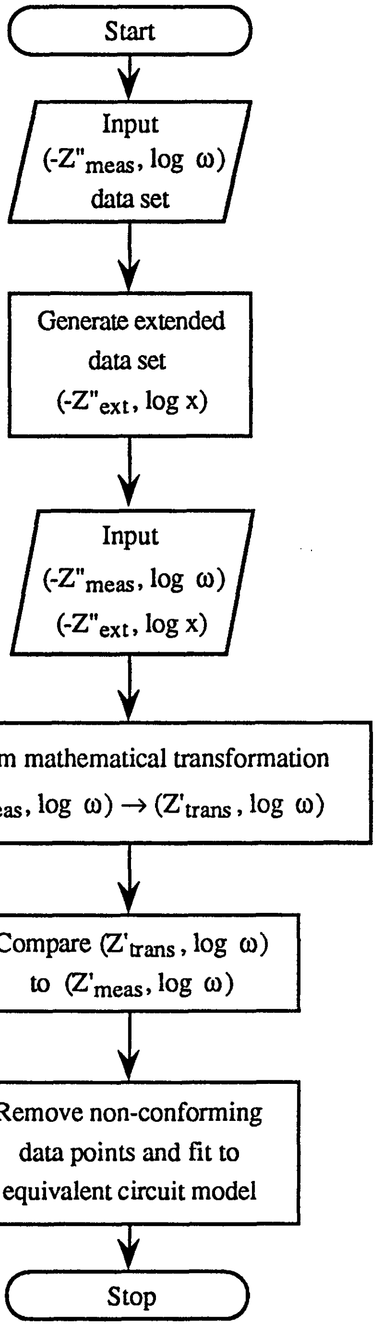
Start
Input
(-Z"meas, log ω)
data set
Generate extended
data set
(-Z"ext, log x)
Input
(-Z"meas, log ω)
(-Z"ext, log x)
Perform mathematical transformation
(-Z"meas, log ω) → (Z'trans, log ω)
Compare (Z'trans, log ω)
to (Z'meas, log ω)
Remove non-conforming
data points and fit to
equivalent circuit model
Stop

Figure 10.31 Flow chart of overall sequence of imaginary-to-real Kramers-Kronig transformation.

The steps used to perform the KK transformations are outlined in the following paragraph. Details pertaining to each step in the process are provided in subsequent sections.

The measured data set ($-Z''_{meas}$, log ω) has one data point per angular frequency. For the purposes of the transformation, it is important to have a data set with a large number of data points. An extended data set is therefore generated by interpolating the measured data points at closely spaced frequencies. The logarithm of the angular frequency of the extended data set is designated as log x, in order to avoid confusion with the logarithm of the angular frequency of the measured data set (log ω). Both the measured and extended data sets will be utilized in the actual transformation, which will convert a measured imaginary data set ($-Z''_{meas}$, log ω) to a transformed real data set (Z'_{trans}, log ω). This transformed data set (Z'_{trans}, log ω) will then be compared to the experimentally measured real data set (Z'_{meas}, log ω) to see whether or not the data points constitute a valid impedance. Only those points which constitute a valid impedance will be input to the modeling process.

The majority of the calculations in the KK process are contained in two steps: the generation of the extended data set, and the performance of the actual transformations. Both steps are explained in detail below.

10.3.1.1 Generation of the Extended Data Set

A large data set is normally utilized when performing numerical transformations in order to achieve a high degree of accuracy. The number of impedance data points measured in a typical EIS experiment is insufficient to achieve the accuracy needed to perform the KK transformations. Increasing the number of experimentally acquired data points would lead to an unacceptable increase in measurement time. This difficulty can be overcome by interpolating the measured data set in order to generate an extended data set having data points which are much more closely spaced than in the measured set. The extended data set can then be used in the calculation routine for improved accuracy.

An overview of the generation of the extended data set is shown in Figure 10.32. An explanation of this procedure is provided in the following paragraphs.

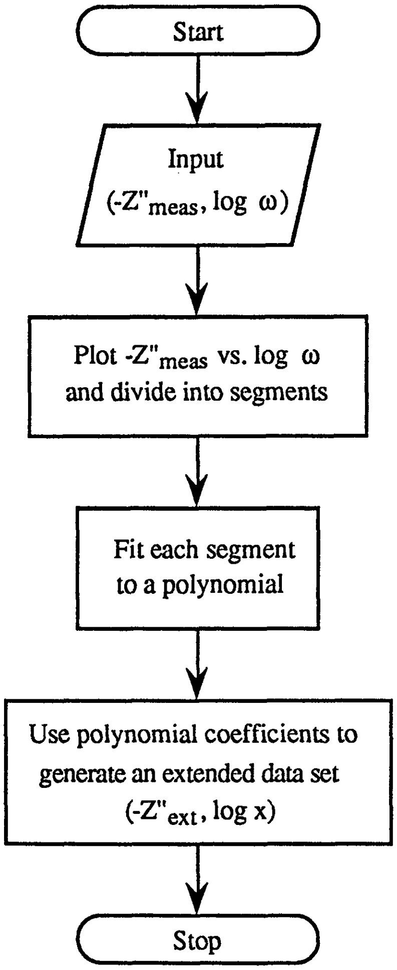
Start
Input
(-Z"meas, log ω)
Plot -Z"meas vs. log ω and divide into segments
Fit each segment to a polynomial
Use polynomial coefficients to generate an extended data set
(-Z"ext, log x)
Stop

Figure 10.32. Overview of the generation of the extended data set.

In order to interpolate the data, the data set ($-Z''_{meas}$, $\log \omega$) was plotted and subdivided into segments, as shown in Figure 10.33. Segment borders were located at maxima, minima, or inflection points in order that each segment could be fit to a distinct polynomial.

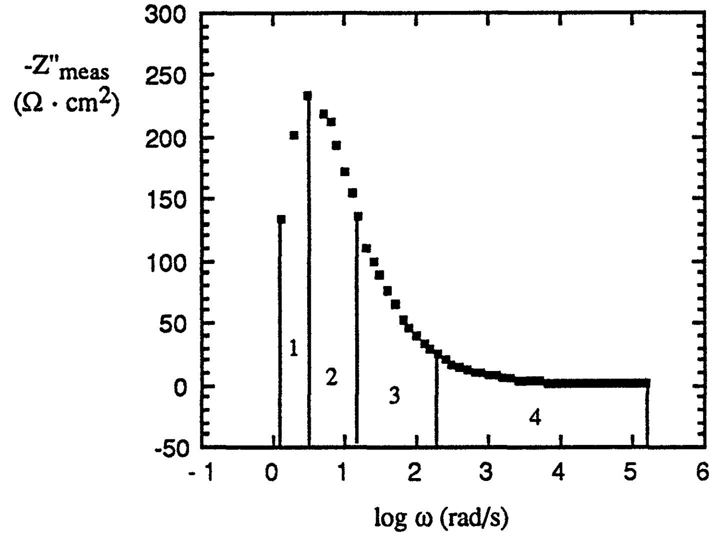

Figure 10.33 Division of impedance data into segments to facilitate polynomial fitting.

Each segment is fit to a polynomial such that:

$$[10.33]\quad -Z''_{meas}(\log \omega) = \sum_{i=0}^{i=n} a_i \cdot (\log \omega)^i = a_0 + a_1 \cdot \log \omega + \ldots + a_n \cdot (\log \omega)^n$$

where a_i represents the coefficients of the polynomial and n is the order of the polynomial. It was found that the segments could be fit accurately using polynomials of fifth-order or less, such that a maximum of five polynomial coefficients are obtained for each segment.

An example of polynomial fitting is provided in Figure 10.34 for segment 2 of the data set previously shown in Figure 10.33.

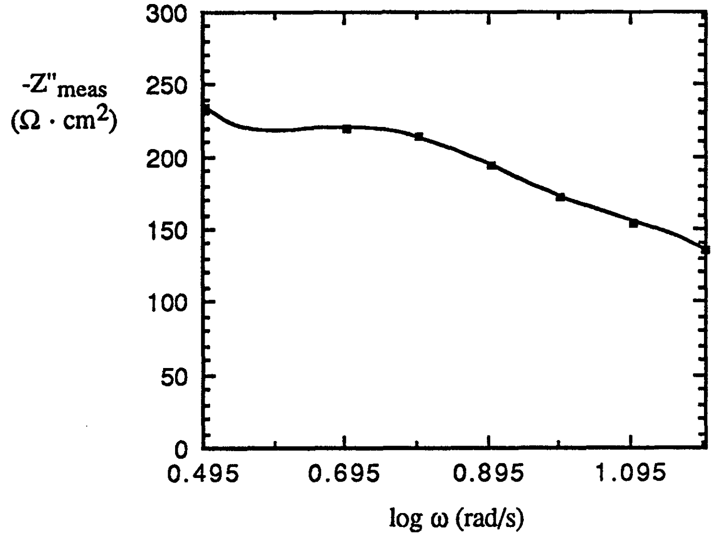

Figure 10.34 Polynomial fit to one segment (segment 2) of the data shown in Figure 10.3.

The data points in this segment were fit to a fifth-order polynomial, and the actual fit is superimposed on the data. The six coefficients derived from the fit (a_0-a_5) are shown below in the equation which mathematically describes segment 2:

$$[10.34] \quad -Z''_{meas} = 4904 - 29158 \cdot \log\omega + 70765 \cdot (\log\omega)^2 - 83581 \cdot (\log\omega)^3 + 48037 \cdot (\log\omega)^4 - 10795 \cdot (\log\omega)^5$$

Once the polynomial coefficients have been obtained from the fitting procedure, a set of extended data points can be generated at uniformly spaced angular frequencies, log x. Since equation [10.34] provides a mathematical relationship between $-Z''_{meas}$ and any given frequency in segment 2, a value of $-Z''_{ext}$ can be calculated for any selected frequency in the segment. Angular frequencies were chosen at small, logarithmically spaced frequency intervals (50 data points per frequency decade), in order to construct an extended data set with closely spaced frequency values as required for transformation accuracy. Extended data sets were generated for all segments, and then combined to form one complete extended data set having the form ($-Z''_{ext}$, log x). The extended data set is shown graphically in Figure 10.35.

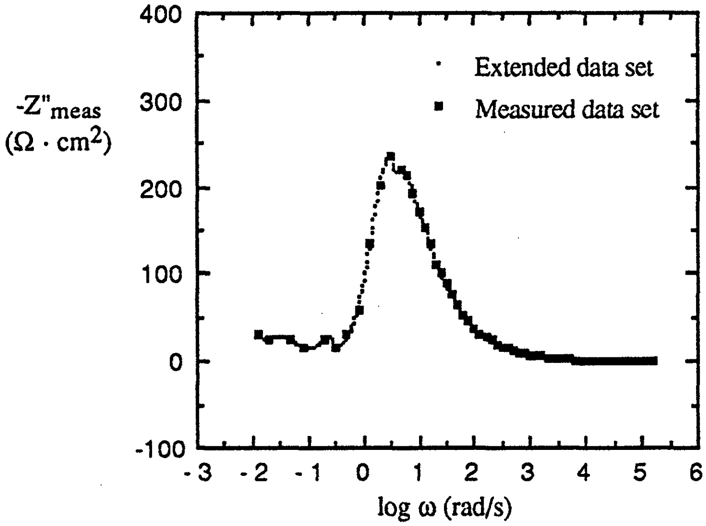

Figure 10.35 Extended data set which was generated at closely spaced angular frequencies by interpolation of the measured data. The measured data set is shown to demonstrate the agreement between the two data sets.

10.3.1.2 Execution of the Kramers-Kronig Transformations

Once the extended data set has been generated, the actual KK transformations can be performed. The transformation procedure is described on the following pages.

All frequencies must be converted from logarithmic format (log ω or log x) to linear format (ω or x) before performing the transformations, since the actual transformations are all performed using linear values. The extended data sets could have been generated directly in linear form if the polynomials were fit to ($-Z''_{meas}$, ω) rather than to ($-Z''_{meas}$, log ω), but the use of logarithmic plotting facilitates the fitting process since the data spacing is much more uniform than if linear plotting is used. It is thus simpler to perform the fit using logarithms, and to then convert to linear values just before performing the transformation.

The linear form of the extended data set ($-Z''_{ext}$, x) and the measured data set ($-Z''_{meas}$, ω) are both utilized in the actual KK transformation procedure, according to the imaginary-to-real transformation equation [102]:

$$[10.35] \quad Z'_{trans}(\omega) = Z'_{meas}(\infty) + \left[\frac{2}{\pi}\right] \cdot \int_0^{\infty} \frac{x \cdot Z''_{ext}(x) - \omega \cdot Z''_{meas}(\omega)}{x^2 - \omega^2} \cdot dx$$

Since frequency cannot be measured over an infinite bandwidth, the actual calculation is performed using the finite difference form of [10.35]:

$$[10.36] \quad Z'_{trans}(\omega) = Z'_{meas}(\omega_{max}) + \left[\frac{2}{\pi}\right] \cdot \sum_{x_{min}}^{x_{max}} \frac{x \cdot Z''_{ext}(x) - \omega \cdot Z''_{meas}(\omega)}{x^2 - \omega^2} \cdot \Delta x$$

where $Z'_{meas}(\omega_{max})$ is the real part of the impedance at the highest measurement frequency. The calculation is performed by considering only one angular frequency at a time. For each ω, the summation is performed for the entire extended data set by iterating x from x_{min} to x_{max}. The result of the summation is one Z'_{trans} data point, at the given angular frequency. The process is then repeated for the next angular frequency. This procedure is performed until the Z'_{trans} has been calculated for every measurement frequency. A (Z'_{trans}, ω) data set is thereby acquired, which can be converted to ($-Z''_{trans}$, log ω) and then compared to the measured data as in Section 10.2.

A similar procedure is utilized to transform the measured real data set (Z'_{meas}, ω) to the imaginary data set ($-Z''_{trans}$, ω), using a slightly different equation [102]:

$$[10.37] \qquad Z''_{trans}(\omega) = -\left[\frac{2\omega}{\pi}\right] \cdot \int_0^{\infty} \frac{Z'_{ext}(x) - Z'_{meas}(\omega)}{x^2 - \omega^2} \cdot dx$$

The finite difference form of [10.37] is:

$$[10.38] \qquad Z''_{trans}(\omega) = -\left[\frac{2\omega}{\pi}\right] \cdot \sum_{x_{min}}^{x_{max}} \frac{Z'_{ext}(x) - Z'_{meas}(\omega)}{x^2 - \omega^2} \cdot \Delta x$$

The transformed imaginary data set ($-Z''_{trans}$, ω) can be converted to logarithmic form ($-Z''_{trans}$, log ω) and then compared to the measured imaginary data set ($-Z''_{meas}$, log ω).

In order to perform the lengthy summations associated with the KK transformations, a computer program was written in Microsoft QuickBasic®. A printout of the source code used to perform the imaginary-to-real transformation is included in Appendix 10.4.

The average error (AE) of the transformed data can be determined using [102]:

$$[10.39] \qquad AE = \frac{100 \cdot \sum_{\omega_{min}}^{\omega_{max}} \left| Z_{meas}(\omega) - Z_{trans}(\omega) \right|}{(\text{\# of measurement frequencies}) \cdot Z_{max}}$$

A separate computer program was written to perform the AE calculation. This program is not provided as part of the present document.

10.4 Source Code for Imaginary-to-Real KK Transformation

```
'Variable Initialization:

'~~~~~~~~~~~~~~~~~~
'Simple Variables
'~~~~~~~~~~~~~~~~~~

logstep!=0
linstep!=0
zmax!=0
zreinfin!=0
AE!=0
aetermsum!=0
ord%=0
imax%=0
i%=0
j%=0
datpts%=0
imaxsum%=0
imaxsum2%=0
imaxseg%=2
n%=0
m%=0

'~~~~~~~~~~~~~~~~~~
'String Variables
'~~~~~~~~~~~~~~~~~~

a$=""
de$=""
dum$=""
outdatfil$=""
inlogwfil$=""
inzimagfil$=""
inavgerrfil$=""
v$=""
linlog$=""
h$=""
AE$=""

'~~~~~~~~~~~~~~~~~~~~~~~
'Start of Main Program
'~~~~~~~~~~~~~~~~~~~~~~~

LOCATE 10,19
PRINT "KRAMERS-KRONIG TRANSFORMATIONS FOR EIS DATA"
LOCATE 11,19
PRINT "PROGRAM 1:  IMAGINARY-TO-REAL TRANSFORMATION"
LOCATE 12, 29
PRINT "(Steve Attanasio, 1/95)"
LOCATE 20,28
INPUT "Press return to continue",dum$
CLS
```

```
LOCATE 5,28
PRINT "PROGRAM OBJECTIVE:"
LOCATE 10,5
PRINT "This program takes (log w,Z"(w)) data and transforms it to (log w, Z'(w)) data."
LOCATE 12,5
PRINT "{Note that in this program, w is used to represent angular frequency (omega)}"
LOCATE 22,27
INPUT "Press return to continue",dum$
CLS
LOCATE 5,29
PRINT "IMPORTANT NOTE:"
LOCATE 10,6
PRINT "This program requires that you have separate datafiles for the"
LOCATE 12,5
PRINT "log w and for the Z"(w).  Both data files must be located IN the QuickBasic folder"
LOCATE 14,9
PRINT "Each file MUST be in Text (ASCII) format, with the data in column A."
LOCATE 22,27
INPUT "Press return to continue",dum$
CLS
LOCATE 10,6
PRINT "This program requires that you have fit the Z"(w) data to polynomials"
LOCATE 12,5
PRINT "The polynomial coefficients from each fitting segment will be input to the program"
LOCATE 22,27
INPUT "Press return to continue",dum$
CLS
LOCATE 10,6
PRINT "The program also requires the high frequency limit of the real impedance,"
LOCATE 12,25
PRINT "Z'(∞), as an input."
LOCATE 17,6
INPUT "Please input this parameter (Z'(∞)):  ",zreinfin!
LOCATE 22,27
INPUT "Press return to continue",dum$
CLS
LOCATE 3,10
INPUT "Select the output filename, for example, 'Z'trans.605f'",outdatfil$
LOCATE 6,10
INPUT "What is the name of the log w (angular frequency) file";inlogwfil$
LOCATE 9,10
INPUT "What is the name of the Z"(log w) file";inzimagfil$
LOCATE 12,10
INPUT "What is the number of data points in each file";datpts%
datpts%=datpts%+2

'Typical file format:
'

'Input files:  logwexper.605f and Z"exper.605f (for file 605f)
'Output files:  "logwexper.605f" and Z'trans.605f
'Note there is actually no transformation of the frequency data itself
'So there are only three files rather than four
'----------------------------------------------------------------
'Fill the experimental data array {exper!(datpts%,2)}
'----------------------------------------------------------------

'Max data pts. arbitrarily chosen as 200 - can change
```

```
DIM exper$(200,2)
DIM exper!(200,2)

OPEN "I", #2, inlogwfil$
FOR i%=1 TO datpts%
   INPUT #2, exper$(i%,1)
   exper!(i%,1)=VAL(exper$(i%,1))
   NEXT i%
   CLOSE#2

OPEN "I", #3, inzimagfil$
FOR i%=1 TO datpts%
   INPUT #3, exper$(i%,2)
   exper!(i%,2)=VAL(exper$(i%,2))
   NEXT i%
   CLOSE#3

'---------------------------------------------------------------------------
'Generate the extended data set using the polynomial fits to the measured data
'---------------------------------------------------------------------------

CLS
LOCATE 5,10
PRINT "As a check, the extended data set will be saved"
LOCATE 10,10
INPUT "Name of the extended data set (generated data):  ",testfil$
'We will use this as a check to verify that the correct data set has been used
logstep!=.02
'Note this is the logarithmic step size for the extended data set
OPEN testfil$ FOR OUTPUT AS #1
DIM logx!(400,2)        'logx!(400,2) is the GENERATED data array
CLS
LOCATE 5,5
INPUT "Input the number of segments into which the data are divided:  ",seg%
DIM a!(6,seg%)
DIM aterm!(6,seg%)
DIM logxmin!(1,seg%)
DIM logxmax!(1,seg%)
DIM xmin!(1,seg%)
DIM xmax!(1,seg%)
FOR j% = 1 TO seg%
CLS
LOCATE 5,23
PRINT "Segment #:  ",j%
LOCATE 10,15
PRINT "The program will now generate the data for segment:",j%
PRINT
PRINT
   INPUT "Minimum log angular frequency of segment (rad/s)",logxmin!(1,j%)
   INPUT "Maximum log angular frequency of segment (rad/s)",logxmax!(1,j%)
   INPUT "Order of polynomial used to fit this segment",ord%
   imax%=0
   'Fill the polynomial Z=a0+a1*logx+a2*(logx)^2+a3*(logx)^3+a4*(logx)^4+a5*(logx)^5
   '(Note that if you plan to run the program more than once, you can open up the program
   'list and input the polynomial coefficients and max and min segment values to avoid
   'typing them in several times).
   INPUT "a0:  ",a!(0,j%)
   INPUT "a1:  ",a!(1,j%)
   IF ord%=> 2 THEN INPUT "a2:  ",a!(2,j%)
   IF ord%=> 3 THEN INPUT "a3:  ",a!(3,j%)
   IF ord% => 4 THEN INPUT "a4:  ",a!(4,j%)
   IF ord% = 5 THEN INPUT "a5:  ",a!(5,j%)
xmin!(1,j%)=10^logxmin!(1,j%)
xmax!(1,j%)=10^logxmax!(1,j%)
imax%=50*(LOG(xmax!(1,j%)/xmin!(1,j%))/LOG(10))
'Must get last point of last segment in as well - add one to imax%
IF j%=seg% THEN imax%=imax%+1
imaxseg%=imaxsum%+imax%
imaxsum2%=imaxsum%+1
FOR i%=imaxsum2% TO imaxseg%
   logx!(i%,1)=logxmin!(1,j%) + logstep!*(i%-imaxsum2%)
   a1term!(1,j%)=a!(1,j%)*logx!(i%,1)
   a2term!(2,j%)=a!(2,j%)*(logx!(i%,1))^2
   a3term!(3,j%)=a!(3,j%)*(logx!(i%,1))^3
   a4term!(4,j%)=a!(4,j%)*(logx!(i%,1))^4
   a5term!(5,j%)=a!(5,j%)*(logx!(i%,1))^5
logx!(i%,2)=a!(0,j%)+a1term!(1,j%)+a2term!(2,j%)+a3term!(3,j%)+a4term!(4,j%)+a5term!(5,j%)
   PRINT #1, logx!(i%,1);CHR$(9);logx!(i%,2);CHR$(9)
   NEXT i%
   imaxsum%=imaxsum%+imax%
NEXT j%
CLOSE #1

'~~~~~~~~~~~~~~~~~~~~~~~~~~~~~~~~~~~~~~~~~~~~~~~~~~~~~~~~~~~~~~~~
'Actual K-K transform calculations
'~~~~~~~~~~~~~~~~~~~~~~~~~~~~~~~~~~~~~~~~~~~~~~~~~~~~~~~~~~~~~~~~


CLS
LOCATE 10,10
PRINT "Calculations are now underway...there will be a delay at this point"

'Calculations cannot be made until logs are changed to linear!!

OPEN outdatfil$ FOR OUTPUT AS #4
DIM term!(imaxseg%)
DIM num!(imaxseg%)
DIM den!(imaxseg%)
DIM zre!(datpts%,1)
DIM linexper!(datpts%,2)
DIM linlogx!(imaxseg%,2)
'convert logs to linear
FOR m%= 1 TO datpts%
linexper!(m%,1) = 10^exper!(m%,1)
linexper!(m%,2) = exper!(m%,2)
NEXT m%
FOR n% = 1 TO imaxseg%
linlogx!(n%,1) = 10^logx!(n%,1)
linlogx!(n%,2) = logx!(n%,2)
NEXT n%
FOR k% = 1 TO datpts%
   FOR l% = 1 TO imaxseg%
      IF linlogx!(l%,1) = linexper!(k%,1) THEN
         term(l%) = 0
         'Above allows us to avoid dividing by zero
      ELSE
         IF l% =imaxseg% THEN
```

```
        linstep! = linlogx!(l%,1)-linlogx!(l%-1,1)
         ELSE
        linstep!=ABS(linlogx!(l%+1,1)-linlogx(l%,1))
         END IF
       num!(l%)=(linlogx!(l%,1)*linlogx!(l%,2)-linexper!(k%,1)*linexper!(k%,2))*linstep!
       den!(l%)=((linlogx!(l%,1))^2-(linexper!(k%,1))^2)
        term(l%)=num(l%)/den(l%)
      END IF
  zre!(k%,1)=zre!(k%,1) + term!(l%)
   NEXT l%
  zre!(k%,1)=zreinfin! + (2/3.1415927#)*zre!(k%,1)
PRINT #4, exper!(k%,1);CHR$(9);zre!(k%,1);CHR$(9)
NEXT k%
CLOSE #4

LOCATE 18,24
PRINT "The calculations are now complete."
LOCATE 20,25
INPUT "Please press return to continue",dum$
CLS
LOCATE 15, 15
INPUT "All done - please return to end program",dum$

STOP
END
```

10.5 Evaluation of Mechanism 2 via Linear Elastic Fracture Mechanics

In Section 6.3.4.1, two potential anodic cracking mechanisms were identified, one of which was the possibility that pits might be acting as critical flaws in the material; this possible cracking mechanism was designated mechanism 2. Mechanism 2 can be evaluated by considering the pits as semi-elliptical flaws in the metal surface; cracking can then be quantitatively analyzed using the tenets of Linear Elastic Fracture Mechanics. The mathematical relationships between stress, crack length, and stress intensity factor for this geometry are well-known, and the governing equation for a semi-elliptical flaw is [113]:

$$K = 1.12 \cdot \sigma \sqrt{\pi \cdot a} \tag{10.40}$$

where K is the stress intensity factor, σ is the stress level in the material, and a is the maximum crack length. In the present analysis, the length of the semi-elliptical flaw as a function of immersion time, $a = a\ (t)$, is equal to the pit depth at any time during the life of the material. Using the pit depth versus time data shown in Figure 5.26, it should be possible to calculate the stress intensity factor, $K = K\ (t)$, as a function of immersion time.

The stress intensity factor is an extremely important quantity, since it has been shown that this parameter ultimately controls the cracking behavior of a given material [113]. When the stress intensity factor exceeds the plane-strain fracture toughness of the material (K_{IC}), rapid and unstable fracture will occur. Plane-strain conditions are expected to prevail, since the size of the plastic zone at the crack tip should be much smaller than the thickness of the test sample. The validity of assuming the plane-strain condition is verified at the end of the present section.

The main obstacle to calculating the stress intensity factor using equation [10.40] is that the stress level in the material is unknown, because the stresses are residual rather than applied. A quantitative determination of the residual stress level in the material is difficult to make, even if x-ray diffraction methods are utilized. The stress intensity factor thus cannot actually be determined as a function of time for the samples utilized in this study. The inability to calculate this parameter is a significant drawback, since it precludes an effective comparison of K (t) to the measured fracture toughness of the material. The fact that the residual stress level in the test samples is unknown indicates that an alternative approach to equation [10.40] must be used in order to quantitatively evaluate the fracture of Nd-Fe-B.

Equation [10.40] can be rearranged in the following form:

[10.41]
$$\sigma_{res} = \frac{K}{1.12 \cdot \sqrt{\pi \cdot a}}$$

As stated above, the primary purpose of the calculations is to evaluate the validity of mechanism 2 cracking at 9 days of immersion. For this condition, both of the variables on the right side of Equation [10.41] are known, as K must be equal to K_{IC} at fracture and a is the maximum pit depth at 9 days. Equation [10.41] can therefore be solved for the value of residual stress needed to cause mechanism 2 cracking after 9 days of immersion.

The crack length at 9 days was estimated using the pit depth versus time plot shown in Figure 5.26, from which the maximum pit depth at 9 days was taken as 31 μm via interpolation. A plane-strain fracture toughness of approximately 2.05 MPa$\sqrt{m}$ has been determined for Nd-Fe-B (alloy composition: Nd16-Fe76-B8) [114]. Using Equation [10.41], it is found that the residual stress in the material must be equal to 186 MPa in order that mechanism 2 fracture would be observed after 9 days of immersion.

There are two possible ways to determine if the calculated value represents a reasonable residual stress level in this material. The obtained value will first be compared to the estimated yield stress of Nd-Fe-B, and then to the magnitude of tensile residual stresses imparted to a similar material by a conventional machining process.

The maximum residual stress level permissible in a material is equal to its yield stress, since residual stresses greater than this level would result in plastic flow and a subsequent relaxation of residual stresses below the yield point. If the calculated residual stress needed to cause unstable fracture with a critical crack length of 31 μm were greater than the yield stress, a pit clearly could not be serving as a critical crack after 9 days of immersion (i.e. mechanism 2 would be invalid). Although a yield strength value has not been determined experimentally for Nd-Fe-B, an estimate of σ_{ys} can be developed by using an empirical relationship known to hold for brittle materials (such as Nd-Fe-B) [115]:

$$[10.42] \qquad 0.8 \cdot \sigma_{uts} \leq \sigma_{ys} \leq 0.9 \cdot \sigma_{uts}$$

The ultimate tensile strength (σ_{uts}) of Nd-Fe-B has been determined as 800 MPa, and the yield strength of the material is then approximately 640 - 720 MPa according to equation [10.42]. The residual stress necessary to cause fracture at a critical crack length of 31 μm (186 MPa) is therefore seen to be significantly less than σ_{ys}, and is thus seen to be a permissible residual stress value for this material. The residual stress level necessary to cause mechanism 2 cracking after 9 days is only about one-third of the estimated yield strength of the material.

It is not unreasonable to expect that a machining treatment might result in the generation of residual stress levels of 186 MPa or more. Residual stresses generated by the machining of hardened steel have previously been measured, as shown in Figure 6.15. The hardness of

Nd-Fe-B is known to be similar to that of hardened steel. Since a gentle machining treatment results in compressive rather than tensile stresses at the metal surface according to Figure 6.15, the machining treatment performed on the present samples must be classified as either conventional or abusive, in order to explain the observed cracking in the absence of applied stress. Conventional or abusive grinding can lead to the generation of significant residual stresses at or just below the metal surface, according to Figure 6.15. The maximum tensile stress generated by conventional grinding was approximately 90 ksi, which corresponds to 620 MPa. A conventional machining treatment is therefore clearly capable of producing residual stresses of more than 186 MPa, which is the residual stress level needed to produce unstable cracking after 9 days, if pits are assumed to serve as the critical cracks in Nd-Fe-B (mechanism 2). The foregoing analysis clearly indicates that pits *could* possibly be directly involved in the observed APC cracking by acting as critical cracks.

The viability of mechanism 2 relies upon the supposition that a semi-elliptical crack 31 μm in length can directly induce rapid, unstable fracture. The prediction of 31 μm as a critical crack length merits further analysis, as this value is considerably lower than the critical value determined in other materials. It is qualitatively expected that the critical crack length in Nd-Fe-B would be substantially lower than the value of a* determined for other metals, since the presence of the brittle intermetallic $Nd_2Fe_{14}B$ leads to a very low fracture toughness for Nd-Fe-B. The feasibility of 31 μm as a critical crack length in residually stressed Nd-Fe-B can be evaluated using Table 10.6, which contains a* values for two other metals (cast Fe, Ti-6Al-4V) under the same cracking conditions assumed to be present if mechanism 2 leads to failure after 9 days (i.e. semi-elliptical flaw, σ_{res} = 186 MPa).

Table 10.6 Plane-strain fracture toughness values for three metals, and the resulting critical crack lengths assuming that the critical flaw is semi-elliptical and that the residual stress level in the metal is 186 MPa.

Material	K_{IC} (MPa-$\sqrt{m}$)	a* (mm)
Nd-Fe-B	2	0.03
Cast Fe	20	2.9
Ti-6Al-4V	60	26.4

It is observed that the critical crack length is highly dependent upon the value of K_{IC}. The reason for this strong dependence can be observed by setting a equal to a* and K equal to K_{IC} in Equation [10.40] (i.e. assuming fracture conditions) and then rearranging the equation to solve for a*:

$$a^* = \frac{K_{IC}^2}{1.12^2 \cdot \sigma^2 \cdot \pi} \qquad [10.43]$$

which shows that for a given level of stress, a ten-fold increase in fracture toughness results in a one hundred-fold increase in critical crack length. The most important aspect of Table 10.6 is its demonstration that because of the extreme brittleness of Nd-Fe-B, it is reasonable to conclude that a microcrack in this material can be just as severe in terms of its propensity to cause fracture as a macroscopically observable crack in many other metals.

As discussed in Section 6.3.4.1, although it was not mathematically possible to adjudicate between mechanisms 1 and 2 using quantitative fracture mechanics, it appears that a more simple method can be used to eliminate mechanism 2 as a cause of the observed cracking. Small, macroscopically visible chips were observed to be present on several of the machined samples used in the present study. The chipping of the samples presumably occurred during machining. Most of these chips were small in dimension, but were clearly greater than 31 μm in size. If the critical crack length in the material were indeed 31 μm (as required for the validity of mechanism 2), it would be expected that such surface discontinuities would have resulted in rapid cracking. The fact that such cracking was not observed appears to be inconsistent with the proposed mechanism 2. It thus appears that either mechanism 1 cracking or an alternative mechanism such as corrosion product wedging is responsible for the observed fracture.

It is emphasized at this point that the quantitative fracture mechanics analysis described above is still valuable, since it demonstrates several useful concepts regarding the anodic fracture of Nd-Fe-B. First of all, the critical crack length in the material will be far less than than in other metals under similar stress conditions. The above analysis has also quantitatively demonstrated the sensitivity of the material to residual stress in terms of the effect of this stress on the critical crack length in the material. If a lower residual stress level is imparted to the samples, a larger critical crack will be needed to cause unstable fracture, which agrees with the experimental evidence obtained on machined and non-machined samples in the present study. The calculation also shows that abusive machining treatments can conceivably lead to stresses which will result in extremely small critical crack lengths for the material, which is a dangerous condition in terms of its susceptibility to fracture. The above analysis also provides a quantitative introductory basis for further study.

10.5.1 Verification of Plane-Strain Condition in EAC Tests

Plane-strain conditions are obtained when the size of the plastic zone at the crack tip, r_y, is small relative to the sample thickness in a direction perpendicular to the crack propagation direction, t. The specific criterion utilized to define plane-strain conditions is [113]:

$$\frac{r_y}{t} \leq 0.1 \qquad [10.44]$$

An estimate of the parameter r_y can be obtained using the following equation [113]:

$$r_y \cong \frac{1}{2\pi} \cdot \frac{K^2}{\sigma_{ys}{}^2} \qquad [10.45]$$

where K will be assumed equal to K_{IC} at the time of fracture. Using the yield strength estimate in Section 6.3 ($\sigma_{ys} \sim 680$ MPa), r_y is estimated as 1.45 µm. This value indicates that a thickness value greater than 14.5 µm will correspond to the plane-strain condition. It is difficult to accurately determine t for cylindrical geometry. However, a reasonably good estimate of this parameter can be made by evaluating the distance from one end of the cylinder to the other at the tip of the propagating flaw. For simplicity, this flaw will be assumed to take the form of a growing pit at the time of fracture, as shown in Figure 10.36. The value of t shown in Figure 10.36 can be evaluated using geometrical considerations, as shown in Figure 10.37. The distance from the center of the cross-section to the base of the pit is the cross-section radius (3000 µm) minus the maximum pit depth measured after 9 days (31 µm), which equals 2969 µm. The hypotenuese of the triangle shown is clearly equal to the radius of the cross-section, and the value of t/2 can thus be evaluated using the Pythagorean theorem. A value of 860 µm was calculated for t, which indicates that plane-strain conditions are controlling the experiment in question.

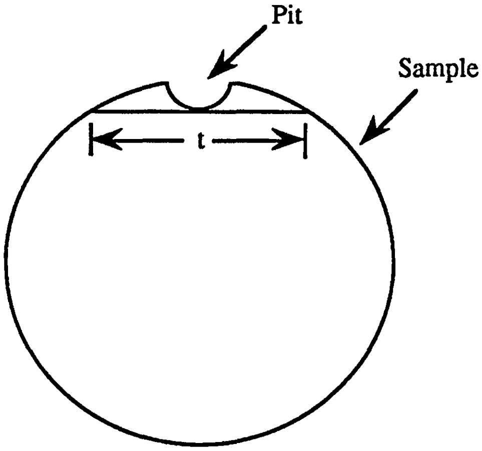

Figure 10.36 Estimate of the thickness at the tip of a growing pit in the cylindrical samples used for the EAC investigation.

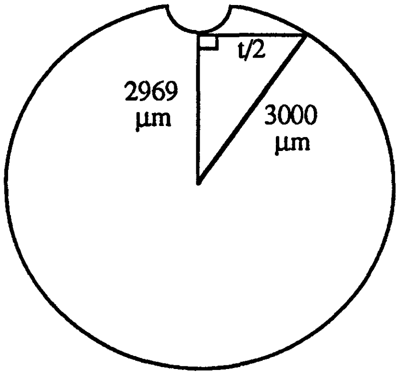

Figure 10.37 Determination of the thickness, t, after 9 days of immersion, using geometric considerations.

Several assumptions were made in the above derivation. The K value in equation [10.45] was assumed to equal K_{IC}, and the critical flaw was assumed to be a propagating pit. Any errors resulting from such assumptions are not expected to alter the results of the estimate, owing to the fact that the estimated value of t (860 µm) is so much larger than the minimum value of t needed for the plane-strain condition (14.5 µm).

11. Bibliography

1. L. R. Moskowitz, "Fundamentals of Magnetism", *Permanent Magnet Design and Application Handbook*, Krueger Publishing, Malabar, FL, 1986, p. 35.
2. S.G. Sankar, *JOM*, 43 (2), 1991, p. 30.
3. D. Howe, *Magnetism and Magnetic Materials*, p. GC-01.
4. K. Mitchell, *Can. Eng. Digest*, **35** (1) 1989, p. 51.
5. P. G. Boswell and T. Bercé, "The Economic Impact of Nd-Fe-B Magnets", *European Research on Materials Substitution*, I.V. Mitchell , P. Nosbusch (Eds.), p. 241.
6. L. Christensen, "Ferrites, Sm-Co, NdFeB in Motors a Comparative Study", *Hard and Soft Magnetic Materials with Applications Including Superconductivity*, TMS, Warrendale, 1987, p. 81.
7. J.F. Herbst, R.W. Lee, and F.E. Pinkerton, *Ann. Rev. Mater. Sci.*, **16**, 1986, p. 467.
8. R. Ramesh, J.K. Chen, G. Thomas, and L.K. Rabenberg, "Microstructure and Properties of Rare Earth Magnets", *Hard and Soft Magnetic Materials with Applications Including Superconductivity,* TMS, Warrendale, 1987, p. 1.
9. J.J. Croat and J.F. Herbst, *Mater. Res. Soc. Bull.*, **13** (1988) 37.
10. E.A. Nesbitt and J.H. Wernick, *Rare Earth Permanent Magnets*, Academic Press, New York, 1973, p. 1.
11. R.S. Tebble and D.J Craik, *Magnetic Materials*, Wiley-Interscience, London 1969, p. 412.
12. J. F. Shackleford, *Introduction to Materials Science for Engineers*, Macmillian, New York, 1985, p. 493.
13. A.L. Robinson, *Science,* **223** (1984) 920.
14. J.W. Fiepke, "Applications of NdFeB Permanent Magnets", *Hard and Soft Magnetic Materials with Applications Including Superconductivity*, TMS, Warrendale, 1987, p. 75.
15. K.S.V.L. Narasimhan, *J. Appl. Phys.* **57** (1985) 4081.
16. Gorham Advanced Materials Institute, "The Impact of Nd-Fe-B Magnets on the Permanent Magnet Industry in the 1990's": Executive Summary, 1989.
17. R.W. Lee, *Appl. Phys. Lett.* **46** (1985), p. 790.
18. Magnequench Application Bulletin, (Magnequench a Business Unit of Delco Remy, Division of General Motors, 1988).

19. R. Mason, Magnequench, personal communication, August, 1995.

20. R.K. Mishra, *J. Appl. Phys.*, **61** (1987) 3778.

21. R.K. Mishra, *J. Appl. Phys.*, **64** (1988) 5562.

22. T. Chu *et al.*, *J. Appl. Phys.*, **69** (1991) 6046.

23. A. Hutten and P. Haasen, *Scripta Met.*, **21** (1987) 407.

24. L. Li, D.E. Luzzi, C.D. Graham Jr., *J. Appl. Phys.*, **70** (1991) 6459.

25. R.K. Mishra, *J. Magn. Magn. Mater.*, **54-57** (1986) 450.

26. R.K. Mishra and R.W. Lee, *Appl. Phys. Lett.*, **48** (1986) 733.

27. J.F. Herbst and J.J. Croat, *J. Magn. Magn. Mater.*, **100** (1991) 57.

28. R.W. Lee, *Appl. Phys. Lett.*, **46** (1985) 790.

29. J.D. Livingston, *Proceedings of the Eighth International Workshop on Rare Earth Magnets and Their Applications*, K.J. Strnat (Ed.), Univ. of Dayton Press, Dayton, 1985, p. 423.

30. J. Fidler and K.G. Knoch, *J. Magn. Magn. Mater.*, **80** (1989) 48.

31. P. Shuming, L. Jinfang and L. Helie, *J. Magn. Magn. Mater.*, **89** (1990) 79.

32. J.F. Herbst, J.J. Croat, F.E. Pinkerton and W.B. Yelon, *Phys. Rev. B*, **29** (1984) 4176.

33. R.K. Mishra, *J. Mater. Eng.*, **11** (1989) 87.

34. J. Fidler and L. Yang, *Proceedings of the Eighth International Workshop on Rare Earth Permanent Magnets and their Applications*, K.J. Strnat (Ed.), Univ. of Dayton Press, Dayton, 1985, p. 647.

35. M. Tokunaga, M. Tobise, N. Meguro and H. Harada, *IEEE Trans. on Magnetics*, MAG-22, 1986, p. 904.

36. K. Hiraga, M. Hirobayashi, M. Sagawa, and Y. Matsuura, *Jpn. J. Appl. Phys.*, **24** (1985) 699.

37. Y. Matsuura, S. Hirosawa, H. Yamamoto, S. Fijimura, M. Sagawa, and K. Osamura, *Jpn. J. Appl. Phys.*, **24** (1985) L635.

38. J. Fidler, *Proc. 5th International Symposium on Magnetic Anisotropy and Coercivity in Rare Earth-Transition Metal Alloys*, C. Herget, H. Kronmuller, and R. Poerschke (Eds.), Bad Soden, FRG, vol. 2 , 1987, p. 363.

39. J. Fidler, *IEEE Trans. on Magnetics,* MAG-21, 1985, p. 1955.

40. W. Tang, S. Zhou, R. Wang, C.D. Graham, Jr., *J. Appl. Phys.*, **64** (1988) 5516.

41. R.K. Mishra, *J. Appl. Phys.*, **62** (1987) 967.

42. R. Ramesh, J.K Chen, and G. Thomas, *J. Appl. Phys.*, **61** (1987) 2993.

43. K. Ohashi, Y. Tawara, T. Yokoyama and N. Kobayashi, *Proceedings of the Ninth International Workshop on Rare-Earth Magnets and their Application*, Bad Soden, FRG, 31 August - 2 September, 1987, Deutche Physikalishe Gesellshaft, p. 355.

44. S. Hirosawa, S. Mino, and H. Tomizawa, *J. Appl. Phys.*, **69** (1991) 5844.

45. R.K. Mishra, J.K Chen and G. Thomas, *J. Appl. Phys.*, **59** (1986) 2244.

46. M. Sagawa, S. Hirosawa, H. Yamamoto, S. Fujimura, and Y. Matsuura, *Jpn. J. Appl. Physics*, **26** (1987) 785.

47. T. Minowa, M. Yoshikawa and M. Honshima, *IEEE Trans. Magn.*, **25** (1989) 3776.

48. P. Campbell, *Permanent Magnet Materials and Their Application*, Cambridge University Press, Cambridge UK, 1994, p. 77.

49. H. Bala, S. Szymura, J.J. Wyslocki, *J. Mater. Sci.*, **25** (1990) 571.

49a. H. Bala, S. Szymura, M. Rabinovich, V.V. Sergeev, G. Pawlowska, and D. V. Pokrowskii, *Revue Phys. Appl.*, **25** (1990) 1205.

50. T.S. Chin, R.T. Chang, W.T. Tsai, and M.P. Hung, *IEEE Trans. Magn.*, **24** (1988) 1927.

51. G.W. Warren, G. Gao, and Q. Li, *J. Appl. Phys*, **70** (1991) 6609.

52. K. Kang, B. Kim, and J. Song, *J. Mat. Sci: Mat. in Electron.*, **6** (1995) 4.

53. J. Shain, Magnequench, personal communication, May, 1993.

54. K. Sugimoto, T. Sohma, T. Minowa, M. Honshima, *Japan Metals Society Fall Meeting*, 1987, p. 604.

55. D.F. Cygan and M.J. McNallan, *J. Magn. Magn. Mater.*, **139** (1995) 131.

56. P.J. McGuiness, A. Ahmed, D.G.R. Jones, I.R. Harris, S. Burnsd, and E. Rozendaal, *J. Appl. Phys.*, **67** (1990) 4626.

57. T. Minowa, Magnequench, personal communication, August, 1994.

58. R. Mason, Magnequench, personal communication, July, 1995.

59. C.J. Willman and K.S.V.L. Narasimhan, *J. Appl. Phys.*, **61** (1987) 3766.

60. T. Minowa, M. Yoshikawa and M. Honshima, *IEEE Trans. Magn.*, **25** (1989) 3776.

61. A.S. Kim and J.M. Jacobson, *IEEE Trans. Magn.*, Vol. MAG-23, 1987, p. 2509.

62. A.S. Kim, F.E. Camp, and S. Constantinides, *Corrosion of Electronic and Magnetic Materials*, ASTM STP 1148, P.J. Peterson (Ed.), ASTM, Philadelphia, 1992, p. 68.

63. O. S. Abdul-Hamid, *Diffusion of Hydrogen in Titanium*, PhD Thesis, MIT, 1993.

64. M.G. Fontana, *Corrosion Engineering*, 3rd ed., McGraw-Hill, New York, 1986.

65. E. J. Kelly, *J. Electrochem. Soc.*, **124** (1977) 987.

66. D. Halliday and R. Resnick, *Fundamentals of Physics*, 2nd ed., John Wiley & Sons, New York, 1986.

67. J.L. Dawson and M.G.S. Ferreira, *Corrosion Sci.*, **26** (1986) 1009.

68. J.L. Dawson and M.G.S. Ferreira, *Corrosion Sci.*, **26** (1986) 1027.

69. J. Mankowski and Z. Szklarska-Smialowska, *Corrosion Sci* ., **15** (1975) 493.

70. P.Q. Zhang, J.X. Wu, W.Q. Zhang, X.Y. Lu, and K. Wang, *Corrosion Sci.*, 34 (1993) 1343.

71. D. Sinigaglia, G. Rondelli, G. Taccano, B. Vincentini, G. Dallaspezia, L. Galelli, B. Bazzoni, *Werkst. Korros.*, **31** (1980) 855.

72. Z. Szklarska-Smialowska, *Pitting Corrosion of Metals*, NACE, Houston, 1986, p. 302.

73. E. McCafferty, *J. Electrochem. Soc.*, **126** (1979) 385.

74. R.M. Kain, T.S. Lee, and J.W. Oldfield, "Use of Electrochemical Techniques for the Study of Crevice Corrosion in Natural Seawater", *Electrochemical Techniques for Corrosion Engineering*, R.Baboian (Ed.), NACE, Houston, 1986, p. 261.

75. Z. Szklarska-Smialowska, *Pitting Corrosion of Metals*, NACE, Houston, 1986, p. 321.

76. R. Mason, Magnequench, personal communication, August, 1995.

77. B.E. Wilde, *Corrosion*, **27** (1971) 326.

78. R.M. Latanision, O.H. Gastine, and C.R. Compeau, "Stress Corrosion Cracking and Hydrogen Embrittlement: Differences and Similarities", *Proceedings of the Enviornment-Sensitive Fracture of Engineering Materials Symposium*, Z.A. Foroulis (Ed.), TMS-AIME, Warrendale, 1977, p. 48.

79. H.W. Pickering and R.P. Frankenthal, *J. Electrochem. Soc.*, **119** (1972) 1297.

80. J.H. Shivley, R.F. Hehemann, and A.R. Troiano, *Corrosion*, **23** (1967) 215.

81. R.J. Gest and A.R. Troiano, *Corrosion*, **30** (1974) 274.

82. B.E. Wilde and C.D. Kim, *Corrosion*, **28** (1972) 350.

83. Z. Szklarska-Smialowska, *Pitting Corrosion of Metals*, NACE, Houston, 1986, p. 352.

84. W.F. Linke, *Solubilities of Inorganic and Metal Organic Compounds*, Van Nostrand, Princeton, 1958, p. 1190.

85. Society of Automotive Engineers Information Report: *Residual Stress Measurement by X-Ray Diffraction - SAE J784a*, 2nd ed., SAE, New York, 1971, p.5.

86. W.M. Baldwin Jr., "Residual Streeses in Metals", *Proceedings of the American Society for Testring Materials,* **49** (1949) 40.

87. D.A. Jones, *Principles and Prevention of Corrosion*, Macmillian, New York, 1992, p. 238.

87a. J.H. Chun, *Modeling of Chemistry Related to Enviornmentally Assisted Cracking in Low-Alloy Steels*, PhD Thesis, MIT, 1990, p.26.

88. R.N. Parkins, *Enviornment-Induced Cracking of Metals*, R.P. Gangloff and M.B. Ives (Eds.), NACE, Houston, 1990, p. 1.

89. E. Han, Chinese Academy of Sciences, personal communication, August, 1995.

90. H.W. Pickering, *Corrosion*, **42** (1986) 125.

91a. F. Mansfield and E.P. Parry, *Corrosion Sci.*, **13** (1973) 605.

91b. L.H. Hihara and R.M. Latanision, *Corrosion*, **48** (1992) 546.

91c. K. Hosoya, R. Ballinger, J. Pryblowski, and I.S. Hwang, *Corrosion*, **44** (1988) 838.

91d. J.R. Galvele ans S.M. De Micheli, *Corrosion Sci.*, **10** (1970) 795.

91e. J.C. Rowlands, *Corrosion Sci.*, **2** (1962) 89.

92. M. Pourbaix, *Atlas of Electrochemical Equilibria in Aqueous Solutions,* NACE, Houston, 1974, pp. 163, 193, 312.

93. C.G. Munger, *Corrosion Prevention by Protective Coatings*, NACE, Houston, 1984, p. 129.

94. L.H. Hihara, *Corrosion of Aluminum-Matrix Composites*, PhD Thesis, MIT, 1989.

95. M.A. Buonanno, *The Effect of Processing Conditions and Chemistry on the Electrochemistry of Graphite and Aluminum Metal Matrix Composites*, PhD Thesis, MIT, 1992.

96. J.F. Herbst , R.W. Lee, and F.E. Pinkerton, *Ann. Rev. Mater. Sci.*, **16** (1986) 467.

97. A. Glassner, "The Thermochemical Properties of the Oxides, Flourides, and Chlorides to 2500°K", Argonne National Laboratory, Argonne, Illinois, ANL-5750, Oct. 1965.

98. D.R. Gaskell, *Introduction to Metallurgical Thermodynamics*, 2nd ed., McGraw-Hill, New York, 1973.

99. R. A. Sharma, *JOM*, **39** (2), 1987, p. 33.

100. H. Anton, *Calculus with Analytical Geometry*, 2nd ed., John Wiley & Sons, New York, 1984.

101. F. Mansfield, S. Lin, S. Kim, and H. Shih, *J. Electrochem. Soc.*, **137** (1990) 78.

102. M. Urquidi-Macdonald, S. Real, and D.D. Macdonald, *J. Electrochem. Soc.*, **133** (1986) 2018.

103. B.J. Dougherty and S.I. Smedley, "Validation of Experimental Data from High Impedance Systems Using the Kramers-Kronig Transforms", *Electrochemical Impedance: Analysis and Interpretation*, ASTM STP 1188, J.R. Scully, D.C. Silverman, and M.W. Kendig (Eds.), ASTM, Philadelphia, 1993, p. 154.

104. H.A. Kramers, *Phys. Z.*, **30** (1929) 521.

105. R. de L. Kronig, *J. Opt. Soc. Am.*, **12** (1926) 547.

106. J.R. Macdonald, *Impedance Spectroscopy Emphasizing Solid Materials and Systems*, John Wiley & Sons, New York, 1987.

107. J.R. Park and D.D. Macdonald, *Corrosion Sci.*, **23** (1983) 295.

108. A.J. Bard and L.R. Faulkner, *Electrochemical Methods Fundamentals and Afploications*, John Wiley & Sons, New York, 1980, p. 8.

109. F. Mansfield. M.W. Kendig, and W.J. Lorenz, *J. Electrochem. Soc.*, **132** (1985) 290.

110. P.Q. Zhang, J.X. Wu, W.Q. Zhang, X.Y. Lu, and K. Wang, *Corrosion Sci.*, **34** (1993) 1343.

111. D. R. Franceschetti and J.R. Macdonald, *J. Electrochem. Soc.*, **82** (1977) 271.

112. C. Gabrielli, M. Keddam, and H. Takenouti, "Kramers-Kronig Transformation Relation to the Interface Regulating Device", *Electrochemical Impedance: Analysis and Interpretation*, J.R. Scully, D.C. Silverman, and M.W. Kendig (Eds.), ASTM, Philadelphia, 1993, p. 140.

113. R.W. Hertzberg, Deformation and Fracture Mechanics of Engineering Materials, 2nd ed., John Wiley & Sons, New York, 1983.

114. S. Szymura, Y.M. Rabinovich, H. Bala, and A.D. Maysterenko, *J. Phys.: Condens. Matter*, **6** (1994) 3573.

115. E. Han, Chinese Academy of Sciences, personal communication, July, 1995.

12. Biographical Note

The author was born on June 5, 1967 to Madeline and Arthur Attanasio of Queens, New York. He lived in Queens until the age of eight, when the birth of his twin brothers forced the family to move to a larger home in suburban Westwood, New Jersey. Over the next several years, the author's main interests included baseball, wrestling, rock music, and hanging out with his friends. He graduated from Westwood High School in June 1985.

The author moved on to study engineering at Lafayette College in Easton, Pennsylvania. He joined the Phi Kappa Psi fraternity and spent his first two years either studying or attending critical fraternity events (parties), with little time for sleep. At the beginning of his junior year, he chose to major in metallurgical engineering, and also began dating Cathy Jordan, a classmate whom he had known since early in their freshman year. The author was elected President of his fraternity, and spent his time writing lab reports and pleading with the dean not to place Phi Psi on probation. He graduated from Lafayette in May 1989.

The author began his graduate work in September 1989. Cathy simultaneously enrolled in a Ph.D program at Lehigh University, thus beginning the longest weekend romance in history. After passing his qualifying examinations, the author spent three months as a summer research intern at the Naval Surface Warfare Center in Annapolis. The author was dedicated to his thesis work during the next few years. Visits with his friends, family, and girlfriend helped him retain his sanity. Steve and Cathy were engaged in September 1993.

The author has accepted a job to work at the Knolls Atomic Power Laboratory in the fall of 1995. He will be working on corrosion problems in the steam generator section of the nuclear engines used to propel U.S. Naval submarines. His fianceé has accepted a job as a physical metallurgist in the same laboratory. The couple plans to be married on October 21 (1995), and will then reside in Clifton Park, New York (outside of Albany).